Study of the Far Infrared Emission of Nearby Spiral Galaxies

Willie Drouhet

UNIVERSITÉ PARIS SUD

Comprendre le monde, construire l'avenir®

DE LA RECHERCHE À L'INDUSTRIE

cea

Université Paris-Sud

Ecole Doctorale 127 :
Astronomie et astrophysique d'Ile-de-France
Laboratoire : CEA

Discipline : Astrophysique

Thèse de doctorat

Soutenue le 07/11/2013 par

Willie Drouhet

Etude de l'émission dans l'infrarouge lointain des galaxies spirales proches

Directeur de thèse :	Marc Sauvage	Directeur de recherche (CEA Saclay)
Composition du jury :		
Rapporteurs :	Maarten Baes	Directeur de recherche (Université de Gent)
	Alessandro Boselli	Directeur de recherche (Laboratoire d' Astrophysique de Marseille)
Examinateurs :	Alain Abergel	Professeur (Institut d' Astrophysique Spatiale)
	Jonathan Braine	Directeur de recherche (Université Bordeaux 1)

Contents

About this thesis, research, dust and galaxies...

The way I pass never yet was run - Dante - Divine Comedy

We are all very ignorant, but not all ignorant of the same things - Albert Einstein
Quand le danger nous semble léger il cesse de l'être - Francis bacon
Is it not careless to become too local when there are [hundreds of] billions of stars in our galaxy alone - A. R. Ammons
Dusting is a good example of the futility of trying to put things right. As soon as you dust, the fact of your next dusting has already been established - George Carlin

Men think highly of those who rise rapidly in the world; whereas nothing rises quicker than dust, straw, and feathers - Lord Byron
Your idol is shattered in the dust to prove that God's dust is greater than your idol - Rabindranath Tagore
I'm not a prophet, but I always thought it was natural for dictatorships to fall. I remember in 1989, two months before the fall of the Berlin Wall, had you said it was going to happen no one would have believed you. The system seemed powerful and unbreakable. Suddenly overnight it blew away like dust - Salman Rushdie
I consider the positions of kings and rulers as that of dust motes. I observe treasures of gold and gems as so many bricks and pebbles. I look upon the finest silken robes as tattered rags. I see myriad worlds of the universe as small seeds of fruit, and the greatest lake on Earth as a drop of oil on my foot - Buddha

Mourning is not forgetting... It is an undoing. Every minute tie has to be untied and something permanent and valuable recovered and assimilated from the dust - Margery Allingham

Tout ce qui est, est passé - Anatole France

Introduction

In this thesis we will mainly focus on the stellar emission and interstellar dust emission of nearby disk galaxies.

However we will first highlight a few processes known to have occured during the formation of these objects so as to clarify how these processes are related to the presently observed physical content and morphological aspects of disk galaxies. In the following section we will do so by discussing successively the main stages of disk galaxy formation.

We will in a subsequent section elaborate upon the morphology of galaxies in the nearby universe in the optical and the near infrared (NIR). We will thereafter confine our study to disk galaxies and discuss their gaseous and stellar content. We will then detail the links between these latter phases and the dust phase inside these galaxies, while also reviewing structures observed in the dust phase and the dust emission.

After this detailed introduction on the context of this thesis, we will state a few central issues this work specifically adresses, then explicit the galaxy sample we will study and why we chose to study it. At this point we will give the layout of this work and explain in more details the spirit in which it was drawn up.

Formation of disk galaxies

Before first disk galaxies formed ...

Since the Big Bang, matter concentrated under gravity to form aggregates named stars as well as huge assemblies of stars, gas and dust that we name galaxies. We will now catch the main steps of these processes.

At present, it is common knowledge that the farthest celestial phenomenon whose light can be detected is the Cosmic Microwave Background (CMB).

This is the testimony to ages approximately 13.79 billion years ago (as found by Planck Collaboration, 2013b) roughly 378,000 years after the Big Bang (at redshift[1] $z = 1090.51 \pm 0.95$, see Hinshaw et al., 2009), when our universe was much hotter ($\sim 3000\ K$) and homogeneous than today. This prompts the question of how did the Universe became as inhomogenous as it is seen today on the galactic scales? The CMB is a signature of the universe going from an opaque plasma to a neutral transparent gas. At this epoch long after Big Bang baryogenesis and nucleosynthesis (see Steigman, 2007), the universe already has a visible matter content dominated by hydrogen and helium in proportions very close to the one it harbours at present.

Although already created, visible matter was not substantially gathered together. Before this happened to be the case, the universe first expanded and cooled. One of the main components

[1] We assume standard cosmology with $H_0 = 67.3 \pm 1.2\, km/s/Mpc$, so we refer to Carmeli et al. (2006), Macdonald (2013) and Planck Collaboration (2013a) for an easy relation between cosmic times and redshifts.

of the mass-energy budget of the universe, namely dark matter, condensated into significantly large and dense clumps under the gravitational influence of previously existing but tiny inhomogeneities (see van der Kruit and Freeman, 2011). These clumps in turn relaxed to virial equilibrium, their angular momentum having been acquired from cosmological torques (see Dutton, 2009 and Governato et al., 2012).

Only then these clumps gravitationally attracted visible matter, as well as more dark matter.

The currently observed distribution of specific angular momentum (angular momentum per unit mass) of disk galaxies suggest very specific formation scenarios (although uncertainties remain, see Dutton and van den Bosch, 2012). Namely, the infalling gas is traditionnally deemed to have been shock-heated (see Wang and Abel, 2008) to the dark halo virial temperature, even though some studies showed the important role played by "cold-mode" filamentary gaseous infalls for which shock-heating is less efficient (see Stewart et al., 2013, Dubois et al., 2012). In the shock-heating scenario the distribution of specific angular momentum assumed to be first acquired by baryons, after shock-heating is the same as that of the pre-existing dark matter halo. As brought forward by Dalcanton et al. (1997), Mestel et al. (1963) showed that the angular momentum distribution of a galactic disk is very similar to that of a sphere in solid body rotation. Thus it was then assumed that the collapse of a uniformly rotating gaseous protogalaxy was a good model for disk formation. As explained in Kaufmann et al. (2006), to obtain the observed exponential decrease of stellar density with radius, very little angular momentum transport is expected to have occured in the gas while it was collapsing inside dark halos. It is also expected that the angular momentum is responsible for eventually halting the collapse and that dark halos originally have a radial density profile such that the observed rotation velocity profile of disks are mainly flat at large distances from the center (see Dalcanton et al., 1997).

The gas then necessarily cooled radiatively from inside out as shown by the bluer colors of outer regions of disk galaxies (see Wang et al., 2011) as well as their decreasing dust content with increasing galacto-centric radius (see Muñoz-Mateos, 2012).

Thereafter, the relative timing of disk formation with respect to the first main star formation episodes is constrained by the dynamics of disk galaxies. More precisely as explained by van der Kruit and Freeman (2011), and because stellar content is mainly non dissipative, the observation of disks close to centrifugal equilibrium entails that disks formed before the onset of the main star formation episode.

Two other characteristics of disk galaxies, their prevalence and fragility, shed light on their subsequent growing process. For instance, as galactic disks are as well very easily "puffed up" by mergers (see van der Kruit and Freeman, 2011) and ubiquitously observed, they are thought to be alternatively destroyed by mergers and reformed by gas accretion. This process is thought to have occured from the very early times. Furthermore if disks are destroyed/thickened during mergers, as the majority of stellar mass resides in disks in the local Universe, the dominant galaxy formation mechanism that leads to galaxies currently observed cannot be merger driven, and is rather, presumably, the more quiescent process of cold gas accretion (see Driver et al., 2013).

Once the first disks were formed, the gas they contained condensed to much higher densities (see Naoz et al., 2008) and formed stars quiescently.

In finer details, star formation occured at different paces in different environments. For example, most intense star forming episodes occured in smaller systems as cosmic time went by. But the formation of small scale high-density structures such as stars has to be distinguished from the build-up of structures as large as or larger than galaxies. On these larger scales, smaller

agregates of matter, e.g. galaxies, appeared first before gravity and mass acquisition resulted in production of larger ones (see Searle and Zinn, 1978).

It was shown that the first generation of stars had specific consequences on galaxy formation processes and evolution. The CMB temperature had to decrease to lower than 60 K ($z < 20$) before the first stellar objects, preferentially massive fast-spinning stars (see Chiappini et al., 2011; Jaskot and Oey, 2013), forming between 150 million and one billion years after the Big Bang (see for instance Becker et al., 2001; Bond et al., 2013), very probably caused reionization of interstellar and intergalactic medium (see figure 1 for a schematic view of reionization; Bovill and Ricotti, 2009, Morales and Wyithe, 2010 for details about reionization; McKee and Ostriker, 2007 for star formation processes). Reionization is expected to have had a significant regulatory role in galaxy formation for instance by impeding gas cooling (see Dutton, 2009) notably in dwarf galaxies.

It can be noted here that galaxy formation and evolution in the early universe is peculiar (see Bovill and Ricotti, 2009) because of the lack of efficient cooling elements (C, O, etc.) and the small sizes of dark matter halos. Cooling elements have been shown to be crucial to star forming processes in local galaxies because more cooling elements could enable gas clouds to cool more quickly therefore enhancing their capability to contract and form stars. Without such elements, stellar feedback on molecular gas creation occuring in pre-reionization era was shown to be strongly different from molecular gas creation processes in local galaxies.

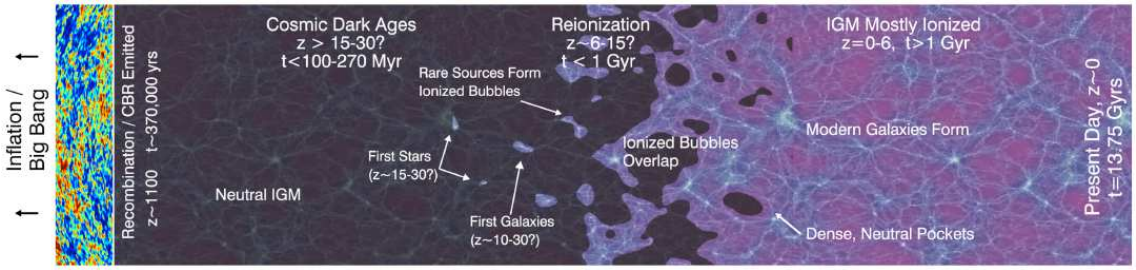

Figure 1: A picture illustrating the cosmic reionization taken from Robertson et al. (2010). The transition from the neutral intergalactic medium (IGM) left after CMB emission, to the fully ionized IGM observed today is named cosmic reionization. Hydrogen in the IGM remained neutral until the first stars and galaxies formed at $z \sim 15 - 30$. These primordial systems released energetic ultraviolet photons capable of ionizing local bubbles of hydrogen gas. As the abundance of these early galaxies increased, the bubbles increasingly overlapped and progressively larger volumes became ionized. This reionization process completed at $z \sim 6 - 8$, approximately 1 Gyr after the Big Bang. At lower redshifts, the IGM remains highly ionized through radiation provided by star-forming galaxies and gas accretion onto supermassive black holes that power quasars.

Very generally, most galaxies earlier than 3 billion years after the Big Bang ($z \geq 2 - 3$) are peculiar (see Jiang et al., 2013). These peculiarities along with the early fragmentation of disks into giant clumps, as observed before 3 billion years after the Big Bang ($z \geq 2$), could be due to turbulence created by local accretion of metal-poor gas in clumpy streams penetrating deep onto the galaxy following the potential well (see Mannucci and Cresci, 2010). These streams would also explain the giant clumps being sites of efficient star formation. In turn these clumps could possibly be the progenitors of the central spheroids observed to appear later on in galaxies.

Galaxies observed in later cosmic times point to the prototypical instability of early disks, which can be compared to the known marginal stability of presently observed disks (see van der Kruit and Freeman, 2011). For instance, most galaxies less than 4.3 billion years after the Big Bang ($z = 1.5 - 3.6$) were found by Law et al. (2012a) to exhibit small, clumpy aspects and tri-axial structures, with high gas fractions and velocity dispersion, thus still differing strongly from galaxies observed in the recent and local universe (even though this difference was rendered a little less striking by the observation of already exponential surface brightness profiles in these galaxies extending out to more than $6 \times r_e$, with effective radii $r_e \approx 0.7 - 3\,kpc$). These authors interpreted their findings as at least proving a markedly asymmetric distribution of stellar mass in these early objects. They further suggested these galaxies are not in stable dynamical equilibrium but on the contrary exhibit short-lived gas disks, continually forming and reforming from recently accreted gas until stabilized. But, before the establishment of the disk, outflowing gas at high velocities and large distances from galactic centers may have arisen (see Law et al., 2012b).

These outflows proved important for the creation of the more recent and more neatly-organized thin rotating disks. They were possibly created by feedback from low to intermediate mass stars or AGN in early clumpy objects, and probably provided galaxies with the ability to dissipate energy, e.g. from velocity dispersion of infalling gas, on timescales smaller than the galactic free fall timescale, thus precluding excessive bulge formation (see Driver et al., 2013).

It was reported by Law et al. (2012b) that at least some star-forming galaxies between 2 and 3 billion years after the Big Bang ($z \sim 2 - 3$) were transiting from clumpy irregular systems to more regular (albeit thick) disks (see van der Kruit and Freeman, 2011 for thick disk formation scenarios).

Furthermore, Labbé et al. (2003) detected disk-like galaxies between 2 and 4.5 billion years after the Big Bang ($1.4 < z < 3.0$), whereas the most ancient galactic spiral structure has been reported inside a galaxy's thick disk by Law et al. (2012c) 3.01 billion years after the Big Bang ($z = 2.18$) although this spiral structure may have arisen from a minor merger and not from galactic secular evolution.

Furthermore, the long standing rule of exponentially decreasing surface density of stars with increasing galacto-centric radius in the inner regions of galactic disks has been shown to fail at larger radii where localised changes in exponential slope, named breaks, are observed (see Pohlen and Trujillo, 2006, and references therein). These breaks were interpreted as hinting at precise properties of disk dynamics and/or star forming processes. It was reported by Roskar et al. (2008) that disk breaks have been observed in the distant universe as soon as 6 billion years after the Big Bang (out to $z \sim 1$), implying that they are a generic feature of disk formation. Several theories for the formation of downward-bending breaks have been suggested. The most common interpretations include angular momentum-limited collapse, star formation threshold either due to a critical gas density or the lack of a cool equilibrium in the interstellar medium (ISM) phase. Alternatively, breaks have also been attributed to angular momentum redistribution. They are now also thought to be strongly linked with radial migration of stellar material.

Besides, it is expected that star formation had a strong impact through supernovae (SN) feedback on shaping galactic disks either in the recent and earlier Universe. More precisely (see Dutton, 2009, Governato et al., 2012) the role of energy driven outflows due to SN is crucial and already closely related to the formation, in the context of ΛCDM cosmology, of exponential disks and galactic breaks observed in the local Universe. Especially models with momentum driven outflows or no outflow at all are shown to overpredict sersic index for low mass galaxies, thus these models are not efficient enough at removing mass from low mass galaxies.

Although these results proved the fundamental role of outflows in shaping disk galaxies, taking place after the main first star formation episodes, Dutton (2009) showed that, even with outflows taken into account, no universal exponential density profile emerges for stellar content in disk galaxies, especially at small radii. This bolsters deeper analysis of stellar profiles close to galactic centers, thus probing bulges and connections between disks and bulges.

Inner galactic structures and the evolution of galaxy morphology in the early Universe ($z \lesssim 2$)

The prominent inner structures of disk galaxies are already under close scrutiny and their formation are on the process of being elucidated. As explained by Driver et al. (2013), early epochs saw the rise of Active Galactic Nuclei (AGN) activity which is almost always coincident with massive star formation episodes and also directly linked to the formation and growth of the associated super-massive black holes (SMBH). Galactic center evolution, including AGN and SMBH activities, are strongly expected to interact with galactic bars. For instance bars, through tidal torques and shocks, induce substantial mass transfer towards these circumnuclear regions probably causing early star formation episodes inside them (see Roussel et al., 2001a). It is interesting to note here that early Universe studies of galaxies are biased, because of redshift, against detection of bars (see Eskridge et al., 2000) as bars are increasingly difficult to detect at bluer rest wavelengths. This bias is likely to hinder future research on the formation of the inner parts of galactic disks. The effects of bars in the form of spiral-bar resonance (see Minchev et al., 2010) or galaxy evolution and morphology (see Masters et al., 2010a) are indeed very complex and important subjects, though they are not the main focus of this thesis.

SMBH were in turn linked to spheroid formation via the well established SMBH-bulge relations (see Gebhardt et al., 2000, Ferrarese and Merritt, 2000). Moreover, as recently found by Debattista et al. (2013) this relation also implies that as disks formed and reformed through accretion around bulges, these disks compressed bulges, inducing a pronounced SMBH growth. This shows a substantial growth of SMBH along with disks. The compression of bulges by disks is a natural explanation of de Jong (1995b) finding that bulge and disk scalelengths were correlated (see for more details).

Conflicting claims have been made concerning the link between spheroid galaxies and bulges of disk galaxies. For instance, studies of the very rapid evolution of galaxy sizes have argued that the compact elliptical systems seen between 2.6 and 4.5 billion years after the Big Bang ($1.4 < z < 2.5$) might represent the naked bulges of present day spiral systems (see Driver et al., 2013). This could possibly link early type galaxies observed in the distant Universe to modern times disk galaxies. Though as such a link would predict projected axis ratios (minor axis over major axis) to decrease on average when spheroids acquire disks, as cosmic time passes, along with a possible increase in mass, such a prediction seems dubious with regards to figure 7 of Chang et al. (2012) (see figure 2) at least for galaxies more massive than $log(M_\star/M_\odot) \sim 10.7$. We see on this figure that in similar bin of mass, the average projected axis ratio varies modestly or increases when time passes. Thus it seems reasonable to conclude that massive elliptical galaxies, mainly become rounder when ageing.

Chang et al. (2012) found that early type galaxies were on average flatter before 6 billion years after the Big Bang ($z = 1$), thus proving an increased disk-like aspect of massive early type galaxies before this cosmic time (see also Bruce et al., 2012). Many early type galaxies of this early epoch were found by these authors to host pronounced disks. Furthermore they showed that the median projected axis ratio (minor axis over major axis) at a fixed mass decreases with redshift. It suggests that all early types more massive than $log(M_\star/M_\odot) \sim 10.7$ gradually and partially loose their disk like characteristics.

They further noted the very most massive early type galaxies ($log(M_\star/M_\odot) > 11.3$) later

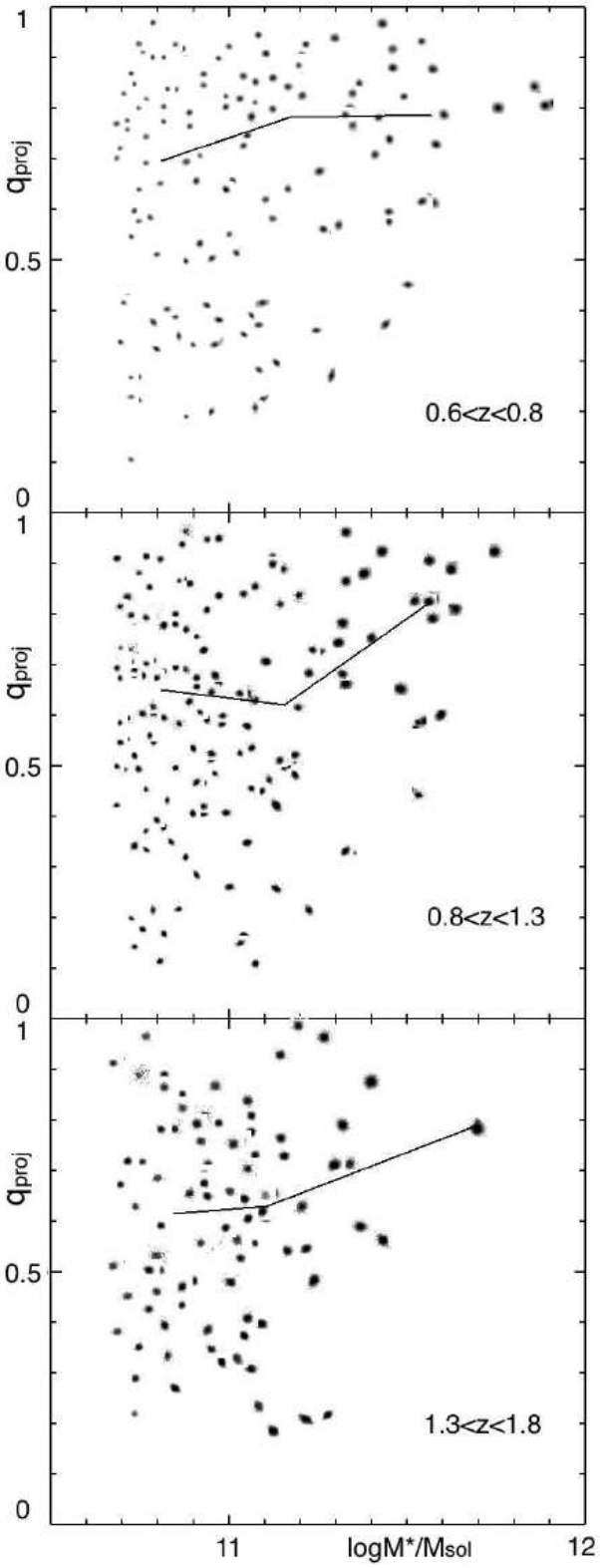

Figure 2: Fig. 7 of Chang et al. (2012). On this figure are shown the projected axis ratio versus stellar mass for their early-type galaxy sample, split into three redshift bins. The symbols are K-band images of the galaxies. The lines represent running median values of the axis ratio. Up to the highest redshift bin, the most massive galaxies appear to be the roundest and overall the galaxies in the highest redshift bins are also flatter than their lower-redshift counterparts.

than 3 billion years after the Big Bang ($z \leq 2$) are the roundest with a pronounced lack of galaxies that are flat in projection. They interpreted this result as a hint towards a universal ceiling mass for the formation of disks independent of cosmic epoch.

The study of early Universe galaxies also hinted at different chronologies for the emergence of massive disks and massive spheroids as well as an evolution of disk galaxy morphology. To substantiate this we can refer to Elmegreen et al. (2005, fig 7) showing that the typical shapes of the brightest elliptical galaxies have probably been produced earlier than roughly 5 billion years after the Big Bang[2]. These authors showed that disk galaxies of these ancient times are 2 or 3 times thicker than they are now. This further implies that the settling of visible matter in thin galactic disks as observed today probably operated on much longer timescale than the time necessary for building up shapes of large elliptical galaxies. Thus the observed disk more than likely shifts with time from thick disks for ancient disk galaxies to thin disks for more local disk galaxies (see also van der Kruit and Freeman, 2011).

The dichotomy of forming galactic disks through accretion and spheroids through mergers was recently questioned by Sales et al. (2012) studying galaxy simulations. These authors suggested that disk dominated objects are made of stars formed predominantly in situ by baryons mostly accreted late from a hot corona. Baryons forming disks have coherent spin alignment, producing less than 5% of counter rotating stars. On the other hand, direct filamentary accretion of cold gas, especially when accompanied by substantial spin misalignments, favours the formation of slowly rotating spheroids. The less massive spheroid may thus form even in the absence of mergers. This kind of spheroid formation could be confirmed or falsified by the observable imprint it is likely to leave in galactic spheroids, namely overlapping stellar populations of distinct age, kinematics and, possibly, metallicity.

This morphological separation between disks and spheroids may also evolve with cosmic times, as Driver et al. (2013) reported a transition epoch 4 billion years after the Big Bang ($z = 1.7$) from galactic spheroid formation, growth via mergers and/or collapse called "hot mode evolution" to disk formation, growth via gas infall and minor mergers called "cold mode evolution". This transition is in agreement with the findings of Sales et al. (2012).

This evolution should have taken place simultaneously with the hierarchical build-up of large scale structures. For instance from the Big Bang on, the merging rate of galaxies is first increasing with cosmic time then decreasing (see Kitzbichler and White, 2008). This maximum of merging rate occurs later when one increases the lower stellar mass of the two merging galaxies. The value of this maximum merging rate is also decreasing with increasing stellar masses. The slowing pace of mergers is connected to the emergence of more and more coherent structures in the universe. An illustration of this point is the decreasing fraction of irregular galaxies from ~ 30 %, 6 Gyr after the Big Bang ($z \sim 1$), to less than 10%, 9 Gyr after the Big Bang ($z \sim 0.4$) and 5% in the local universe ($z \sim 0$; see Abraham and van den Bergh, 2001). These authors thus claimed that earlier than 6 Gyr after the Big Bang 30% of galaxies are sufficiently peculiar for galactic morphological typology defined through minute examination of nearby galaxies (such as the Hubble tuning fork, see section) to be of no avail.

This morphological evolution was probably accompanied by a strong evolution of galaxy properties towards enhanced far infrared (FIR) output in the past (see Dole et al., 2008) as the cosmic infrared background (CIB), mainly emitted by galaxies 6 billion years after the Big Bang ($z \sim 1$), accounts for roughly half of the total energy in the optical/infrared extra-galactic background light (EBL), whereas locally the infrared output of galaxies is only a third of the optical one. This was probably due to early dust production, itself enabled by the early increase of galactic metallicities, as previously noted.

[2]See Elmegreen et al., 2005 studying the Hubble Ultra Deep Field(HUDP) ; Xu et al. (2007) for a sample of objects of the HUDP giving an average redshift of $z \sim 1.4 \pm 0.84$

Although much later in cosmic time, systematic deviations from nearby universe morphological typology are already present in the Universe observed 3.5 billion years ago ($z = 0.3$; see Abraham and van den Bergh, 2001). Even as soon as 1 billion years ago ($z \geq 0.1$) galaxies are less well developed and their structures are more disturbed in the optical and rest frame-UV than local galaxies (see Jiang et al., 2013).

Morphological classifications of galaxies in the local Universe

In cosmic times more recent than 1 Gyr ago, galaxies fit well in the morphological classifications defined from studies of local galaxies e.g. the Hubble tuning fork (see figure 3).

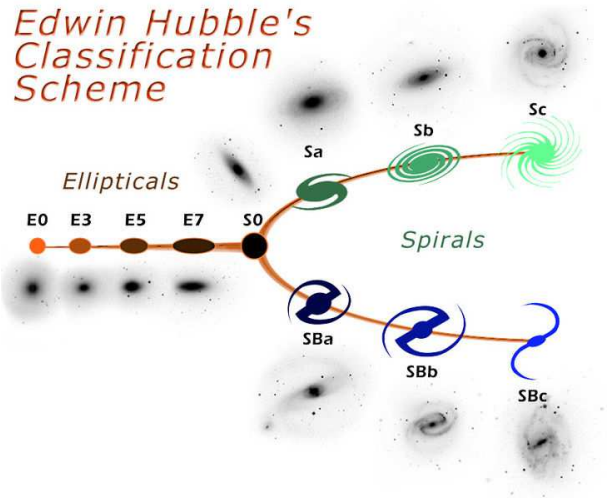

Figure 3: Diagram of the Hubble sequence.

This classification built by Hubble (1926) defines three main galaxy types: spiral, elliptical and irregular, with irregular objects amounting for only 3% of present-day galaxies. Spirals were subdivided by Hubble (1926) in barred and non-barred types depending on whether they presented "a bar of nebulosity [extending] diametrically across the nucleus. In these spirals, the arms spring abruptly from the end of this bar". Another subclassification was added subdividing further barred and non-barred spirals into late, intermediary and early types. Contrary to the usual temporal meaning of these adjectives, they here only refer to a progression from simple (early) to complex (late) observed structural forms comprising " a progression in nuclear luminosity, surface brightness, degree of flattening, major diameters, resolution and complexity".

A widely used extension to the Hubble sequence is the de Vaucouleurs classification (see table 1, de Vaucouleurs, 1959, de Vaucouleurs et al., 1976, de Vaucouleurs et al., 1991). In its present form the de Vaucouleurs classification uses a three coordinate system (stage s, family f, variety v), the three of which are mutually orthogonal, i.e. independant. The stage s is very similar to but more precise than the Hubble type, and mainly correlated with global luminosity. The main morphological stages are gE: giant ellipticals, L: lenticular galaxies, S: spiral galaxies, Im: irregular galaxies. Disk galaxies are more finely classified as spiral galaxies or lenticular galaxies. Spiral galaxies are disk galaxies within which spiral arms and substantial star forming activity are observed, whereas lenticular galaxies are disk galaxies within which no spiral arms nor star forming activity can be found. The main causes of this star formation quenching in lenticulars are gas stripping and gas exhaustion (see van der Kruit and Freeman, 2011). Spiral, lenticular and elliptical galaxies are the majority of luminous nearby galaxies (see Jiang et al., 2013).

Family f (ordinary A, barred B, transition AB) is also close to but finer than the Hubble barred or non-barred type. Variety v (spiral-shaped s, ring shaped r, transition rs) concerns inner structural details other than the bar.

Main properties of the de Vaucouleurs classification

We here review fundamental trends observed between physical properties and de Vaucouleurs morphological classification.

Along with de Vaucouleurs et al. (1991) and Simien and de Vaucouleurs (1986) we define L_T the total luminosity of the galaxy. These authors fitted on the central region of azimuthally averaged surface brightness radial profile of galaxies, $S_g(r)$, seen as functions of the galacto centric radius r, a specific model named "$r^{1/4}$", defined such that $S_{model}(r) \propto r^{1/4}$. They computed the integrated luminosity of this latter pure $r^{1/4}$ spheroid component, quantifying the bulge luminosity and noted L_{bul}. The difference of $r^{1/4}$ and total component B-band magnitude, itself due to the presence of a disk, is a measure of the total-to-bulge ratio, noted $\Delta m_{tot-to-bul}$. The quantity $\Delta m_{tot-to-bul} = 2.5 \log (L_T/L_{bul})$ is increasing with stage from $0 - 0.5$ for giant ellipticals (gE), to > 5 for (Sdm). This trend mainly marks the growing importance of the disk component, from inexistent (gE), to prominent (Sdm) when one considers later type galaxies. We emphasize that for types as late as or later than Sc the bulge components are relatively weak as compared to their disk counterpart. This total-to-bulge ratio is not calculated for the remaining (Sm) and (Im) types which are too irregular to yield meaningful measurements.

For positive stage types, difference of the 21 cm and B-band magnitudes (see de Vaucouleurs et al., 1991, or equation (13), tables 12, 13, 14 of Buta, 1994), both corrected for extinction and self absorption, decreases with type from 2.63 (S0/a) to 0.59 (Im). So for same B-band magnitude there is more atomic gas in later types. Such comparison holds as long as the stage type is positive.

The concentration index is defined as the ratio of diameters of circular apertures transmitting 3/4 to 1/4 of the B-band flux of the galaxy. The logarithm of the concentration index decreases with type from 0.8 (gE) to 0.435 (Im), thus showing that later types are less concentrated than earlier types.

The mean effective B-band surface brightness, i.e. the mean surface brightness inside the effective aperture (the circular aperture enclosing one-half of the total flux), corrected for galactic and internal extinction, and to face-on orientation has a minimum for stage type 0 (S0/a) and 1 (Sa) and a maximum for stage type 10 (Im). Therefore, except for stage types less than 0 (early types), later stage types have lower average surface brightnesses. This trend links morphological appearances (types) to the history of these objects as it was shown by MacArthur et al. (2004) that stellar surface density, on which B-band measurements strongly depend, is a more fundamental parameter than total stellar mass to determine star formation history, especially recent one.

These authors further demonstrated the role of local galactic potential in shaping galactic interstellar medium (ISM) properties. More precisely they showed in a combined optical and NIR study of nearby positive morphological type galaxies, that locally, inside each galaxy, regions having higher surface brightnesses in the optical and NIR are also older and have higher metallicities.

They also explored the global galactic potential, and deduced that age and to a lesser extent, metallicity gradients show radial structures, with steeper gradients in inner galactic regions.

Comparing galaxies in their sample, they found that the trends linking stellar history and galactic matter composition vary with dynamical and morphological properties. More precisely the age and metallicity they measured at one scalelength in K band ($2.2\mu m$) increase with earlier

de Vaucouleurs class	gE	L	S0/a	Sa	Sab	Sb	Sbc	Sc	Scd	Sd	Sdm	Sm	Im
Hubble stage type	-5	-2	0	1	2	3	4	5	6	7	8	9	10

Table 1: De Vaucouleurs Classification of stages as presented on NED website. From left to right we have giant ellipticals (gE), lenticular (L), spirals (S) and irregular galactic objects (Im).

Hubble type, higher luminosity, larger rotational velocity and higher central surface brightness.

They concluded that higher surface brightness regions of galaxies probably formed their stars earlier than lower surface brightness regions, or at a similar epoch but on shorter timescales, and the SFHs at a given surface brightness (SB) level, which lead to age radial gradients, are modulated by the overall potential of the galaxy such that at fixed mass, brighter/higher rotational velocity galaxies formed earlier. These authors also invoked stellar feedback as possibly impeding star formation in low mass systems, thus making their conclusions not contradictory with more massive galaxies forming later. The trends reported above reach saturation for the brightest and highest central surface brightness galaxies.

Moreover, either older stellar populations or higher metallicities may create redder galactic colors. These two are mostly degenerate in observed optical colors of unresolved stellar populations. Dust extinction possibly produced by more metal rich environments is only a secondary contributor to such color gradients (see MacArthur et al., 2004), at least in optical and NIR colors.

As can be expected from the arguments shown above, globally determined galactic colors also change with morphological types, as later types have bluer colors. More precisely the effective color indices corrected for galactic and internal extinction between U and B as well as B and V bands show systematic trend from early type being reddish objects to late types being bluer objects.

NIR morphologies

In this subsection we will review some important morphological trends observed by shifting wavelengths from optical to near infrared (NIR).

Buta et al. (2010b) found that on average, at $3.6\mu m$, morphologies are very close to blue light ($\lambda \sim 445\,nm$) morphologies, with only the most dusty galaxies exhibiting drastic morphological differences between the two wavelengths (see also Jarrett et al., 2003). Systematical morphological differences between the two wavelengths seem consistent on average with S0/a to Sc galaxies appearing of earlier type at $3.6\mu m$ than in blue light. This is caused by a slightly increased prominence of the bulge, the reduced effects of extinction in the NIR, and the reduced (but not completely eliminated) effect of the extreme population I stellar component[3]. Population I stars include most recently formed stars and thus massive and scarce short-lived stars. For instance those stars bias direct estimates of stellar mass from blue light toward lower values as massive stars represent only a tiny fraction of galactic stellar masses. This is one of the main interests of studying galaxy morphology in the NIR instead of in the optical.

The increased weight of the bulge in NIR as compared to optical is readily explained by redder colors of the bulge as compared to the disk (as seen on figure 8 of MacArthur et al., 2004). This difference could be due to dust extinction, though as previously stated, this is currently seen as a parameter of lesser importance than age and metallicity to explain color gradient inside galaxies.

Another important yield of recent morphological studies in the NIR is the observation that

[3]Population I stars are the most recent stellar generation as opposed to population II (intermediate) and population III (oldest, still hypothetical, and very metal poor).

approximately half of all massive disk galaxies contain bars. The fraction of strong bars increases twofold, from 30% in the optical, to 60% in dust-penetrating NIR wavelengths, while the total bar fraction does so by up to 35%, either when bar detection is carried out through visual classification or via quantitative methods (see Sánchez-Janssen and Gadotti, 2012).

It was also recently found in NIR bands that (S0) lenticular galaxies had on average weaker bars than spirals, even compared to their closest spiral counterpart S0/a (see Buta et al., 2010a). This was interpreted as a possible continuing evolution of bars proceeding during and after gas depletion.

It is also known that spiral structure which may appear "flocculent" in blue light and I band (at $0.8\mu m$), can appear more global (i.e. continuous and large-scale, or "grand design") in K band (at $2.2\mu m$; see Buta et al., 2010b).

Disk galaxies in local universe

From a general point of view, the vast majority of galaxies of the local Universe can be described as consisting of a compact smooth spheroidal component containing a predominantly pressure-supported old high-metallicity stellar population, and/or an extended flattened star-forming disk component containing intermediate-age and young stars with a wide range in metallicities, having smooth rotation and embedded in an extensive gaseous cold gas disk (see Driver et al., 2013).

More precisely, 70% percent of galaxies in the nearby Universe exhibit prominent spiral arms inside a disk (see D'Onghia et al., 2013). Chang et al. (2012) also noted that all but the most massive galaxies in the present day Universe have disk-like structures and are rotating.

These arguments make studies of spiral galaxies and more generally disk galaxies fundamental for understanding the local Universe.

We will now focus more particularly on disk galaxies and discuss the main properties of these objects. We will successively describe the main observed structures of these objects in their gaseous, stellar and dust phases as well as important links between these components.

Gas content and structures

The gaseous content of disk galaxies of the local universe is mainly constituted of atomic and molecular hydrogen (resp. H and H_2).

An easy way to observe atomic hydrogen is through the detection of its hyperfine structure splitting which produces the famous 21-cm hydrogen emission line also called HI (in the radio part of the electromagnetic spectrum). We will use from this point on HI as refering to atomic hydrogen. This emission line enables the precise measurement of rotation velocities and velocity dispersions inside galaxies and its study subsequently yielded remarkable constraints on orientations of disks (see Carignan, 1990, Daigle et al., 2005, Dicaire et al., 2008).

In disk galaxies, HI is mainly found in disk-shaped structures. These are much more extended than optically observable disks. The ratio of HI diameter to the optical diameter (at 25 B-mag arcsec^{-2}) is about 1.7 with a large scatter, but does not depend on morphological type or luminosity. There is also a very good correlations between $\log(M_{HI})$ and $\log(D_{HI})$ with a slope of about 2, M being the globally integrated mass of HI in the galaxy and D the diameter of the HI disk. This implies that the HI surface density averaged over the whole HI disk is constant from galaxy to galaxy, independent of luminosity or type. There is also a relatively well-defined maximum HI surface density in disks of observed galaxies, which amounts to about $10 M_{\odot}.pc^{-2}$ (see van der Kruit and Freeman, 2011).

The most exterior regions of HI disks are known to exhibit ubiquitous deviations from the main plane of the inner disk, in the forms of flaring and warps. Most researchers from this field seem to agree that these phenomena have something to do with a constant accretion of material with an angular momentum vector misaligned to that of the main disk (see van der Kruit and Freeman, 2011).

On the contrary molecular hydrogen (H_2) is much more restricted to inner regions and spiral arms. A usual method to characterize the galactic content in H_2 is the well established CO-to-H_2 conversion factor (often noted X_{CO}).

For instance these techniques to estimate HI and H_2 were used by Leroy et al. (2008), to obtain radial surface densities of molecular gas in nearby spiral galaxies, yielding an approximately constant star formation efficiency across the disk as well as a neatly defined transition region from mainly molecular to mainly atomic hydrogen. In the outer parts of spiral galaxies and in dwarfs, where $\Sigma_{HI} > \Sigma_{H_2}$, the star formation efficiency declines steadily with increasing galacto-centric radius.

Another analysis of molecular and atomic gas surface density lead to precise conclusions linking variations of both physical state and density of matter across galactic disks. Making use of the link between CO and H_2 reported above, Biegel and Blitz (2012) successfully demonstrated a remarkably reduced scatter of galactic gaseous radial profiles especially in nearby spirals not experiencing interactions with their environments. The reduced scatter is obtained if H_2 and HI are combined into a single quantity $\Sigma_{HI+H2}/\Sigma_{HI+H2}(r_{HI=H2})$. This quantity is the surface density of gas normalized to the surface density of gas where HI and H_2 are present in equal proportions. This transition occurs at around $\Sigma_{\text{gas}} \approx 14\, M_{\odot}.pc^{-2}$. This result was interpreted as conversion of HI into H_2 being governed primarily by the midplane hydrostatic pressure in galactic disks. In that case, the location where the gas in the disk goes from being primarily molecular in the inner regions, to where it becomes primarily atomic in the outer regions, should occur at a constant stellar surface density. This constancy is good to about 40% and have values varying from $120\, M_{\odot}.pc^{-2}$ to $81 \pm 25\, M_{\odot}.pc^{-2}$ depending on the study.

We now define star formation rate (SFR) as the total mass of stars created per year (in $M_{\odot}.yr^{-1}$), and the star formation surface density as the SFR of a region of a galactic disk, divided by the surface this region occupies on the galactic disk (the SFR surface density can be expressed in $M_{\odot}.yr^{-1}.kpc^{-2}$).

It is well known since Schmidt et al. (1959) that star formation surface density is caused in the local Universe by enhanced gas surface density. This link is embodied by the Schmidt-Kennicutt law which states

$$\Sigma_{SFR} \propto \Sigma_H^n$$

with n between 1 and 2, but whose slope steepens (in the sense of larger decrease of SFR when hydrogen surface brightness decreases) when $\Sigma_H \lesssim 10\, M_{\odot}.pc^{-2}$. It was shown that on average $n = 1.4 \pm 0.15$ (see Kennicutt et al., 1998).

Exploring the evolution of this law with cosmic time provided clues as to how galaxy evolution could have been impacted by dust presence and galactic interstellar radiation fields (ISRF). This is examplified by Gnedin and Kravtsov (2010), studying simulated galaxy evolution, comparing galaxies 2 billion years after the Big Bang ($z \sim 3$) and in the local Universe, showing a systematic decrease of star formation efficiency in lower mass galaxies. Decreasing supernovae prevalence in lower mass systems was ruled out by these authors as a possible explanation for this decrease, and leaving out low dust abundances and high far ultraviolet (FUV) fields as very plausible phenomena suppressing star formation in low metallicity and low mass halos.

In the local Universe pristine HI forms H_2 mainly on the surface of dust grains and star formation stems from molecular H_2 clouds. So star formation is mainly linked to both molecular gas and dust phases. It is established that dust and gas are related so that tracers of gas built on

cold dust emission have been envisionned by many authors (see Galametz et al., 2012, Holwerda et al., 2013).

It also consequently follows that study of gas and dust distribution in local galaxies is essential to understand and put severe constraints on galaxy evolution (see Pohlen et al., 2009). More precisely the rate at which gas is accreted and converted into stars regulates not only the star formation history (SFH) but also the chemical evolution of galaxies (see Pohlen et al., 2009).

In the following subsection we will go through the main properties of stellar content observed in disk galaxies.

Stellar content and structures

Stellar emission

The emission of disk galaxies at shorter wavelengths than NIR wavelengths is mostly dominated by their stellar emission. In disk galaxies the stellar content gather most of the visible mass. As mentionned earlier, to probe the bulk of stellar content and also to eliminate dust extinction, galaxies can be studied in the NIR.

Spatially, stellar emission is often analysed as caused by many morphologically diverse components. The most prominent ones are structures called the exponential disk and the bulge (see van der Kruit and Freeman, 2011). Chang et al. (2012) stated that in present day Universe $58 \pm 7\%$ of stars are in spheroids and $42 \pm 7\%$ are in disks. These two structures are axisymmetrical with respect to the axis of rotation of the galaxy. Other important stellar components are spiral arms and bars. These are not axisymmetrical.

A census of finer structures was attempted by Gadotti (2008) and Tasca and White (2011). The former authors estimated the distribution of the stellar mass $M_\star$ for galaxies more massive than $10^{10}\,M_\odot$, and the latter authors examined the distribution of the r and i band luminosity, L, for a sample of galaxies complete down to a magnitude limit of 15.9:

- 36% of $M_\star$ and $54 \pm 2\%$ of L is found inside in disks;
- 32% of $M_\star$ and $32 \pm 2\%$ of L is found inside elliptical galaxies;
- 28% of $M_\star$ and $7 \pm 2\%$ of L is found inside bulges;
- 4% of $M_\star$ and $7 \pm 2\%$ of L is found inside bars.

Stellar disk

Studies of hydrodynamical simulations enabled to predict that galactic matter in disks had been subjected to mild evolution associated with particularly quiescent merger histories. This is examplified by Driver et al. (2013) reporting that the stellar mass still residing in disks has assembled and lived on without experiencing major mergers. As almost all starbursting galaxies in the nearby Universe are mergers (see Duc et al., 1997, Elbaz and Cezarsky, 2003), it suggests that most matter composing disks did not experienced starbursting events created by mergers, which are known to be destructive events as far as disks are concerned.

Furthermore it seems interesting to precisely detect where non axisymmetric features are present in disk galaxies as non axisymmetric and axisymmettric patterns do not have the same consequences on disk galaxy stability (see Freeman, 1970 and Toomre, 1964). This detection and identification of the diverse components is feasible through the use of ellipse fitting on isophotes and especially the study of their axis ratios and position angles as explained in the subsection "Results and discussion" of Aguerri et al. (2000) and references therein.

Below we show a widely used (e.g. see Dutton, 2009 refering to Blanton, 2005, or van der Kruit and Freeman, 2011), recent and general parameterization of disk galaxy radial profile of surface brightness, namely the Sérsic profile :

$$I_s(R) = I_{s,0} \times e^{\left[-(R/R_s)^{1/n}\right]} \quad (1)$$

where R is the distance from the center of the galaxy to the region emitting the intensity $I_s(R)$, $I_{s,0}$ is the central intensity, R_s the scale radius and n the Sérsic index. Values for n of $(4, 1, 0.5)$ respectively correspond to the de Vaucouleurs (see de Vaucouleurs, 1959), exponential or gaussian profile. The use of Sérsic profiles enables to quantify the proportion of different types of decreasing intensity profiles amid galaxies and especially disk galaxies. Using this methodology, Dutton (2009) provided an estimate of the proportion of purely exponential disk galaxies, which this author showed to be relatively rare ($\leq 0.1\%$ of Milky Way like galaxies are purely exponential disk).

We may add to these considerations that the exponential stellar disk model often taken for granted can be questionned. We read in Dutton (2009), quoting Dalcanton et al. (1997), that in a gas disk with solid body angular momentum distribution in centrifugal equilibrium (i.e. close to observed exponential disks), the center is more concentrated than the pure exponential law and there is an outer cut-off at around 4 disk scalelengths, at least for stellar bands.

Although purely exponential disks are relatively seldom, by the time of Freeman (1970) landmark paper, it is already known that in most spiral and lenticular galaxies, a substantial range of radii can be found, over which the decrease of surface brightness is close to exponential.

Thus a very usual model used to describe at least a part of stellar disk radial intensity curve in isolated galaxies is given by:

$$I_d(R) = I_{d,0} \times e^{-R/h} \quad (2)$$

where R is the distance from the center of the galaxy to the region emitting the intensity $I_d(R)$.

It has first to be emphasized that for the same galaxy and same wavelength band, literature values of scalelengths h may vary by up to 20% from one author to another because of differing methods of measurement (see similar conclusions drawn by Giovanelli and Haynes, 1994 and, on a broader basis, by van der Kruit and Freeman, 2011). More precisely Knapen and van der Kruit (1991) named h_1 the disk scalelengths found by Grosbol (1985) in visible red band, and h_2 the disk scalelengths found by other authors for the same galaxies in either blue or red band. They showed that the average value of the discrepancy $d = 2 \times |h_1 - h_2|/(h_1 + h_2)$ for more than 120 galaxies is 23% with a standard deviation of 20%. These authors did not find any systematic trend nor correlation of this discrepancy with obvious galactic parameters such as morphological type, arm class or inclination. Discrepancies of 50% are no exceptions and are not confined to one study.

Besides, due to absorption effects, in wavelength ranges subjected to this effect (e.g. I band), the observed scalelength (h) and central surface brightness ($I_{d,0}$) characterizing exponential disks may differ from the un-absorbed e-folding scalelength and central surface brightness as shown in Fig. 4 of Giovanelli and Haynes (1994).

This in turn forces to distinguish between observed morphological parameters and intrinsic physical quantities of disk galaxies. It also seems to indicate that an interesting way to measure the unabsorbed e-folding scalelength and central surface brightness would be to consider maps

made from disk galaxies observation at wavelengths where absorption is negligible e.g. NIR wavelengths. But, as galactic emission at some NIR wavelengths exhibits excesses not linked with stellar emission (e.g. PAH emission, see Mentuch et al., 2010), multiwavelength analysis in the NIR is required to finely estimate stellar NIR continuum.

Amid disk galaxies, many structural properties of the stellar phase are related to one another. For instance, many morphological trends were summarized by van der Kruit and Freeman (2011) as follows: galaxies of smaller stellar masses have statistically smaller scalelengths in optical wavelengths as well as smaller isophotal sizes, fainter central surface brightnesses and later morphological types. Giovanelli and Haynes (1995) found similarly that more luminous galaxies have higher central brightnesses, this effect being amplified at K band as compared to I band (and more generally as compared to visual bands).

Furthermore structural properties of disk galaxies have intrinsic distributions. For example morphological studies with statistically meaningful approaches (ruling out selection effects and the limit of detection of disk galaxy samples) found a specific intrinsic surface brightness distribution for disk galaxies. Namely this includes the paucity of high surface brightness and large scalelength systems, as well as a bright end limit in terms of surface brightness, whereas no faint end limit of surface brightness could be found (see Giovanelli and Haynes, 1995, de Jong, 1995a).

Structural properties of stellar and dust phases are linked. This link can be revealed by studying stellar light extinction inside disk galaxies as was hinted at by Giovanelli and Haynes (1994). These authors studied I band scalelength variations with galactic inclination. They found their results consistent with the scaleheight of the absorbing material in disk galaxies being approximately equal to about half that of the stellar content or less.

Properties of inner galactic regions and dust extinction were studied through examination of broadband structural parameters of disk galaxies. de Jong (1995b) showed that bulge and disk scalelengths are positively correlated and thus suggested that formation of these two structures were coupled. They also highlighted the decrease of central intensity (i.e. $I_{d,0}$) when the galaxy type increases in all 6 bands (B, V, R, I, H, K). More precisely a very pronounced trend is the galactic extinction corrected effective surface brightness of the bulge decreasing with increasing morphological type. This trend is stronger for K band than B band. Explanations for this involve bulges being brighter in redder filters than bluer ones, circumnuclear star formation and dust lanes affecting more B band than K band. These authors also stated that the K band (near IR) is well suited to probe the bulk of the stellar mass mainly made of old stellar populations without being hampered by dust extinction. They found a typical extinction level of 0.06 mag (much less than in bands with smaller wavelengths).

Comparing scalelengths and sizes of disks Giovanelli and Haynes (1995) showed a systematic trend that can be taken into account to reduce the dispersion of scalelengths in galaxy samples. These authors found that scalelengths extracted from global exponential fits of Sc galaxies (these galaxies have weak bulge component as compared to their disk counterpart) in visual bands are to first order proportional to the overall size of the galaxy as measured at some external isophote e.g. at 25 $\mathrm{B}-\mathrm{mag.}(''')^{-2}$ (see NED "diameter" section). That is a good argument to divide scalelengths by an isophotal diameter of the galaxy before comparing scalelengths between two galaxies.

These same authors showed that these scalelengths vary little with wavelength from blue to red, even if the scatter is large. Backing up this argument, Dutton (2009) showed in a

cosmological approach to exponential galactic disk formation, that the expected scalelengths in K band are related to optical band scalelengths. These authors also showed that even if observationnally K band is considered a good stellar mass tracer, the scalelength in the K band is typically 1.2 times larger than the scalelength in stellar mass. They thus conclude that in order to derive stellar mass scalelengths from observations, it is necessary to take into account the color gradients which will result in stellar mass-to-light ratio gradients, even in the near infrared (NIR).

In more local approaches, it was made clear (see Pohlen and Trujillo, 2006) that 90% of spiral galaxies exhibit at least 2 radial ranges where the surface brightness decreases exponentially with different slopes, such that *breaks are ubiquitous in nearby galactic disks.*

In the same outer regions where edge-on galaxies tend to exhibit sharp or complete cut-off, Pohlen and Trujillo (2006) examining face-on to moderatly inclined disk galaxies, found no cut-off. According to these authors studies of edge-on galaxies introduce severe problems caused by the effects of dust and the line-of-sight integration, such as masking the actual shape of the truncation region, or interfering with the identification of other important disk features (e.g. bars, rings, or spiral arms).

In outer regions of non edge-on galaxies, classical downbending breaks are more frequent in later types while the fraction of upbending breaks rises towards earlier types.

For classical downbending breaks (60% of the 90 galaxies studied by Pohlen and Trujillo, 2006) the break galacto centric radius (in *kpc*) is larger for more luminous galaxies although it is located at 2.5 ± 0.6 times the inner scalelength. Downbending breaks are thought to be created either by star formation threshold, or outer Lindblad resonance associated with the bar when the break is located at around twice the bar radius (see Pohlen and Trujillo, 2006).

Upbending breaks (30% of the sample of Pohlen and Trujillo, 2006) appear to be located at 4.9 ± 0.6 times the inner scalelength, thus further out than downbending breaks. For more than 60% of upbending galaxies a good indication was found that the outer upbending part is a disk-like structure (e.g. by finding spiral arms). Close physical neighbours and slightly disturbed morphology suggested in several cases interaction as a possible origin.

Besides, as stated in Giovanelli and Haynes (1995) and in Giovanelli and Haynes (1994) internal extinction of stellar light in disk galaxies may be studied through careful evaluation of scalelengths corrected for face-on aspect of disk galaxies, in I band. Dust extinction will be further reviewed in a following dedicated subsection. As far as stellar light is concerned, the conclusion of Giovanelli and Haynes (1995) are that galactic disks are more transparent to stellar light at larger galacto centric radius.

Moreover, according to Giovanelli and Haynes (1994) the ratio of dust-to-stellar scale heights, more likely to reproduce measured profiles of edge-on galaxies, is around $\zeta \sim 0.5$. ζ is decreasing, at least in the I band, when overall luminosity of the galaxy increases, meaning the dust responsible to starlight attenuation is more tightly confined to disk plane in more luminous galaxies (see page 1067 of Giovanelli and Haynes, 1995). However these authors say it is customary to assume that dust scalelength is similar to stellar scalelength. This has been shown to be true except for a 10% increase of dust scalelength as compared to stellar scalelength (see Muñoz-Mateos, 2009, studying the SINGS galaxy sample).

It was also showed that there is no reliable correlation between scalelength or bulge-to-disk ratios and galaxy types (see de Jong, 1995b). They found a strong correlation (in the studied sample of 86 face-on galaxies) between bulge and disk separately for magnitudes and scalelengths, but no correlation between bulge and disk central intensities. The correlation between

scalelengths of the disk and the bulge was interpreted by these authors as showing that the formations of the bulge and the disk were coupled (see section).

Dutton (2009) mentionned that viscous processes may explain the existence of exponential disks in galaxies, but that it requires initial conditions where disks are less concentrated than exponential, which does not correspond to natural yields of the ΛCDM paradigm. This author added that viscous evolution fails to produce bulgeless galaxies with only exponential disks. Instead, he proposed a possible exponential disk formation process through supernovae driven outflows and density dependent star formation, in the general and up-to-date context of ΛCDM initial conditions for galaxies. In many of the resulting simulated galaxies, realistic stellar surface brightness profiles were observed, with disk exponential over several scalelengths, but upturns in very inner regions of the so created "exponential" disk are found ubiquitously. This finding is similar to conclusions previously reached by Dalcanton et al. (1997), showing that a gas disk with solid body angular momentum distribution in centrifugal equilibrium inside a dark matter halo exhibits inner regions more concentrated than exponential. It therefore seems rather reasonable to posit that some upturns of light at small galactic radii may well be part of the disk. We will explore further this question in the next section.

Bulges

Bulges are defined by Kormendy and Kennicutt (2004) as inner regions of disk galaxies where light are found in excess of the extrapolated exponential behaviour of the disk.

They may or may not include more inner structures like nuclear star clusters and bars. Mendez-Abreu et al. (2007) reported strong correlations between the bulge and disk parameters. About 80% of bulges in unbarred lenticular and early to intermediate spiral galaxies are not oblate but triaxial ellipsoids. The interplay between bulge and disk parameters favors scenarios in which bulges have assembled from mergers and/or have grown over long times through the migration of stellar or/and non stellar material from turbulent disk secular evolution (see Driver et al., 2013).

In a study of simulated galaxies (see Sales et al., 2012) it was shown that star formation in spheroids proceeds episodically, leaving behind populations of stars of similar age but distinct kinematics. These populations originate from the accretion of gas whose angular momentum is misaligned relative to that of earlier-accreted material. The misalignment destabilizes any pre-existing disk, prompts the rapid transformation of gas into stars, and reduces the net rotational support of the system. In the core regions the gravitational coupling of the baryons with the dark-matter may allow it to exhibit a pseudo-pressure (see Driver et al., 2013). In general the greater the merger-rate the more bulge-dominated the final galaxy population appears (see Driver et al., 2013).

Bulges are nowadays usually classified as pseudo or classical bulges. Pseudo bulges are as flattened as disks with disky or boxy/peanut edge-on shapes whereas classical bulges are thicker and spheroidal (see Okamoto, 2012).

While these differences point out different formation processes for classical and pseudo-bulges, significant overlaps in their properties were found (see Gadotti, 2008), indicating that these different processes might happen concomitantly. Classical bulges contain 25 per cent of the total stellar mass of galaxies more massive than $10^{10}\,M_{\odot}$ in the nearby Universe and pseudo-bulges contain only 3 per cent, although approximately a third of disk galaxies of the nearby Universe hosts pseudo-bulges.

As reported in Gadotti (2008), pseudo bulges have Sérsic indices broadly $n < 2$ and are often exponential bulges, these pseudo bulges are expected to be flattened, rotationnally supported,

mainly built through disk instabilities and mostly undergoing fierce star forming episodes. These pseudo bulges are actually very similar to disks in graphs of mean effective surface brightness against effective radius. The mass-size relation of pseudo bulges is close to the one of bars.

On the contrary classical bulges have $n \geq 2$, are more pressure supported and thought to be created through minor mergers. Most of them are quiescent thus not forming stars. Classical bulges are more concentrated than pseudo bulges at fixed bulge-to-total luminosity ratio. More precisely figure 14 of Gadotti (2008) (see figure 4) clearly shows that as compared to scalelength of the disk, scalelength of pseudo bulges are always larger than scalelength of classical bulges at a fixed value of the bulge-to-total luminosity ratio. This figure also shows that bulge to disk scalelength ratios are correlated to bulge-to-total luminosity ratios thus suggesting that the Hubble sequence is not scale-free, if it is a bulge-to-total sequence. Incidentally the petrosian concentration index, defined as the ratio R90/R50, where R90 and R50 are, respectively, the radii enclosing 90 and 50 per cent of the galaxy luminosity, was reported a better proxy for the bulge-to-total luminosity ratio than the Sérsic index. Actually the petrosian concentration index was shown by these authors to correlate even better with a bulge-and-bar-to-total luminosity ratio.

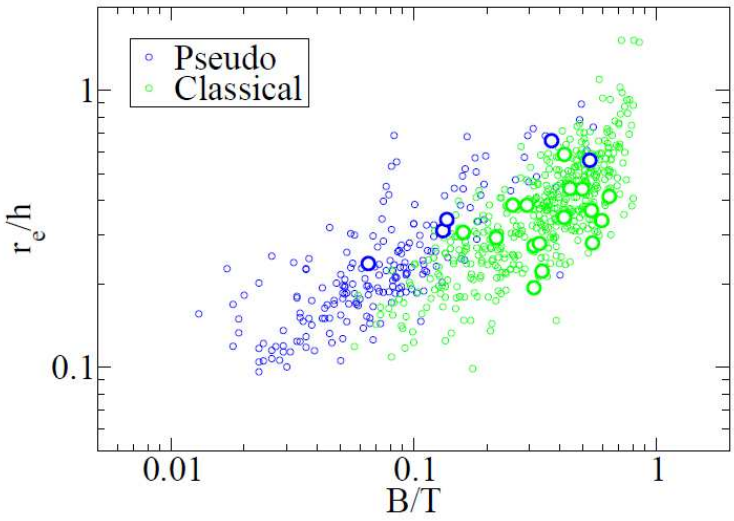

Figure 4: Figure 14 from Gadotti (2008) plotting ratio between the scale-lengths of bulges and disks against B/T for pseudo-bulges and classical bulges. Interestingly, pseudo-bulges and classical bulges seem to follow offset relations. Bigger, white-filled circles with similar colour coding are pseudo-bulges and classical bulges in galaxies with $0.5 < b/a < 0.7$ (b/a being the ratio of minor to major axis), and portray similar patterns.

Indeed in graphs of Sérsic bulge radius against I band surface brightness, classical bulges seem to be related to elliptical galaxies whereas pseudo bulges have only broadly similar surface brightnesses as elliptical galaxies (see figure 5).

But it seems also worth noting that classical bulges are on a slightly steeper mass-size relation than pseudo bulges: for the same increase in mass, size increases more for classical bulges, though classical bulges are definitely more massive than pseudo bulges. On the contrary classical bulges and ellipticals follow heavily offset mass-size relations (for the same increase in mass, size increases much more for ellipticals) suggesting that high-mass bulges cannot be considered as high-mass ellipticals that happen to be surrounded by a disk.

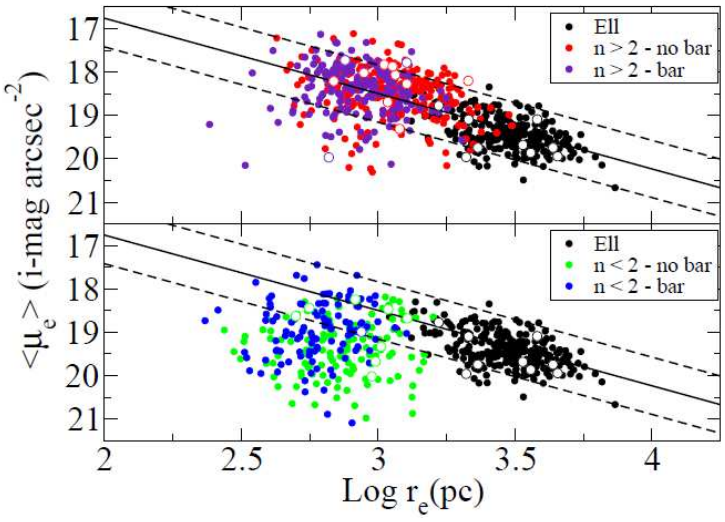

Figure 5: Figure 8 from Gadotti (2008). This figure represents one criterion to distinguish classical and pseudo-bulges. It shows the mean effective surface brightness within the effective radius of the bulge plotted against the logarithm of the effective radius of the bulge. It displays elliptical galaxies and, separately, bulges with Sersic index above and below 2. Barred and unbarred galaxies are indicated. The solid line is a fit to the elliptical galaxies and the two dashed lines point out its $\pm 3\sigma$ boundaries. Bulges that lie below the lower dashed line are classified as pseudo-bulges, independently of their Sersic index. Bigger, white-filled circles represent systems with $0.5 < b/a < 0.7$ (b/a being the ratio of minor to major axis), with similar colour coding. While the threshold in Sersic index ($n = 2$) can be considered as an approximation to identify pseudo bulges, it is clear that it can generate many misclassifications.

Spiral arms

Spiral arms are very frequently observed in disk galaxies. They correspond to location where density of the galactic material is enhanced. Theories explaining their formation are diverse and there is still no consensus on which one best corresponds to reality. Indeed spiral arms cannot be both permanent structures and rotating at the same speed as stars because if they do they would be rapidly very tightly wound which is not observed. This is called the winding problem.

A preferred scenario for spiral arms creation is the so called density wave theory. In this model spiral arms are over densities passing through rotating stars (see Cedrés et al., 2013).

Grand et al. (2012) have challenged the claim that spiral arms were formed from density waves. They found that it was possible to produce transient spiral arms from galactic material rotating with stars. They simulated a barred spiral galaxy and found that spiral arms are transient recurring features. Transiency is ubiquitously found in spiral arms simulations studies. These authors found that the pattern speed is decreasing with radius overall, and may be affected by the presence of a bar. The un-barred case shows convincing co-rotation with the rotational velocity. The weak bar case shows slight departure from rotational velocity at larger radii, and the stronger bar case shows a systematically faster pattern speed overall. They therefore suggested that the bar may boost the pattern speed.

They also found in each studied case, that some stellar particles were drawn by the spiral arms at all radii creating a systematic motion toward the outer (resp. inner) regions for stellar particles accelerated from behind (resp. decelerated in front of) the arm, though these remained on the trailing side (resp. on the leading side) of the arm. This migration effect occured at all radii in their simulation all the way through right until the spiral arm disappeared. In each case the amount of heating (resp. cooling) for stellar particles migrating toward the outer (resp. inner) regions was less than a percent of the total energy of a given particle. Hence this migration effect does not contribute significantly to disk heating. However the cause of this heating and cooling is as yet not identified.

No offset was found between the distribution of young star particles (< 200 Myr) of different ages around the spiral arm at two different radii. This is consistent with recent observations.

These authors showed their simulation attested that the bar is a powerful driver of spiral structure and may help to maintain the spiral arm feature for longer even though they have not probed particularly strong bar cases.

They found that their simulated spiral arms are not consistent with the long-lived, rigidly rotating spiral arms of a classical spiral density wave theory. On the contrary, their spiral arm pattern speed decreases with radius and is similar to but slightly faster than the rotation velocity of the star particles. However, significant radial migration over a wide range of radii is repeatedly observed despite the differences in pattern speed.

Another interesting study by D'Onghia et al. (2013) studied spiral arms formation through incorporation in galactic disk of density inhomogeneities with properties similar to those of giant molecular clouds. They showed results inconsistent with the idea that spirals are static density waves because the arms in their simulations fluctuate in time. Moreover, their results are different from what is expected based on forced-wake theory because these showed that the arms can be long-lived and are not necessarily transients even when the original perturbations responsible for driving the patterns are removed.

The spiral patterns in their simulations are not global as predicted by the classical static density wave theory but locally they appear to fluctuate in amplitude with time. It is the local balance between the shear that stirs waves, breaking the arms, and the self-gravity that makes up the arms that gives the visual impression that the patterns are global whereas they are actually segments produced by local under-dense and over-dense regions, at least for relatively low mass disks. The arm-interarm density contrasts reported here are around 7 which can

be compared to values often obtained by numerical models of 3-9 reported by Franco et al. (1993, page 8/395) and molecular gas arm-interarm density contrast of 2-3 found in M51 by Koda et al. (2012). These under-dense and over-dense regions act as perturbers, keep alive the spiral activity and probe an entirely new regime in which the linear theory is no longer fully applicable. The dynamical response in the disk originates at the corotation resonance between the perturbers and the surrounding stars. This implies that spiral arms features that wrap up and get replaced statistically have angular speeds that are not constant with location, but decrease with radius. Spiral arms features are found by these authors to have speeds slightly differing from the surrounding stars, explaining why the arms do not wind up while being at the same time long-lived.

D'Onghia et al. (2013) believed that there was already some observational support for their picture. Their model predicts that there should exist red disk galaxies with no gas but that may still have arms. Galaxies such as this have been discovered (see Masters et al., 2010b) and current theories for spiral arm formation do not explain their morphologies. In their model, the pattern speeds of the spiral features should vary with location within a disk, as has been claimed for some nearby spirals. These authors also predicted that the number of arms in galaxies should decrease from around 20 (diffuse arms) to 4 (high contrast) when the disk to total mass ratio is increased from 0.01 to 0.04. They also predicted that low velocity dispersions observed when matter settlement inside the disk is well advanced, should be correlated with more prominent arms. These predictions are readily testable and relevant observational studies should provide strong tests of this kind of models.

Besides, the spiral structure causing resonant angular momentum exchanges probably result in stellar migration. The latter is a possible cause for breaks observed in stellar density profiles of disk galaxies (see Roskar et al., 2008).

Metallicity

In astrophysics, metals refer to atomic nuclei strictly heavier than helium. These heavier elements are typical outputs of stellar nucleosynthesis, released in the ISM by deaths of stars, while they also are the junction between stars and dust as dust is mainly composed of metallic elements.

Metallicity is usually defined as $12+log\left(\frac{O}{H}\right)$ where $\frac{O}{H}$ is the ratio of oxygen over hydrogen abundances in the interstellar medium (ISM). The quantity $12+log\left(\frac{O}{H}\right)$ is expected to get values within $[7.5, 9.1]$ (see Mannucci and Cresci, 2010) and an empirical upper limit to the gas-phase oxygen abundance of around 9.1 independent of redshift was shown to exist in star-forming galaxies (see Zahid et al., 2013).

In disk galaxies, metallicity depends on two key parameters: the star formation rate and the total mass of the galaxy. We will now further explain these two dependencies, to afterward discuss the essential conclusions reached by current research on the subject about how galaxies work.

First, metallicity is usually decreasing with galacto-centric radii in spiral galaxies with a slope of around -0.5 dex $/R_0$, with R_0 the galaxy's isophotal radius (see Zaritsky et al., 1994). This is explained by galactic outskirts being less subjected to star formation, thus having lower SFR because of lower surface gas densities.

The second key parameter for global metallicity in disk galaxies is the mass of the galaxy. In disk galaxies, heavier masses are tightly related to larger inclination-corrected maximum rotation velocity V_C (see Shen et al., 2009) and observations showed that metallicity is increasing with V_C (see Zaritsky et al., 1994). This is readily explained by systems with greater masses

being more likely to retain metal rich ejecta of their supernovae but alternative explanations have been brought forward like "downsizing" (a systematic dependence of the efficiency of star formation with galaxy mass), variation of the initial mass function (IMF) with galaxy mass, and infall of metal-poor gas (see Mannucci and Cresci, 2010).

More precisely, it was found that at low stellar mass, metallicity decreases sharply with star formation rate (SFR) whereas at higher stellar mass ($log(M_\star/M_\odot) > 10.9$), metallicity does not depend on or increase with SFR (see Mannucci and Cresci, 2010, Zahid et al., 2012). Thus the metallicity as parameterized by galaxy mass and SFR can be called the fundamental metallicity relation (FMR) as it describes as well all galaxies from the nearby Universe up to 2.6 billion years after the Big Bang ($z \sim 2.5$, see Mannucci and Cresci, 2010).

To further explain the FMR, Mannucci and Cresci (2010) suggested that many local galaxies can be in quasi steady-state situations, in which gas infall, star formation and metal ejection occur simultaneously. Assuming it is thus valid that infall and SFR are slowly evolving with respect to the timescale of chemical enrichment, these authors stated it could be shown that outflows are inversely proportional to mass and increase with SFR.

Dust emission, content and structures in disk galaxies

As in this thesis we explore properties of disk galaxies in the infrared (IR) and focus specifically on the far infrared domain where cosmic dust dominates the emission, we wish to introduce in details common knowledge about cosmic dust.

In extragalactic astrophysics, the infrared wavelengths are roughly separated into near infrared (NIR: $0.7-5.0\mu m$), mid infrared (MIR: $5.0-24\mu m$) and far infrared (FIR: $24-500\mu m$).

Main dust contributors according to wavelength ranges

In disk galaxies of the nearby Universe ($z \approx 0$), dust emitting in the ISM has three prominent components, i.e. polycyclic aromatic hydrocarbon (PAH), graphite and silicate (see for more details Zubko et al., 2004 and Galliano et al., 2011).

The NIR spectrum of the interstellar medium (ISM) is dominated by stellar emission, but dust emission bands also contribute (such as polycyclic aromatic hydrocarbon, "PAH" emission, see Mentuch et al., 2010).

MIR emission of the ISM in disk galaxies is dominated by dust emission, emission line from the gas and emission from hot dust in AGN accretion disks (see Galliano, 2004). More precisely, MIR spectra of spirals can be fitted with 3 components: PAHs bands are fitted by lorentzian profiles (PAH major emission bands are between 3 and 13 μm); ionic lines, whose contribution is small in general, are modeled with gaussian profiles (the largest [NeII] at $12.8\,\mu m$, is seen toward galactic nuclei) and the continua assumed to have powerlaw shapes (see Vogler et al., 2005). There are primarily 2 types of MIR emiting dust in galaxies: small particles or large molecules (e.g. PAHs) producing emission bands; and very small grains (VSGs) with typical sizes of 1 to 150 nm from which originates the MIR continuum longward of 11 μm (see Vogler et al., 2005). The PAHs dominate in energy over the small grain continuum emission in the wavelengths from 4 to 18 μm. The energy powering the MIR emission of galaxies is mainly coming from the star forming processes. We will focus on the ties between star formation and dust in a dedicated subsection.

FIR emission from the ISM is dominated by dust emission with also some emission lines from the gas phase (see figure 6).

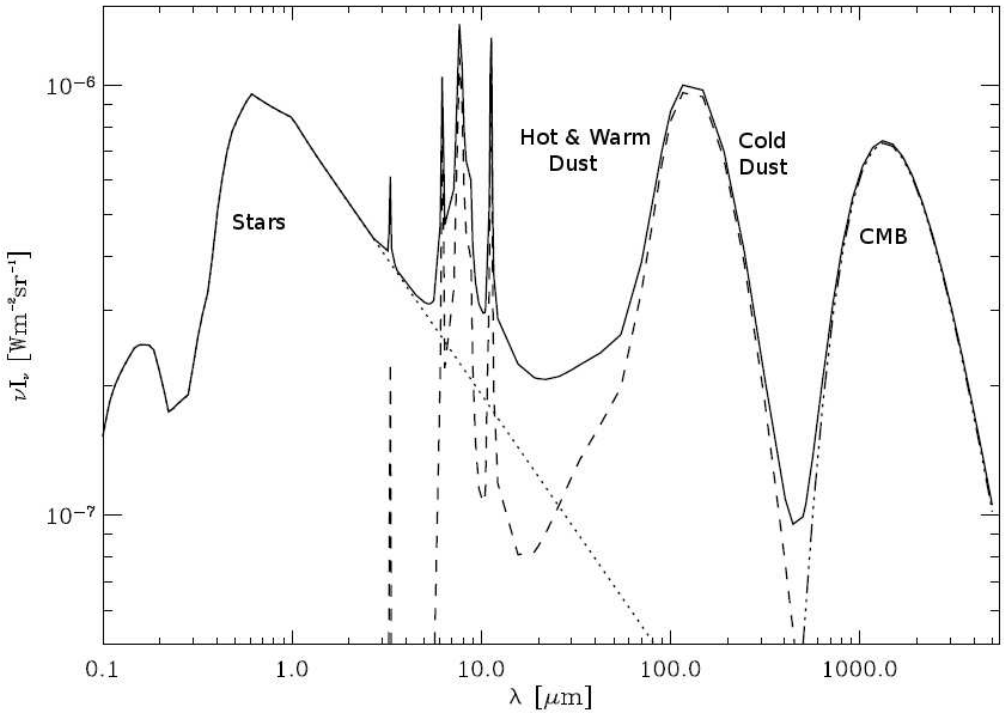

Figure 6: Figure A.3 from Galliano (2004). This figure represents the local ISM spectrum inside our Milky Way. CMB is for Cosmic Microwave Background. ν is the frequency, λ the wavelength, I_ν the monochromatic intensity.

In the two following sections we will present, first in the NIR-MIR and then in the FIR, the different structures observed in dust emission maps of disk galaxies. We will also highlight the main heating regimes of interstellar dust as well as potential heating sources.

Dust heating regimes and structures observable in IR galaxy maps

Some structures, conspicuous in optical maps of disk galaxies, which are dominated by stellar radiations, are also observed in maps dominated by dust emission (e.g. $\geq 20\mu m$). Depending on the galaxy, these structures can be (see Sauvage et al., 2010) prominent spiral arms, bars, stellar disk dusty counterpart seen as diffuse emission between and outside spiral arms, the core, stellar bulge dusty counterpart (see Groves et al., 2012) and rings. The core component is more conspicuous, smaller and more concentrated than the bulge dusty counterpart (see Bendo et al., 2007).

Throughout the range of infrared wavelengths, the dust emission regime in the interstellar medium (ISM) is currently mainly seen as twofold.

Either dust is stochastically heated, for instance warm dust emitting bands. This mainly concerns NIR, MIR and FIR wavelengths up to $\approx 100\mu m$.

Or dust can be at thermal equilibrium with its surrounding and thus emit a thermal emission like cold dust for example, which is dominant in FIR wavelengths between $100\mu m$ and $500\mu m$.

Dust heating regime and heating sources in the NIR and in the MIR

Dust emitting in the NIR and MIR is mainly stochastically heated, undergoing large temperature fluctuations of the order of a few hundreds of K on short timescales as a result of single photon heating processes. Very small grains (VSGs) emitting in the MIR could be either stochastically heated or in thermal equilibrium depending on grain sizes and radiation field properties. Both PAH and VSGs are excited mainly by UV photons in the vicinity of active star forming regions (although PAHs can also be excited by optical photons as evidenced by their presence in the diffuse interstellar medium (ISM) and elliptical galaxies; see Vogler et al., 2005). Thus at least some stellar emission is spatially tightly correlated with warm dust. In turn, this partly explains why optical, NIR and MIR galactic map are morphologically similar.

Furthermore in optical, NIR and MIR maps, galaxies have smaller diameters than in the FIR (see Sauvage et al., 2005). Interestingly, MIR/radio and FIR/radio local correlations on scales of 500 pc (for FIR wavelengths smaller than $200\mu m$) were reported to have similar slopes which was interpreted as FIR and MIR being powered by the same UV photons (see Sauvage et al., 2005), though we note that, at the time, there was no data beyond 200 microns.

Dust heating regimes and heating sources in the FIR

Dust emitting in the FIR wavelengths is either stochastically heated or at thermal equilibrium.

Studying the core/disk dichotomy in M81 (NGC 3031), M99 (NGC 4254) and M100 (NGC 4321) with FIR maps ($24 - 500\mu m$), Sauvage et al. (2010) found small core-to-total luminosity fractions ($\leq 20\%$). These core components were almost always very well represented by gaussians. Comparing between these three galaxies, they also found a significant variation of FIR core colors but relatively homogeneous FIR disk colors.

It was already known at that time that the $200\mu m$ emission is not arising from localised sources but rather from the diffuse ISM and that its corresponding scalelength is comparable to or slightly larger than the scalelength of stellar dominated optical emission, as well as greater than scalelengths associated with 60 and $100\mu m$ emission, even if dust emitting at $200\mu m$ is not always seen beyond the edge of the optical disk. Scalelengths were thus shown to increase with wavelength in the FIR. These observations were interpreted as $200\mu m$ emission arising from grains of the diffuse disk heated by a radially decreasing radiation field (see Sauvage et al., 2005). Davies et al. (1999), studying $200\mu m$ emission, also showed that the cold dust was more extended than molecular gas but still less extended than the HI gas (a notable exception is M100/NGC4321 in which dust can be found almost out to the HI edge; see Sauvage et al., 2005 and Pohlen et al., 2009).

In a galaxy map pixel, the flux in the FIR is due to very numerous dust clouds located along the line of sight. These clouds are supposed to be of different masses and different typical temperatures. Although FIR colors taken separately cannot disentangle between increasing column density and dust temperature, this can be achieved through modelling and fitting of FIR spectral energy distribution (SED).

The cold dust emission in disk galaxies is usually fitted by a modified black body spectrum with T_d the dust temperature, ν_0 a reference frequency, and β the emissivity index (see Galliano, 2004):

$$B_\nu(T_d) = \left(\frac{\nu}{\nu_0}\right)^\beta \frac{2h\nu^3}{c^2} \frac{1}{exp(h\nu/kT_d) - 1} \tag{3}$$

For instance Sauvage et al. (2005) explained that the M31 overall ISOPHOT spectral energy distribution (SED) between 20 and 170 μm can be well described as a superposition of

two modified $\beta = 2$ Planck curves with dust temperatures T_d of 16 and 45 K. They further characterized the FIR emission from the main morphological components of spiral galaxies as:

- nucleus: an unresolved warm source with $T_d \sim 30K$;
- spiral arms, as a superposition of:
  - ▶ localised warm emission with $40 < T_d < 60K$ from HII regions (star forming regions);
  - ▶ localised cold emission with $15 < T_d < 20K$ from parent molecular clouds;
  - ▶ diffuse emission running along the arms;
- disk: an underlying diffuse (predominantly cold) emission with $12 < T_d < 20K$ (for example ring structure).

Cesarsky and Sauvage (1999) also showed that the peak of the FIR spectral energy distribution (SED) is shifted from $100 - 200\mu m$ in normal disk galaxies to $60 - 100\mu m$ in starburst galaxies, implying a warmer dust temperature in starburst galaxies probably due to more intense average ISRF intensity.

Other studies (Cesarsky and Sauvage, 1999, Galliano et al., 2011, see also references therein) stressed that the probable value of the emissivity index of cold dust at thermal equilibrium in the ISM of spirals is around $\beta = 2$. Recently an anti-correlation between β and cold dust temperature T_d has been shown to exist in the study of the Kingfish sample of galaxies (see Galametz et al., 2012). This result was interpreted as either due to possible uncertainties in flux measurements, a real emissivity variation of dust grains with temperature or a dust temperature mixing along the line of sight. We see that the precise physical origin of β is as yet an open field of research.

Galametz et al. (2012) also reported that a two modified blackbody fit of spectral energy distribution (SED) from 24 to 500 μm with β decreasing from 2.0 to 1.5 yielded dust masses systematically lower by 25 % to 46 %. It shows that still acceptable variations in β create a specific uncertainty on dust masses.

They also showed that if the cold dust emissivity index is fixed to a standard $\beta = 2.0$, a smooth radial decrease of the cold dust temperatures is observed toward the outer parts of the galaxies. Whereas if β is free as well as dust temperature, barred spirals show temperature distributions similar to those obtained with a fixed β and homogeneous emissivity index. For non-barred galaxies, β seems to decrease with radius and cold dust temperatures are homogenous. According to these authors, in these latter galaxies, temperature maps seemingly not related to any dust heating sources question the use of a free β in these galaxies.

These authors also showed that in some disk galaxies the temperature distribution of cold dust follows the distribution of star-forming regions (NGC 3627 for instance). This is in agreement with Gordon et al. (2004), finding that M81 (NGC 3031) has a significant amount of cold dust, emitting at $\lambda \leq 160\mu m$, associated with spiral arms and mostly heated by recent star formation even at the longest MIPS wavelength ($160\mu m$).

This seems also consistent with the conclusion drawn by Grootes et al. (2013) from analysing data spanning FIR wavelengths $100 - 500\mu m$ for a sample of 74 late-type galaxies. They found that most of the submm emission of these galaxies originates from grains residing in translucent structures exposed to UV in the diffuse interstellar radiation field.

These are two important arguments hinting at some dust emitting in the FIR being heated by star formation processes and radiations of hot stars.

Similarly, exploring the light from young stars in near ultraviolet (NUV : 2310$\mathring{A}$) and far ultraviolet (FUV: 1530$\mathring{A}$), reradiated by dust in M101 (NGC 5457), Popescu et al. (2005) found that the high values of the $[100\mu m]/[FUV + NUV]$ ratio trace the interarm region and more specifically have a tight dependence on galacto-centric radius. This was interpreted in terms of the presence of a large scale distribution of diffuse dust having a face-on optical depth which decreases with radius and which dominates over the more localised variations in opacity between the arm and interarm regions.

However more contrasted claims have been made by Bendo et al. (2010) studying M81 (NGC 3031). They showed that galacto-centric radius is accounting for more than 70% of the variance of surface brightness ratios in the wavelength range $160-500\mu m$. Bendo et al. (2010) concluded that radial variations of FIR colors, especially 250/350 and 350/500 color ratios which are dust temperature indices (see Pohlen et al., 2009), imply that the dust emission is more strongly affected by the evolved stellar populations in the bulge and disk of M81. This is consistent with Muñoz-Mateos (2009) finding that dust as a whole is heated by an average ISRF, monotonically decreasing with galacto-centric radius. These are also consistent with similar findings by the Pohlen et al. (2009) study of M99 and M100. Bendo et al. (2010) further anticipated that dust emitting at $160-500\mu m$ in galaxies with relatively large fractions of old stars (E-Sab galaxies) would have $160-500\mu m$ colours that depend upon radius, but galaxies with relatively large fractions of young stars (Sc-Im galaxies) would have $160-500\mu m$ colours that may depend more on infrared surface brightnesses, as heating by the evolved stellar population becomes insignificant. These show that another part of dust emitting in the FIR is actually heated by old stellar populations.

Pohlen et al. (2009) also showed that dust dominated FIR maps exhibit breaks in similar radial regions to stellar dominated optical maps. This suggests that in these galaxies dust emission could possibly stem from intermediate-age stellar population emission.

Another study by Groves et al. (2012) ruled out gas-grain collisions, AGN and young stellar populations as possible heating sources for the warm dust (up to $35^{\circ}K$) in the bulge of M31, thus linking its emission with old stellar populations ($\geq$ 6 Gyr old).

They found that their model overestimated dust temperatures as compared to measurements. They interpreted this as the sign of dust properties in the bulge of M31 differing from the standard diffuse dust in the Milky Way. They also invoked the fact that dust was likely to be in a clumpy distribution in M31 bulge with some self-shielding occurring.

We conclude that dust heating sources in the FIR have to be assessed on a case by case basis, i.e. in general all star forming processes, young stellar populations and evolved ones are likely to contribute to dust FIR emission.

In the following section we will briefly review the main role of dust in star formation and how dust emission can trace star formation.

Dust role in star formation

Dust has at least two important roles in star formation. First, dust grains are the main catalyst for HI conversion to H_2, thus molecular clouds are mainly formed on the surface of dust grains. Secondly dust grains are the main coolant in star forming galaxies, therefore as dust cools the gas reservoirs, it enables them to be more prompt to collapse under gravity. We may add that if dust is dense enough and far enough from young stellar populations, it shields the gas from the ultraviolet radiations of these young stellar populations, and so keeps gas clouds cool enough to continue to produce stars. Hence dust is also observed in large quantities where H_2 collapses into stars (see Pohlen et al., 2009, and references therein).

We will now review to what extent dust can be seen as a star formation tracer.

The main star formation tracer is the H_α $656.3nm$ recombination line. It mainly comes from atomic hydrogen atoms located near or inside HII regions. In these HII regions, hydrogen is ionized because gas column density is too low to prevent the penetration of FUV photons from massive and young stars. These regions also contain enough atomic hydrogen for its emission to be detected. It was hence surmised that these regions are very recent or ongoing star forming regions.

Regions of star formation are believed to create photodissociation regions (PDR) at the boundary of a giant molecular clouds (see figure A.1 of Galliano, 2004). Inside PDRs, gas column density is higher, hydrogen is predominantly neutral, far ultraviolet (FUV) photons strongly influence the gas chemistry and act as the most important source of heat. For instance in the MIR, PAH are observed to peak in the PDR regions whereas VSGs emit prominently in nebular regions.

It is also remarkable that, altogether, gas temperature, the main gas cooling process through the [CII] $158\mu m$ emission line, luminosity of dust and UV intensity are all strongly correlated inside PDRs (see Sauvage et al., 2005). On larger scales however the correlation between dust emission in the NIR, MIR and FIR with H_α line although being strong, have strongly dissimilar explanations.

PAH emitting in excess of the stellar continuum in the NIR is globally linearly correlated with extinction corrected H_α emission, thus linking this excess emission with star forming processes (see Mentuch et al., 2010). More precisely star formation is correlated with PAH emission on scales larger than 1 kpc and Bendo et al. (2009) found that they are not on sub-kpc scales. These authors explained the large scale correlation of PAH and star formation, by PAH enhancement indirectly induced through increases in the interstellar radiation field (ISRF). This increased ISRF is accompanying more active star formation.

Globally integrated MIR emission correlation with globally integrated H_α is non-linear. This non-linearity is due to the fact that MIR luminosities mix together contributions from central regions and from the disk (see Sauvage et al., 2005). For instance disk surface brightnesses of $6.75\,\mu m$ and $15\,\mu m$ emission are separately linearly correlated with extinction corrected H_α surface brightnesses. Therefore, although the MIR emission from the disk of spiral galaxies does not originate directly in the star-forming regions, but rather from the PDRs around them, it is the energy from the star-formation process that powers the MIR luminosity in the disk.

MIR global luminosity was showed by Roussel et al. (2001b) to give an accurate tracer of star formation provided it was corrected for the core galactic contribution and H_α was specifically corrected for extinction in these inner regions, and it was subsequently demonstrated that $6.75\,\mu m$ luminosity is still a good tracer of star formation in the central regions of spiral galaxies as it was in their disks.

The non-linearity in the global $6.75\,\mu m$-H_α diagrams is attributed to the increase of extinction from the disk to central star forming regions. As for the global $15\,\mu m$ emission, even taking into account the extinction, its correlation with H_α is non-linear because the star forming processes occuring in more inner galaxy regions shift the emission of very small grains towards shorter wavelength by changing their thermal regime. These arguments show that global properties cannot be interpreted without local knowledge.

Globally integrated FIR-H_α correlation is also non-linear. More precisely globally integrated FIR-H_α correlation is linear for warm FIR emission and non-linear for cold FIR emission.

This is backed up by the warm FIR / radio linear correlation found to be in agreement with warm dust being heated within star forming regions, the scatter coming from a small component inside the diffuse disk (produced either by transiently heated grains or by grains heated by old stellar populations) as well as the likely variation of HII regions dust temperatures within and between galaxies.

Thus FIR emission considered in isolation is a poor star formation rate (SFR) estimator because old and young stars emission powers it. Furthermore, depending on the FIR/submm wavelengths, the UV powered dust emission arises in different proportions from within the localised component (HII regions) and from the diffuse component. For instance, in the case of NGC 891, an edge-on spiral, it was determined that although the bulk of the FIR emission emerged from the diffuse component, the dust was predominantly heated by UV photons (see Sauvage et al., 2005). It was found by Sauvage et al. (2005) that the diffuse disk-like component gathers the bulk of the dust cold FIR emission, and that this trend is more pronounced in the most quiescent galaxies. This speaks in favor of FIR emission being less powered by star forming processes in the galaxies where star formation is comparatively weaker.

The non-linearity in terms of cold FIR increasing more slowly than H_α is readily explained by the different spatial locations of sources producing respectively these two emissions, the higher contribution from optical photons in heating the grains in more quiescent galaxies and the increased contribution of the diffuse component with increasing FIR wavelengths. This can be linked with the fact that optical photons heat dust more when the galaxy stellar mass increases (see Pierini and Möller, 2003). This can be interpreted as more massive galaxies being on average less subjected to star formation, and thus possibly being less prompt to heat dust through radiation from hot stars.

To more precisely assess the dust heating sources, notably for dust emitting in the FIR, and the link between dust emission and SFR, the extinction must be taken into account properly, since a quantitative interpretation of dust emission in terms of SFRs and star formation history (SFH) requires all ultraviolet (UV), optical, FIR and submillimeter (submm) spectral energy distributions (SED) as well as a self consistent model for the propagation of photons.

Other more complex comparisons to SFR involve IR/radio emission correlations. For example, it was reported that an universal correlation existed between spatially integrated FIR and radio emission in spirals. Although the warm FIR / radio correlation is linear, the cold FIR / radio correlation was found slightly non-linear. To explain this latter non-linearity it was argued that both cold FIR and radio emission were likely to have non-linear behaviour with SFR. For the radio, an enhancement of the small free-free component with SFR could account for this effect whereas for the cold FIR emission, a detailed analysis of the dependence of local absorption and opacity of the diffuse medium on SFR is required to understand the non-linear trend of the correlation (see Sauvage et al., 2005).

Dust production and distribution of mass

In this subsection we will first present dust mass distribution and dust production processes.

Muñoz-Mateos (2009) computed that 1% of the dust mass, heated by fierce localised ISRF, accounts for 10% of the total dust IR luminosity. This observation warns about the natural bias of eyes being drawn toward more luminous regions inside FIR maps whereas these regions do not necessarily contain larger dust amounts than fainter ones (especially in wavelengths $\lambda < 100\mu m$).

Muñoz-Mateos (2009) also confirmed that dust is less abundant in earlier spirals, typically having surface densities below $10^5\,M_\odot.kpc^{-2}$, but also in Sdm and later, where it drops below $10^4\,M_\odot.kpc^{-2}$. The dust density profiles they derived from measurements are exponential. They also showed that a wide range of attenuations ($1-2$ mag) can be found for a given observed (i.e. projected) dust mass surface density. The minimum values of attenuation are always found in Sc galaxies and later, while for the same amount of dust, earlier spirals (especially Sb-Sbc ones) exhibit larger extinctions. Their interpretation of this result is that in late type dust and stars are arranged in a clumpy geometry, many UV photons being able to leak through lines of sight clean of dust, which they claimed is not the case in Sbc spirals and earlier types. This is consistent with the spatial organisation of dust w.r.t. stars in these earlier type spirals leaving less room for line of sight clean of dust around stars.

It is interesting to compare this study stemming from analysis of radial profiles to the study of integrated properties of galaxies by Zahid et al. (2012). In their sample, including star forming galaxies as well as quiescent ones, they showed that galaxies with less than $10^{10}\,M_\odot$ of stellar content exhibit a negative correlation between SFR and dust extinction whereas they found the opposite trend in galaxies with stellar content more massive than $10^{10}\,M_\odot$ (see also Grootes et al., 2013). The trends found by Zahid et al. (2012) reversing at high stellar masses have similar counterparts with dust extinction replaced by metallicity (see Yates et al., 2012). We conclude that in massive galaxies larger SFRs yield larger metal abundances and greater dust column densities. As SFR is unlikely to strongly depend on atomic hydrogen surface density (see figure 7), in regions of massive galaxies where the measurement of O/H is possible, when SFR increases there is also larger absolute quantities of metals.

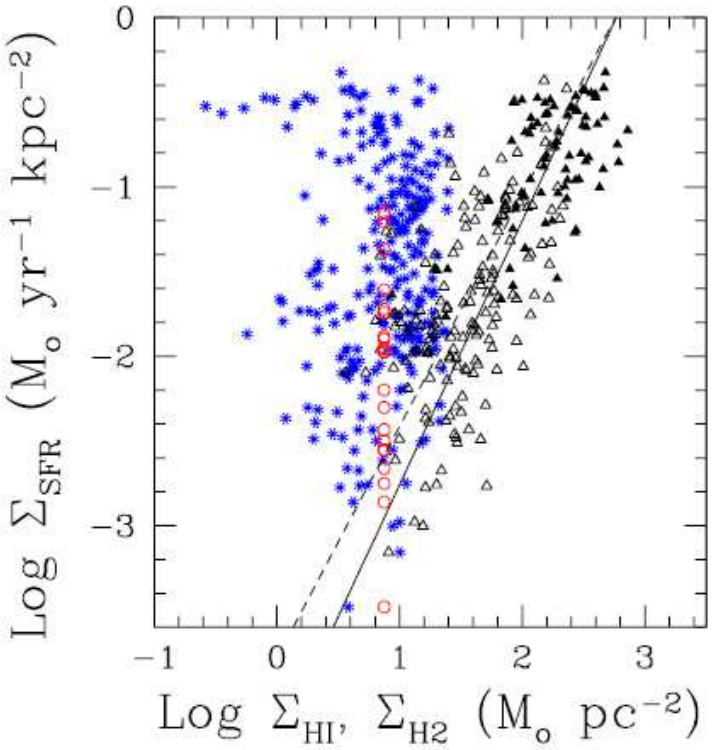

Figure 7: Figure 4 from Kennicutt (2008) illustrating the relationship between the SFR surface density and the HI (asterisks) and H2 (triangles) surface densities for the same regions in M51.

Fundamentally, the main known producers of elements composing cosmic dust are asymp-

totic giant branch (AGB) stars and supernovae (SNe). A way to enhance dust yield is molecular clouds in which dust growth occurs. It has been shown by Asano et al. (2011) that dust production is mainly driven by ISM dust growth in the Large Magellanic Cloud (LMC) and Small Magellanic Cloud (SMC) with only a few percent due to AGB stars. This issue was also studied in disk galaxies (see Muñoz-Mateos, 2009, Mattsson and Andersen, 2012) and very similar conclusions were reached. We note that except in the most quiescent spirals, the cold dust does not dominate the energy emitted by dust but rather the total dust mass (see Sauvage et al., 2005, Pohlen et al., 2009), thus we expect to probe the bulk of dust masses of disk galaxies in the ISM in the form of cold dust at thermal equilibrium, mainly emitting in the FIR.

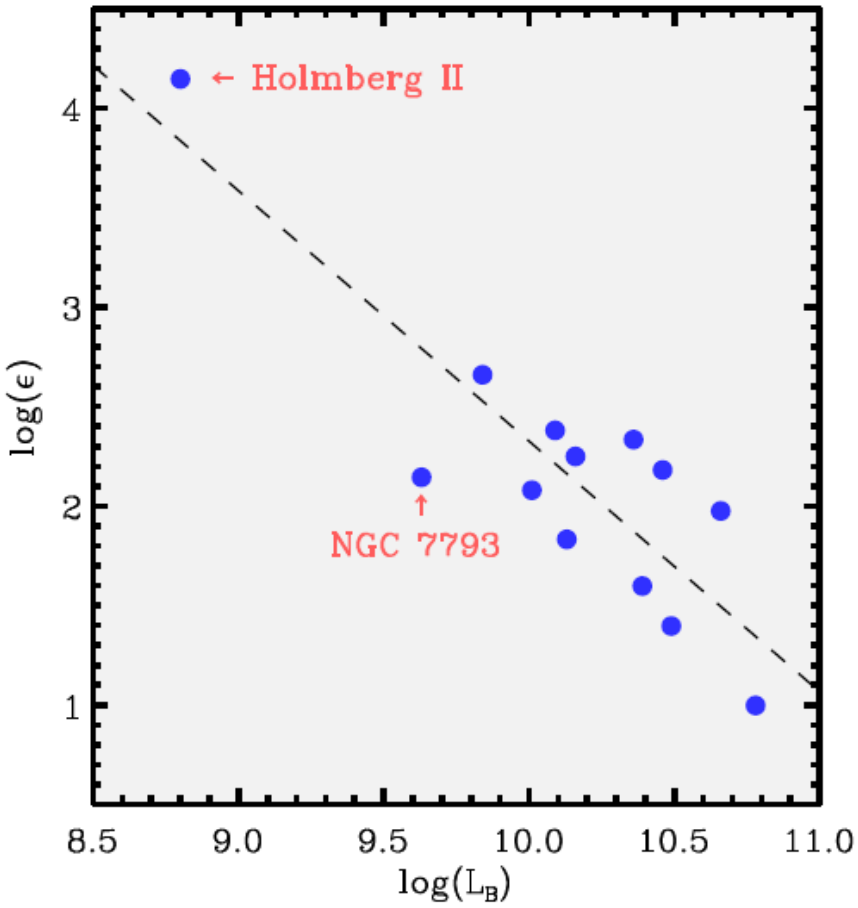

Figure 8: Part of figure 3 from Mattsson and Andersen (2012) illustrating the correlation between the dust-growth parameter ϵ (for models where the fitting does not imply $\epsilon \to 0$) and the B-band luminosity of each galaxy in their sample.

Interestingly Mattsson and Andersen (2012) defined a grain growth parameter inversely proportionnal to the timescale of dust grain growth (see equations (24) and (27) of Mattsson et al., 2012). The grain growth parameter is essentially treated as a free parameter of the model regulating the rate of change of the dust-to-gas ratio due to accretion of metals on to pre-existing dust grains in the ISM. These authors showed that there exists a correlation between B band galaxy luminosity and the so called grain growth parameter they defined (see figure 8), which seems to hint at low luminosity systems, reknown to be mainly weakly star forming, developing more suitable environment for dust growth in molecular clouds. They also mentionned the

conclusions of Gordon et al. (2004) according to which cold dust emitting at $\lambda \leq 160\mu m$ would be primarily heated by young stellar populations *in spiral arms* (see above). Indeed where dust is mainly heated by young stellar populations, too strong a star forming activity could impede dust formation, because energetic radiations of hot stars may shatter dust grains to small splinters (see Mattsson and Andersen, 2012).

However as it is also specified by Gordon et al. (2004) that cold dust is usually stated to be heated by old stellar populations, where and if that is the case, the link between star forming activity and dust formation seems more complex to understand. Thus one could conclude that dust is mainly grown far from high luminosity regions and heated by old stellar populations.

This view has to be pondered with observations by Galametz et al. (2012) showing that not only the dust mass surface density usually peaks in the center of galaxies but it also seems to coincide with extra-nuclear peaks of star formation at the end of the bars (usually corresponding to molecular gas reservoirs). Besides, spiral arms, reknown for their strong star forming activity, dense molecular clouds and dusty counterpart, may be the preferred location to search for dust creation in the ISM, and especially to assess the role of star formation and dust creation in the ISM. The possible major role of molecular clouds in spiral arms formation through swing amplification (see D'Onghia et al., 2013) may be the sign of a link between these molecular clouds and spiral arms in dust formation. We see that the main growing mechanism of cosmic dust and the location where this mechanism takes place still is an active field of reasearch. There is not as yet a definitive answer.

Furthermore, the role of molecular clouds in the dust cycle inside galaxies is also questionned by Grootes et al. (2013). These authors studied the relation between specific star formation rate and stellar mass with a model using stellar surface density and dust extinction in the B band as inputs. They concluded that the large majority of refractory dust resides in the diffuse ISM, rather than in opaque clouds. These authors made a largely model-independent inference requiring the rapid (re-)formation of dust grains after their destruction in the ISM, as has also been inferred from chemo-dynamical modelling of the dust cycle in the Milky-Way and external galaxies.

Thus there is a specific role played by faint galactic regions in growth and (re-)formation of dust grains. For instance, not only dust emission in the FIR was detected in many nearby disk galaxies to at least the optical radius defined by R25 (see Pohlen et al., 2009) especially in types Sb-Sd (see Muñoz-Mateos, 2009), but it was already noted by Sauvage et al. (2005) and earlier studies that disk associated cold dust scalelengths were larger than those of stellar content. It was recently precisely assessed by Muñoz-Mateos (2009) to be a $\sim 10\%$ increase of dust density scalelength with respect to stellar emission scalelength. These argue in favor of a relative agreement between stellar distribution and dust distribution. One of the key results of this thesis is that the link between the two distributions is less trivial than what appeared at first sight. Linking quantitatively these two distributions requires taking into account other parameters than only the old stellar population and dust phase emission maps.

This was already hinted at by Muñoz-Mateos (2009). They found many early type disk galaxies exhibiting central plateaus or holes in their dust density profiles, whereas stellar density continues building up till the center (sometimes even with a steeper slope than in the disk whereas this is very rare for dust). Such a low central density of dust is also seen in the bulge of M31 by Groves et al. (2012). Sauvage et al. (2005) already speculated either that there was a mechanism to transport grains from the inner disk (star forming regions) to the outer disk or that the typical lifetimes of grains against the destruction by shocks was longer in the outer disk than it was in the inner disk.

These arguments hint at least at a certain degree of dissimilarity between stellar and dust surface density radial profiles notably at small radii.

This issue was raised to a new level by the recent study of Mattsson and Andersen (2012) confirming that dust destruction due to supernovae (SN) and dust creation by asymptotic giant branch (AGB) stars are not as crucial as dust growth in the ISM (especially in dense molecular clouds) to account for observed dust-to-gas ratios in galaxies. Dust destruction was defined by these authors as atomization of dust grains. In particular they showed that in none of their galaxies was dust destruction necessary to explain dust-to-gas ratios in the intermediate and outer regions of disks. What is more, for the majority of galaxies in their sample, they succeeded to account for the whole observed dust-to-gas radial profile with no dust destruction at all (see part 3.4 of Mattsson and Andersen, 2012 for further details). As there is no doubt dust destruction or atomization exists close to supernovae, the latter study is still compatible with some dust destruction if it is a relatively inefficient phenomenon as compared to dust growth in the ISM. If this is not the case another way to make dust destruction compatible with observations would be to state that dust masses derived from observations are overestimated (we will see later in this section that such claims are readily found in recent articles). These results call at least for more research to precisely assess whether dust column densities are overestimated or whether there is a way to explain dust rapid re-formation in the ISM.

Mattsson and Andersen (2012) authors found dust-to-gas ratios to be decreasing with radius as what was previously expected from the results of Pohlen et al. (2009).

This is also in agreement with Roussel et al. (2001a) study of 69 nearby spiral galaxies finding no indication that destruction of aromatic bands dust carriers occurs at the scale of circumnuclear regions.

We can also mention Zahid et al. (2012) invoking that dust destruction would predict *opposite* trends for dust extinction and metallicity. This is due to the fact that dust extinction is proportionnal to dust column density, thus as dust destruction involves atomizing dust hence releasing metals from dust in the ISM, dust destruction should decrease dust column density and increase metallicity. However as opposite trends between dust extinction and metallicity is not observed, dust destruction seems unlikely to strongly affect global galactic dust budget. This in turn calls for weak or non existent dust destruction in galactic regions most representative of global census of dust extinction. If these are inner galactic regions, the latter argument would probably rule out altogether dust destruction as a possible explanation for the decreasing slope of dust surface densities with radius observed at small galacto-centric radii by Muñoz-Mateos (2009).

It should be noted that Mattsson and Andersen (2012) claimed dust abundances to be overestimated, because at small galacto-centric radii a few of their data points still exhibit dust-to-metals ratio exceeding unity and they already used oxygen abundances at the high end of the possible range. They duly asserted their claim was supported by Madden et al. (2011) studying the gas-to-dust content of dwarf galaxies. Mattsson and Andersen (2012) explained that their working hypothesis of fixing the grain-size distribution and specific compositions of different dust species to solar neighbourhood measurements, was probably an oversimplification not reflecting dust properties in other galaxies. In spite of that, these authors trust their results at least qualitatively. They state that the down scaling of dust densities they applied to derive acceptable dust-to-metals ratios, would be a systematic error not affecting the radial slope of dust density with radius.

This issue has to be mitigated with Galametz et al. (2012) noticing that the dust mass estimates seem to be affected by resolution, with a systematically larger total dust mass in the "resolved" case as compared to the dust mass globally determined. These authors interpret their results as massive cold dust clouds undetected as if diluted out by hotter dust clouds.

This calls for more finely spatially resolved FIR maps, and suggests that one could attempt a correction of this dust mass underestimation effect by monitoring how the total dust mass is affected when the resolution is decreased.

As the dust mass underestimation due to resolution is very unlikely to affect in the same proportion maps of oxygen abundances, there is thus an important effect of resolution on dust-to-metals ratios.

To explore the problem further we highlight that for instance Mattsson and Andersen (2012) had to apply a downscaling factor to the radial surface density profiles of dust masses obtained from Muñoz-Mateos (2009) to obtain dust-to-metal ratios below unity. This concerns spatially resolved dust mass estimates. However Galametz et al. (2012) found that global estimates are underestimating dust masses w.r.t. local dust mass estimates. These authors produced factors that have to be applied to global estimates so that they reach agreement with local estimates.

We remark from Galametz et al. (2012) that one has to increase global estimates by 11 % and 69 % respectively for NGC 7793 and NGC 3621 to match local estimates; but we also note that Mattsson and Andersen (2012) had to decrease local dust mass estimates altogether by respectively 15% and 35% respectively for NGC 7793 and NGC 3621 to avoid obtaining local dust-to-metal ratios larger than unity. We see that to some extent these two corrections compensate each other, thus global dust estimates may well be rather in agreement with litterature values of metallicity.

Furthermore as the model used by Mattsson and Andersen (2012) to account for dust-to-gas ratios was mainly based on metallicity gradients and dust growth in the ISM (see also Mattsson et al., 2012) entailing generally strong negative radial gradient of dust-to-metals ratios inside disk galaxies, they concluded it is too simple to say that extinction scales with metallicity, especially for integrated diagnostics of disk galaxies. This was already prefigured by Bot et al. (2004) showing that a simple linear dependence between gas-to-dust ratios and metallicity does not apply for the diffuse medium of the Small Magellanic Cloud (SMC).

We conclude that the diffuse ISM play a major role in dust (re-)formation from metals, that earlier type spirals probably have less clumpy dust-star organization in the sense that there is less line of sight clean of dust from stars outward in these galaxies. In more massive galaxies, when SFR increases, metals abundances in the ISM and dust column densities increase. The dust and stellar density profiles seem rather in agreement in a large part of disks of disk galaxies, although dust surface density tends to increase more slowly than stellar surface density at small radii. This behaviour is in turn rather well explained by dust formation models if one admits the existence of an ISM specific dust formation process more efficient than dust destruction, e.g. by supernovae. We also stress that some conflicting claims have been made about dust densities either under or overestimated.

Central questions driving my thesis work

As we showed, the links between various galactic components inside disk galaxies are known to be very intricate. In this thesis we explore mainly the links between the stellar component and the dusty component of the ISM.

The original idea behind this thesis is based on results of Bendo et al. (2011), especially the surface brightness ratios at long wavelengths, i.e. $[250\mu m]/[350\mu m]$ and $[350\mu m]/[500\mu m]$ colors, being more tightly correlated with the starlight from total stellar populations rather than with $H\alpha$ emission from young stellar populations. The same authors also found that the emission of dust at short wavelengths seems to be more strongly correlated with $H\alpha$, even if at wavelengths larger than $160\mu m$ dust emission seems more correlated with the total stellar population emission.

Thus it seems legitimate to ask the following questions: what is the precise link, if such a link exists at all, between the total and especially the old stellar component and the cosmic dust inside the stellar disk? Is there a dusty counterpart to the stellar disk, and if there is at least one link between these two phases, what is its meaning ? Is it possible to link dust emission to heating sources or stellar luminosity inside galactic disks ? Is there a link between how dust and stellar surface densities vary with galacto-centric distance inside disk galaxies ?

These questions drove my work.

The goals and the sample

Resolved submillimeter studies from the ground remain limited to the very nearby universe and large surveys of more distant galaxies are unfeasible by these means. But with the help of Herschel space observatory mapping dust emission combined with the number of recent high resolution surveys tracing the gas mass, astrophysicists are now able to study the distribution of gas, metals and dust on a kpc scale for hundreds of local galaxies (see Pohlen et al., 2009).

In this thesis we aimed at probing the structural properties of dust inside disk galaxies as well as the variations of physical properties of dust inside those objects, and possibly explore whether there is a link between some dust structures and physical properties. Thus we focus our efforts on analysing cosmic dust emission maps of some resolved disk galaxies (closer than $30\,Mpc$).

To extract the physical properties of dust inside disk galaxies we need to finely sample the spectrum of cosmic dust emission. Thus we used galaxy maps at 3.6, 4.5, 5.8 and $8.0\,\mu m$ (IRAC) ; 24, 70, $160\,\mu m$ (MIPS) ; 70, 100, $160\,\mu m$ (PACS) ; and 250, 350, $500\,\mu m$ (SPIRE). Standard data reduction procedures were used to produce all our maps except for PACS data which were reduced through the scanamorphos pipeline (see Roussel, 2013). Full width at half maximum (FWHM) of point spread functions (PSF) of studied maps are shown in table 2. This work is therefore a multi-wavelength study, ranging from observation of the long wavelength emission of old stellar populations black body emission ($4.5\,\mu m$), to tiny grains of dust not at thermal equilibrium ($24\,\mu m$) or at thermal equilibrium ($> 100\,\mu m$).

Amid the maps we use, the smallest spatial resolutions are obtained in maps at $500\mu m$ (SPIRE) and $160\mu m$ (MIPS). The number of disk galaxies that have been observed by the Herschel Space Observatory at $500\mu m$ and are resolved in this band remains limited at present. Most of them could be found in the sample of galaxy nammed " Key Insights on Nearby Galaxies: a Far-Infrared Survey with Herschel " (further called Kingfish, see Kennicutt et al., 2011) and the Very Nearby Galaxy Survey (further called VNGS, see Baes et al., 2011). The Kingfish sample is made of resolved galaxies, spanning broad ranges of physical properties, star formation properties, and local interstellar environments. For simplicity, we only study in this thesis objects from the Kingfish survey. Adding the VNGS data would increase the sample by $\sim 30\%$ at most.

Thus the galaxy sample we consider throughout this work is a subsample of the Kingfish sample. We excluded from Kingfish sample irregular galaxies, elliptical galaxies and NGC 5398 because it is irregular in appearance (NGC 5398 is categorized as SB(rs)dm in de Vaucouleurs et al., 1991).

The method

Some authors already studied cosmic dust emission of Kingfish galaxies on a pixel-by-pixel basis (see Galliano et al., 2011, Aniano et al., 2012 and Galametz et al., 2012). They mainly were

Table 2: Spatial resolutions of maps

	Irac				Mips			Pacs			Spire		
λ (μm)	3.6	4.5	5.8	8.0	24	70	160	70	100	160	250	350	500
PSF (")	1.66	1.72	1.88	1.98	6	18	38	7.2	8.2	13.6	18.2	24.9	36.3

interested in understanding in more detail properties of cosmic dust as well as the physical links between the dust phase and other properties characterizing the galactic medium (such as the global or local star formation rate) as well as other galactic phases such as the molecular or atomic gas phases.

This thesis has a slightly different focus which is to explore cosmic dust structure in connection with the old stellar phase. As we previously showed the structure of this latter phase is nowadays relatively well documented. For this purpose we will examine shapes of isophotes in dust dominated emission maps of disk galaxies. The shapes of these isophotes provide clues on how dust is distributed inside disk galaxies. We will see in the first chapter of this thesis that this can be used to bring to light disk structures in the dust phase.

Another objective of the present work is to relate dust structure to physical properties of dust. To achieve this we will make use of the disk structures extracted in the first chapter, to analyse, in a second chapter, the physical properties of the dust phase inside these structures and if these properties are related to the ones of the old stellar phase.

Layout of the thesis

Thus we will describe in a first chapter how to devise without a priori the inclination of a galactic disk from its maps in the NIR, MIR and FIR, and how to evidence disk structures in the dust phase of disk galaxies. Then in a second chapter we will use the results of the first chapter to study the physical properties of dust with respect to the stellar content in dust disks.

Foreword

We remark that in numerous studies extracting structural parameters of disk galaxies, e.g. exponential disk parameters (see section 2.2 Giovanelli and Haynes, 1994 and also section 2.2 of Prieto et al., 2000) systematic visual inspection played an important role, not only to study the results of the extraction, but also as a key step of the extraction process itself.

Though, as long as data analysis methods are biased by the subjectivity of investigators through systematical personal inspection, these methods are bound to be less efficient for studying large data sets than entirely automatic routines.

Thus in the present work we aimed as much as possible at building automatic methods that could be used on larger data sets than the one we studied here.

Chapter 1

Evidencing dust disks

We will here present the method we used to examine whether it was possible to derive without a priori a disk orientation from infrared maps, robust under change of wavelength, as well as representative of as large a galacto-centric radial range as possible, i.e. supporting the existence of a dust disk.

The original idea behind this work naturally emerges from a simple fact: many litterature studies extract the disk orientation of a disk galaxy by fitting an ellipse on a single external isophote of the galaxy map. There is a bias in such an orientation measurement due to the level of luminosity chosen to extract the isophote (or similarly to the semi-major axis length of the isophote) and to the band map used to make this measurement. As we have the chance to peer inside resolved maps of disk galaxies in many wavelength bands, it is now possible to precisely quantify whether and how well isophotes can be associated with the disk structure. This can be done by comparing the shapes of many isophotes inside galactic maps.

However before following this roadmap we will first explain how we extract isophotes from galactic maps and how we can compare their shapes.

1.1 Extraction of the background sky signal

We need first to evaluate the noise in each galaxy map. In our maps, especially in FIR maps ($\geq 24\mu m$), the noise is mainly produced by the sky background including high z galaxies in SPIRE bands. In first approximation this noise is gaussian (see section 4.3 of the online Herschel Observers' Manual) and thus can be charaterized by its first two moments, i.e. its average intensity and standard deviation.

These parameters were extracted from all intensity maps via an automatic method.

We constructed the histogram of the intensities of map pixels and fitted a gaussian law on the part of this histogram closest to the nul intensity.

This method enables to get the standard deviation and average intensity of the background sky signal.

It is very likely that this method overestimates the single pixel noise level in regions close to the galaxy inside our FIR maps [1]. This is due to pixels far from the galaxy, and notably close to regions where there is no coverage, i.e. where the only available intensity value is Not a Number (NaN), having smaller coverage duration than in the center of the image. Thus these pixels have been observed less time than those close to the galaxy. Therefore the pixels far from the galaxy contribute more to the low intensity noise in the image and probably unduly

[1] " close " to the galaxy here simply means: inside the region of interest as defined in section 1.2.

increase the obtained standard deviation as compared to a standard deviation which could be obtained by taking into account only a region closer to the galaxy.

1.2 Region of interest around each galaxy

At this point we want to reject some parts of the galactic maps especially the pixels close to the edges of the maps which are (especially in FIR bands) fraugth with larger noise levels, e.g. due to smaller exposure times.

We thus use coordinates of the galactic center of each galaxy, found on the web page of KINGFISH project to compute the histogram of distances of non-NaN pixels to the center of each galaxy.

The radius R_M where the number of pixels with non-NaN intensity is maximum is very close to the region of the map where NaN-valued pixels prevail, i.e. the edge of the map. So we cut a circle around each galaxy center at a radius of $R_{ROI} = \frac{3}{4} \times R_M$. This defines what we call the region of interest (see picture 1.1).

The size of this region varies in each map. We focused our study on shapes of isophotes extracted from all our wavelength bands containing dust emission (3 bands of MIPS, 3 bands of PACS, 3 bands of SPIRE, thus 9 bands) and we chose to pick only one extra wavelength representing stellar continuum emission, namely $4.5\,\mu m$, because it is reknown to be, amid all IRAC bands, the least affected by dust (see page 4/5 of Saha et al. (2009)). In these 460 maps (46 galaxies, and for each 10 wavelengths) $3/4 \times R_M/R25 \in [0.3, 18.1]$, but $3/4 \times R_M/R25$ has a mean value of 2.34 with a statistical dispersion associated with the average of 0.10 (only one galaxy map has $3/4 \times R_M/R25$ between 0.3 and 0.4 : IRAC 3.6 map of NGC 4631 (type SB(s)d); but 12 galaxy maps of various galaxies have $3/4 \times R_M/R25$ between 0.4 and 0.5, these maps are only found in MIPS 160 and IRAC bands). This shows that the region of interest is usually covering a region twice larger than the optical disk.

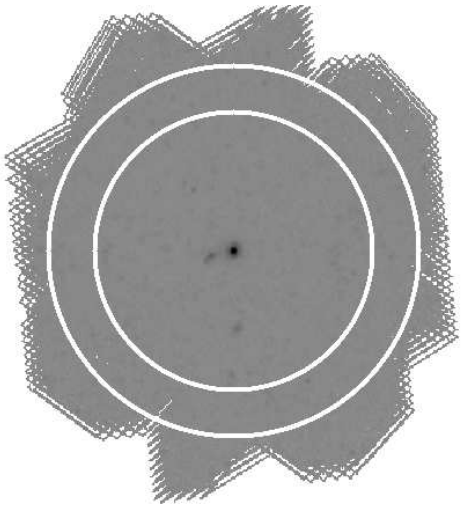

Figure 1.1: NGC 2798 viewed with SPIRE $250\mu m$. Grey scale is inversely proportional to the logarithm of the intensity. The larger and smaller white circles have respective radius R_M and $3/4 \times R_M$, the latter being the region of interest for this map. No pixel outside the small white circle is used for isophote extraction. Here $3/4 \times R_M/R25 \sim 7.3$, with $R25 \sim 78''$ for NGC 2798 (see NED). $3/4 \times R_M$ change with bandmap and galaxy.

1.3 Isophote extraction

This region of interest was submitted to thresholding processes to extract isophotes. This enables to consistently reject pixels close to the border of NaN valued regions in the map. Since some of these pixels near the boundaries of the meaningful image can be saturated or have irregular values of intensity, it is a good thing not to take them into account.

After a region of interest was selected around each galaxy in each galaxy map, we chose intensity levels, and at each intensity we created a corresponding isophote. These levels were computed as the sky background average intensity level (μ) plus an integer or half-integer multiple, between 0 and 19, of the sky background standard deviation in intensity (σ). As we chose $4.5\mu m$ plus all 9 dust bands (MIPS, PACS, SPIRE), this process resulted in 39 isophotes level for 460 galaxy maps. For consistency our analysis method of each image was automatic.

Concerning surface brightnesses higher than $\mu + 19\sigma$, the involved pixels are almost all very much inside the galaxy. Because in those regions intrinsic galactic structures affect strongly isophote shapes, these inner pixels can usually provide only second hand information about disk orientations. Thus we did not take into account isophotes with intensities higher than $\mu + 19\sigma$ in any image.

Once the intensity levels are chosen the region of interest in the map is thresholded at these levels. Each pixel with intensity higher than the chosen one is set to unity.

In the next step any pixel at zero in the thresholded map stays at zero. All pixels at one in the thresholded map are subjected to potential modifications.
Either:
-(a) they have, in the thresholded map, a zero pixel amid their 8 neighbours. These pixels are on the contour of the isophote so they stay at one.
-(b) they do not have, in the thresholded map, any zero pixel amid their 8 surrounding neighbours. These pixels are in the interior of the isophote so they become zero.
This process gives the isophote map.

1.4 Disk orientation extraction and distance between ellipses

Our aim is to make a comparison between orientations of disks galaxies that we derive and litterature values.

In the following we apply one method to fit ellipses on images of isophotes (hereafter named ISO-B2AC method) extracted from galaxy maps (see image 1.2). This ellipse fitting method was created by using Fitzgibbon et al. (1999) and Maini (2005). We choose this method rather than other routines fitting ellipses directly on region of interest like thresholded images, because what we really want is an elliptical shape representing an isophote and not a region of interest or an elliptical blob. We acknowledge that in the idealistic case of a pure ellipse, many ellipse fitting methods yield very similar results. However isophote extraction results in pixel selections whose shapes vary from strongly elliptical to rather distorted ellipses. These latter more realistic cases are precisely the ones in which different ellipse fitting routines yield discrepant results. These arguments favor the specific choice of ellipse fitting technique we opted for.

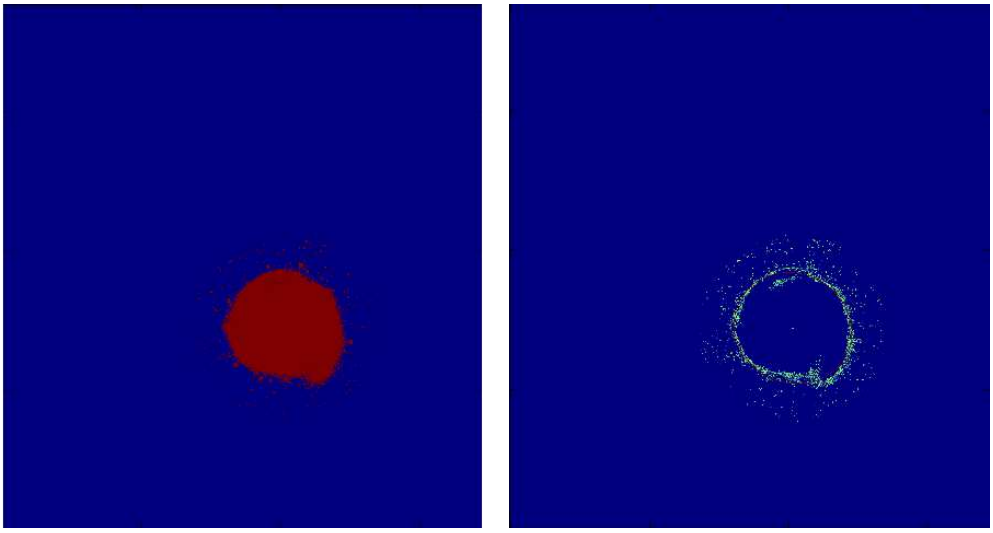

Figure 1.2: The image used here is the $4.5\,\mu m$ map of NGC 4321. The intensity level selected is $I = \mu + 5\sigma$. We get first the image on the left which is the thresholded image at intensity I. Another process is applied which suppresses, i.e. puts to zero all un-connected small patches around the largest region of selected pixels. We then extracted isophotes by the method explained at the end of section 1.3 obtaining images like the one on the right. ISO-B2AC fits ellipses on isophotes images similar to the one on the right.

To quantitatively compare disk orientations from different studies as well as define radial ranges of galaxy maps where consistent disk orientations can be extracted, we built a method to compare ellipse shapes.

As disk of disk galaxies are oblate spheroids expected to gather the bulk of visible matter, including the largest portion of stars and dust, it is worthwhile devising a way to consistently extract and compare orientations of these disks.

Inside images of these disks, the intensity is decreasing with radius in a roughly exponential way. Therefore isophotes of decreasing mean surface brightnesses can be roughly described as ellipses with increasing semi-major axis. From the shapes of these ellipses the orientation of the disk can be deduced.

This picture becomes more complicated for inner galactic isophotes which are perturbed by structures like spiral arms, classical bulges and bars. Thus our study will focus on external

isophotes.

Furthermore, probing at the same time variations of both position angle and axis ratios across galactic disks can be fruitful as we shall see later on that proximity between disk orientations, or equivalently ellipse shapes of isophotes, depends in an intrincate way on position angle as well as axis ratio.

Thus to compare elliptical shapes, we only compared position angles and axis ratios between two ellipses without taking into account their centers or semi-major axis. The rationale for this is twofold.

First it is not critical to take into account differing centers because as disk galaxies are very regular objects, their centers are clearly defined. We refer the reader to the most recent NED centers defined for all galaxies in our sample to a precision much smaller than a fraction of R25. These most accurate NED galactic center coordinates are the same as those given on the official Kingfish website. We will thus hereinafter indifferently use the denomination Kingfish center or NED center to refer to the galactic center coordinates.

Secondly, we will also not consider the change in semi-major axis because as disk galaxies are well described by one oblate spheroid, shapes of isophotes representative of this disk should have similar axis ratios and position angles even though they differ in semi-major axis value.

The method we will see below will prove useful in the next chapter, for the identification of regions (in terms of galacto-centric radius range) in which elliptical shapes associated to isophotes do not to vary much around one average shape. This enabled us to assess the practicability of extracting the orientation of the disk in our galaxy maps.

We shall keep in mind that one of the goals of this work is to find out whether our data support the existence of an underlying disk distribution of IR light and if so measure its geometrical parameters: axis ratios and position angles.

This is what drives us to compare axis ratios and position angles once all ellipses have the same centers. It would enable later on to determine on what range of galactocentric radius a certain shape (position angle and axis ratio) will correspond to the shape of isophotes.

This work is also assessing whether there is support for and consistency in azimuthally averaging our bidimensionnal maps of galaxy intensity into radial profiles of intensity.

Discrepancy between two ellipses

We will devise in this subsection an easy approach and non mathematical insight of how to quantify the fact that an ellipse resembles another one. We encourage readers mainly interested by the precise, more mathematical approach to skip this and continue reading at the beginning of next section where it will be developped.

The main recipe to distinguish two ellipses is to compute an indicator of how much points of each ellipse are distant from one another. This has to get a more precise meaning. First the unit circle is bidimensionnal and polar coordinates are adequate to describe location of points inside of it. We will therefore use these coordinates to define our discrepancy indicator.

We note that thus, naturally, emerges the idea that two ellipses can be discrepant radially (along a radial semi-axis) and azimuthally (along a circle, see table 1.3).

It seems however more legitimate not to single out a certain radial direction or a certain size of circular arc. Thus we summed the discrepancies shown on table 1.3 over different directions (on the left) and over different circular arcs (on the right, see table 1.4).

Figure 1.3: Radial (left) and azimuthal (right) discrepancy between two ellipses. These discrepancies are respectively quantified, here, by the continuous violet segment on the left and the continuous cyan circular arc on the right.

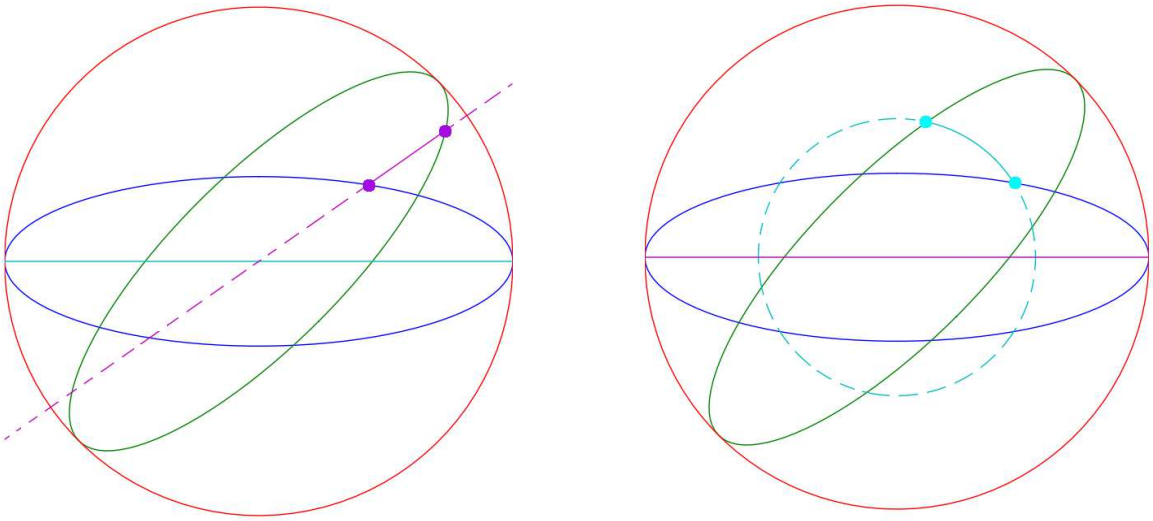

Figure 1.4: Radial discrepancies (left) and azimuthal discrepancies (right) between two ellipses. These discrepancies can be quantified by lengths of black segment (left) or lengths of black circular arcs (right).

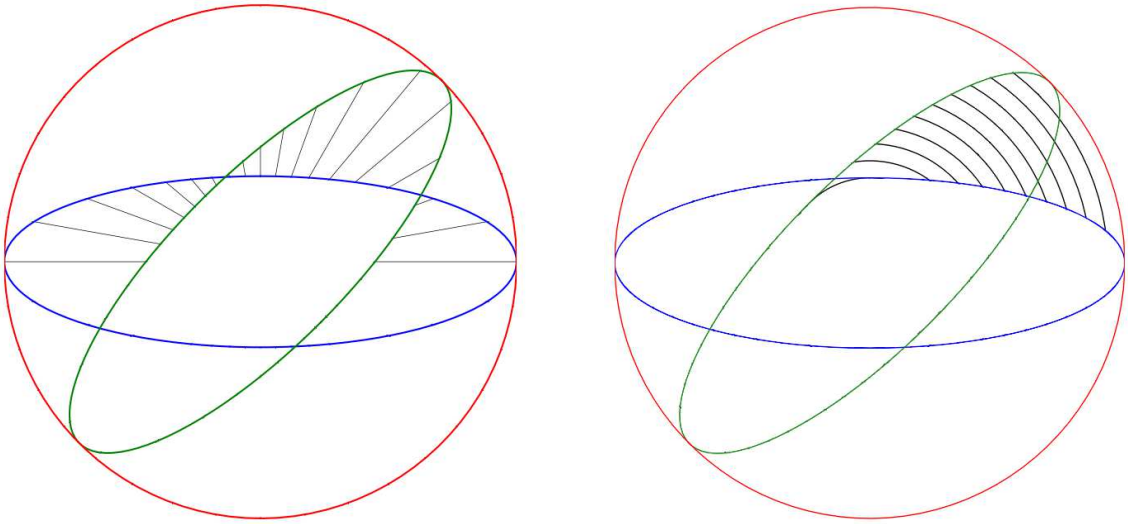

We also see that for radial discrepancies the summation is azimuthal, i.e. over different directions (see left picture of table 1.4). This summation can take into account all possible angles, or just the half plan of positive abscissa. Both are exactly equivalent because on both halves of the plan, the summation yields same results.

Similarly, for azimuthal discrepancies, the summation is radial, between a radius equal to the bigger axis ratio of the two ellipses and unity.

To avoid ambiguously defining circular arcs, we should first try to consistently consider only one half of both ellipses. More precisely we decided to take into account only one half of each ellipse cut out from this ellipse to be on the same side w.r.t. the semi-minor axis (see. green and blue square brackets on left picture of table 1.5 indicating which part of green and blue ellipses we considered). This is the reason why we have not considered arcs like the yellow-dotted arc.

These azimuthal discrepancies to be further correctly defined should be zero when both ellipses are the same. This is why circular arcs we use here should link corresponding halves of each ellipse (contrary to red-dotted circular arcs on table 1.5). Each half ellipse side is considered to be left side (resp. right) if it is on the left (resp. right) of the semi-major axis (see table 1.5). Thus we can define arcs linking sides on the left (resp. right) of both semi-major axis as "left arcs" (resp. "right arcs"). In this case we clearly have all left arcs AND right arcs entirely contained in only one and the same half plane. We stress here that the choice is NOT to consider especially short rather than long arcs nor the opposite but rather to define left and right arcs in a consistent and univocal manner.

The azimuthal discrepancy used here cannot legitimately single out right or left arcs as right arc is transformed into left arc by exchanging position angle (see picture on the left of table 1.5). As exchanging position angle is not changing how different both ellipses are one from the other, azimuthal dispcrepancy should take into account both right and left arcs.

Furthermore, in the case of ellipses with same axis ratio, at fixed radius (see picture on the right of table 1.5), left and right arcs have same length. As these ellipses are strongly different, the azimuthal discrepancy should give a non zero result, thus lengths of right and left arc should not be subtracted but added together or for instance arithmetically averaged.

1.4.1 Azimuthal integral of absolute value of the difference in square radii

We will now focus on a specific way of quantifying the difference between two ellipses, namely an integral over different angles of a difference of squared radii (see left figure 1.4 page 48).

From this point on and unless otherwise specified, we measure ellipse position angles as real numbers in $]-\pi/2, \pi/2]$ and (minor over major) axis ratios as real numbers in [0,1].

We can first compute the following azimuthal integral:

$$I_a(PA_1, PA_2, e_1, e_2) = \frac{1}{2}\int_{\theta=0}^{\theta=\pi} |R_1^2(\theta) - R_2^2(\theta)|.d\theta = \frac{1}{4}\int_{\theta=0}^{\theta=2\pi} |R_1^2(\theta) - R_2^2(\theta)|.d\theta \qquad (1.1)$$

where PA_i and e_i respectively are the position angle and the axis ratio of the i^{th} ellipse. In this integral $R_1^2(\theta) - R_2^2(\theta)$ is the difference between squared vector radius from origin to each ellipse at a fixed θ. Indeed we have that $I_a(PA_1, PA_2, e_1, e_2) = I_a(PA_2, PA_1, e_1, e_2) = I_a(PA_2, PA_1, e_2, e_1)$, see equation (4.5), page 150 for functions $R_i^2(\theta)$. In the latter series of equalities, each of the first and last equalities can independantly be seen, either as exchange of position angles, or exchange of axis ratios (see table 1.9). The last equality can also be seen as a symmetry w.r.t. the top left hand corner to bottom right hand corner diagonal in pictures 1.6, 1.7 and 1.8. In the same series of equalities, the equality between the left-hand member and the right-hand member, omitting the central member, only shows that I_a is symmetrical under permutation of the order according to which each ellipse description enters I_a. Though as the

Figure 1.5: We first consider regions of green and blue ellipses indicated by square brackets. The left (resp. right) side of the green ellipse is marked "LEFT"(resp. "RIGHT") on the left (resp. right) of the semi-major axis. Left (resp. right) arcs linking left (resp. right) sides of each ellipse have starting and ending point in cyan (resp. light green). Examples of circular arcs not linking corresponding sides of ellipses are shown with ending and starting point in red. If discrepancy between ellipses were designed from those red-dotted arcs, this could result in a non zero discrepancy between two ellipses which are the same. The yellow-dotted arc is a left arc but which links a left side of the green ellipse included in the green square bracket-indicated region to a blue ellipse left side in a region excluded by the blue square bracket. Thus we do not consider such yellow-doted arc. We see that for ellipses with same axis ratios (on the right) left arcs and right arcs have same length, whereas it is not the case (on the left) when both ellipses have different axis ratios. It is clear from the picture on the left that when position angles are exchanged, lengths of left arcs become lengths of right arcs and vice versa.

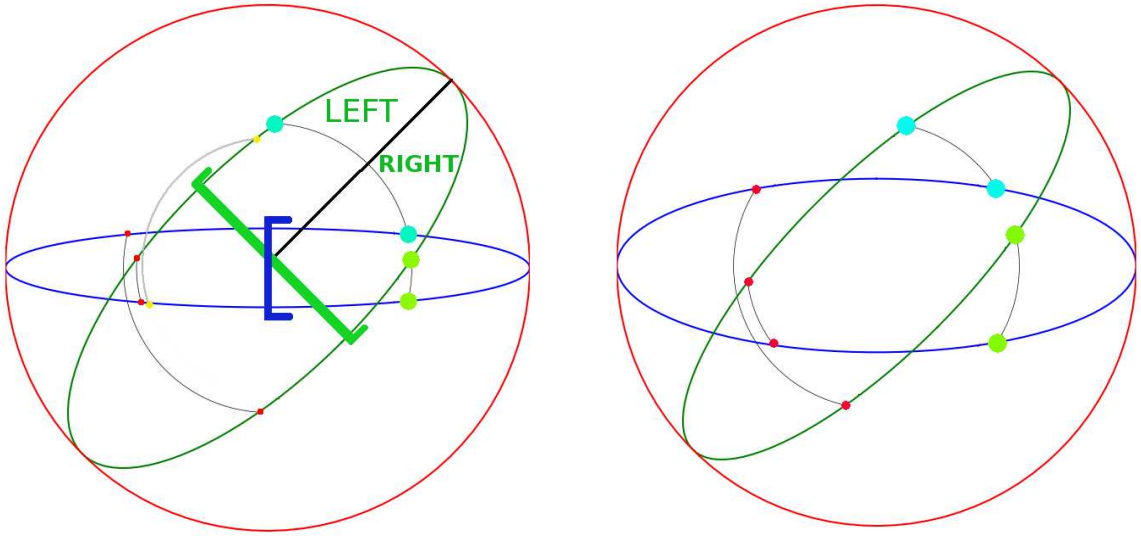

evaluation of $I_a(PA_1, PA_2, e_1, e_2)$ exhibits a small asymmetry with respect to the exchange of PA_2 and PA_1 (computationnally, $I_a(PA_1, PA_2, e_1, e_2) \neq I_a(PA_2, PA_1, e_1, e_2)$, possibly because of non sufficiently small discretization steps in computing the integral), I decided to compute the average

$$I_{a,m}(PA_1, PA_2, e_1, e_2) = \frac{1}{2} \times (I_a(PA_1, PA_2, e_1, e_2) + I_a(PA_2, PA_1, e_1, e_2))$$

to ensure the theoretical symmetry of (1.1) when one permutes PA_2 and PA_1 (see table 1.9), is preserved in computed values of $I_{a,m}$. The symmetry of $I_{a,m}$ with exchange of e_1 and e_2 has been checked computationnally.

We can plot $I_{a,m}$ for different couples of ellipse, see the graphs 1.6, 1.7 and 1.8.

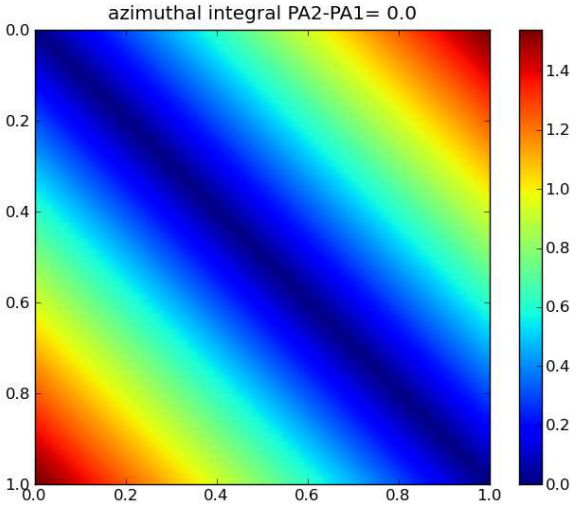

Figure 1.6: Values of the azimuthal integral ($I_{a,m}$) for ellipses of same position angle and axis ratios varying from 0 to 1. In the dark red corners we consider a flat ellipse and circle: the obtained value for the azimuthal integral is half the area of the circle ie $\pi/2$.

$I_{a,m}$ has a geometrical meaning: it is half of the non overlapping area of the two ellipses (see picture 1.10).

$I_{a,m}$ has a minimum value of 0 when the two ellipses are the same, and this integral reaches its maximum value of $\pi/2$ when one ellipse is flat and the other is a circle.

This makes sense as zero values of $I_{a,m}$ for same ellipses is what we expect for a function discriminating well between ellipses (see top left hand corner to bottom right hand corner diagonal of picture 1.6). The behaviour of $I_{a,m}$ when axis ratios are radically different from one another (top right hand and bottom left hand corners of pictures 1.6, 1.7 and 1.8) is very much in agreement with this notion too.

On the other hand, we see that $I_{a,m}$ always have relatively small values when axis ratios are the same, even when the difference of position angle is 45° or 90° (see top left hand angle of 1.7 and 1.8). Actually this can also be seen as an approximate symmetry, namely

$$I_{a,m}(PA_1, PA_2, e_1, e_2) \sim I_{a,m}(PA_1, PA_2, 1 - e_1, 1 - e_2)$$

In a more illustrative way, this is the symmetry w.r.t. the bottom left hand corner to top right hand corner diagonal in pictures 1.6, 1.7 and 1.8, which is creating a bad behaviour for $I_{a,m}$ at non zero position angle differences for weak axis ratios. This is unfortunate and to build a robust notion of distance between ellipses we have to take that fact into account.

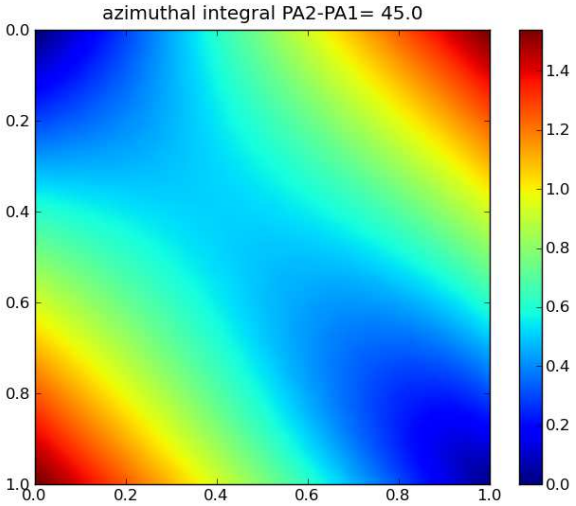

Figure 1.7: Values of the azimuthal integral ($I_{a,m}$) for ellipses with a difference of position angle of 45° and axis ratios varying from 0 to 1.

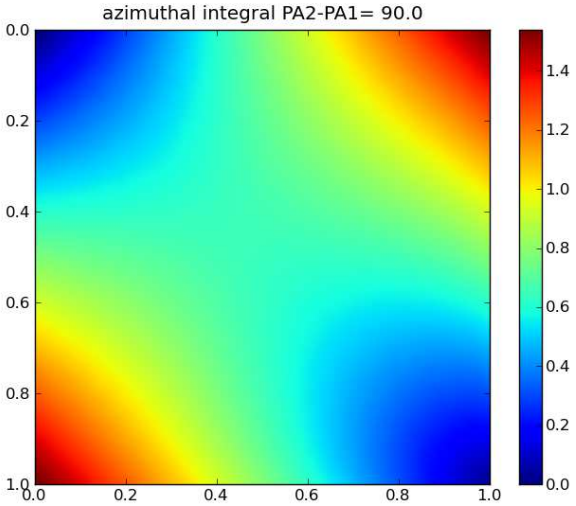

Figure 1.8: Values of the azimuthal integral ($I_{a,m}$) for ellipses with a difference of position angle of 90° and axis ratios varying from 0 to 1.

Figure 1.9: Effect of exchanging PA_1 and PA_2. Both area obtained are equal thus there should be no variation of I_a under this exchange. This is enforced by the computation of $I_{a,m}$ instead of I_a. With the same idea it is possible to show that $I_{a,m}$ only depends on both axis ratios and on the absolute value of the difference between position angles of both ellipses.

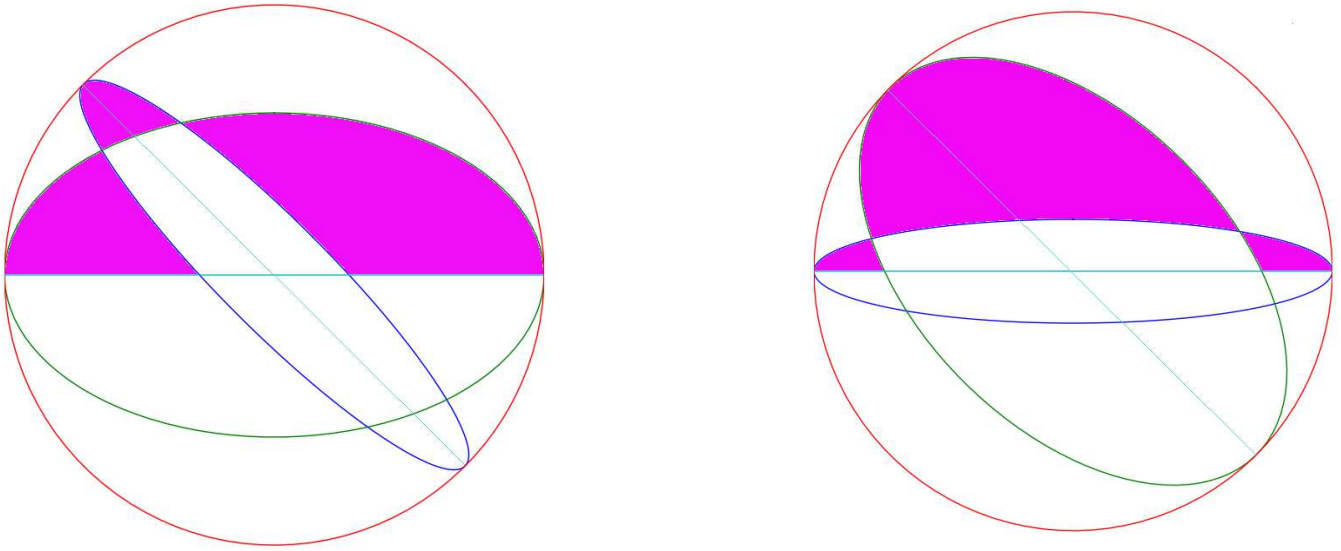

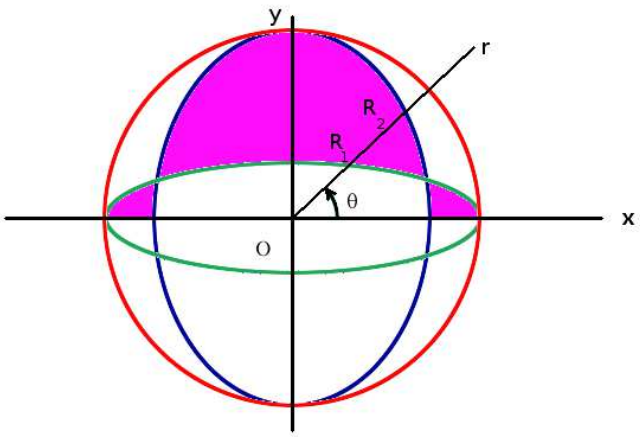

Figure 1.10: The geometrical meaning of the azimuthal integral defined in equation 1.1 is drawn here. It is half of the non overlapping area (in pink) between two ellipses (in blue and green) with same center and same semi-major axis. We also drew the unit circle in red. $R_1(\theta)$ (resp. $R_2(\theta)$) is defined for each $\theta = (Ox, Or)$ as the distance between the origin O and the intersection between $[Or)$ and the green (resp. blue) ellipse.

1.4.2 Radial integral of circular arc length between each ellipse side

We will now focus on another way of quantifying the differences between ellipses, namely an integral over different radii of a circular arc length (see right figure 1.4 page 48).

The issue discussed at the end of the previous section could have been expected, as an indicator based on purely radial differences is bound to have smaller values with smaller axis ratios (in polar coordinates (r, θ), purely radial differences mean same θ, different r; and purely azimuthal differences mean same r, different θ). Thus we will see whether azimuthal differences could complement radial differences to discriminate between different ellipses. This is the driving idea of the present section.

We therefore computed another complementary notion of distance. This is the average of two radial integrals from $r = max(e_1, e_2)$ to $r = 1$ of circular arc lengths. At each radius r, the first (resp. the second) type of arc is defined as the portion of circle of radius r whose endpoints are closest intersection between the circle of radius r and the part of each of the two ellipses on the left (resp. on the right) of its major axis (see figure 1.11). To define each portion of circle (see section 1.4) we only consider one of the two halves of ellipses (we define both half of an ellipse as being separated by the semi-minor axis).

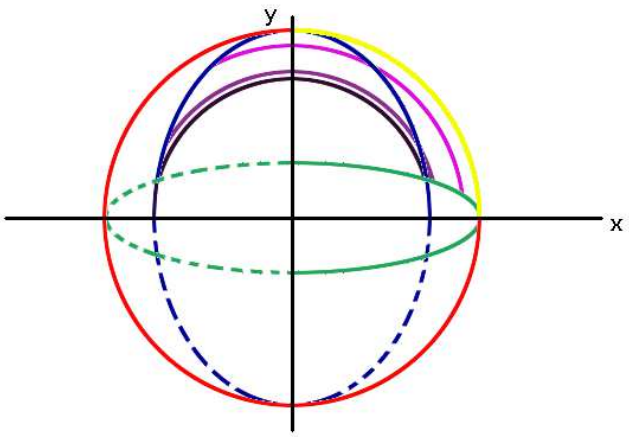

Figure 1.11: The unit circle is in red. The two ellipses we compare are in green and blue. The most exterior circular arc obtained in this case is in yellow (it is characterized by $r = 1$). The most interior circular arc is in dark violet with radius $e = max(e_1, e_2)$. Other circular arcs between left sides of each ellipse are in pink and light violet. Heavy-dash ellipse parts are halves of ellipses not considered for being starting point or ending point of parts of circular arcs.

The average of integrals is:

$$\begin{aligned} & I_r \quad (PA_1, PA_2, e_1, e_2) = \\ = \quad & \frac{1}{2} \times \int_{r=max(e_1,e_2)}^{r=1} \left\{ |\theta_{le,1}(r) - \theta_{le,2}(r)|_{min,\pi} + |\theta_{ri,1}(r) - \theta_{ri,2}(r)|_{min,\pi} \right\} . r.dr \end{aligned}$$

where $\theta_{ri,i}(r)$ (resp. $\theta_{le,i}(r)$) is the angular polar coordinate of the intersection between the circle of radius r and the side of the i^{th} ellipse right (resp. left) to the major axis, see equations (4.6) and (4.7), page 151. We have to stress here that integrals of each of the terms of the sum between braces are generally not the same. Their contributions are shown on figure 1.15. As lengths of left arcs and lengths of right arcs are permutted by exchange of position angles, and

using the definition of I_r (see equation (1.2)) it is possible to show I_r only depends on the axis ratios of each ellipse and the absolute value of their position angle difference.

To consistently define θ_{le} and θ_{ri} as well as "closest" left (resp. right) sides of ellipses we enforce that the absolute value of the principal determination of the difference of position angle between the two ellipses is the smallest.

Furthermore to make sure that for example $\theta_{le,1}(r)$ and $\theta_{le,2}(r)$ correspond to the closest intersections between the circle of radius r and the sides left to the major axis of each ellipse, we compute the angular quantity:

$$a_{min,\pi} = min(a, |\pi - a|)$$

We have also:

$$\begin{aligned} |\theta_{le,1}(r) - \theta_{le,2}(r)|_{min,\pi}(PA_1, PA_2, e_1, e_2) &= |\theta_{ri,1}(r) - \theta_{ri,2}(r)|_{min,\pi}(PA_2, PA_1, e_1, e_2) \\ &= |\theta_{le,1}(r) - \theta_{le,2}(r)|_{min,\pi}(PA_2, PA_1, e_2, e_1) \end{aligned}$$

Thus we get:

$$I_r(PA_1, PA_2, e_1, e_2) = I_r(PA_2, PA_1, e_1, e_2)$$

We can plot the values of I_r for different couple of ellipses, see the graphs 1.12, 1.13 and 1.14.

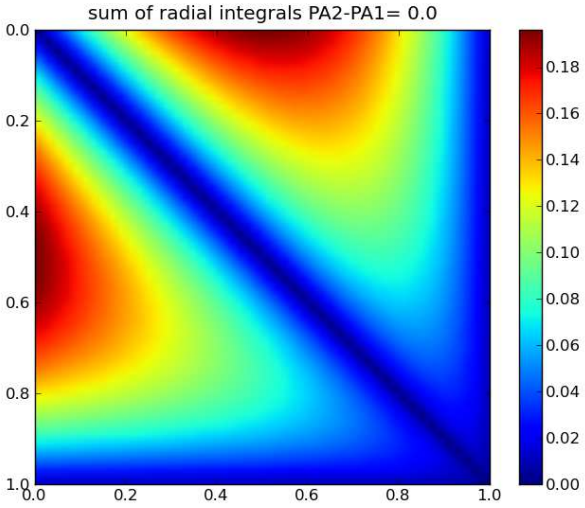

Figure 1.12: Values of the radial integral, I_r, for ellipses with no difference of position angle and axis ratios varying from 0 to 1

I_r also has a geometrical meaning: it is the average of the areas respectively between the closest left sides or the closest right sides of the two ellipses (see figure 1.15).

This integral is equal to 0 when the two ellipses are identical and it reaches its maximum value of $\pi/4$ when both ellipses are flat and with a position angle difference of 90° thus in a case where the $I_{a,m}$ value is very close to zero. This can be observed by comparing top left hand corner of pictures 1.8 and 1.14. We see that this trend is also observed in picture 1.13 as compared to 1.7. Even though the maximum level of I_r in 1.13 is lower than in 1.14, which is

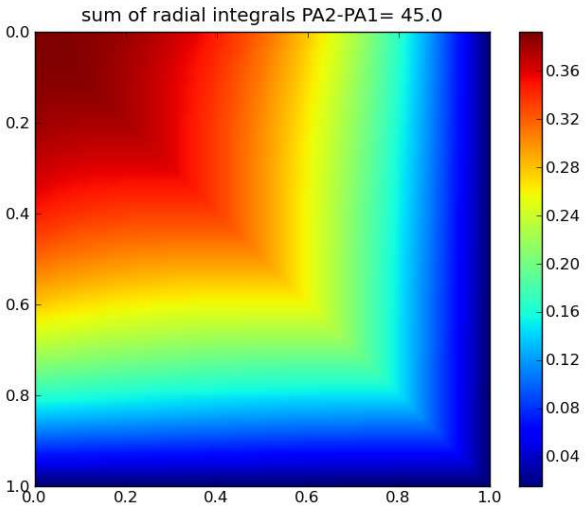

Figure 1.13: Values of the radial integral, I_r for ellipses with a position angle difference of 45° and axis ratios varying from 0 to 1.

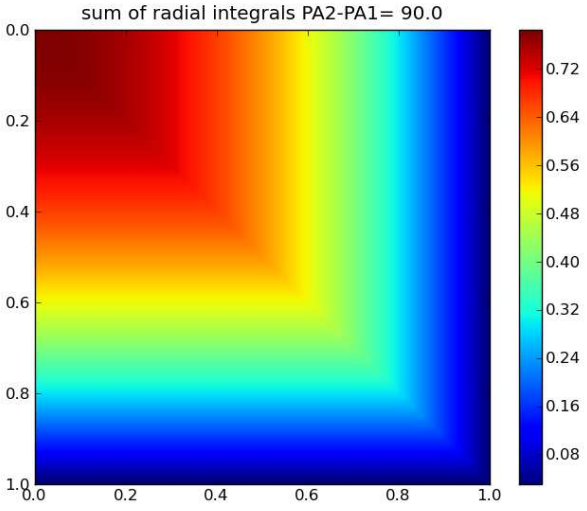

Figure 1.14: Values of the radial integral, I_r, for ellipses with a position angle difference of 90° and axis ratios varying from 0 to 1. See section 4.4 for more details about the shapes of the iso-I_r in this figure.

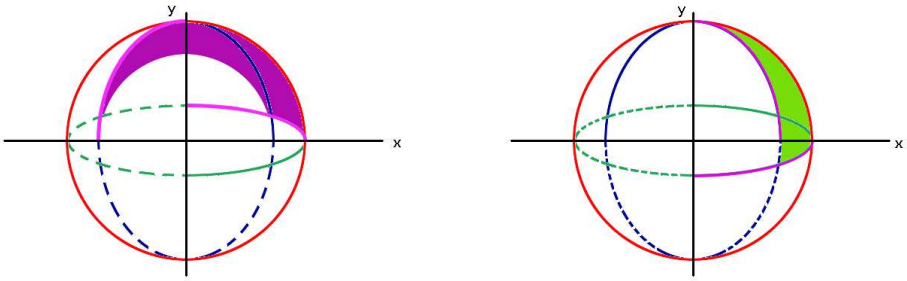

Figure 1.15: The heavy-dash sides are not considered and in each figure the important sides are in light pink. On the left (resp. right), circular arc between left (resp. right) sides of each ellipse are shown. The unit circle is still in red, in the background. The two ellipses we compare are in green and blue. The area between the closest left (resp. right) sides of both ellipses, shown on the left (resp. right), in violet (resp. light green) is the area associated to the part of the radial integral for the " le " indices (resp. the " ri " indices). The average of green and violet area is the value of I_r.

meaningful as flat ellipses with position angle difference of 45° are closer in shapes than with a position angle difference of 90°.

For instance we note that for non zero position angle differences, there is no symmetry anymore w.r.t. the bottom left hand corner to top right hand corner diagonal in pictures 1.12, 1.13 and 1.14.

This seems a legitimate reason to expect I_r is complementary to $I_{a,m}$ to discriminate between different ellipses.

We can see that I_r is always 0 when two ellipses are the same (top left to bottom right diagonal of picture 1.12) which makes sense for an indicator dicriminating between ellipses and its non nul values for small axis ratios once the position angles are not the same can be interpreted in the same way (see top left angles in pictures 1.13 and 1.14).

Indeed as for $I_{a,m}$, I_r has small values once both axis ratios are close to 1, because in this case ellipses are very similar. This is also a good behaviour for an indicator of how different two ellipses are.

We also have to acknowledge that I_r has small values when only one axis ratio is close to 1 and the other is notably different from 1 (bottom and right blue lines, including bottom left and top right corners), whatever the position angles are (see pictures 1.12, 1.13 and 1.14)

In the particular cases of $(e_1, e_2) = (0, 1)$ or $(e_1, e_2) = (1, 0)$, this behaviour does not indicate how different the 2 ellipses are (see top right and bottom left hand corners of pictures 1.12, 1.13 and 1.14). In these cases, however, $I_{a,m}$ has non zero values (see top right and bottom left hand corners of pictures 1.6, 1.7 and 1.8). Thus it seems reasonable to imagine that a linear combination of I_r and $I_{a,m}$ will discriminate better between different ellipses than each of I_r and $I_{a,m}$ taken separately.

1.4.3 Distance (D) between two ellipses of same semi-major axis and same center

The notion of distance D between two ellipses can indeed be better represented by a function proportionnal to $2\, I_r + I_{a,m}$. Choosing this linear combination ensures we get the same discrepancy D between almost flat ellipses with a difference of position angle of 90° ($I_r = \pi/4 \sim 0.79$

in the top left angle of picture 1.14 while $I_{a,m} = 0$ in the top left angle of picture 1.8) and for a circle compared to a flat ellipse whatever the position angles($I_r = 0$ in the top right and bottom left corners of pictures 1.12, 1.13 and 1.14, while $I_{a,m} = \pi/2 \approx 1.6$ in the top right and bottom left corners of picture 1.6, 1.7 and 1.8).

Since in the former and latter cases, the maxima of I_r (resp. $I_{a,m}$) are obtained when $I_{a,m}$ (resp. I_r) is null, we can normalize $2\,I_r + I_a$ by $\pi/2$ to obtain an indicator broadly varying between 0 and 1 in the cases mentionned above. So we get:

$$D = \frac{4I_r + 2I_a}{\pi}$$

Hereinafter, this notion of "distance" or discrepancy will be called D, and with no further notice will always mean $D(PA_1, PA_2, e_1, e_2)$.

1.4.4 Qualitative examination of the variations of D for all couples of ellipses

We have plotted D for different couples of ellipse on pictures 1.16, 1.17 and 1.18. We will examine these cases one after the other.

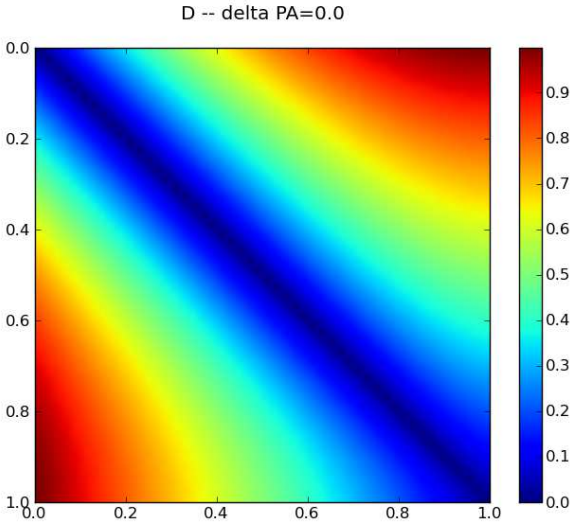

Figure 1.16: Values of D, giving an idea of the difference between ellipses of same position angle and axis ratios varying from 0 to 1. On this plot we see that D is well behaved when position angle is the same for both ellipses, D is closer to zero if axis ratios are closer to one another, and D climbs to high value if axis ratios become very different.

D is discriminating well between different ellipses for $|\Delta PA| = 0°$, on figure 1.16, even if the clear enlargement of the blue zone when axis ratios increase can be questionned. More precisely common sense is not supporting the interpretation of this enlargement according to which the distance between two ellipses with same position angles depends on the average axis ratio of the two ellipses.

In figure 1.17, it appears that when position angles of both ellipses differ from one another, as long as axis ratios are strongly different, D has a large value (i.e. bottom left hand and top right hand corners). However if position angles stay different and axis ratios are the same (top left hand to bottom right hand diagonals of picture 1.17 and 1.18), D does not only have small

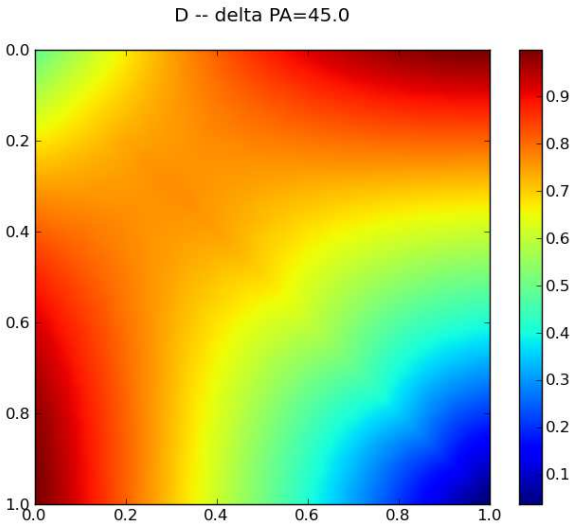

Figure 1.17: Values of D, giving an idea of the difference between ellipses with a position angle difference of 45° and axis ratios varying from 0 to 1.

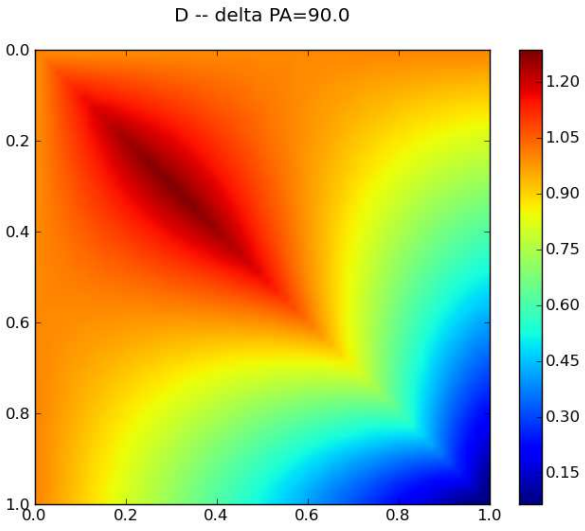

Figure 1.18: Values of D, giving an idea of the difference between ellipses with a position angle difference of 90° and axis ratios varying from 0 to 1.

values for large axis ratios (lower right corner), but D is also somewhat small for small axis ratios as long as position angle difference is not 90° (e.g. $D = 0.5$ when axis ratios are small and $|\Delta PA| = 45^\circ$, see top left hand green corner of picture 1.17).

This behaviour seems to go contrary to the perspective of using D as an indicator of how different two ellipses are. But if we fix the condition $|\Delta PA| = 45^\circ$, when axis ratios are both close to zero we see (on picture 1.17) that the minimum of D is not as low as the one reached when both axis ratios are close to 1. Thus this drawback of D even if present is not as troublesome as it may first appear (in a more detailed fashion, we remark that on top left-hand corner of picture 1.17, $D = 0.5$ whereas in the following we will mainly use D threshold between 0.1 and 0.3 e.g. consequently excluding the top left-hand corner of picture 1.17).

We see on picture 1.18 ($|\Delta PA| = 90^\circ$), that $D(PA_1, PA_2, e_1, e_2)$ is in this extreme case well behaved: the only region where small values of D can be seen are for large axis ratios.

As we can see on the expressions defining D, all components of D depend only on axis ratios of both ellipses and the absolute value of the difference of position angles.

Thus another way of representing the complete range of variations of D is by making the plots of $D(PA_1 = 0, PA_2 = |\Delta PA|, e_1, e_2)$ for $|\Delta PA| \in [0^\circ, 90^\circ]$ and $(e_1, e_2) \in [0, 1]^2$ (see table 1.19).

We will end this section on the remark that it is possible to devise other expressions ($D_{\theta,lin}$,$D_{\theta,arccos}$ and D_{flat}) quantifying the difference between elliptical shapes, as is shown in section 4.5, page 151. We acknowledge that amid all distances between ellipses built in section 4.5, $D = D_{integ}$ presented in the previous chapter seems the easiest to understand. This is not merely because D_{integ} is the easiest distance to build, but because it is relatively easy to relate point-to-point distances between ellipses (along radial lines or circular arcs) and D_{integ}. Indeed, as we shall see in section 4.5, such a link exists also between each of these new discrepancy expressions and "distances" between ellipses, though it is somewhat more difficult to understand. On the other hand these other discrepancy expressions are much easier to compute and less time-consuming to evaluate than D_{integ}.

1.4.5 Ellipse neighbours to one specific ellipse, at a fixed value of the discrepancy D.

We see on table 1.19 that for a fixed $D_0 < 0.9$, at each value of e_1 with $PA_1 = 0$, there always exists at least one of the three ellipses[2] defined by their (e_2,PA_2), with $PA_2 \in [0^\circ, 90^\circ]$ and $D(PA_1, PA_2, e_1, e_2) = D_0$, such that:
- $e_2 < e_1$, $|\Delta PA| = 0$ (thinner neighbour),
- $e_2 > e_1$, $|\Delta PA| = 0$ (fatter neighbour),
- $e_2 = e_1$, $|\Delta PA| \neq 0$ (rotated neighbour).

We examplified where we find these ellipses on figure 1.20.

To get a deeper insight about the behaviour of these elliptical neighbours we will illustrate their use on a concrete example.

[2]Each of these sorts of ellipse characterized by (e_2, PA_2) are in the neighbourhood of (e_1, PA_1). These therefore are three possible kinds of neighbours for (e_1, PA_1) which we can name for convenience the thinner neighbour (with smaller axis ratio), the fatter neighbour (with larger axis ratio) and the rotated neighbour (with non zero position angle difference).

Figure 1.19: Variations of D. Axis ratio e_1 is varying by steps of 0.1 from 0 to 1 in reading order. Values of e_2 are ordinates and $|\Delta PA|$, abscissa.

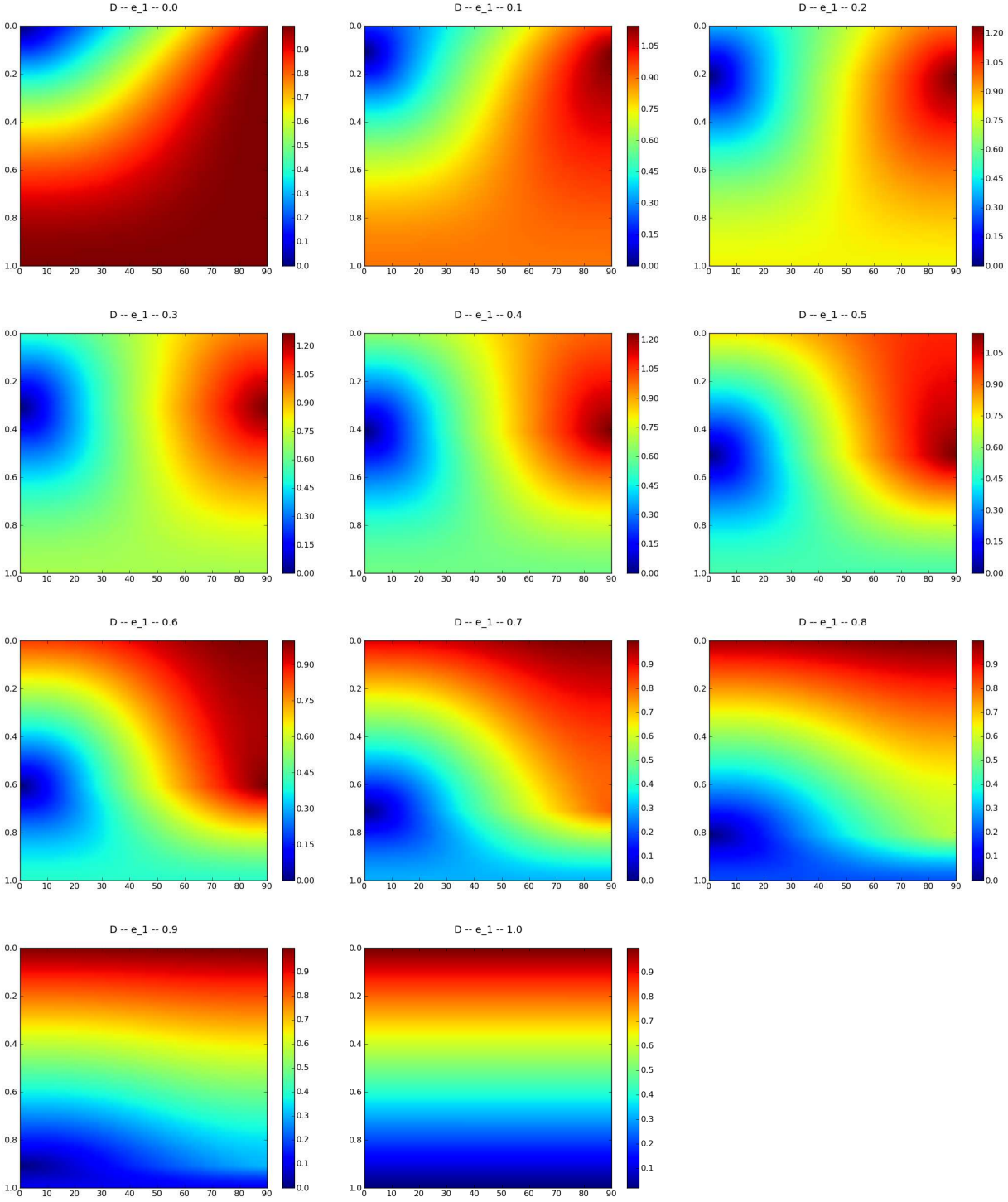

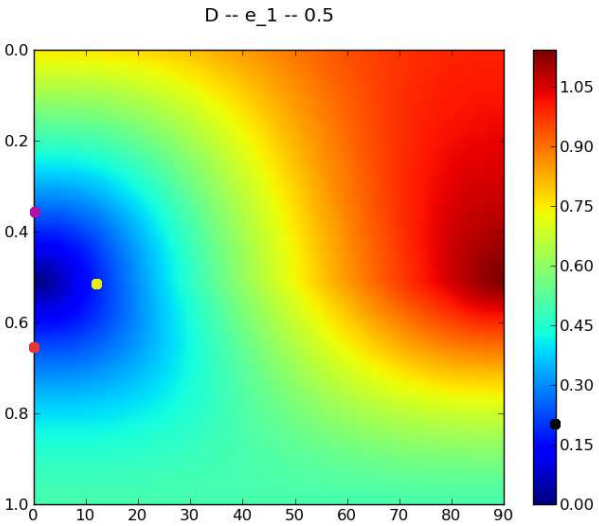

Figure 1.20: On this figure we show D as measured between a fixed reference ellipse with axis ratio equal to 0.5 and another second ellipse. D varies when the elliptical parameters of the second ellipse are varied. The variations of the second ellipse parameters (axis ratio and position angle) are shown on the axis. We show for this specific reference ellipse, the location of the three neighbouring ellipses in the (e_2, PA_2) plane for $D = 0.2$ (black dot on the color scale). Thinner, fatter and rotated neighbours respectively are in violet, orange and yellow. The reference ellipse can be represented by a dot at $(e_2 = 0.5, PA_2 = 0)$. We see as expected that D reaches zero (blue color) near the point representing the reference ellipse.

On picture 1.21 we show in red, K_s band "isophotal" ellipse for NGC4321 (see Jarrett et al., 2003). All ellipses in this image have same center and semi-major axis as this one. The ellipse in blue has the same (e, PA) as the one fitted through ISO-B2AC method with center fixed on Irac,2 map 0.33 MJy/sr isophote (for the same galaxy). The latter intensity level was deliberately chosen to correspond to a similar but different isophote than the "isophotal" ellipse of Jarrett et al. (2003).

There exists a lot of ellipses with different (e, PA) parameters, though equally similar to the red ellipse in terms of the D distance. The three main ways to be at similar D distance from the red ellipse as the blue ellipse are shown in yellow, light magenta and violet. We respectively called them the thinner, fatter and rotated neighbours of K_s band "isophotal" ellipse [3].

We also see, while comparing blue and red ellipses ("physical" ones), that the blue ellipse is close to the yellow (thinner neighbour) one but a bit tilted as compared to the red one, though not as much as the light magenta one (rotated neighbour).

We note that the axis ratio difference between violet and red ellipses (respectively the "fatter neighbour" ellipse and the reference ellipse) is larger than the axis ratio difference between

[3]On the figure 1.21 red and blue ellipses are at a D distance of 0.26. The three neighbours of K_s band "isophotal" ellipse shown here are actually located at $D = 0.2$ away from the red ellipse. It is impossible to show three neighbours at $D = 0.26$ from the K_s band "isophotal" ellipse considered here, because this latter ellipse has an axis ratio of 0.78 which is too high and there is no fatter neighbours; that is the reason why we show $D = 0.2$ neighbours instead.

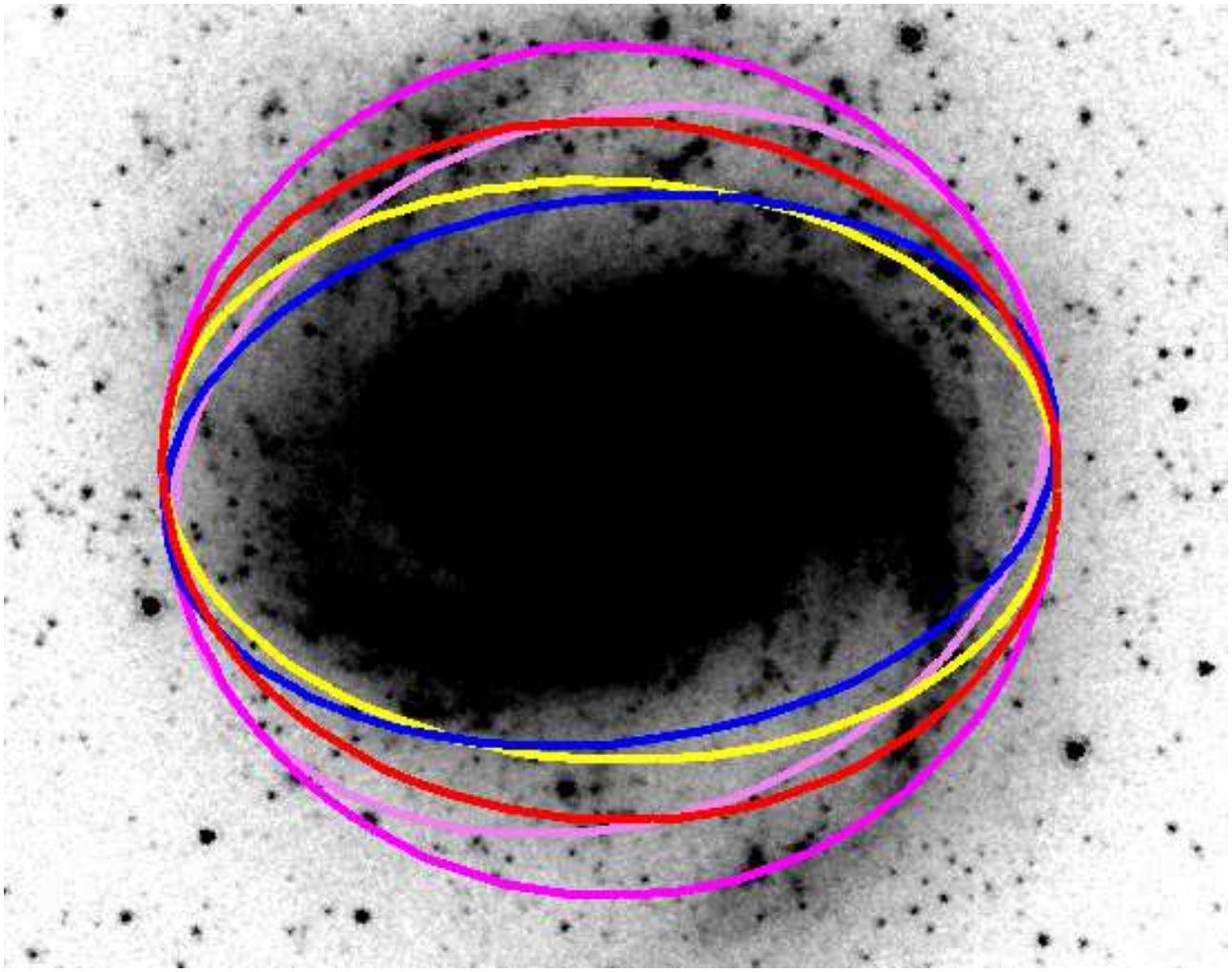

Figure 1.21: In the background is the central part of NGC 4321 IRAC,2 map. To compare only the effect of changes in the (e, PA) parameter plane, ellipses shown here all share a lot of characteristics with K_s band "isophotal" ellipse: they all have its center and semi-major axis. Different colors are used for different (e, PA) couples (axis ratio and position angle). In red is shown the (e, PA) of the K_s band "isophotal" ellipse. (e, PA) of the ellipse fitted through B2AC method with center fixed on Irac,2 map 0.33 MJy/sr isophote are shown in blue. D between (e,PA) of blue ellipse and red ellipse is very close to 0.2. The thinner, fatter and rotated neighbours of K_s band "isophotal" ellipse for a D distance of 0.2 respectively are in yellow, light magenta and violet.

yellow and red ellipse (respectively the "thinner neighbour" ellipse and the reference ellipse)[4]. The phenomenon can be seen on the pictures $e_1 = 0.7$ and $e_1 = 0.8$ of table 1.19 too. Actually it can be explained by comparing respective behaviours of $I_{a,m}$ and I_r at constant e_1 in pictures 1.6 and 1.12. In the former, $I_{a,m}$ grows in the same way when e_2 increases from $e_2 = e_1$ or when e_2 decreases from $e_2 = e_1$, even at high e_1 value. In the latter, I_r also grows when e_2 increases from $e_2 = e_1$ but not so much and it actually decreases soon after to reach a zero at $e_2 = 1$ for any e_1 value, whereas the increase of I_r is much sharper, when e_2 decreases from $e_2 = e_1$ (see the behaviour of I_r on any vertical line on picture 1.12).

To sum up this argument $I_{a,m}$ increases symmetrically when $|e_2 - e_1|$ increases from $e_2 = e_1$ (when e_1 fixed) whereas I_r increases also but more sharply when $e_2 - e_1$ decreases than when it increases from $e_2 = e_1$. Thus as the weight of I_r is twice the one of $I_{a,m}$, the asymmetry of I_r is inducing a pronounced similar asymmetry in D that can be observed on picture 1.16 as e.g. an enlargement of the vertical size of the blue valley when the abscissa is increased.

The non-symetrical behaviour of D on either side of the $e_1 = e_2$ valley is induced by the I_r component, which has this drawback to be very close to zero when either ellipse is close to a circle (either axis ratio close to 1); this drawback has already been noted in subsection 1.4.2, but we see that it still has bad consequences for D behaviour. The compensation for this drawback we hypothesized (namely creating D as a linear combination of $I_{a,m}$ and I_r) has not completely suppressed the problem.

There is a continuity of neighbouring ellipses at a fixed D distance from one ellipse, and not only the three kinds of neighbouring ellipses we introduced. But the latter are extreme cases that enable to have a realistic insight of what is implied when one talks about ellipses at the same distance D from each other (iso-D ellipses), i.e. ellipses " as " different as each other, from a particular one, in terms of (e, PA) parameters.

We have drawn the characteristic parameters of each sort of ellipse, keeping D fixed to 0.2 and 0.4 on table 1.22. We see on these graphs that for the same axis ratio (for both compared ellipses) and distance D fixed, increasing axis ratios from the value 0.25 implies rapidly increasing position angle difference (see both the figures on the right of table 1.22). This is natural and has already been explained [5].

For couples of ellipses of same axis ratio, when the axis ratio decreases from 0.25, the fact that the acceptable position angle difference increases is a drawback of D and also has been explained in details[6]. It has to be mentionned that this unwanted behaviour is interestingly reduced when the value of D goes from 0.4 to 0.2. This is not an exception. On the left we see that all non-linear behaviours[7] of the D distance are very much shrunk when D decreases. We can also mention that when D goes from 0.4 to 0.2, the range of axis ratio on which the fixed D constrains either the axis ratio (first two columns of table 1.22) or the position angle of the other ellipse (last column of table 1.22) is wider clearly indicating that $D = 0.2$ is a more stringent condition than $D = 0.4$ (see e.g. left column of table 1.22, for $D = 0.4$, $\Delta_{tot} e_1 = 0.7$; whereas for $D = 0.2$, $\Delta_{tot} e_1 = 0.85$). The reason why we get more extensive contraints for

[4]Numerically: $(0.95 - 0.78 = 0.17) > (0.78 - 0.65 = 0.13)$.

[5]It corresponds to the fact that for bigger axis ratios, a couple of ellipses with fixed position angle difference tends to describe more similar ellipses.

[6]It corresponds to the spreading of the blue patch on the $|\Delta PA|$ axis in the upper part of the first three graphs of table 1.19, when e_1 axis ratio is reduced (from the right to the left). The source of this is elucidated at the beginning of subsection 1.4.4 when we analyze picture 1.17. It is connected to the green patch top left of picture 1.17 page 59, observed for D values with $|\Delta PA| = 45^\circ$

[7]For instance when D decreases, the variation of e_2 with e_1 (for thinner and fatter ellipse neighbours) remains linear on a wider extent when D decreases.

larger fixed D values is because ellipse parameters are bounded as can be seen on table 1.19 page 61.

Figure 1.22: Variations of ellipse parameters for the three kinds of ellipse neighbour with constant distance ($D = 0.2$, upper panel; $D = 0.4$, lower panel). From left to right are shown the only useful parameter of the thinner neighbour (left picture - with smaller axis ratio but same position angle), the fatter neighbour (middle picture - with larger axis ratio and same position angle) and rotated neighbour (right picture - with non zero position angle difference and same axis ratio as the reference ellipse). When no neighbour parameter is associated to a possible value of e_1 it means there is no such type of neighbour for this parameter. For instance in the top left hand picture the abscissa value $e_1 = 0.1$ is not associated with any ordinate e_2. There is no thinner neighbour associated with this e_1 value at $D = 0.2$ because reducing the axis ratio from $e_1 = 0.1$ and keeping the position angle fixed is not sufficient to atteign the value $D = 0.2$; i.e. all ellipses having smaller axis ratio than an ellipse with 0.1 axis ratio but same center, same semi-major axis and same position angle, are at a D distance smaller than 0.2 from this ellipse.

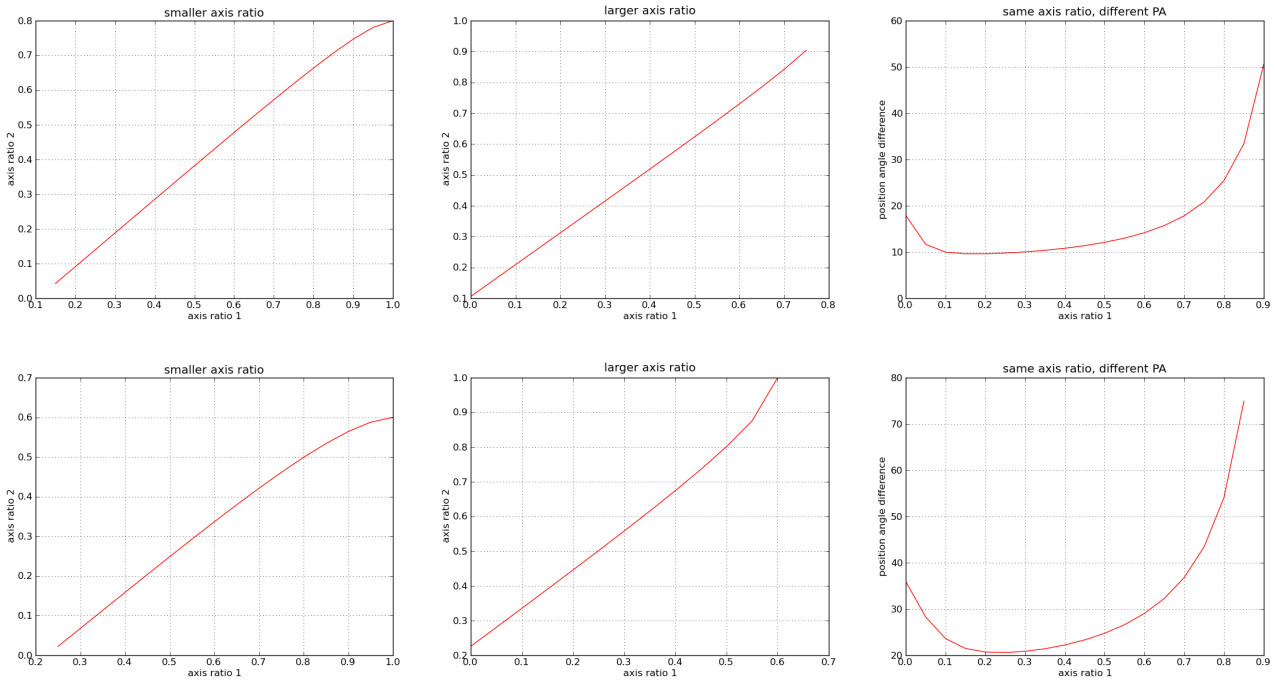

One of the main conclusions of this is that ellipse comparison in terms of (e, PA) parameters requires comparing not only differences of position angles for different axis ratios but also axis ratio differences for different axis ratios.

This is illustrated by the fact that the acceptable position angle difference between two ellipses depends on the axis ratio of both ellipses. For instance comparing two ellipses with same axis ratio, when the axis ratio is close to 0 (see left figure 1.23), the difference between the two ellipses (i.e. the distance between points of each ellipse) is non zero if the acceptable position angle difference is non zero. However, when the axis ratio increases toward 1, the acceptable position angle difference becomes as large as possible (see right figure 1.23).

Figure 1.23: We represent on this figure two thin ellipses with a position angle difference of 30° (axis ratio of 0.1) and two round ellipses with a position angle difference of 90° (axis ratio of 0.9). We can see here that for points of one ellipse to be close to the ones of another ellipse, the acceptable position angle difference between the two ellipses depends on the axis ratio of both ellipses.

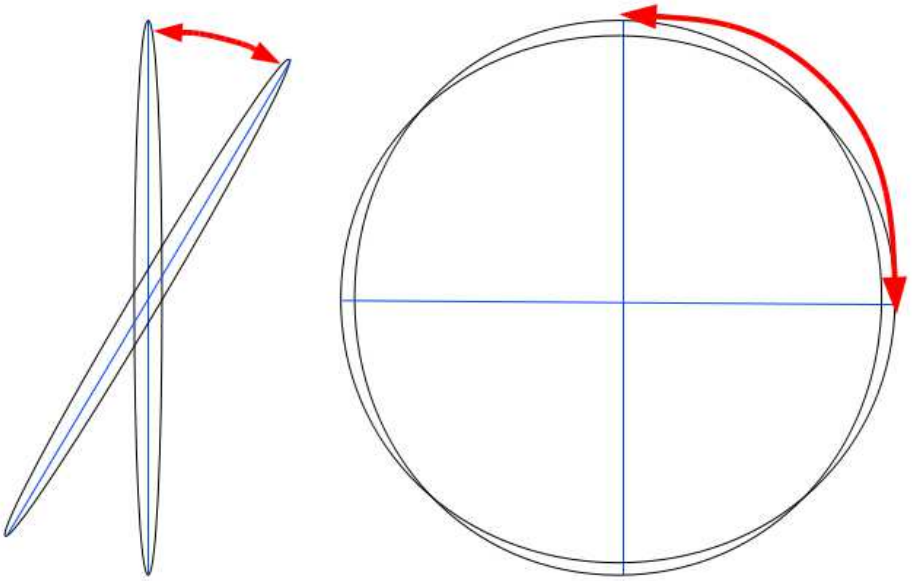

1.5 Difference of disk orientations

We wish to examine the consistency and quantify the difference between our disk orientations and litterature orientations. We also want to extract a typical value of the distance D, under which two ellipses distant of D can be regarded as describing the same galactic disk.

Thus we present in this section the difference of disk orientations obtained in the NIR by Jarrett et al. (2003) and us by using similar photometric methods. We then compare visible wavelength photometric disk orientations and HI kinematics disk orientations.

First we extract isophotes at a constant surface brightness of 0.33 MJy/sr on IRAC 2nd band maps ($\lambda \approx 4.5\mu m$) and fitted ellipses on them (hereinafter ISO-I2 ellipses). This surface brightness level of 0.33 MJy/sr was chosen to only roughly visually correspond to the radial location where "isophotal" axis ratios and position angles were extracted by Jarrett et al. (2003). These latter parameters were extracted by Jarrett et al. (2003) through ellipse fitting of isophotes, selected at a roughly constant surface brightness in 2MASS K_s band ($\lambda \approx 2.2\mu m$, hereinafter ISO-K_s ellipses). We then computed for each galaxy of our sample the D distance from our ISO-I2 to ISO-K_s ellipses.

To further illustrate these ideas, we plot on figure 1.24, axis ratio and position angle differences between ISO-I2 and ISO-K_s ellipses, against axis ratios of ISO-K_s ellipses. Along with them are also plotted axis ratio and position angle differences between ISO-K_s ellipses and elliptical neighbours (see section 1.4.5) at fixed D of 0.2, 0.3, 0.4.

We see on figure 1.24 that differences (crosses) between ISO-I2 and ISO-K_s roughly fall inside the same iso-D lines (dots) for both graphs. This suggests that the D distance provides a quantitative and relatively precise measurement of how similar are the yields of two methods aimed at extracting disk orientations.

We also see that axis ratio and position angles differences on both graphs are mainly smaller than those associated with D=0.2, though for some galaxies they are between D=0.2 and D=0.4 (the average D value obtained between ISO-K_s and ISO-I2 ellipses is 0.18 ± 0.17, the uncertainty is the error on the average). Similar methods can thus yield approximate elliptical shape difference as high as $D \approx 0.2$.

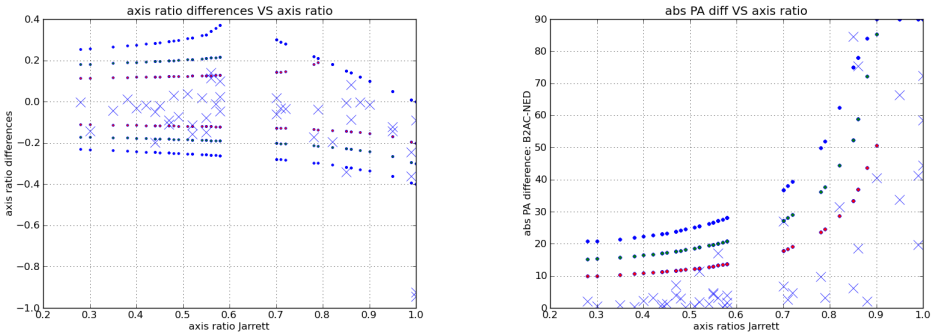

Figure 1.24: Crosses correspond to axis ratio difference (left) and position angle difference(right), between ISO-I2 and ISO-K_s ellipses, against ISO-K_s axis ratios for all galaxies in our sample. Red, green and blue circles indicate the upper limits (in terms of D) at respectively $D = 0.2$, $D = 0.3$, $D = 0.4$. The latter circles correspond to fatter (upper points) or thinner (lower points) ellipse neighbours on the left and to rotated ellipse neighbours on the right.

We then compared orientations obtained by photometric study in blue light by RC3 (see NED or de Vaucouleurs et al., 1991) to orientations obtained through HI dynamics studies by

Daigle et al. (2005) and Dicaire et al. (2008). For all of the 28 galaxies which were also present in the sample of galaxy we studied, the average D distance between these two studies was $D = 0.135 \pm 0.01$ (the uncertainty is the error on the average). We thus considered that the last figure represented an acceptable disk orientation difference with regards to the litterature. We therefore choose that two fitted ellipses are declared to trace the same disk if they differ by less than $D_{thres} = 0.1$.

1.6 Method for extracting consistent disk orientation

In this section we present a method for extracting a disk orientation that is robust under a change of map wavelength and extracted from a radial region as extended as possible.

We start by presenting isophote selection rules used to exclude isophotes extracted but not appropriate to identify the disk (subsection 1.6.1). We then explain our method for extracting consistent disk-like regions (EXT regions, see subsection 1.6.2). The average properties of these disk-like regions are thereafter examined separately in different bands and according to different morphological types (in subsection 1.6.3). We group bands into stellar, warm dust and cold dust to extract deeper insight of how different types of contents affect the properties of our disk-like regions (see subsection 1.6.3). Afterward, we compare disk-like region orientations between different bands for each object and extract a category of objects, that we call the CDO sample, in which this comparison enables to define a disk orientation robust under the change of band (see section 1.6.4). The properties of this category of objects are reviewed (in section 1.6.5). From this point on, we compute the differences between our disk orientations and litterature ones, across our total sample of galaxies and in CDO galaxies (see section 1.6.6).

1.6.1 Isophote selection

We aim at comparing the elliptical shapes of all the isophotes we extracted on each of the 460 maps to detect whether some of them are coherent with the idea of a disk.

Thus we imposed the following selection criteria:

- First to exclude very inner regions in which variability of elliptical shapes of isophotes is important because of intrinsic galaxy structures (bars, spiral arms, bulges) we select isophotes whose semi-major axis are larger than $0.3 \times R25$.

- To be confident that the isophotes extracted from images are mostly signal coming from the galaxy and not from the extragalactic background we select isophotes whose average intensities are higher than $\mu + 3\sigma$ (μ and σ respectively are the average pixel-wise surface brightness of the background and the pixel-wise standard deviation of the background signal surface brightness distribution).

- Because the fitting procedure is less reliable when performed on isophotes with smaller number of pixels we decide to further remove isophotes circumscribing regions with fewer than 47 pixels. The pixel sizes in our maps go from $1.2''$ in all four IRAC band maps, to $18''$ in MIPS 160 maps. For both cases we compute the average over our galaxy sample of our threshold isophote diameter (≈ 7 pixels) multiplied by the band map pixel size in arcsecond, divided by R25 in arcsecond. This gives a rough idea about how inner is the smallest considered isophote as compared to the visible size of the galaxy. We find these figures to be 0.03 for IRAC bands and 0.45 for MIPS 160. This explains why we extract rather outer isophotes in MIPS 160 as compared to the $0.3 \times R25$ limit defined above.

- As our method hypothesizes that isophotes all have same center, we want to exclude isophotes which are trivially non symmetric around the NED center. Some of the non symmetric isophotes are located around bright regions which are not centered on the galaxy center. To exclude the bulk of these cases we opt for fitting on extracted isophotes, both ellipses with center fixed to the NED center as well as ellipses with center left as a free parameter. We call the center of the ellipse fitted with center free the luminous center associated to the intensity of the isophote (the luminous center also depends on the band). We note for each isophote, x and y the semi-major axis lengths respectively associated

with the ellipse fitted with center fixed, and free. We also note d the distance between the Kingfish center and the luminous center. With these notations we decide to include only cases where $y \geq 2d$. Thus selected isophotes all have ellipses fitted with center free whose semi-major axis are larger than the distance between luminous and NED center.

- We also decide to reject cases for which the ellipse fitting was not coherent between center fixed and center free because of strongly non elliptical shapes of isophotes. Thus for $y \in [2d, 6d]$ we only include isophotes for which $|y - x| < d$.

As we find no evidence of discrepancies between ellipses fitted with center fixed and free in cases with $y \geq 6d$ we do not impose any further selection criteria on the concerned isophotes.

The penultimate condition is not perfect and its typical flaw can be pinned down by examining when the Kingfish center is allowed to be outside the ellipse fitted with center free. The minimum d value to produce such a case is $y \times e$ with e the minor over major axis ratio. This produces a Kingfish center on the minor axis of the ellipse fitted with center free. Putting together the exclusion condition and the minimum d value found in the previous sentence we get $1/2 \geq d/y \geq e$. Thus for Kingfish center to be outside of the ellipse fitted with center free, the axis ratio of this ellipse should be smaller than 0.5 (thus the galaxy is very probably not face-on). As our axis ratio distribution has a minimum of 0.3, with preferably larger axis ratio (more intermediately inclined to face-on galaxies), these cases are rare. This selection criteria could be much less efficient for a sample of more edge-on galaxies. In sets with large numbers of close to edge-on disk galaxies however the extraction of isophotes representing the disk has to overcome more serious problems such as systematic contamination by the central structures of disk galaxies (e.g. bulges and bars) of the parts of disk associated isophotes close to the galaxy center.

As the isophote extraction could be affected by the borders of the region of interest, we checked that no ellipse fitted on isophote was found to have a semi-major axis larger than $\frac{9}{10}R_{ROI}$ (see section 1.2). This is not a selection criteria but rather a sanity check ruling out substantial limiting effect due to the size of the region of interest, e.g. potentially perturbing the shapes of the isophotes we extracted.

After applying these selection criteria we compute the rejection rate for each map (see figure 1.25 page 71), that is the number of isophotes excluded as compared to the 33 isophotes extracted per map (assuming $\alpha \in [3, 19]$). The range of obtained rejection rates completely spans the interval [0,1], though rejection rates strictly comprised between 0 and 1 represent less than 1/3 of the maps. Around 2/3 of the maps have rejection rates equal to 0 (all extracted isophotes are within the requirements), and around 10% maps are completely striped of their isophotes by selection criteria, i.e. none of the extracted isophotes can be associated to what common sense could define as a galactic disk.

We remark that any galaxy with average rejection rates higher than 80 % (over all different maps), have nonetheless average rejection rates different from unity. This means that even for galaxies with average rejection rates of 80%, we succeeded in extracting in some band maps, isophotes meeting the selection criteria. No galaxy is completely stripped of all its isophotes in all bands.

Interestingly we note that for galaxies with larger axis ratios, i.e. more face-on ones, the upper value enveloppe of rejection rates is higher (see figure 1.25). This can be understood in the following way: as galactic structures being mainly contained inside a disk, more edge-on galaxies leave less room for isophotes to deviate from the observed disk shape than more face-on galaxies in which isophotes whose shapes deviate from the global disk structure are often found, e.g. because of spiral arms.

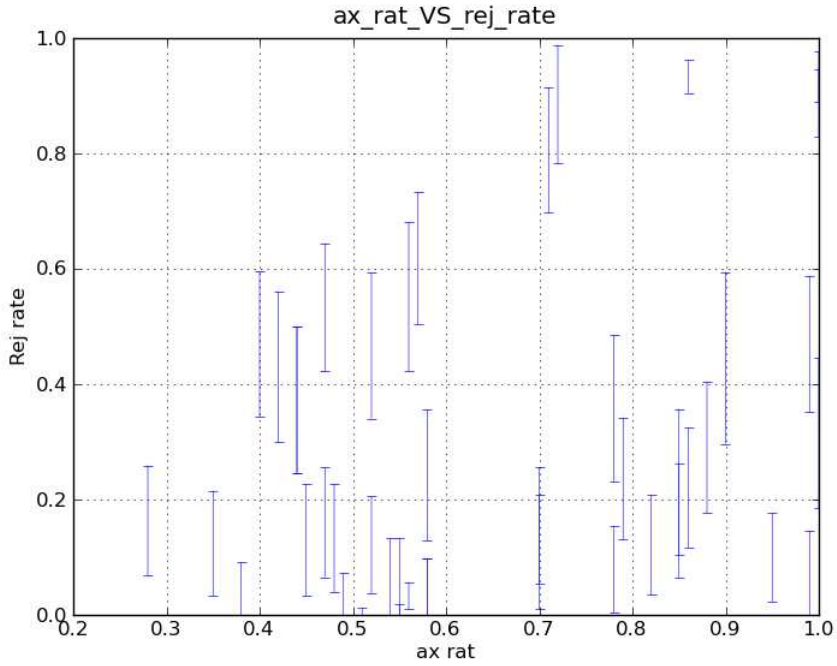

Figure 1.25: For each galaxy of our sample we plot here the average over different maps of rejection rates, against axis ratio provided by Jarrett et al. (2003).

1.6.2 Disk-like regions

The aim of this study is to extract a consistent disk orientation.

We shall now take a simple example of disk, namely a disk with zero thickness and axisymmetric radially-decreasing distribution of intensity. One such disk has concentric isophotes. These isophotes are observed to have same position angle and axis ratio, while their semi-major axis decrease when their average intensities increase. In this ideal case, the disk orientation is equally well described by the observed elliptical shape of any of its isophotes and the D distance between any isophote is 0.

For real disk galaxies we know that the link between orientation and isophotal shapes is also complicated by the spheroidal nature of the disk (see Hubble, 1926). However, we note that there is neither axis ratio nor position angle variation on the full radial range of a perfect spheroidal disk with a single orientation and a single thickness. Thus the search for a single position angle and axis ratio is therefore a search for the best description of the galaxy as a perfect spheroidal disk galaxy and all observed changes of axis ratio and position angle with varying semi-major axis are due to non axisymmetric structures, radial variations of disk orientation or thickness. However, as disk galaxies are mainly dynamically cold thin disks, we expect that the main cause for variations of position angle and axis ratio will be non axisymmetric structures.

As we want to assess whether different isophotes could be legitimately associated with a perfect spheroid whose perceived intensity is radially decreasing, we note that a region in which variations of elliptical shapes with radius are small can be used to extract consistent orientation for the disk. Conversely, regions where elliptical shapes are strongly perturbed by structures like spiral arms, exhibit strong variations of elliptical shapes with radius.

In order to make such a comparison, we ordered fitted ellipses by increasing semi-major axis

values and computed the distance D between consecutive ellipses. As isophote intensities are not necessarily decreasing with galacto-centric distance, the radial ordering ensured we compared ellipses physically close on the galaxy map.

We thus obtained for each of our 460 maps the variations with radius of the distance between consecutive ellipse. This is telling how elliptical shapes of isophotes are varying with radius. We thereafter used the D threshold ($D_{thres} = 0.1$, see section 1.5) under which variations of elliptical shapes could be considered small, to extract contiguous radial ranges (CR) over which the D distance between consecutive elliptical shapes of isophotes was under D_{thres}. The largest of these regions was called the largest contiguous region (LCR ; see an example on figure 1.26).

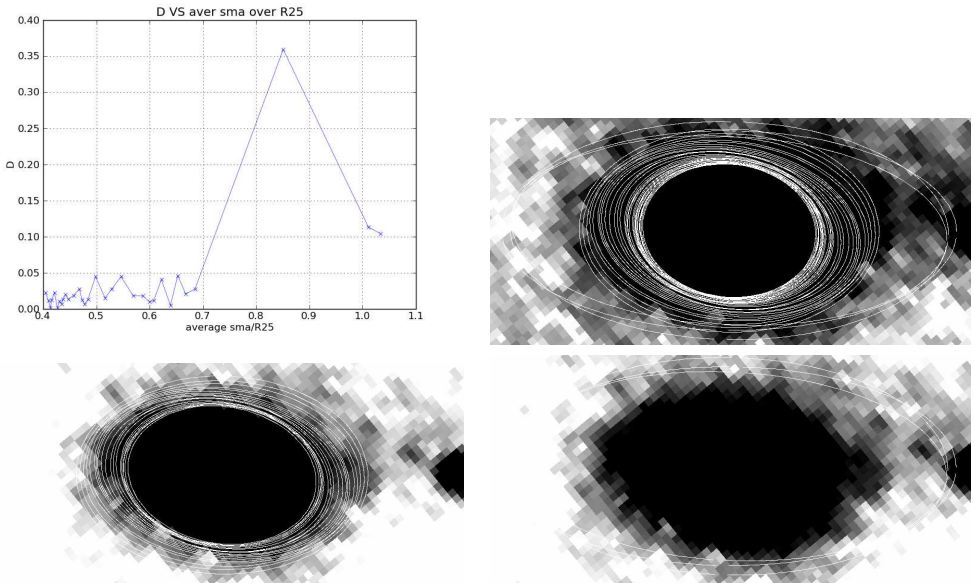

Figure 1.26: The upper left figure shows the D distance between consecutive ellipses plotted against the arithmetic mean of their semi-major axis length in units of R25. The top right hand side image represents ellipses fitted on isophotes meeting selection criteria. Bottom left and right hand side images respectively represent ellipses inside the LCR region and not inside LCR. For this map of NGC 1512 in MIPS 160, EXT sample of isophotes is the same as LCR.

To detect one specific disk orientation in multiple unconnected radial ranges in galaxy maps, we compared the average elliptical shape of the LCR to every average elliptical shape of CRs extracted from the same map. The average shapes are defined by the separately computed arithmetic averages of position angles and axis ratios.

We decided to extend the disk-like region from LCR only, to LCR plus some CRs when the average shape of LCR was coherent with those CRs. Thus:

- either the average elliptical shape of the LCR and at least one average elliptical shape of CR were separated by a distance $D < D_{thres}$, in which case all isophotes of each CR compatible with the LCR were added to LCR isophote to form an extended region (EXT);
- or the LCR was more distant to any other extracted CRs than D_{thres}, in which case we named extended (EXT) region the LCR itself.

We here remark that the use of the D distance to build EXT regions limits per se the influence on EXT regions of inner structures or noisy external isophotes whose shapes are non

relevant to represent the disk. But this is the case only if one can be confident that most of the isophotes from which EXT regions are extracted are representing the disk. This is one of the fundamental reasons why we used radial range limitations (in terms of $R/R25 > 0.3$ and $I \geq \mu + 3\sigma$) in extracting isophotes.

Furthermore we consider that filtering isophotes to only extract those close to our definition of a disk also enables to assess the availability of these types of isophotes inside disk galaxies. On the reverse, cutting loose of any selection criteria imposed on isophotes would leave out the possibility that EXT region might describe isophotes very perturbed by localised emission that common sense would probably not associate with any axisymmetric structure such as galactic disk.

No a priori on galactic disk orientation is used to build these EXT regions. For each of our maps EXT regions are independently extracted sets of isophotes as radially extended as possible. EXT regions more radially extended and with more numerous isophotes support more the idea of a galactic disk underlying the light distribution of the map.

1.6.3 EXT Regions

In this subsection we give statistical properties of extended regions according to each wavelength band, Hubble stage type and bar type (see table 1.1).

General properties of EXT regions across all bands

Cumulated sizes of EXT regions - $< s >$

To compute the intrinsic extension of each EXT region we added together the sizes of all contiguous regions it is made up by. We call this size measurement, the EXT region cumulated size. We examine these sizes divided by R25. These cumulated sizes differ from global or absolute sizes of EXT regions computed as the maximum of major axis of isophotes included in the EXT region, minus the minimum major axis of isophotes included in the EXT region. Possible holes inside EXT regions do not add up for EXT cumulated sizes.

In general we remark that no band has an $< s >$ value larger than 1/3 of R25. In more detail, bands can be ordered into four groups by examining EXT region sizes. IRAC 4.5, MIPS 160 which have the largest EXT sizes, all three SPIRE bands which have only large EXT sizes ($< s >= 0.25$), PACS 160 and MIPS 70 which have smaller EXT region sizes and finally MIPS 24, PACS 70,100 which have the smallest EXT region sizes.

Except for IRAC 4.5 we see that bands with larger PSF have larger EXT region sizes.

Dispersions of elliptical shapes inside EXT regions - $< d >$

We compute the distance between each ellipse of the EXT region and the average ellipse of the EXT region. We then take the average of these distances over all isophotes of each EXT region. This a measure of the dispersion of elliptical shapes inside the EXT region (see table 1.1).

As we defined EXT regions as isophote samples in which the D distance between ellipses consecutive in semi-major axis is less than $D_{thres} = 0.1$, we expect values of $< d >$ to be relatively low, though no upper limit in d is strictly imposed by EXT region extraction method.

There are at least two means of obtaining $< d >$ values exceeding D_{thres}. One is accessible even if the EXT region is made up by only the LCR. It involves a smooth change of ellipse parameters when moving from one isophote to another so that consecutive isophotes are not more distant than D_{thres} but the change exceeding D_{thres} is obtained by considering the difference between ellipses non consecutive in semi-major axis. The other way to obtain $< d >$ values exceeding D_{thres} involves including in EXT regions CRs that are on average less distant from

Instruments	IRAC	MIPS			PACS			SPIRE		
Wavelength (μm)	4.5	24	70	160	70	100	160	250	350	500
N_{gal}	44	43	44	45	32	41	42	43	44	38
PSF (")	1.72	6	18	38	7.2	8.2	13.6	18.2	24.9	36.3
$< s >$	0.32	0.16	0.21	0.33	0.08	0.12	0.21	0.25	0.25	0.25
$\sigma(< s >)$	0.02	0.02	0.03	0.03	0.01	0.01	0.02	0.02	0.03	0.03
$< d >$	0.11	0.09	0.07	0.07	0.07	0.07	0.1	0.07	0.07	0.06
$\sigma(< d >)$	0.02	0.02	0.01	0.01	0.03	0.01	0.03	0.01	0.01	0.01
$< N_{iso} >$	26.36	19.42	20.73	24.53	11.72	16.49	25.88	25.56	22.09	19.66
$\sigma(< N_{iso} >)$	1.69	1.83	1.9	1.79	1.96	1.86	1.53	1.68	1.91	2.02
$< \alpha >$	10.06	8.02	9.44	10.23	5.75	7.46	9.87	10.09	9.16	8.14
$\sigma(< \alpha >)$	0.46	0.46	0.73	0.62	0.49	0.53	0.43	0.47	0.53	0.54
$< N >$	2.32	2.28	1.98	1.87	1.94	2.07	2.05	2.16	2.43	2.18
$\sigma(< N >)$	0.23	0.24	0.18	0.18	0.21	0.19	0.17	0.19	0.2	0.26
$< MIN >$	0.4	0.45	0.51	0.66	0.36	0.39	0.44	0.5	0.49	0.48
$\sigma(< MIN >)$	0.02	0.02	0.02	0.05	0.01	0.01	0.02	0.03	0.02	0.02
$< MAX >$	0.74	0.67	0.76	1.03	0.46	0.54	0.68	0.8	0.78	0.76
$\sigma(< MAX >)$	0.02	0.04	0.05	0.06	0.02	0.02	0.02	0.03	0.03	0.03
$< R_{repr} >$	0.57	0.55	0.62	0.83	0.39	0.44	0.56	0.65	0.61	0.61
$\sigma(< R_{repr} >)$	0.02	0.03	0.03	0.05	0.02	0.02	0.02	0.03	0.03	0.03

Table 1.1: In this table, statistical properties of extended regions averaged over all available galaxies are given, according to each wavelength bands: cumulated sizes $< s >$ in units of R25 ; dispersion $< d >$ of elliptical shapes inside EXT regions ; number of isophotes $< N_{iso} >$ in EXT regions ; the R/R25, $< R_{repr} >$, of the EXT region isophote closest to the average elliptical shape of the EXT region ; the average intensity quantified by α (see below) of the extended region isophotes as compared to the background ; the number N of LCR and CR used to build the EXT region ; the average R/R25 borders of the EXT regions, noted MIN, MAX. These mean quantities for each band can be compared by using the error on the mean noted σ. The number of galaxies, N_{gal}, from which we succeeded at extracting an EXT region is also given for each band. These are galaxies for which at least two of the extracted isophotes meet the requirements presented above (see subsection 1.6.1) and are less distant than D_{thres} from one another. The total number of galaxies used here is 46. The dispersion of elliptical shapes is computed in terms of the D distance between the average elliptical shape of the EXT region, and each ellipse of the EXT region. We note the intensity of an isophote $I = \mu + \alpha \times \sigma$ with μ, σ the average and standard deviation of the background signal intensity. The table gives the average α for the EXT regions.

LCR average shape than D_{thres} but that contain numerous isophotes more distant from the average shape of the EXT region than D_{thres}. We conclude that $< d >$ values exceeding D_{thres} are revealing the quantity of isophotes that can be considered as outliers w.r.t. the average EXT region orientation. However one should bear in mind that isophotes too distant from the average shapes are actually excluded from EXT regions if the radial change in elliptical shape is too strong. We consistently find that dispersions in elliptical shapes are rather close to the D_{thres}. This considerably rules out large monotonic variations of elliptical shapes with radius in EXT regions e.g. from the outer border of the EXT region to the inner border.

The distribution of these elliptical shape dispersions inside EXT regions does not vary much between different galaxies in all bands.

The maximum values of the dispersion of elliptical shapes are found in increasing order inside the following bands: MIPS 24, PACS 160, IRAC 4.5. But we also have to note that these three bands exhibit relatively larger object-to-object variations of the EXT elliptical shape dispersion.

Number of isophotes inside EXT regions - $< N_{iso} >$

We also note that the bands using the most numerous isophotes (see $< N_{iso} >$, table 1.1) for building EXT regions, are in increasing order, MIPS 160, SPIRE 250, PACS 160, IRAC 4.5. Intermediate numbers of isophotes per EXT region are found in MIPS 24, 70 SPIRE 350, 500 and smallest numbers of isophotes used in EXT regions are PACS 70, 100.

The number of isophotes per EXT region is found linearly correlated with the average sizes of EXT regions (see section 1.27) in the sense that larger EXT regions have more isophotes. This is rather expected if we have relatively standard and homogeneous brightness profiles.

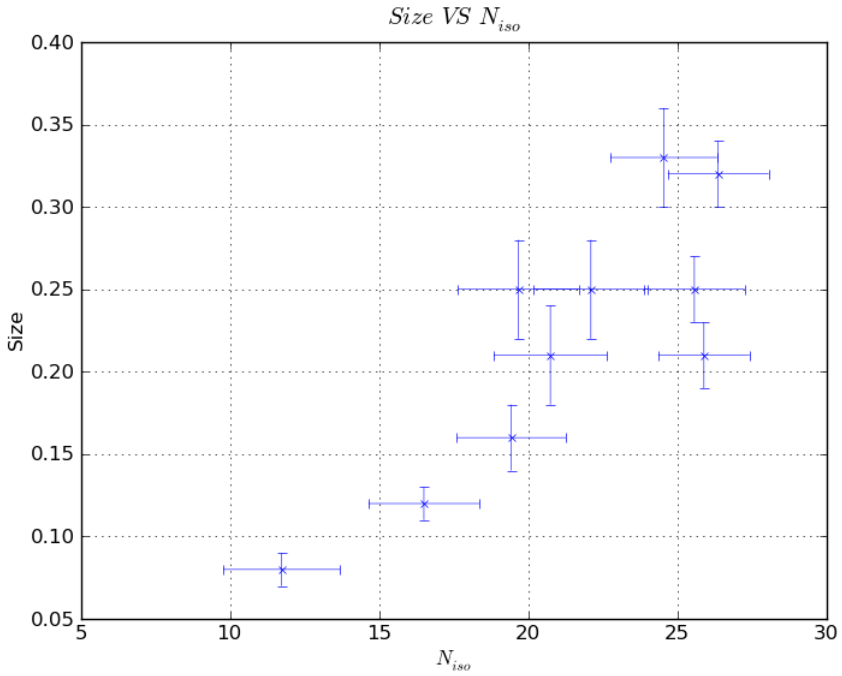

Figure 1.27: For each band we plot the average cumulated size of EXT region against the average number of isophotes inside EXT regions.

EXT region intensities compared to background - $< \alpha >$

There is not much variation of the intensity level of the EXT regions as compared to the background (as quantified by α, see table 1.1) when varying wavelength band. The vast majority of intensity levels are found between $\alpha = 7$ and $\alpha = 13$ (we recall that we selected intensity levels α between 3 and 19 to build EXT region isophotes by steps of $\Delta\alpha = 0.5$).

We note that there is a strong correlation between larger numbers of isophotes selected to build EXT regions and larger average intensity values for EXT regions as quantified by α.

Numbers of LCR and CR used to build EXT regions - $< N >$

The numbers of LCR and CRs used to build the EXT regions do not vary much either with the band and is always between 1 and 3 for most of the galaxies. EXT regions made with only 1 radial range or more than 3 radial ranges are rare.

Borders of EXT regions - $< MIN >, < MAX >$

We have computed the average minimum and maximum R/R25 of EXT regions. We see no strong trend between MIN and MAX R/R25 of EXT regions (in blue on figure 1.28) for different bands.

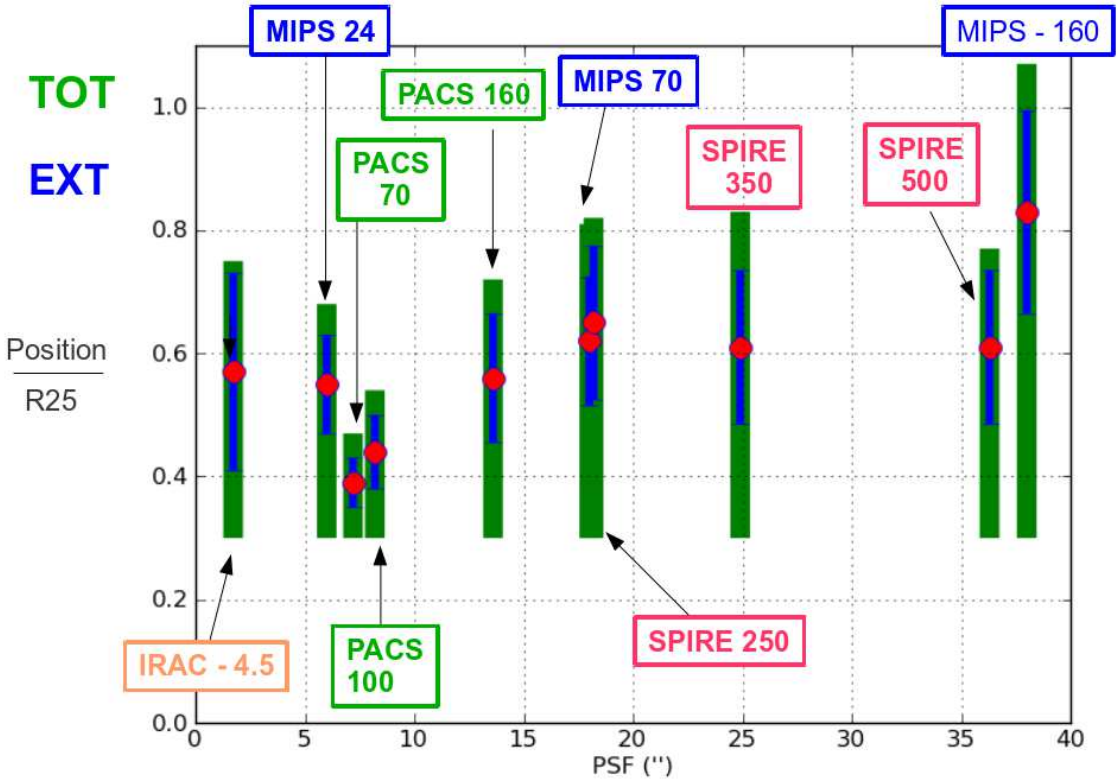

Figure 1.28: We represent on this figure, in green, regions inside which isophotes are extracted against instrumental PSFs. These isophotes are then filtered according to selection criteria and EXT regions are extracted from them. We represent in red the average positions of the isophote best representing the EXT region average orientation, i.e. the disk orientation, and in blue the sizes of EXT regions.

Minimum values of EXT region R/R25 seem gathered around 0.35-0.55, except MIPS 160 for which the inner borders of EXT regions are located in the range 0.55-0.75.

Maximum values are more broadly distributed but many bands outer borders of EXT regions are gathered between 0.6-0.85. The exceptions are PACS 70, PACS 100 and MIPS 160. The outer borders of EXT regions in bands PACS 70, 100 are more between 0.4 and 0.6, whereas MIPS 160 outer EXT borders are more gathered between 0.9 and 1.1.

Thus MIPS 160 have more external EXT regions with EXT regions located between 0.55-0.75 and 0.9-1.1 in terms of R/R25.

PACS 70 and PACS 100 have more inner EXT regions located between 0.35-0.55 and 0.4-0.6.

All other bands have EXT regions between 0.35-0.55 and 0.6-0.85 in terms of R/R25.

Radial position of the most representative EXT ellipse - $< R_{repr} >$

We have located amid the ellipses of the EXT region, the one which best resembles the EXT elliptical shape in terms of the D distance (see 1.1). We will call this ellipse the EXT-r ellipse (for EXT-representative) and its radial location in R25 units, R_{repr}.

The MIN and MAX R/R25 of EXT regions are each separately mildly correlated with R_{repr} though the bulk of the R_{repr} is neither close to MIN or MAX of R/R25.

EXT-r ellipses are found between 0.39 and 0.83 in terms of R/R25. Most bands gather their most numerous EXT-r ellipses around $R/R25 \approx 0.6$, except MIPS 160, PACS 70,100. If we put aside these three exceptions, average EXT-r ellipses are found between 0.55 and 0.65. EXT-r ellipses of MIPS 160 are found between 0.7 and 0.9 in terms of R/R25 whereas those of PACS 70, 100 are found around 0.4.

We also find that although the majority of galaxies have EXT-r ellipses well within their EXT regions, some galaxies exhibit EXT-r ellipses close to the radial ends of their EXT regions in those bands.

In case where the EXT-r ellipse is close to the radial ends of the EXT region, this could be interpreted as the sign that different isophotes from those selected by us could provide more disk representative ellipses. But such a conclusion would require more investigation as neither EXT region ellipses are uniformly distributed inside each EXT region nor are EXT regions probing uniformly distributed R/R25 ranges. Actually EXT region are more densely probing inner regions than outer ones due to the fact that the intensities of EXT region isophotes are linearly spaced in intensity and that galaxies naturally have higher than linear increase of the surface brightness with increasingly inner galacto centric radii. We also warn that this issue does not concern the majority of galaxies which in each band has the bulk of its EXT-r ellipses well within the EXT region radial ends.

These observations seem to support further studies searching for disk representative isophotes at smaller and larger galacto centric distances than the limits chosen here, as well as faster than linear increase of isophote intensity spacing when the intensity is increasing.

Discussion of the results

First we see that the method consisting in selecting consecutive isophotes less different in elliptical shapes than D_{thres} and adding together regions on average less distant from one another than D_{thres}, yields regions in which the global dispersion in elliptical shape is smaller than D_{thres}. This supports the idea that the majority of isophotes satisfying our selection criteria do not differ from the global disk shape by more than D_{thres}.

In the FIR, bands with larger PSFs exhibit larger EXT cumulated sizes, roughly larger numbers of isophotes per EXT region. This seems to indicate that higher spatial resolution reveals finer structures less in accordance with the disk and lower spatial resolution smoothes out

these small structures, enabling the extraction of disk representing sets of isophotes, on broader R/R25 extensions and larger surface brightness ranges. Irac 4.5 and FIR bands respectively and mainly collect stellar light and dust emitted light, thus stellar content seems more smoothly distributed or at least more organized in a disk structure at smaller spatial scales than dust content as amid dust dominated maps only maps with PSF 20 times bigger than IRAC 4.5 yield disk region sizes similar to those obtained in IRAC 4.5.

Furthermore, we note that averaging structures smaller than the visible size of galaxies, e.g. smaller than R25, which is the case when one considers PSF increasing from $6''$ to $38''$ in FIR bands, is expected to bias toward easier disk extraction. This bias may have severe consequences on the accuracy of the disk orientation measurement extracted from EXT region elliptical shapes in bands with higher spatial resolution as compared to bands with lower spatial resolution. We will alleviate this problem by defining the success or failure of our method on each galaxy by checking whether a rather stringent agreement between all orientations extracted in different wavelengths bands is obtained (see the selection criteria chosen to build the CDO sample of galaxies in section 1.6.4).

Disk-like regions can be extracted from large radial ranges in IRAC 4.5 band maps. The detection of a broad disk-like region is relatively easier in this band as compared to other bands even if IRAC 4.5 has the smallest PSF. This is understandable as IRAC 4.5 is mainly gathering starlight from which disk structures have originally been discovered. However, the FIR bands we studied mainly collect light emitted by dust. In these latter bands no morphological study of isophote has yet firmly confirmed the presence of a disk. Keeping in mind the previously mentionned caveats, even if the spatial resolutions of MIPS 160 and SPIRE bands are much coarser than IRAC 4.5, we nonetheless remark that disk-like regions in these bands have extensions as large as or just a little smaller than IRAC 4.5.

If we only take into account the average dispersion of elliptical shapes inside EXT regions, we see that IRAC 4.5, although providing the largest EXT regions, also has the largest dispersion of elliptical shapes inside EXT regions. As IRAC 4.5 gather more isophotes inside EXT regions, the dispersion also increases. Large dispersions are also observed in EXT region extracted from PACS 160 though its EXT regions are smaller than those of IRAC 4.5.

Disk-like regions in MIPS 160 are extracted from more outer sets of isophotes than in other bands. The combined effect of 160 microns being the wavelength of the most intense emission from the cold dust component as well as MIPS 160 being intrinsically more sensitive than PACS 160 to faint extended emission probably because of the larger PSF of MIPS 160, might explain that we extract more outer isophotes at $160\mu m$ than at other wavelengths and in MIPS 160 than in PACS 160. Small dispersions of elliptical shapes in MIPS 160 may be due to more outer radial ranges being probed by EXT regions in this band, because of less intense influence of inner non axisymmetric structures e.g. bars and/or spiral arms.

We find that the two smallest average numbers of isophotes inside EXT regions are seen in PACS 70, 100 which also have the smallest EXT region sizes. In these bands our method tends to extract less radially extended support for the idea of a perfect disk. This might be due to the fact that the dust dominating the emission at these wavelengths is mainly associated with star forming regions in spiral arms, thus probably less well associated with the disk structure.

We see that the number of isophotes per EXT region, the number of galaxies with available EXT regions, the EXT sizes, all increase overall with the PSF size within PACS and MIPS separately whereas comparatively reverse trends or no trend are seen amid SPIRE bands. Thus in PACS and MIPS bands, increased PSF seem to provide more support for disk-like shapes (increased numbers of isophotes inside EXT regions and more galaxies with EXT regions). In SPIRE bands, fewer galaxies with EXT regions, fewer isophotes inside EXT regions as well as constant EXT region sizes from SPIRE 250,350 to 500 seem to hint at increased PSF in SPIRE

bands wavelengths being linked with less successfull disk extraction. This seems to show that SPIRE 250 PSF is the most appropriate to detect the disk in SPIRE bands, whereas MIPS 160 PSF is the most appropriate to detect the disk in MIPS bands and possibly in PACS bands too. We also find that there is an specific effect of PSF on sizes of EXT regions as can be seen on 1.29 when one compares sizes of EXT regions in MIPS 70/PACS 70 and MIPS 160/PACS 160. The difference in EXT region sizes depends not only on the difference of PSF but also on the absolute value of the studied PSFs. Definitive conclusions on these points could possibly be reached by investigating the effect of PSF on disk extraction.

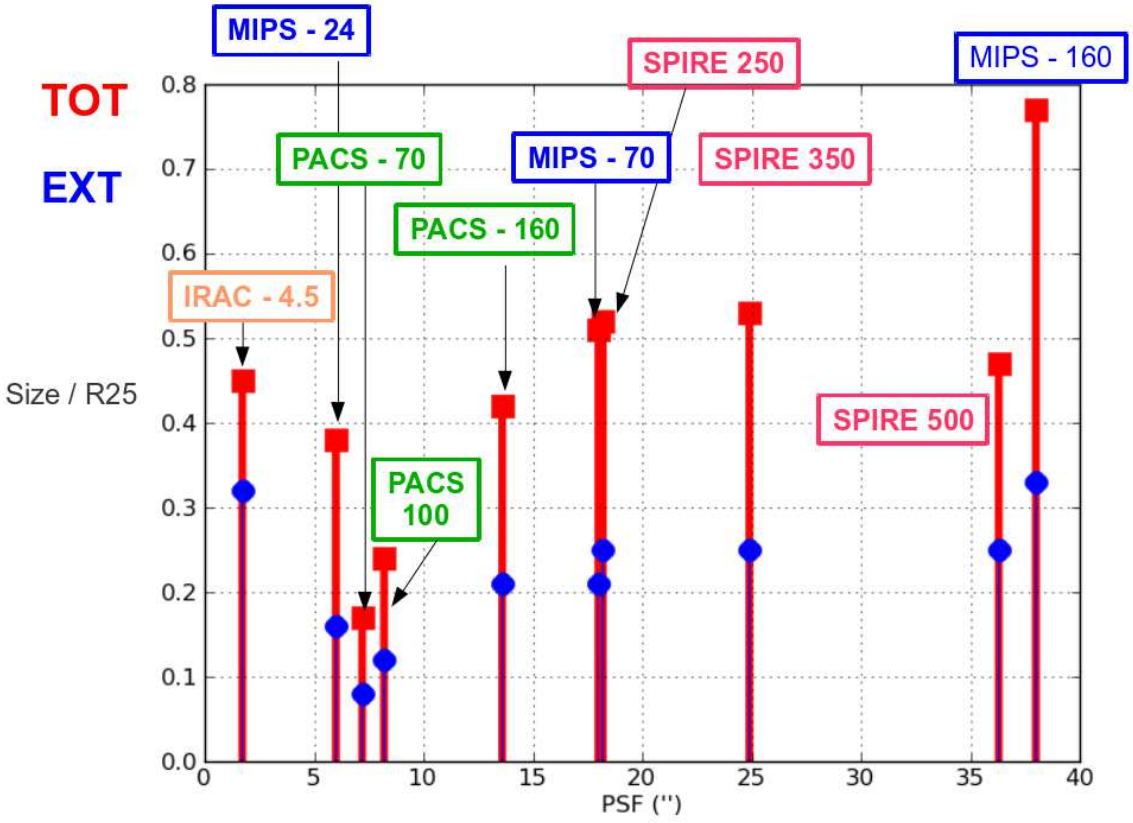

Figure 1.29: In blue are represented average sizes in units of R25 of EXT regions against PSF for each band. In red are shown the average sizes of the regions inside which are extracted EXT regions.

The correlation between larger numbers of isophotes selected to build EXT regions and larger average intensity values for EXT regions seems to confirm our previous conclusion that extracting isophotes at larger and/or smaller radii to build EXT regions could result in other radial ranges being selected to build these regions.

All of the bands except three exhibit disk-like regions located between 0.4 and 0.8 in terms of R/R25. Exceptions are MIPS 160 and PACS 70, 100. In MIPS 160 the isophote extracted even before applying any selection criteria are more outer than in other bands for reasons already discussed, resulting in more outer disk-like regions. The reverse is seen for PACS 70, 100 in which bands extracted isophotes are more inner than other bands resulting in most inner and smallest disk-like regions.

As in most bands, the most inner isophotes ($R/R25 \in [0.3, 0.4]$) are excluded from our EXT regions, because their isophotes are not representative of disk associated regions. We conclude

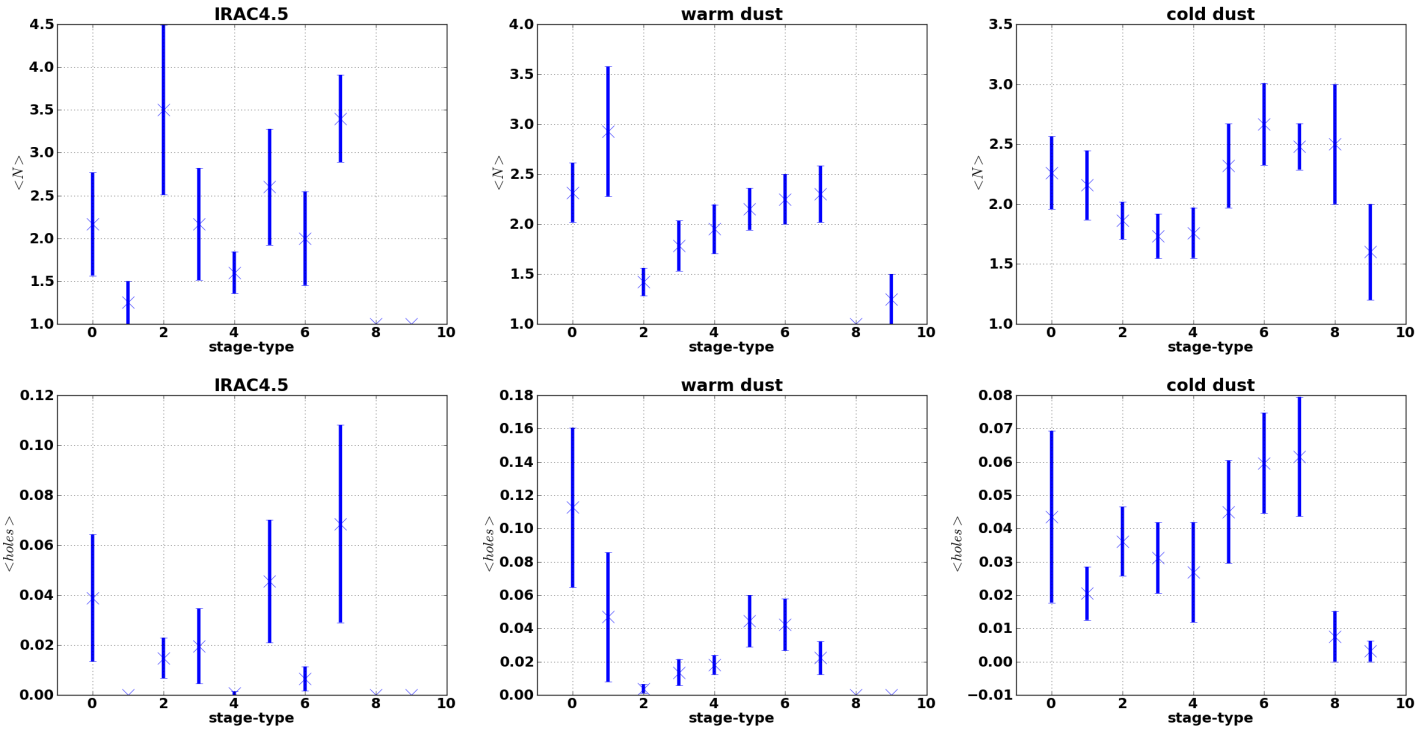

Figure 1.30: Here are displayed average properties of disk associated regions against morphological type. Bands are gathered as follows: left column, IRAC 4.5 ; middle column, "warm dust" ($8.0\mu m < \lambda < 160\mu m$) ; right column, "cold dust" ($\lambda \geq 160\mu m$). Row 1 : numbers of separations inside EXT regions. Row 2 : cumulated sizes of holes inside EXT regions in units of R25 (this is computed as the absolute "MAX minus MIN" size of the EXT region, provided on row 3 of figure 1.31, from which we subtract the sum of sizes of all CR making up the EXT region, provided on row 4 of figure 1.31).

that galactic disk in dust dominated bands are located at radii such that $R/R25 \geq 0.4$.

Properties of EXT regions for cold/warm dust and stellar content.

We will discuss in this section figures 1.30 to 1.31 representing EXT properties according to stage type for IRAC 4.5, warm dust ($8\mu m < \lambda < 160\mu m$), and cold dust bands ($\lambda \geq 160\mu m$). EXT region properties are averaged over all bands included in each of these three groups.

On figure 1.30, a similar evolution is seen with stage types for the number of separations $< N >$ inside EXT regions (on row 1 of fig. 1.30: number of CR regions making up EXT regions) and the cumulated sizes of holes $< holes >$ inside disk-like regions (on row 2 of fig. 1.30).

On figure 1.31 we have plotted the average values of the isophote signal to noise (S/N) ratio $< \alpha >$ inside EXT (on the first row in reading order), the average number of isophotes $< N_{iso} >$ inside EXT region (on the second row in reading order), the absolute size of the disk from which the EXT region is extracted, i.e. the subtraction between the maximum and minimum galacto centric radii of isophotes included inside the EXT region (on the third row in reading order), as well as the EXT region cumulated size (on the fourth row in reading order). This last quantity does not include the possible holes inside the EXT region in the sense that it just includes the LCR size and the sizes of the CRs possibly added to the LCR to form the EXT region.

We see that these trends with stage types are very similar for all these quantities separately inside each column (see figure 1.31).

In IRAC 4.5 the average number of isophotes and S/N intensity of EXT regions (w.r.t. the background) show a minimum around stage 4 for stages earlier than 5. Sizes of EXT regions are clearly decreasing with later types at all stage types earlier than 6 (see the left figures of the last two row of figures 1.31).

We see on figures 1.31 (the two columns on the right) that for all dust bands there is an increase from stage type 2 to 4 of isophote numbers in EXT regions, average intensities of EXT regions and average sizes of EXT regions, both cumulated and absolute. Amid these trends, those in cold dust seem slightly more pronounced than those in warm dust.

Let us now point the most prominent trends we observe for EXT region properties with bar type. For clarity and only when considering bar types, we will not consider SAB and S0 types, but only SA and SB types.

Barred galaxies (SB) are observed to have larger dispersions of elliptical shapes than non barred galaxies (SA), in cold dust bands, whereas the trend is milder in warm dust bands and very weak in IRAC 4.5 (see 1st row of fig. 1.32).

Isophotes whose fitted ellipse best resembles the disk-like region average shape is seen at more inner radii in terms of R/R25 for cold dust bands whereas no clear trend is seen for warm dust and IRAC 4.5 (see 2nd row of fig. 1.32).

The average intensity of the EXT region w.r.t. the background intensity named $< \alpha >$ is lower in SB galaxies than in SA galaxies only in cold dust bands. In IRAC 4.5 and warm dust the trend is less clear-cut (see 3rd row of fig. 1.32).

Similarly the number of isophotes per EXT region is larger for SA than SB galaxies for cold dust bands. In IRAC 4.5 and warm dust bands the number of isophotes per EXT region is roughly the same in SA and SB galaxies (see 4th row of fig. 1.32).

Discussion of the results

On figure 1.30, the similar trends seen inside disk-like regions between the number of separations (on row 1 of fig. 1.30: number of CR regions making up EXT regions) and the cumulated sizes of holes inside disk-like regions (on row 2 of fig. 1.30) seem to indicate a relatively constant single hole size of around $\Delta R/R25 \approx 0.02$ though the uncertainties are high. This could be explained by relatively small irregular structures perturbing shapes of isophotes such as spiral arms.

Interestingly stage 4 galaxies have the largest disk region sizes in cold dust bands as well as in warm dust bands if we exclude S0 stage types (see on fig. 1.31, the middle and right panels of rows 3 and 4 in reading order). This is true, both with or without taking into account the possible holes in disk regions (compare row 3 to row 4). Galaxies at this stage, also have disk-like regions with the highest average intensities of isophotes as compared to the background (see row 1 middle and right panels) and highest number of isophotes inside their disk regions (see row 2 middle and right panels). It is thus interesting to mention here that Muñoz-Mateos (2009) estimated Sb-Sbc (type 3-4) had the largest dust surface densities. We conclude that larger dust surface densities may be related in some way to building disk related regions in the dust phase that are larger in extension and at higher signal to noise ratios. This trend is even more striking in cold dust bands which are more linked with dust mass.

In the stellar band IRAC 4.5, disk sizes decrease with later types in units of R25. This is surprising because we know that the stellar disk is more luminous in later types as compared to the total galactic luminous output. Our method might extract larger "disk" associated regions in earlier type galaxies because the old stellar component is more important in earlier galactic

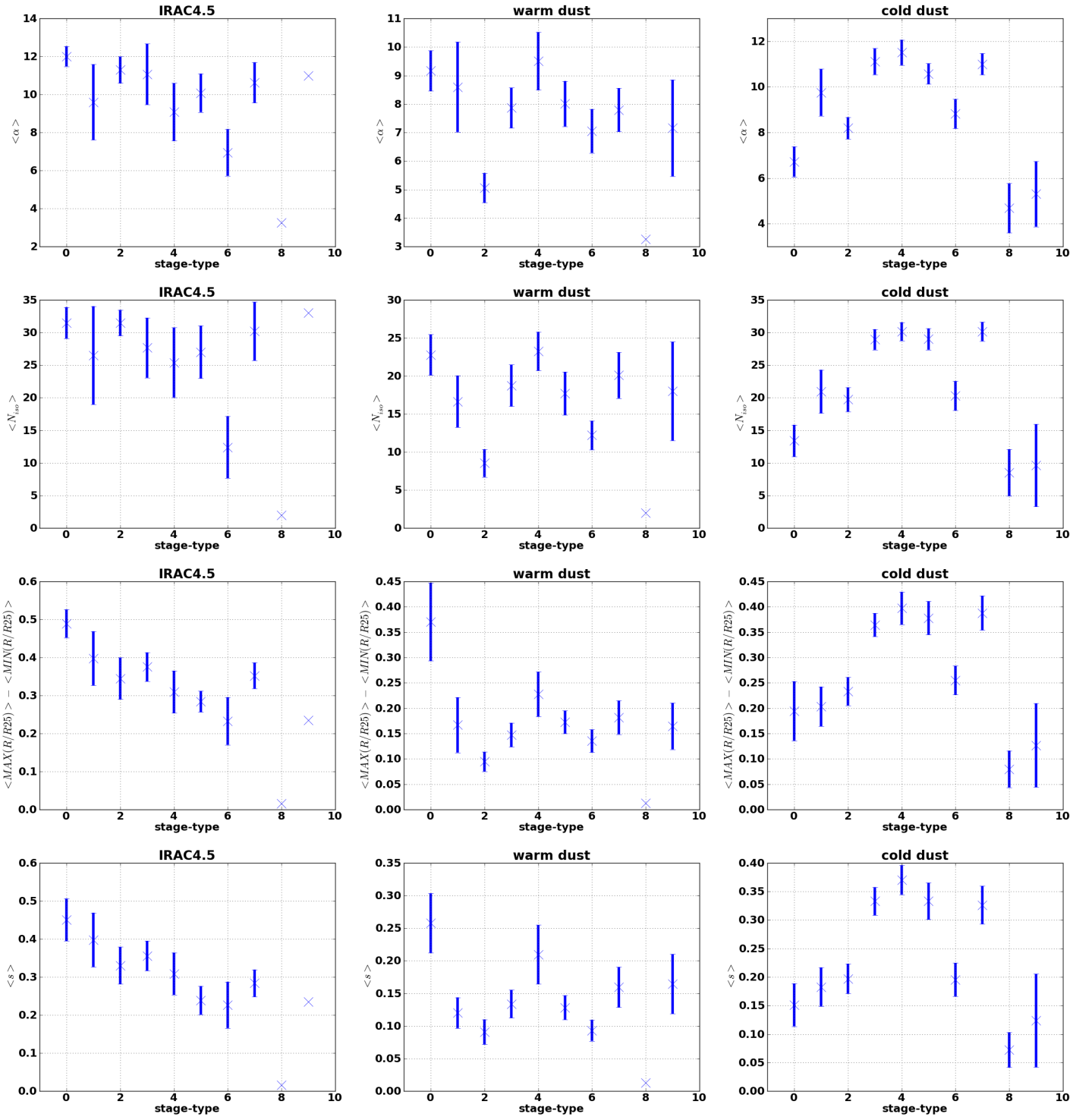

Figure 1.31: On these figures are displayed many properties of the disk-like regions we extracted for different bands: column 1, IRAC 4.5 ; column 2, "warm dust" ($8.0\mu m < \lambda < 160\mu m$) ; column 3, "cold dust" ($\lambda \geq 160\mu m$). Row 1: average intensity of the EXT region as compared to the background. Row 2: average number of isophotes in the EXT region. Row 3: total radial range in which the EXT region is located. Row 4: cumulated sizes of EXT regions.

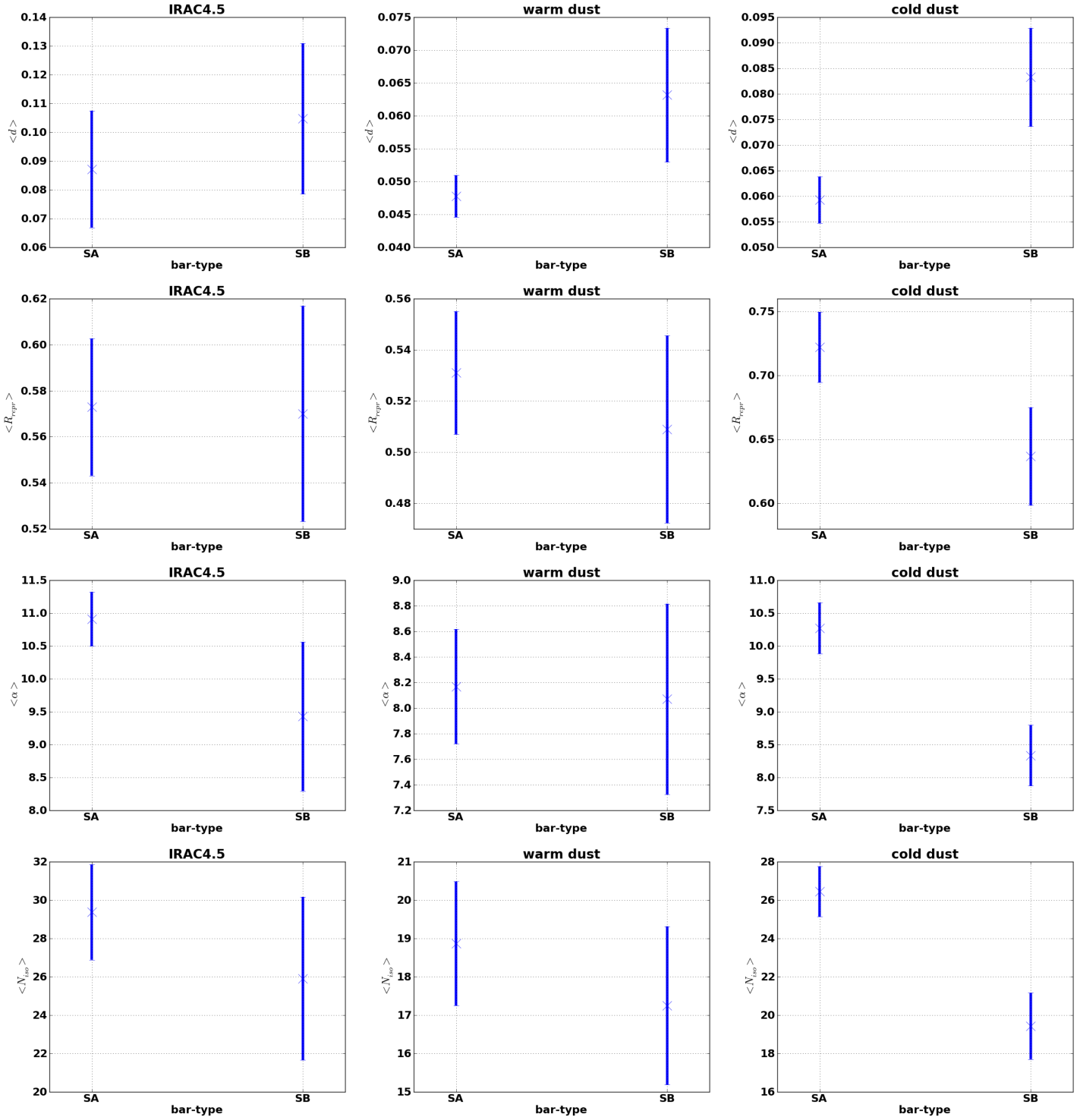

Figure 1.32: On these figures are displayed many properties of the disk-like regions we extracted for different bands: column 1, IRAC 4.5 ; column 2, "warm dust" ($8.0\mu m < \lambda < 160\mu m$) ; column 3, "cold dust" ($\lambda \geq 160\mu m$). SB galaxies are at abscissa 1 and SA at abscissa 0. We did not plot the SAB and S0 types here for simplicity, so as to make it clear whether the presence of a bar is having a significant effect or not. Row 1: Dispersion of elliptical shapes $< d >$ inside EXT regions. Row 2: radial location $< R_{repr} >$ in unit of R25 of the isophote whose fitted ellipse best resembles the EXT region average elliptical shape. Row 3: average S/N $< \alpha >$ of EXT region w.r.t. the background intensity. Row 4: number of isophotes $< N_{iso} >$ per EXT region.

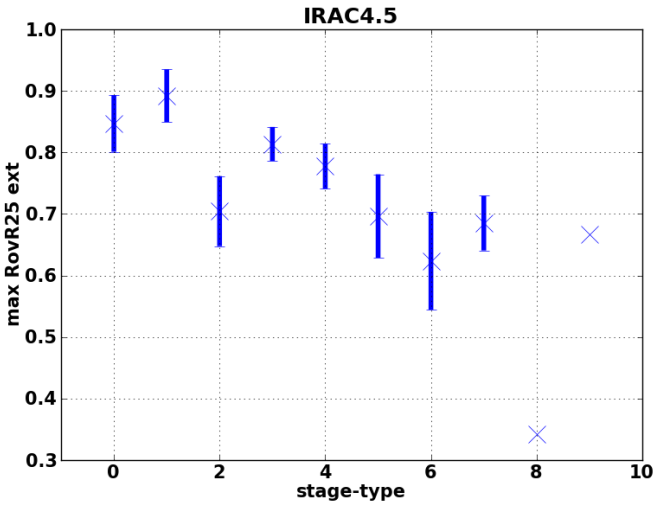

Figure 1.33: This figure shows the IRAC 4.5 maximum $R/R25$ of EXT regions averaged over stage type.

types. This in turn might be the sign that in early disk galaxies our method extracts disk associated regions which may well be associated to central spheroid, that are prominent in early disks, rather than to the faint disk of these early disks.

However our method for extracting disk regions is limited in surface brightness as compared to the background. As we can see on figure 1.33 the maximum R/R25 of isophotes selected to be part of the EXT regions exhibits a strong trend which, together with non significantly varying minimum $R/R25$ of EXT regions, could explain the trend of the stellar disk region sizes with stage type. The decreasing stellar disk region size in later type galaxies thus merely shows that the almost constant minimum surface brightness of isophotes inside EXT regions corresponds to decreasing values of R/R25 in IRAC 4.5. All these could possibly be explained by structure associated to old stellar populations being less present and less extended in later types.

Let us now turn to comparison of disk region properties in barred and non barred galaxies.

The dispersion of isophote shapes is increasing in barred galaxies in a more pronounced way in warm dust than in the stellar band and in cold dust than in warm dust, making it clear that the morphology of disk regions is more affected by the bar in cold dust than in warm dust, and in warm dust bands than in the old stellar component.

The size of the disk region selected here are not strongly affected by the presence of a bar.

In cold dust maps of barred galaxies, disk regions are extracted closer to the background intensity than in non barred galaxies. In bands associated to cold dust, the average R/R25 of the disk-like regions is smaller in barred galaxies than in non barred galaxies. This implies that in SB galaxies regions associated to the disk structure have smaller S/N ratios and are found comparatively closer to the center. This possibly hints at the presence of a bar being linked to a decrease of the surface brightness of cold dust disks.

Interestingly the presence of a bar has close to no effect on disk-like regions in warm dust bands and our stellar band, except to slightly increase the dispersion of elliptical shapes in warm dust bands and to decrease the effective sizes of disk-like regions in the stellar band. It seems that bars have no specific effect on the "quality" of disk regions inside our window of investigation ($I > \mu + 3\sigma$ and $R/R25 > 0.3$) especially for IRAC 4.5 except that of reducing its size. This has to be compared with the strong effect of the bar presence on disk regions as measured in cold dust bands.

1.6.4 Comparing disk orientation in different band maps for each object

The method presented in the previous section enables to extract from each map of every galaxy in our sample an extended disk orientation, without using any a priori. We will now compare between different bands the obtained orientations of disks.

First we should clarify the link between axis ratios of ellipses fitted on isophotes and disk orientations. In the case of a perfect spheroid with radially increasing distribution of intensity, there is a univocal link between disk orientation and the elliptical shape of isophotes. This link has been extensively studied as far as galactic disk orientations are concerned (see Tully, 1988, and references therein). It makes use of the internal axis ratio of the spheroid and namely states:

$$i = \cos^{-1}\left(\sqrt{\frac{q^2 - q_0^2}{1 - q_0^2}}\right) + 3^\circ \tag{1.2}$$

where i is the inclination of the galaxy, $q_0 \approx 0.2$ is the usual axis ratio for disk galaxies (see Tully, 1988) and q is the observed axis ratio. The 3° of the previous formula compensate the usual bias toward lower inclinations due to the ellipse fitting on isophotes. From this point on, to avoid these complications and to preclude possibly inappropriate choice of internal axis ratios, we choose to only work with observed axis ratios and position angles.

As the visible mass of disk galaxies is mainly gathered inside a stellar disk, we investigated in the previous subsection the question whether maps of dust which is a much less massive component than stars, exhibit isophote shapes coherent with the idea of one single perfect disk separately in different bands.

As we also discussed earlier on, studying the variations of position angles and axis ratios in itself enables a precise assessment of this question even without the use of an internal axis ratio.

We now have to compare obtained disk orientations between different band maps for each galaxy. To further discard as much as possible any bias and a priori ideas, we choose to compare each band EXT average elliptical shape to the average of all bands EXT elliptical shapes.

As galactic disks were originally discovered through careful examination of galactic stellar emission and we showed in section 1.6.3 that our method is rather successful at extracting disk-like regions from IRAC 4.5, we tried to extract a disk orientation as coherent as possible with both stellar emission and dust emission. To do so we also compared each wavelength EXT average elliptical shape to IRAC 4.5 EXT elliptical shape.

When comparing average EXT region orientations in all bands, we relax the orientation comparison threshold from $D_{thres,1} = 0.1$ to $D_{thres,2} = 0.3$. We can justify this *a posteriori* by the relatively good agreement between disk orientations thus obtained and litterature orientations (see infra). We thus select galaxies for which EXT region orientations at all wavelengths are closer to the average of all EXT ellipses and closer to IRAC EXT ellipse than a looser maximum threshold of $D_{thres,2} = 0.3$.

12 galaxies in our sample satisfied exactly this condition and we name this group the "restricted sample", and 8 others were very close to satisfying it (see table 1.2). Hereinafter, these 20 galaxies will be refered to as the consistent disk orientations (CDO) set of galaxies and the EXT disk orientations averaged over wavelengths for each galaxy will be called the EXT orientation of the galaxy.

1.6.5 Properties of CDO sample

We plot on graph 1.3 differences in physical properties for CDO and non CDO samples. We see that the CDO building method selected galaxies with somewhat smaller optical luminosities and smaller infrared luminosities w.r.t. optical luminosities. However the maximum rotational

Galaxy	M_A	M_I	$restricted$	CDO	comments
IC0342	0.38	-	NO	NO	NO IRAC4.5 EXT region
IC2574	0.30	0.25	NO	NO	3 EXT regions
NGC0337	0.14	0.17	YES	YES	
NGC0628	0.41	0.40	NO	NO	
NGC0925	0.32	0.35	NO	NO	
NGC1097	0.51	0.51	NO	NO	
NGC1266	0.33	0.32	NO	YES	D(IRAC4.5,MIPS160)=0.32, D(IRAC4.5,other band)<0.28 ; D(aver,PACS70)=0.33, D(aver,other band)<0.24
NGC1291	0.88	0.47	NO	NO	
NGC1316	0.73	0.57	NO	NO	3 EXT regions
NGC1377	0.51	0.74	NO	NO	
NGC1482	0.27	0.42	NO	NO	
NGC1512	0.088	0.17	YES	YES	
NGC2798	0.57	0.75	NO	NO	
NGC2841	0.21	0.16	YES	YES	
NGC2976	0.18	0.17	YES	YES	
NGC3049	0.54	0.7	NO	NO	
NGC3184	0.40	0.37	NO	YES	D(PACS70,aver)=0.40, D(other band,aver)<0.075, D(PACS70,IRAC4.5)=0.37, D(other band,IRAC4.5)<0.06, PACS70 EXT region size is the smallest
NGC3190	0.51	0.56	NO	NO	
NGC3198	0.20	0.25	YES	YES	
NGC3351	0.41	0.42	NO	NO	
NGC3521	0.25	0.37	NO	NO	
NGC3621	0.16	0.28	YES	YES	
NGC3627	1.1	1.1	NO	NO	
NGC3773	0.51	0.33	NO	YES	D(MIPS160,aver)=0.51, D(other band,aver)<0.2, D(MIPS160,IRAC4.5)=0.33, D(other band,IRAC4.5)<0.23, MIPS 160 EXT region size is the smallest
NGC3938	0.34	0.27	NO	YES	D(PACS70,aver)=0.34, D(other band,aver)<0.19, PACS 70 EXT region size is the smallest
NGC4236	0.11	0.19	YES	YES	
NGC4254	0.19	0.25	YES	YES	
NGC4321	0.38	0.37	NO	NO	
NGC4536	0.28	0.42	NO	NO	
NGC4559	0.24	0.26	YES	YES	
NGC4569	0.26	0.42	NO	NO	
NGC4579	0.26	0.30	YES	YES	
NGC4594	0.55	0.77	NO	NO	
NGC4625	0.71	0.61	NO	NO	
NGC4631	0.65	0.8	NO	NO	
NGC4725	0.36	0.37	NO	YES	
NGC4736	0.61	0.61	NO	YES	
NGC4826	0.55	0.58	NO	NO	
NGC5055	0.46	0.49	NO	NO	
NGC5457	0.27	0.34	NO	YES	D(IRAC4.5,MIPS70)=0.34, D(IRAC4.5,other band)<0.3
NGC5474	0.7	0.45	NO	NO	
NGC5713	0.45	0.40	NO	NO	
NGC5866	0.33	0.54	NO	NO	
NGC6946	0.22	0.31	NO	YES	D(IRAC4.5,PACS70)=0.31, D(IRAC4.5,other band)<0.26
NGC7331	0.16	0.21	YES	YES	
NGC7793	0.10	0.14	YES	YES	

Table 1.2: For every galaxy, we computed D distances from each band EXT region average elliptical shape, respectively, to the average elliptical shape of all EXT regions ($D_A(band)$) and to IRAC 4.5 average EXT elliptical shape ($D_I(band)$, $band \neq IRAC4.5$). We wrote in this table M_A and M_I, the respective maximum amid all bands of $D_A(band)$ and amid all bands except IRAC4.5 of $D_I(band)$. We thus have for each galaxy: $M_A = \max_{Band} D\,(\text{aver}, Band)$ and $M_I = \max_{Band} D\,(\text{IRAC4.5}, Band)$. We show the restricted set of galaxies, in which for each galaxy, 2 conditions have to be fullfilled simultaneously: (1) $M_A \leq 0.3$, (2) $M_I \leq 0.3$. By allowing that one EXT region of one band at most exceeds the 0.3 limit, for each of the conditions (1) and (2), we built the consistent disk orientation (CDO) sample of galaxy. We also brought to attention special cases, notably galaxies in which the number of bands where the EXT region extraction is successful is lower than 3.

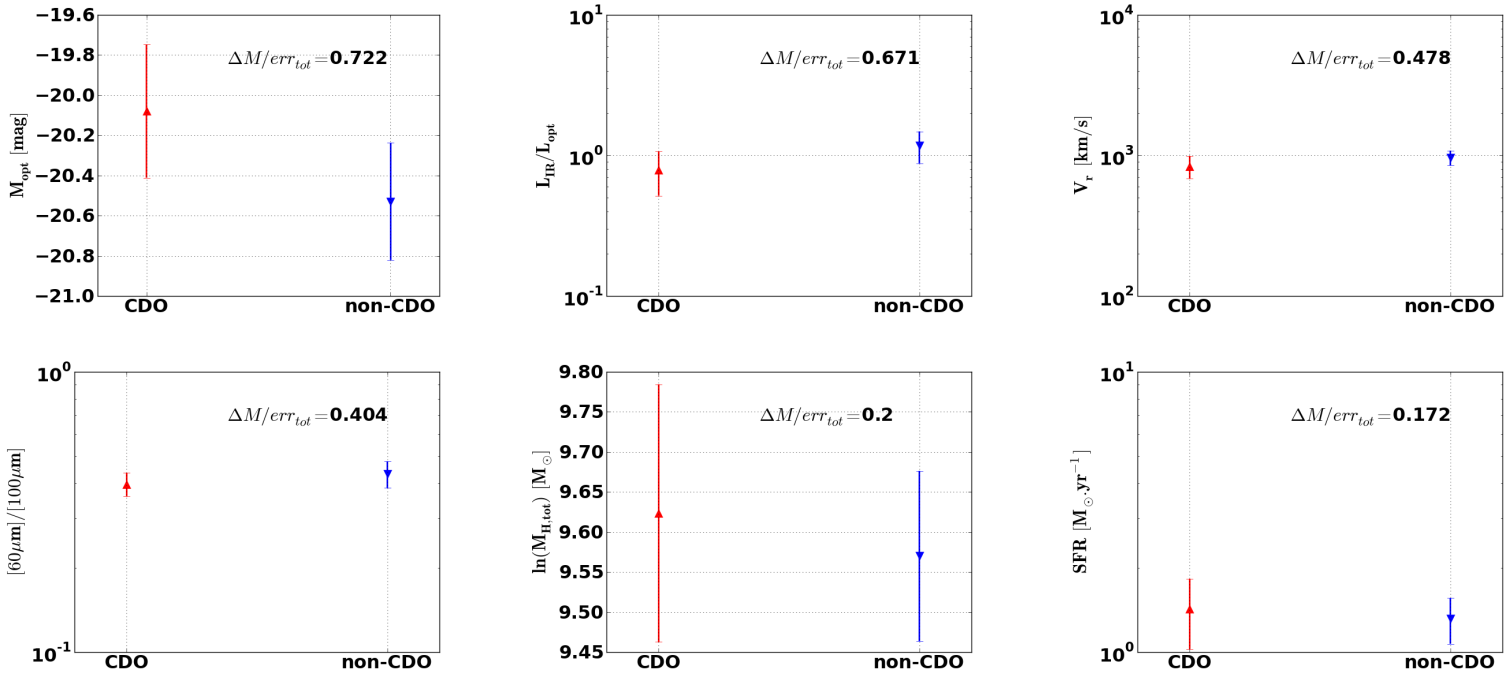

Table 1.3: On these figures are displayed differences in physical properties for CDO (red upward triangles) and non CDO (blue downward triangles) samples. In reading order we find: the absolute magnitude, the IR to optical total luminosity ratio, the maximum rotational velocity in km/s, the $[60\mu m]/[100\mu m]$ color ratio, the total atomic gas mass in solar masses, and the star formation rate in solar masses per year. Properties are ordered by decreasing values of $\Delta M/err_{tot} = \frac{|M_{CDO} - M_{nonCDO}|}{err_{CDO} + err_{nonCDO}}$, with $|M_{CDO} - M_{nonCDO}|$ the absolute value of the difference between average values for CDO and non CDO sample of galaxies, err_{CDO}, err_{nonCDO}, respectively the error on the mean corresponding to M_{CDO} and M_{nonCDO}. $\Delta M/err_{tot}$ is indicated on each graph.

velocity, the $[60\mu m]/[100\mu m]$ color, the total mass of atomic hydrogen, the star formation rate (see figures 1.3) or the bar type are not strongly different between the two samples.

We remark that the CDO sample of galaxies selected more later ($t \geq 5$) than earlier ($t \leq 4$) types, as can be seen on figures 1.34. However the slight excess of non barred (SA) galaxies as compared to barred ones (SB) in CDO is not statistically significant.

In reading order, we see on figure 1.35, that CDO galaxies have on average smaller dispersion of elliptical shapes inside their disk-like regions, disk-like region isophotes with lower S/N ratios, more isophotes in their disk-like regions, larger holes inside their disk-like regions, larger numbers of contiguous regions added together to make EXT regions i.e. larger numbers of separations inside their disk-like regions.

The absolute size of the disk-like regions of CDO galaxies are larger than average though they are not much larger if we remove the holes they contain. We see this on the third row of figure 1.35, because going from column 2 to 3 in this row corresponds to measuring the sizes of EXT regions first including holes, and then excluding them from the size measurement.

To further investigate the increased number of isophotes per EXT regions in CDO galaxies as compared to non CDO galaxies, we compute, before any attempt to compare elliptical shapes of isophotes between one another, the rejection rate associated with isophote selection either due to $\alpha \geq 3$ and $R/R25 \geq 0.3$ (first two selection criteria), or to other subsequently applied selection criteria (see section 1.6.1). We find that for both groups of selection criteria, taken separately,

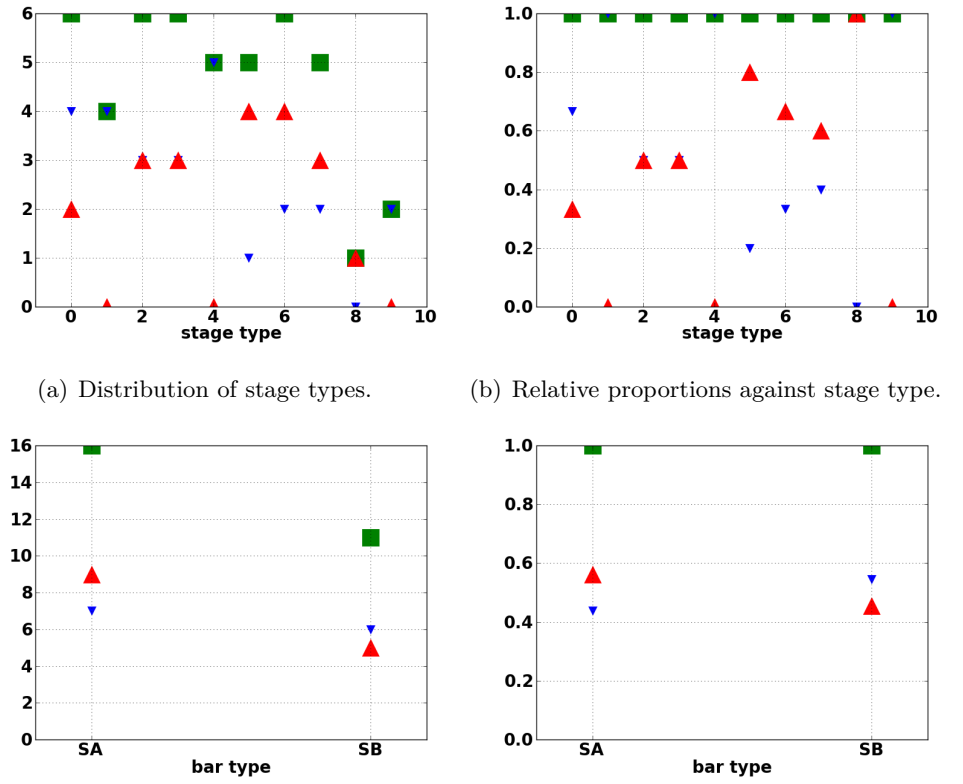

(a) Distribution of stage types.

(b) Relative proportions against stage type.

(c) Number of SA and SB galaxies.

(d) Relative proportions of SA and SB galaxies.

Figure 1.34: Morphological properties of CDO sample.

the rejection rate in CDO galaxies is significantly smaller than the rejection rate in non CDO galaxies, showing that CDO galaxies are overall less affected by selection criteria imposed on isophotes. Although CDO galaxies have smaller rejection rates than non CDO galaxies, there is no axis ratio variations between CDO and non CDO galaxies (see figure 1.36). It suggests axis ratios although changing the accessible rejection rates, have no consequence on the coherence of disk shapes extracted with our method in different bands. Thus we could hypothesize that even if structures can be less coherent with the disk shape in face-on galaxies (explaining why larger rejection rates are accessible for more face-on galaxies), the higher rejection rates in more face-on galaxies does not strongly influence the coherence of disk extraction in different FIR bands, and thus there is no axis ratio difference between CDO and non CDO samples. This may show that our isophote selection is efficient enough, i.e. compensating with higher rejection rates the increased number of isophotes not relevant to extract the disk shape in more face-on galaxies.

We can conclude that to extract coherent disk orientations and thus coherent disk regions between wavelength we chose galaxies whose disk regions were spread on larger radial ranges than average at the cost of being non contiguous. CDO galaxies have on average disk regions including more outer isophotes as well as isophotes with lower S/N ratios. This is illustrated by the smaller than average minimum S/N ratio inside EXT region of CDO galaxies, whereas for all galaxies, EXT regions are built with isophotes with same S/N values. In a less statistically meaningful way, the largest values of α in EXT regions are seen to be smaller for CDO galaxies than total sample and non CDO galaxies. We also see that minimum R/R25 values of

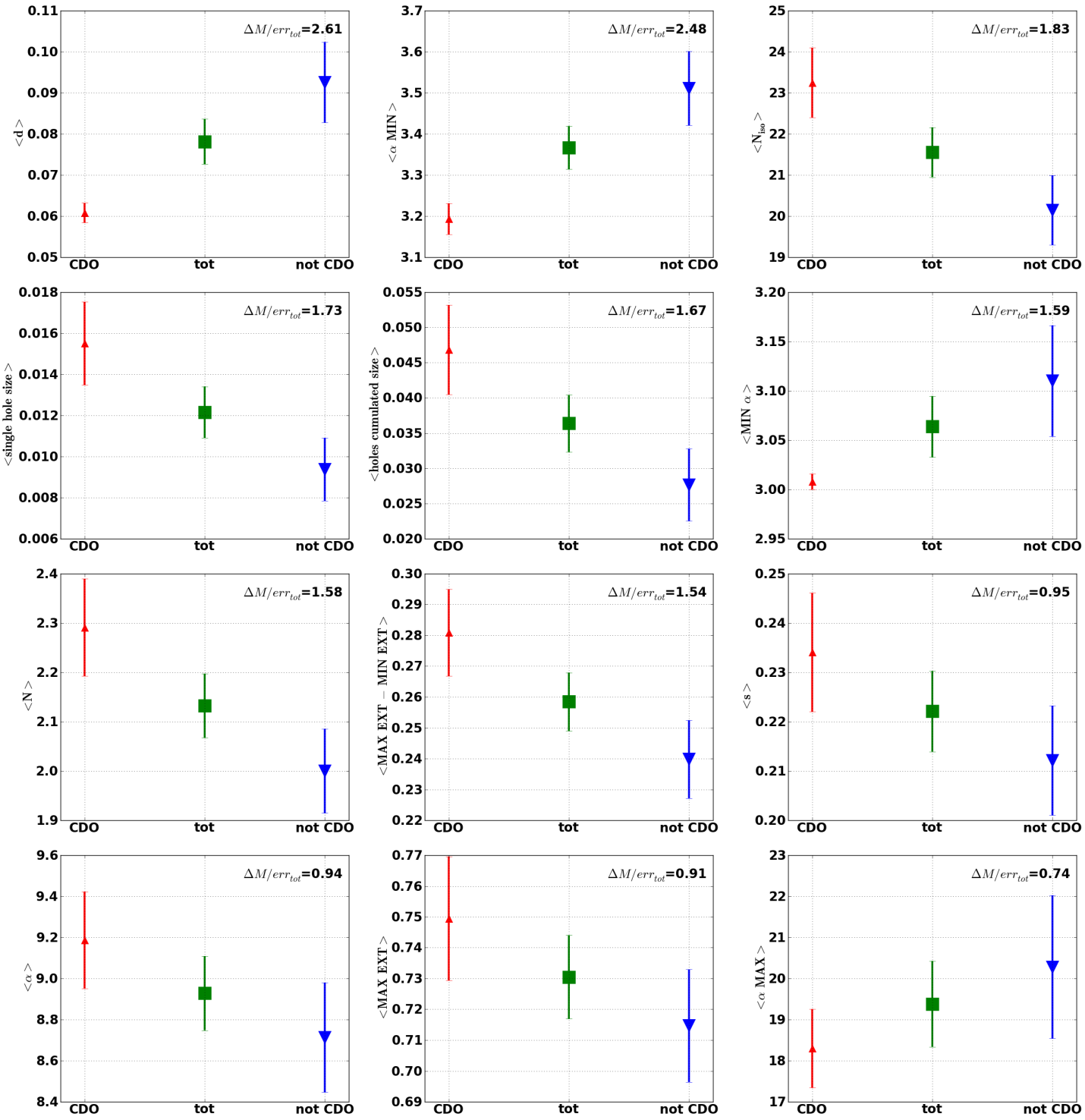

Figure 1.35: On these figures are displayed many properties of the EXT regions we extracted for CDO, total and non CDO sample of galaxies. Properties are ordered by decreasing values of $\Delta M/err_{tot} = \dfrac{|M_{CDO} - M_{nonCDO}|}{err_{CDO} + err_{nonCDO}}$, with $|M_{CDO} - M_{nonCDO}|$ the absolute value of the difference between average values for CDO and non CDO sample of galaxies, err_{CDO}, err_{nonCDO}, respectively the error on the average associated with M_{CDO} and M_{nonCDO}.

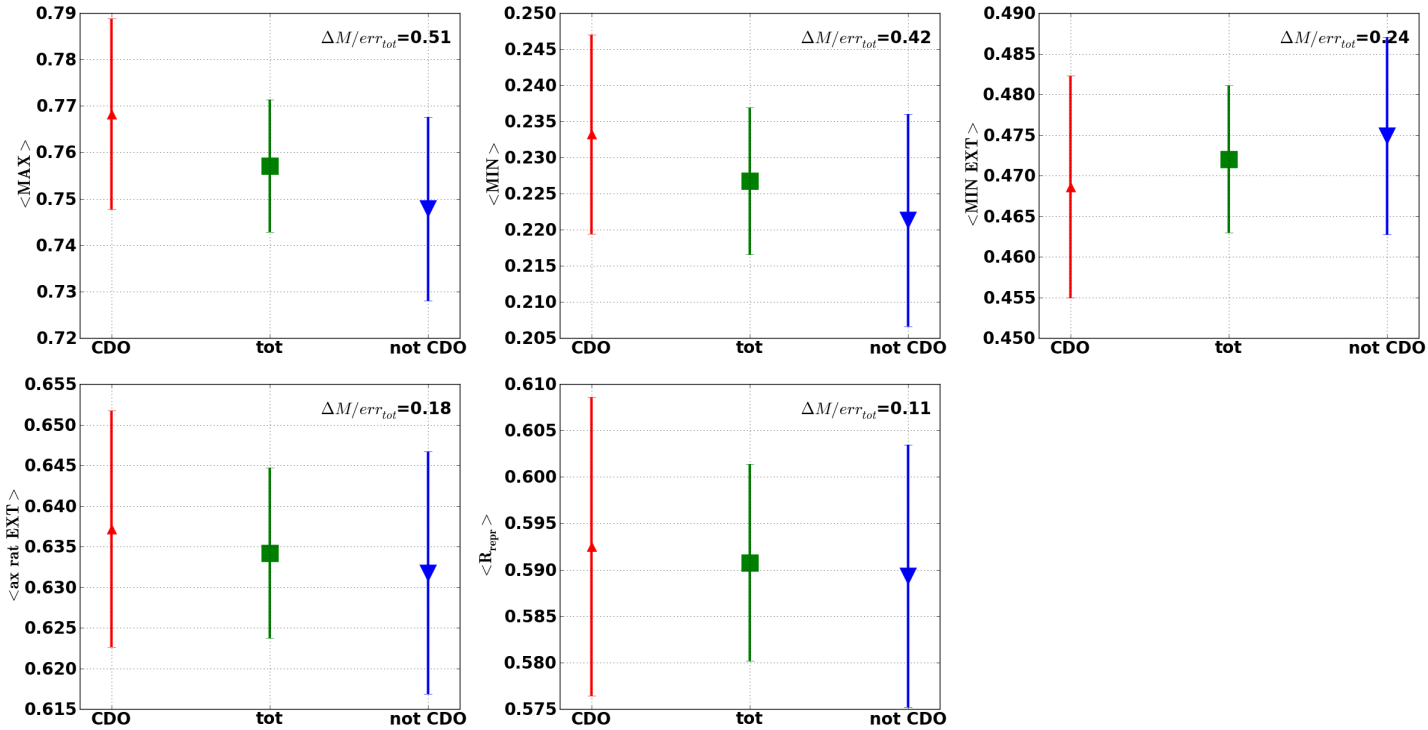

Figure 1.36: On these figures are displayed many properties of the EXT regions we extracted for CDO, total and non CDO sample of galaxies. Properties are ordered by decreasing values of $\frac{|M_{CDO} - M_{nonCDO}|}{err_{CDO} + err_{nonCDO}}$.

EXT regions are compatible with total and non CDO values. Interestingly, in CDO galaxies, maximum R/R25 of EXT regions are marginally larger than average, whereas the maximum accessible R/R25 of isophotes with $\alpha \in [0, 19]$ is not larger than average for CDO galaxies. Thus extracting CDO galaxies consistently selected galaxies in which disk regions are seen at larger radii than average. These arguments further suggest that as disk orientations coherent under change of wavelength were extracted at large galacto centric radii, probing larger radial ranges could possibly help to extract disk structures more coherent under wavelength change, in those cases in which our study failed to extract one. Another interpretation states that in galaxies where the dust disk is morphologically similar to the old stellar disk, disks are found at lower S/N ratios.

In CDO galaxies, our method was not only successful at extracting disk orientations coherent under change of wavelength but also in global disk region extraction, as is shown by the larger number of isophotes included in EXT regions of CDO galaxies. Even if this number was previously linked to the average intensity of the EXT region as compared to the background we see that CDO galaxies do not have much higher average intensities than average. This is explained by CDO galaxies having larger holes and to a lesser extent, larger holes cumulated extensions as well as larger hole numbers than total and non CDO samples.

Disk-like regions inside the CDO sample having on average minimum intensity of isophotes closer to the background as well as marginally larger maximum radius than the non CDO sample, the increase in dispersion of elliptical shapes in the non CDO sample as compared to the CDO sample is not due to intensities of isophotes too close to the background.

As the non CDO sample is probing more earlier stage types and more barred galaxies than CDO, we find in Buta et al. (2005) that the non CDO sample is likely to have galaxies with weaker spiral arms and probably more numerous weak bars than the CDO sample, whereas the

CDO sample is likely to have more non barred galaxies or barred galaxies with bar strengths more dispersed than non CDO sample. Although the trend between bar strength and spiral arm strength found by Buta et al. (2005) is not so strong leaving room for dispersion, we consider that weaker average spiral arms of non CDO galaxies may be a potential distinction from CDO galaxies. As we have already stressed more pronounced spiral arms may be linked to increased presence of dust in galaxies, therefore more pronounced spiral arms could be linked to larger holes inside disks of dust as well as, as conflicting as it may seems, increased prevalence of dust disk, making it easier to detect and when detected more coherent in various dust bands as well as with the stellar disk. We conclude from this that early galaxies with weak bars and weak spiral arms exhibit relatively larger elliptical shape dispersions of isophotes and especially more discrepant disk orientations between stellar and dust bands.

The increased dispersion of elliptical shapes and smaller number of isophotes inside disk regions of non CDO galaxies as compared to CDO galaxies also illustrates that the disk orientations extracted with our method are more coherent when disk regions are larger. Thus in subsequent research it would be interesting to increase the number of isophotes with possibly more efficient isophote extraction techniques. This could increase the chance of extracting isophotes with similar elliptical shapes and even lacks of isophotes with similar elliptical shapes would be more meaningful than what can be concluded from smaller number of isophotes. Though we believe that our conclusions are qualitatively correct: larger disk regions with well defined orientations (weakly dispersed isophotal shapes) and coherent orientations between dust and old stellar phases, are detected inside later type galaxies.

1.6.6 Comparison between extended disk orientations and litterature orientations

Galaxies in the CDO sample do provide robust disk orientations under change of bands. We now turn to assess the difference between our disk orientations and litterature disk orientations.

To assess the consistency of our method for extracting a disk orientation with other previously existing methods, we compared our EXT orientations to litterature orientations, namely the RC3 $25\,\mathrm{B}-\mathrm{mag.}('')^{-2}$ disk orientation (see on NED website the page devoted to diameters of cosmic objects or de Vaucouleurs et al., 1991) as well as disk orientations obtained from studies of the dynamics of the H-alpha gas (see Daigle et al., 2005 and Dicaire et al., 2008). The RC3 disk orientation discussed here is extracted by fitting an ellipse on an isophote at a surface brightness level of $25\,\mathrm{mag.}('')^{-2}$ in the B band. RC3 and H-alpha kinematics axis ratios are obtained from inclinations by using equation (1.2), page 85. The various comparison results are given in table 1.6.6. We only compared orientations of galaxies in common between our sample, RC3 and [Dicaire et al. (2008), Daigle et al. (2005)].

We define the average orientation difference between our method and another method for a specific group of galaxies by computing the orientation difference between the two method for each galaxy of the group, and then averaging this orientation difference over all galaxies of the group.

For our total sample of galaxies in common between these three studies, our method yields orientations more discrepant from the kinematical and photometric studies than those two are from each other. Thus in this case our method fails to yield as coherent orientations as litterature ones.

However when we restrict our sample to galaxies to galaxies in common between the two litterature references and CDO we see that our method is as close or closer to kinematical orientations than RC3 and staying at a respectable distance from RC3 ($D \approx 0.18$). If we restrict even further our sample to the galaxies in common between the restricted sample (see supra) and those two studies, our method is closer to H-α kinematics orientations. The fact

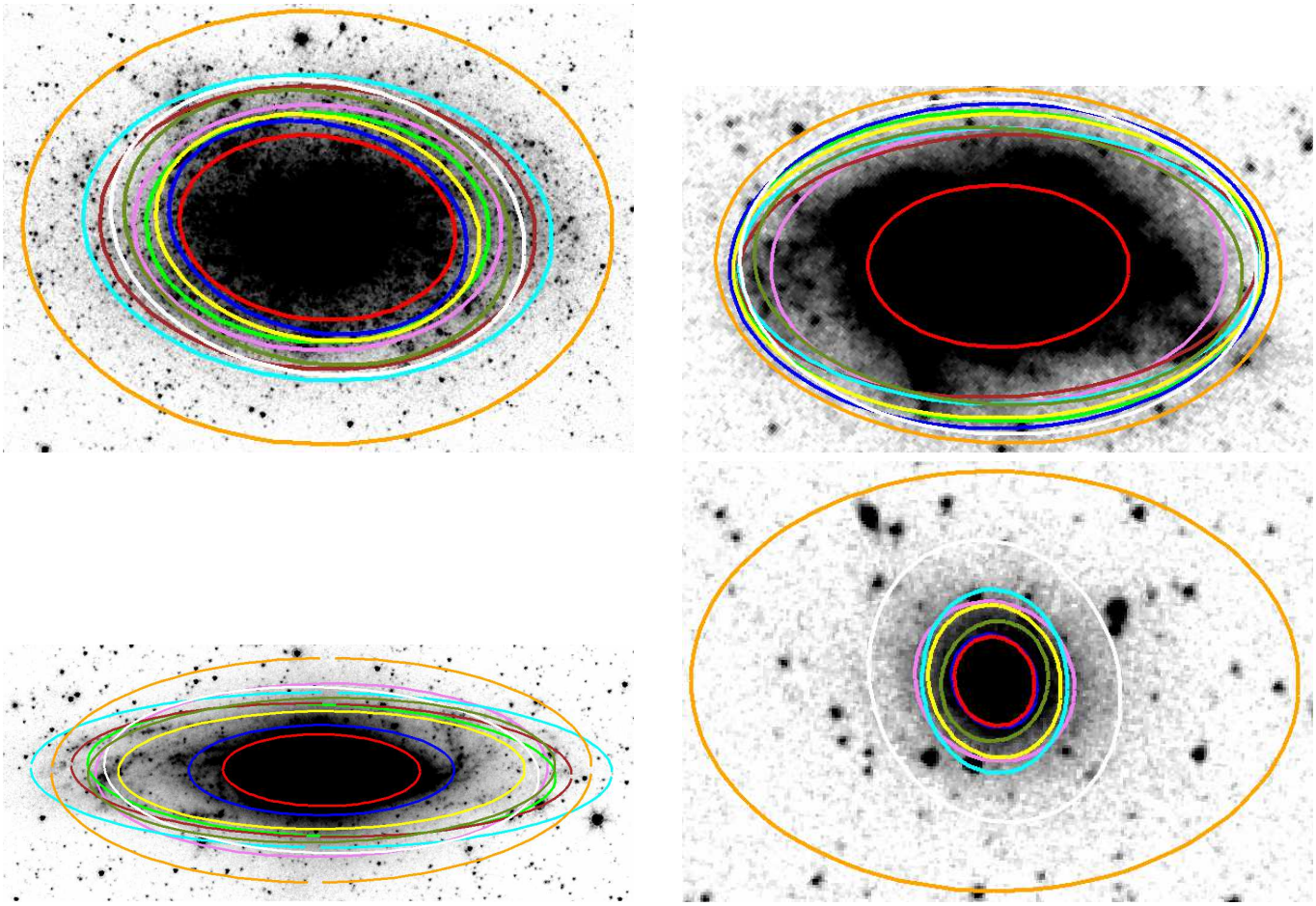

Table 1.4: Here are examples of EXT region average elliptical shapes. Each ellipse presented here has the axis ratio and the position angle corresponding the galaxy EXT region extracted in one band. The semi major axis of each ellipse corresponds to the EXT region best resembling ellipse in each band. Centers are fixed to NED centers. The band-color relation is the following: Mips 24 (OliveDrab), Mips 70 (white), Mips 160 (orange), Pacs 70 (red), Pacs 100 (blue), Pacs 160 (yellow), Spire 250 (cyan), Spire 350 (brown), Spire 500 (green), Irac 4.5 (violet). In reading order are shown NGC 7793, NGC0337, NGC7331, NGC 3773. The three first galaxies are in the restricted sample (see table 1.2) , and all four galaxies are inside the CDO sample.

Methods	Restricted	CDO	Total
kine - RC3	0.166 ± 0.029	0.148 ± 0.025	0.135 ± 0.017
EXT - RC3	0.186 ± 0.035	0.181 ± 0.029	0.217 ± 0.034
EXT -kine	0.139 ± 0.028	0.136 ± 0.021	0.180 ± 0.036

Table 1.5: In this table are given the average D distances between galaxy orientations from H-α kinematics, RC3 and EXT regions. These are given for the restricted sample, the CDO sample and our total sample (see table 1.2).

that our method, which is an entirely photometric one, yields orientations closer to kinematic studies than RC3 is remarkable.

We thus showed that in galaxies where our methodology succeeded at extracting, without a priori, coherent disk orientations for dust and stellar bands, orientations are also in agreement with litterature orientations. We also showed that in galaxies exhibiting the strongest similarities of disk orientation in different bands, our method yields results more similar to a kinematic study than a photometric one.

1.7 Conclusion on disk orientations

At this point we built a method to extract isophotes representative of our galaxies. We found an indicator, namely the distance D, to quantify the difference between ellipse shapes. This indicator is adequate to compare how the shapes of isophotes vary inside disk galaxies.

We first extracted orientations of disks based on a single isophotal level different but close to the one used by Jarrett et al. (2003). We compared the disk orientations we obtained to the one Jarrett et al. (2003) obtained. We then turned to compare litterature disk orientations found independently by either studying H-α kinematics or optical photometry.

These two preliminary studies enabled us to get an insight on the acceptable values of D distances between two isophotes that are describing the orientation of the same disk galaxy. We found that an acceptable value of D in the litterature is $D \approx 0.1$. This latter value was found to be twice smaller than the one we found between our disk orientations extracted at a single surface brightness level and Jarrett et al. (2003) isophotal disk orientations.

If one chooses a surface brightness level, fits an isophote at this level and decides that the shape of the isophote defines the orientation of the disk, this orientation depends on the surface brightness level of choice. As we had the opportunity to peer inside resolved galaxies, we decided to explore whether it was possible to alleviate the specific bias introduced in disk orientations by the choice of one single surface brightness.

Thus we extracted many isophotes in each map of all our disk galaxies. We then created selection criteria to pick amid these isophotes those which were appropriate to describe a disk-like structure inside our galaxies. Mainly these criteria state that to represent a galactic disk well, an isophote should :

- not be found in too inner parts of disk galaxies,
- have an average intensity well off the one of the background signal,
- be represented by a substantial number of pixel of the map,
- be symmetrical around the galaxy center.

We are confident these criteria are relevant to extract disk associated isophotes in all sets of intermediately inclined to face-on disk galaxies.

Interestingly these selection criteria were associated with rejection rates equal to zero for half of our maps, meaning that the isophotes of these maps were already "naturally" fulfilling our selection criteria. This shows our selection criteria are not far-fetched with respect to the majority of isophotes extracted in disk galaxies. We also remark that although some maps were completely stripped of their isophotes by our selecting rules, none of our galaxies had all its maps completely stripped of their isophotes. As we are confident our selecting rules extract isophotes which are close to what common sense would define as disk representing isophotes,

we find all these results coherent with the idea that our galaxies can be faithfully represented by disks in the vast majority of our IR maps, be it dominated by dust or stellar emission.

We also found that more face on galaxies have more isophotes not fulfilling our selecting rules. This could possibly be interpreted as galactic structures confined in a disk perturbing more easily isophote shapes from the typical disk shape, when the disk is seen face-on.

We compared the shape difference of consecutive isophotes to the $D = D_{thres}$ threshold value. We then built (EXT) regions, where the shapes of consecutive isophotes were closer from one another than D_{thres}.

Within these regions, the dispersion in elliptical shapes found to be close to D_{thres} informs us that our EXT region building method (including selection criteria followed by thresholding in consecutive ellipse D difference) leaves little room inside our galaxies for isophotes to significantly differ from an average disk shape by more than D_{thres}. It also means that EXT regions used together with D_{thres} yield disk orientations that can be compared to litterature disk orientations, in the sense that EXT regions are associated with an intrinsic dispersion in elliptical shape similar to or lower than the dispersion found between these litterature methods.

Our results are consistent with lower spatial resolutions biasing toward easier extraction of disk associated sets of isophotes. Maps of lower spatial resolution like MIPS 160 and MIPS 70, each respectively compared to PACS 160 and PACS 70, yield broader EXT regions in terms of R/R25 extensions and larger surface brightness dynamic ranges. However we can turn around this argument because obtaining on average non zero numbers of isophotes in EXT regions built with instruments with the highest spatial resolution (IRAC 4.5, MIPS 24, PACS 70, PACS 100) shows that our selection criteria are matched by non negligible number of isophotes even in dust emission maps with relatively high spatial resolutions (e.g. PACS data w.r.t. MIPS data). Our results are also consistent with the old stellar content dominating NIR emission being more smoothly distributed or at least more organized in a disk structure at smaller spatial scales than the dust content. More quantitatively, we found that we need to look in bands with PSFs 20 times bigger than IRAC 4.5 in dust dominated maps to obtain as similarly extended sets of isophotes associated with the disk.

Our results show that MIPS 160 and all three SPIRE bands exhibit similar number of isophotes linked to the disk structure as IRAC 4.5. This is consistent with relatively cold dust exhibiting disk-like structures on large physical scales inside disk galaxies. Cross examination of different properties of sets of isophotes associated with a disk-like structure hints at $18''$ (SPIRE 250 PSF) being the most appropriate PSF to extract a disk structure in cold dust emission ($250 - 500\mu m$), whereas, as dust gets warmer with decreasing wavelength from 160 to $24\mu m$, we find that a possible combined effect between PSF and heating regime renders disk associated region less prevalent in warmer dust emission. This is consistent with warmer dust being more localized and cold dust emission being more associated with a galactic disk structure.

In most bands the R/R25 range $[0.3, 0.4]$ is not selected in the disk representing region. This is an homogeous result found for dust dominated and stellar dominated (IRAC 4.5) galactic maps. Our disk extraction technique rejects some isophotes located amid radial ranges from which the disk region is usually extracted. The sizes of these holes could be compatible with relatively small isophotal shape perturbations of sizes around $\Delta R/R25 \approx 0.02$.

We saw that disk-like regions in stage type 4 are found to be larger than in other stage types for cold and warm dust. We know that Muñoz-Mateos (2009) concluded Sb-Sbc (stage type 3-4) had the largest dust surface densities. Thus we conclude that at higher dust surface densities the prevalence of a disk structure in dust maps is stronger.

We found that the dispersion in isophote elliptical shapes of EXT regions attributable to the presence of a bar goes from negligible in IRAC 4.5 to medium in warm dust bands and

large in cold dust bands. Thus the bar is having little effect on isophote shapes in galactic maps dominated by old stellar population, whereas the effect is more important in warm dust maps and even more important in cold dust maps. We deduce that the bar is causing more disturbances in isophotal shapes of cold dust maps in the ISM than in isophotal shapes of warmer dust maps.

Besides the best disk representative isophote is found at smaller radius for cold dust in galaxies with a bar ($R/R25 \approx 0.64$) as compared to galaxies without bars ($R/R25 \approx 0.72$) and the average $R/R25$ of disk-like regions are shifted to more inner radii. Thus we conclude that the least disturbed region of the cold dust disks are probably shifted to smaller R/R25 when a bar is present.

Another effect of bars is to decrease the surface brightness of cold dust disks. We will see in the last part of this thesis that this phenomenon could be linked to the decrease of the maximum surface density of dust in barred galaxies w.r.t. non barred galaxies.

The trends seen between galactic bar presence and disk associated regions in cold dust are weaker in warm dust and absent in the stellar band IRAC 4.5.

We then turned to compare the EXT region disk orientations between different wavelength bands. We thus extracted from our galaxies, a specific sample of galaxies (CDO) in which each galaxy exhibits relatively good agreement between EXT region disk orientations in all available wavelength bands.

Thus the bias toward obtaining broader disk-like region and possibly more accurate disk orientations in less spatially resolved bands, is alleviated by defining the success or failure of our disk orientation extraction technique as whether or not a relatively stringent agreement in elliptical shapes of EXT region is reached between all bands.

As the CDO sample is the sample in which our disk orientation extraction is more successful w.r.t. the non-CDO sample, we can check whether our method is more successful in a specific sort of galaxy by inspecting the properties of the CDO sample as compared to the properties of the non CDO sample. If our method is successful at least at identifying those galaxies where a galactic disk is more prevalent in dust and stellar bands, as well as more coherent between those two galactic phases, we have to conclude that this type of galaxies is the kind of galaxies found in the CDO sample.

Thus identifying the properties of the CDO sample is important.

CDO galaxies have smaller intrinsic optical luminosities and smaller IR to optical ratios. We conclude that a consistent disk orientation is found rather in galaxies faint in the IR.

We also find that a consistent disk orientation is found rather in non barred galaxies and galaxies of later types. This is rather consistent with studies in stellar dominated emission maps showing that later types have larger disk-to-total luminosity ratios than earlier types (see page 95 or de Vaucouleurs et al., 1991 and Simien and de Vaucouleurs, 1986). As we found that bars have a strong effect on cold dust increasing the dispersion of isophote shapes, and that later type galaxies have larger disk region sizes at least in cold dust bands, the fact that consistent disk orientations are found more in non barred and later type galaxies is not too surprising.

Consistent disk orientations are found in galaxies with disk-like regions exhibiting smaller dispersion in elliptical shapes of isophotes. CDO galaxies also have isophotes in their EXT regions closer to the background. This can be understood as more accurate disk orientation being found in galaxies where the disk isophotes are extracted far from inner galactic structures, known to be different from the disk (bulge, bars...). CDO galaxies also have more isophotes in their disk-like regions. This is consistent with disk orientations more coherent between bands being obtained in galaxies in which our method selects more isophotes to build EXT regions. It could as well be interpreted as galaxies with more coherent disk in dust and stellar bands (i.e. CDO galaxies) exhibiting more widespread isophotes associated to a disk structure.

We also find that CDO galaxies have larger holes in their EXT regions. This can be interpreted as larger more contiguous EXT regions possibly deviating more strongly from an average disk shape. For instance in this case ellipses could shift more in elliptical shape from the outer end of the EXT region to the inner end. Whereas if an EXT region is non contiguous, we check for each bit whether or not it is coherent with the average elliptical shape of the largest contiguous region. This is a drawback of our method. To improve our method one could for instance locate in EXT regions the place where the consecutive isophotes are varying the least in shape. We could define this point as $(R/R25)_0$ and check whether other isophotes of the EXT region are close or far from the shape of the isophote at $(R/R25)_0$.

The disk orientations we found are more consistent when disk regions are larger. This is coherent with the fact that using more spatially extended isophotes, the disk orientation is probing many regions inside the galaxy thus the estimate of the disk orientation is more accurate. We also find that CDO galaxies, where our method is more efficient at extracting a disk structure, provide isophotes which are less rejected by our selection criteria. This could be interpreted as galaxies in the CDO sample (thus with small IR luminosities as compared to their optical output) exhibiting less dispersed isophotal shapes with respect to the disk.

Interestingly we found that overall our method extracts consistent disk orientations with no preference for a specific galactic disk inclination.

Finally comparing our disk orientation extraction method to RC3 and H-α kinematics disk orientations we find our method obtains disk orientations more similar to H-α kinematical disk orientations than to optical photometric disk orientations obtained by RC3. This could be understood as follows: extracting a disk orientation at a single surface brightness yields results which are less accurate than what can be obtained either with very coherent disk orientations, averaged over many surface brightnesses and in many bands, or with kinematical arguments. However when the agreement between isophotes found at many surface brightness levels and/or in many bands is not extremely good, the disk orientations found this way are more coherent with what drives the shape of isophotes, i.e. the kinematics, rather than with a single surface brightness isophote shape.

Chapter 2

Study of dust physical properties vis a vis stellar content in Kingfish

In the CDO sample of galaxies, defined in the previous chapter, a dust counterpart to the stellar disk can be extracted. In these galaxies the disk orientations we obtained can now be used to average surface brightnesses azimuthally at different radii thus resulting in radially dependent spectral energy distributions (SEDs).

In non CDO galaxies, such a procedure is as yet not entirely justified because azimuthal averaging in these galaxies possibly mixes together contributions from different structures (e.g. spiral arms and inter-arms regions). These structures may well be significantly different from the disk, as we have seen in the previous chapter, and could conceivably dominate the FIR luminous ouput in non CDO galaxies. Thus averaging surface brightnesses at a constant radius in non CDO galaxies likely results in averaging over distributions of pixel surface brightnesses which may not peak around one average value but possibly many (e.g. arm and inter-arm average surface brightnesses). Thus for non CDO galaxies, photometric errors computed in this section are lower bounds to the real photometric errors. A more rigorous study of non CDO galaxies may require a more complex approach involving analyzing the variations with radius of the surface brightness distribution at constant galacto-centric radius.

Azimuthal averaging is a classical photometric methodology for studying disk galaxy emission (e.g. see Pohlen et al., 2009 ; Muñoz-Mateos, 2009). Averaging over increasing numbers of pixels with increasing radius enhances the signal to noise ratio obtained in outer regions of the disk as compared to single pixel-by-pixel analysis. These outer regions are also incidentally the ones from which disk orientations are more easily derived.

By using a dust emission model integrated in the SED fitting procedure we extract properties of the dust phase and the ISRF in which it is bathed. We then examine how these properties change radially within galaxies and between different galaxies.

2.1 Far-infrared modelisation

We use the model described in Galliano et al. (2011) to fit our IR SEDs and gain a more precise insight about dust physical properties. This enables us to get an insight of the distribution of the starlight intensity without assumptions on the star and dust geometry. Thus we assume that dust chemical composition is uniform and in agreement with what is observed inside the Milky Way. In each galactic region on which the model is applied the starlight intensity is parameterized by

$$U = \frac{\int_{0.0912\mu m}^{8\mu m} U_\lambda^\odot(\lambda)\mathrm{d}\lambda}{2.2 \times 10^{-5}\, W.m^{-2}} \tag{2.1}$$

where $U = 1$ corresponds to the intensity in the solar neighbourhood, λ is the wavelength. Here $U_\lambda^\odot = 4\pi J_\lambda$ with J_λ the mean intensity of the ISRF as derived by Mathis et al. (1983):

$$J_\lambda = \frac{1}{4\pi} \int I_\lambda \mathrm{d}\Omega\,.$$

The dust components included in this model are PAH, silicates and graphite. Following Galliano et al. (2011), we kept silicates and graphite fractions to the Milky Way ISM values, whereas the PAH fraction is used to fit the $IRAC_{8\mu m}$ band.

Two heating regimes are represented: stochastical heating, and thermodynamical equilibrium. The bulk of the dust mass is in the second heating regime.

The MIR part of the spectrum is mainly represented by small grains and PAH both out of equilibrium. The FIR part is roughly a pseudo black body emission with an emissivity index of $\beta = 2$.

The model supposes that each SED characterizes luminous emission on the line of sight, intercepting many smaller regions in which the dust mass M and the ISRF heating dust U are related by the truncated power-law function presented by Dale et al. (2001):

$$\frac{\mathrm{d}M}{\mathrm{d}U} \propto U^{-\alpha} \text{ with } U_- \leq U \leq U_+ \tag{2.2}$$

The possible α values are assumed to lie between 1 and 2.5 which respectively corresponds to photodissociation regions near young stars and to diffuse cirrus-like components of the interstellar medium. The reason for this is explained in Dale et al. (2001): in a transparent medium with a strong light source, $U \propto 1/r^2$ with r the distance to the light source, whereas the dust mass is supposed isotropic and homogeneous and follows $M \propto r^3$. In that case $dM \propto r^2 dr$, $dU \propto dr/r^3$, $dM/dU \propto r^5$ thus $dM/dU \propto U^{-2.5}$. In a denser medium U is dampened by dust. We assume for simplicity a parallelepipedic box outside which dust density is negligible and inside which dust density is higher, homogeneous. We suppose that dust is optically characterized by a linear attenuation coefficient τ. The starlight hits the box perpendicularly to one of its faces and attenuation is such that inside the box $U \propto e^{-\tau r}$ with r the distance from the surface of the box where the light enters along a straight light path. In the box the dust mass between $r = 0$ and r is such that $M \propto r$. Thus we get $dU/dr \propto -U$ and $dM \propto dr$, therefore $dM/dU \propto U^{-1}$.

The stellar continuum is also fitted to take into account its contribution to the SED in $IRAC_{3.6\mu m}$ and $IRAC_{4.5\mu m}$. This enables to obtain a notion of stellar mass, thereafter noted $M_{\star,fit}$. This is a photometric estimate of the equivalent mass for a stellar population of 5 Gyr from the PEGASE model (see Fioc and Rocca-Volmerange, 1997). The luminosity fraction of PAH, f_{PAH} is adjusted to match the $8\mu m$ luminosity, whereas NIR-MIR luminosities are used to constrain the fraction of ionized PAH, f_{ion}.

The grain size distribution used by Galliano et al. (2011) called "BARE-GR-S" is taken from Zubko et al. (2004). It supposes that dust is composed of PAH, graphite and silicates. The size distribution is derived by analyzing starlight extinction in the ISM, thermal IR emission per H atom, the average ISRF shining on dust grains, abundance of refractory elements that can be included in dust composition and properties of dust grains. Zubko et al. (2004) found that for the BARE-GR-S dust model, silicates and graphite share equally dust emission longward of $250\mu m$, whereas graphite dominates over silicates at wavelengths between 25 and $250\mu m$, PAH and graphite being the main contributors to dust luminosity in the range $3 - 25\mu m$ (see figure 2.1).

We can represent three of the main output parameters of this model by truncated integrals over the starlight intensity:

$$< U > = \int_{U_-}^{U_+} \mathrm{d}U \, f\,(U) \times U \tag{2.3}$$

$$\sigma^2(U) = \int_{U_-}^{U_+} \mathrm{d}U \, f\,(U) \times (U - < U >)^2 \tag{2.4}$$

$$M_d = \int_{U_-}^{U_+} \mathrm{d}U \, f\,(U) \times M \tag{2.5}$$

where

$$f\,(U) = \frac{1}{M} \frac{\mathrm{d}M}{\mathrm{d}U}$$

with $< U >$ the ISRF heating the dust averaged over the dust mass distribution along the line of sight, this is the typical ISRF seen by the dust which is proportionnal to the average energy emitted by each grain and thus to the average of $< \mathrm{T}^{\beta+4} >$ ($\beta = 2$), with T the grain temperature. We also have $\sigma(U)$ the standard deviation on the ISRF heating dust along the line of sight averaged over the dust mass distribution, which gives an idea of the spread in physical conditions along the line of sight and M_d the total dust mass.

Hence there are $N_f = 7$ output parameters to the SED fitting procedure: $< U >$, $\sigma(U)$, M_d, α, $M_{\star,fit}$, f_{ion}, f_{PAH}.

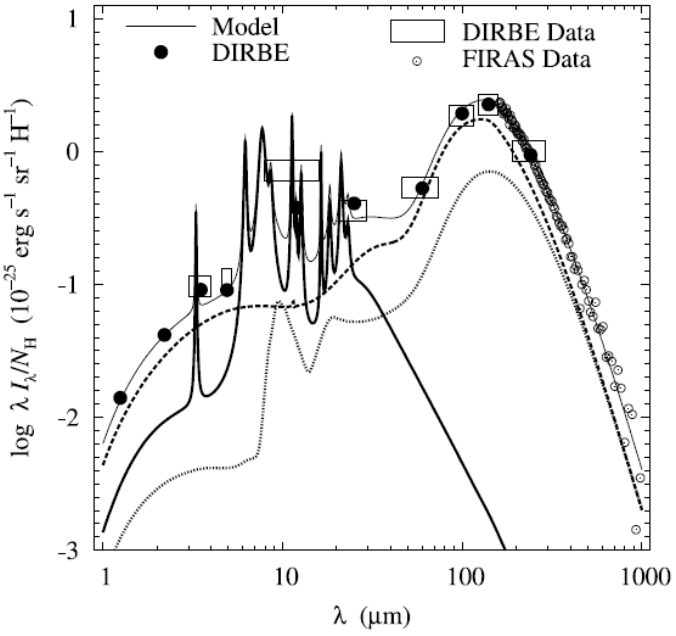

Figure 2.1: We reproduce a part of figure 4 from Zubko et al. (2004). It shows dust emission for the BARE-GR-S model. Silicates contribution is the light densely dotted line, the bold dotted line shows the contribution from graphite, and the continuous strong line shows the contribution from PAH.

2.2 From 2D-maps to radial profile of SEDs

Maps to convert	MIPS (24,70)	MIPS 70	PACS (70,100,160)	SPIRE (250,350)	IRAC (all 4 bands)
... to resolution of ...	SPIRE 500	SPIRE 500	SPIRE 500	SPIRE 500	MIPS 160

Table 2.1: Resolution changes. MIPS 160 and SPIRE 500 were not modified.

We applied the SED fitting procedure to radial profiles of galaxy SEDs. To do this we first convolved our maps to approximately the same point spread function, either MIPS 160 or SPIRE 500 according to PSF-modifying kernels we found in Gordon et al. (2008), see table 2.1. We took axis ratios and position angles from :

- our study, for galaxies on which extended region examination gave consistent results, i.e. the CDO sample, 20 galaxies ;
- H-α kinematics studies Daigle et al. (2005) and Dicaire et al. (2008) for the remaining 26 galaxies ;

and used these orientations to azimuthally average our maps. We did not regrid the maps with small pixels to the pixel size of maps with large pixels such as SPIRE 500 and MIPS 160. Instead in the small pixel maps, many thin elliptical rings correspond to the radial range of one thick ring of the large pixel map. Thus we computed for all of these thin rings, the arithmetical average of I (surface brightness) and I^2 (squared surface brightness) weighted by the number of pixels in each ring. We then compute the data "error on the average" surface brightness in the equivalent large ring, by the square root of the variance as quantified by the Konig-Huygens theorem divided by the square root of the effective number of independent areas inside the ring:

$$\sigma_{ring} = \sqrt{\frac{< I^2 > - < I >^2}{N_{e,pix}}} \tag{2.6}$$

where $N_{e,pix}$ is the effective number of areas in the maps after convolution, which have independent surface brightnesses. This can be estimated approximately by the number of circles with radius the FWHM of PSF that can be put side to side on the ring. We warn that this "error on the average", actually represents an intrinsic variability of surface brightnesses of pixels inside each ring, e.g. including variations of surface brightness when the ring crosses a spiral arm. The surface brightnesses of pixels in each ring are assumed to be at least approximately normally distributed around the average surface brightness of the ring. This is an assumption of our method.

We also selected rings whose average intensities were higher than $\frac{\mu + 3\sigma}{\sqrt{N_{pix}}}$ with μ, σ and N_{pix} respectively being the average background intensity, standard deviation of the background intensity, and the number of pixels in the ring for the unconvolved map.

Thus we got radial profiles of SEDs. In each SED, fluxes correspond to the pixel size of SPIRE 500. In all our SEDs we got at best 13 bands. This procedure revealed intriguing discrepancies between PACS and MIPS. We show on figure 2.2 surface brightnesses in maps, convolved to SPIRE 500 resolution, without regridding. We see that between PACS and MIPS, surface brightnesses at the same wavelength are very close on a large portion of the available radial range but they do differ at small and large radii by a non constant factor[1] (smaller than ≈ 3).

[1]Probable causes for this include non linearity in MIPS at high fluxes, filtering of low surface brightness emission in PACS as well as memory effect in the MIPS detectors.

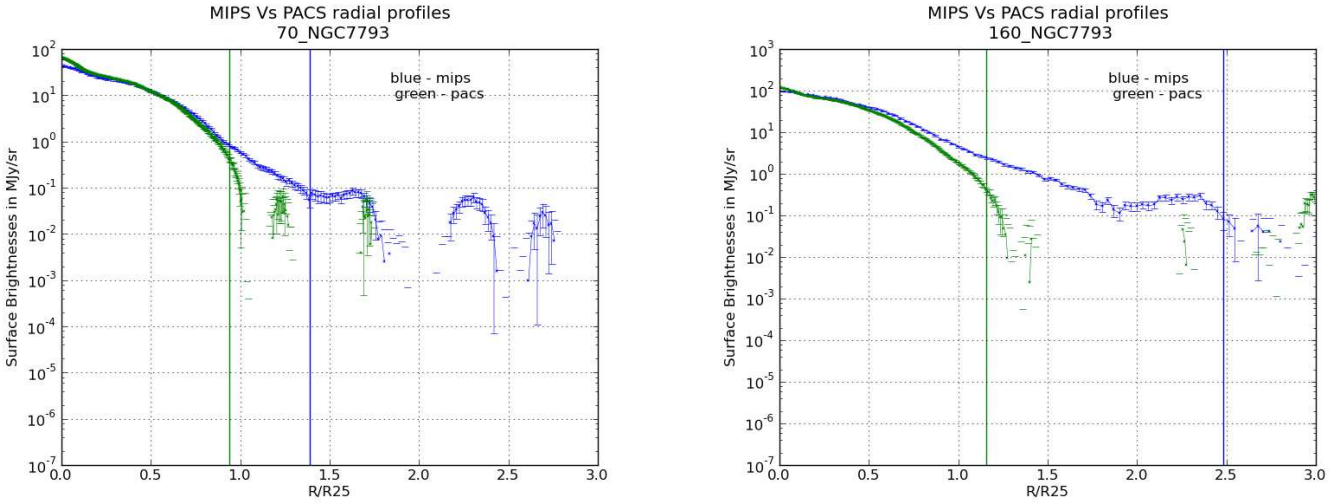

Figure 2.2: We give in these figures surface brightnesses obtained for NGC7793 in rings associated with original map grid for MIPS (blue) and PACS (green), for $70\mu m$ (left) and $160\mu m$ (right) after convolving to resolution of SPIRE 500. In abscissa are shown values of $R/R25$.

Because of these discrepancies, we decided to split up our SEDs into two types of SEDs. We always kept if possible all four IRAC bands, all three SPIRE bands, and MIPS 24. Then we either included (MIPS 70, MIPS 160) or (PACS 70, PACS 100, PACS 160), thus respectively gathering at best either 10 bands in the SED series called the "MIPS data series" or 11 bands for the SED series called the "PACS data series". From this point on the MIPS data series will be in blue and the PACS data series in red unless otherwise specified. We warn the reader that MIPS data series and PACS data series are not refering in the text below to MIPS only data or PACS only data.

Bands	MIPS 24	MIPS 70	MIPS 160	PACS (3 bands)	SPIRE (3 bands)	IRAC (4 bands)
Calibration error in % of the surface brightness measurement	5%	10%	12%	5%	7%	3%

Table 2.2: Calibration errors (see each instrument User's manual for more details).

For each of MIPS data series and PACS data series, we label different bands "b" from 1 to N_b and compute:

$$\chi^2_{red} = \frac{1}{\nu} \times \sum_{b \in [\![1, N_b]\!]} \frac{\left(I_{mod}(b) - I_{meas}(b)\right)^2}{\sigma^2_{cal} + \sigma^2_{ring}} \tag{2.7}$$

with $\nu = N_b - N_f$ the "number of degrees of freedom", $N_f = 7$ being the number of fitted parameters. We also used in equation (2.7) σ_{cal} the calibration error on surface brightness (see table 2.2), σ_{ring} the data error due to averaging over pixels from the large ring corresponding to one radius, I_{mod} the model surface brightness, I_{meas} the measured surface brightness. The fitting procedure takes into account the non zero bandwidth in I_{meas}.

We impose $\chi^2_{red} < 12$ to consider only reasonably well fitted SEDs.

The condition $\chi^2_{red} < 12$ might seem relatively loose, as in fully linear fitting method the acceptable value of χ^2_{red} is 1. However as the model we use to fit SEDs is not linear with respects to fitted parameters, the value of χ^2_{red} only provides a qualitative indication on the quality of fit (see Andrae et al., 2010). We will show how the quality of SED fitting is related to different values of χ^2_{red} in the next section.

2.3 Results of the SED fitting

First we choose NGC 7793 to present a sample of our results because in this galaxy the dusty and stellar disks are very similar (see section 1.6.4). We plot on figures 2.3, 2.4 and 2.5 SEDs fitted respectively at R/R25 of 0.1-0.5, 0.75-0.95 and 1.05-1.20. We choose these radii so that the difference in χ^2_{red} obtained at the same radius respectively for PACS and MIPS data series is clear (here χ^2_{red} is smaller for PACS data series than for MIPS data series on a large radial range and this trend reverses at large radii). The radii for each of the three figures 2.3, 2.4, 2.5 are located on the χ^2_{red} graph 2.7 respectively in light green ($R/R25 \in \{0.1, 0.5\}$), pink ($R/R25 \in \{0.75, 0.95\}$) and light blue ($R/R25 \in \{1.05, 1.20\}$).

We remark that at increasingly large R/R25 radii, surface brightness levels decrease and relative uncertainties increase. We see here that all PACS surface brightnesses go below the noise limit ($\frac{\mu + 3\sigma}{\sqrt{N_{pix}}}$) before any of the MIPS surface brightness does (see figure 2.5). The increase in χ^2_{red} in PACS data series is associated with the successive meeting of each PACS surface brightnesses with the noise limit between $R/R25 \approx 0.95$ and $R/R25 \approx 1.2$ as we can see on figures 2.4 and 2.5. These two figures also illustrate the discrepancy at low surface brightness between MIPS 160 and PACS 160 (by comparing left and right pictures at $R/R25 = 0.95$ and $R/R25 = 1.05$) as well as the difficulty to fit with our SED model low surface brightness SEDs containing both MIPS 160 and the three SPIRE bands (see left pictures at $R/R25 \in \{0.95, 1.05, 1.20\}$). Contrary to MIPS 160, SPIRE bands are always well represented by the SED fitting procedure. This is fortunate as those bands are very important to constrain the bulk of the dust mass.

We conclude from these observations, that increasing χ^2_{red} are associated with increasingly poorly fitted SEDs although we are confident even SED fittings producing $\chi^2_{red} \lesssim 12$ provide valuable information about dust properties.

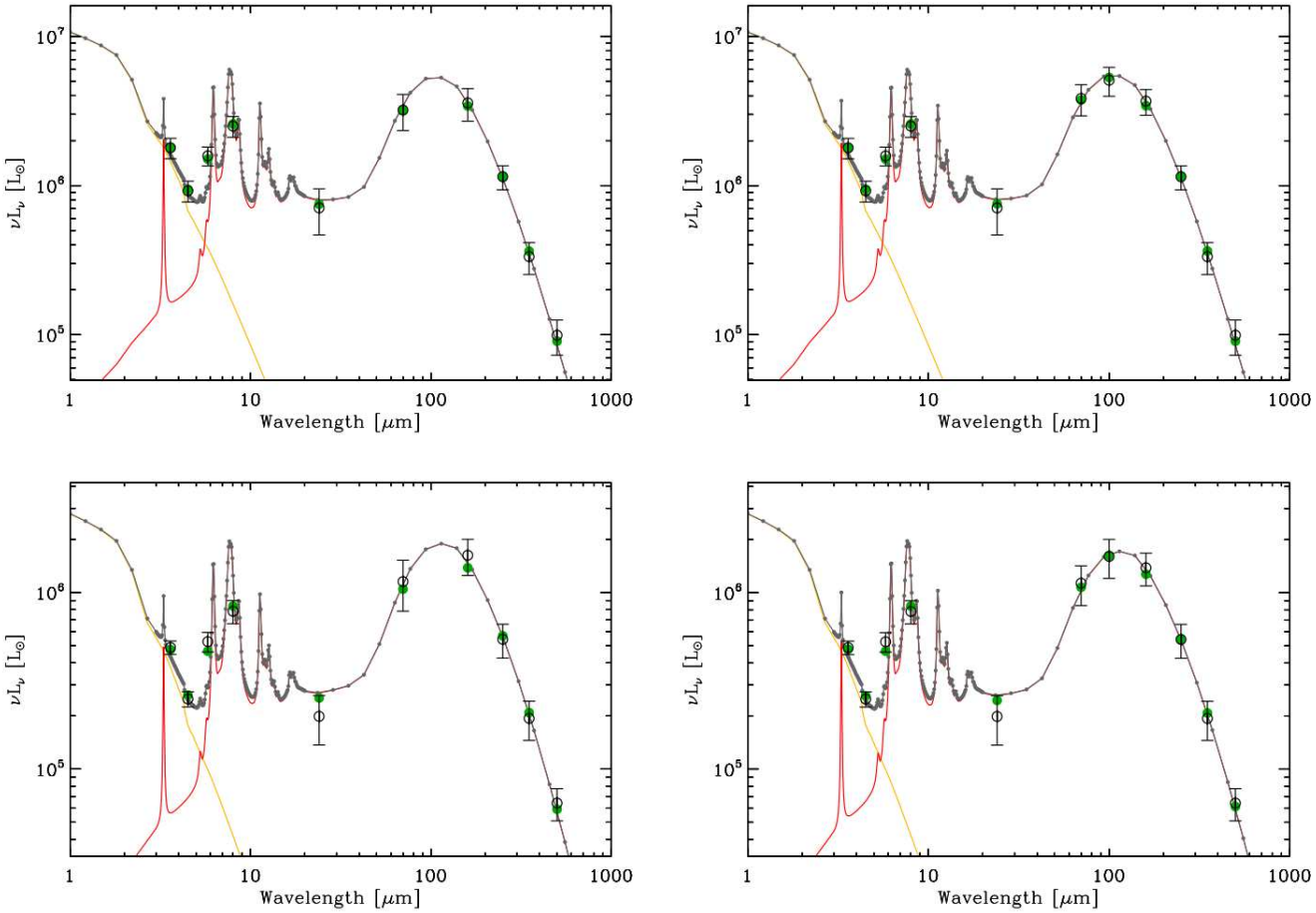

Figure 2.3: We give in these figures examples of fitted SEDs for NGC 7793 at $R/R25 \approx 0.10$ (top), $R/R25 \approx 0.50$ (bottom). On the left are MIPS data series and on the right PACS data series. In reading order, the value of χ^2_{red} associated with each figure respectively is 0.16, 0.16, 1.0, 0.55.

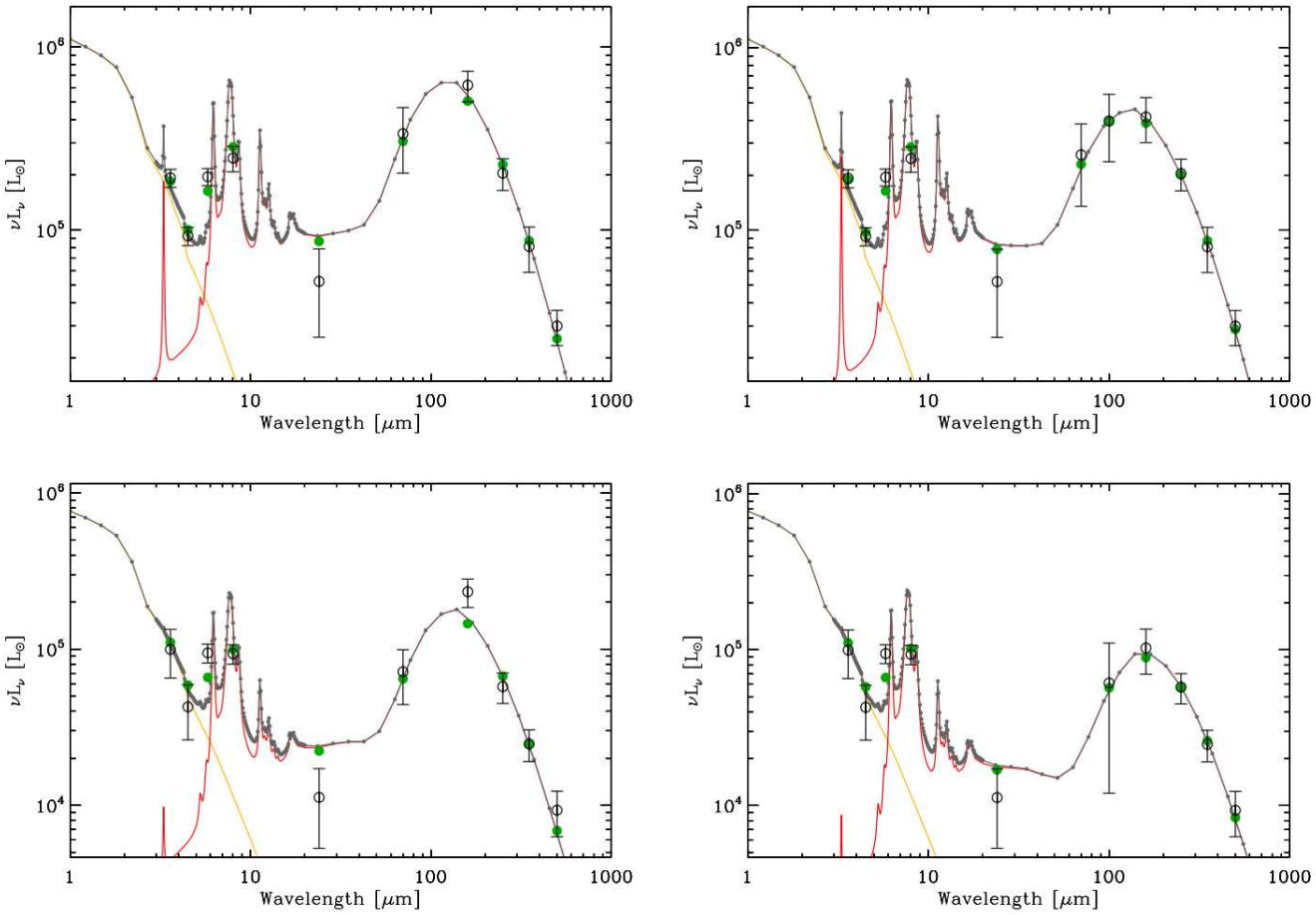

Figure 2.4: We give in these figures examples of fitted SEDs for NGC 7793 at $R/R25 \approx 0.75$ (top), $R/R25 \approx 0.95$ (bottom). On the left are MIPS data series and on the right PACS data series. In reading order χ^2_{red} associated with each figure respectively are 2.47, 1.17, 4.71 and 2.43.

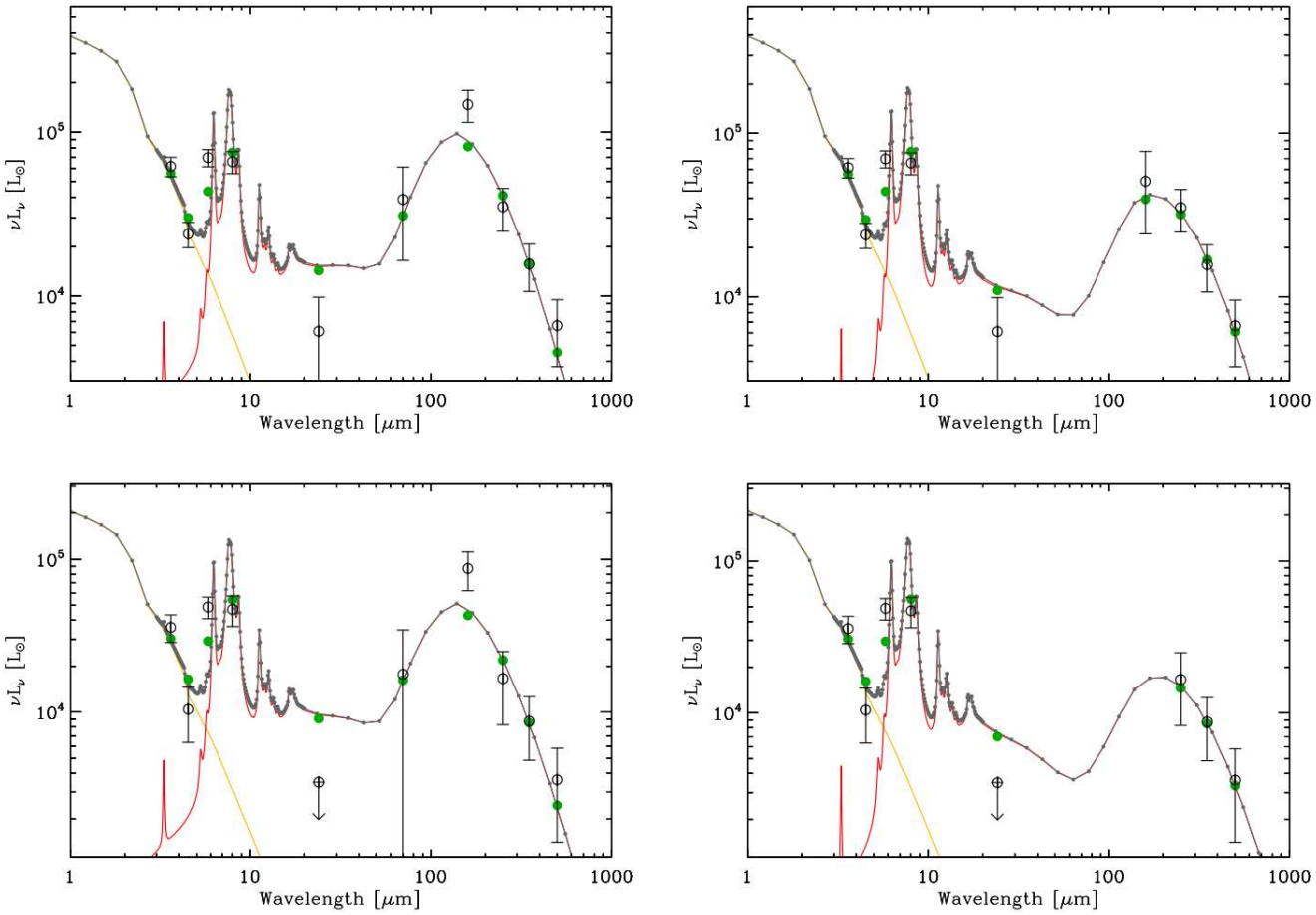

Figure 2.5: We give in these figures examples of fitted SEDs for NGC 7793 at $R/R25 \approx 1.05$ (top), $R/R25 \approx 1.20$ (bottom). On the left are MIPS data series and on the right PACS data series. In reading order χ^2_{red} associated with each figure repectively are 7.74, 7.50, 5.69 and 11.0.

We also plot on table of figures 2.6 and 2.7 the radial profiles of the model ouputs across NGC 7793 for a pixel equivalent galactic surface corrected for inclination of $0.106\,kpc^2$. This surface is the galactic surface of NGC7793 intercepted by the pixel solid angle in SPIRE 500, corrected by a factor a/b (a and b being the major and minor axis lengths). This correction corresponds to the idealistic case of an infinitely thin disk in order to place ourselves in the face-on case. In each galaxy we suppose that all SEDs correspond to a constant disk surface area, although this is generally an approximation throughout the disk as the disk thickness varies with galacto-centric radius. This approximation is particularly erroneous when it comes to small radii with structures differing from the general disk e.g. in case of a pronounced bulge. Let us now comment these results.

On the upper left image of 2.6, we see that the stellar mass in a fixed disk surface decreases almost exponentially with increasing radius in our whole radial range $R/R25 \in [0, 1.4]$. This is coherent with what is known from the density profile of older stellar populations in galactic disks. The mild change of slope visible at around $R/R25 = 1.0$ is consistent with observations from Radburn-Smith (2012).

On the upper right image of 2.6 we see that our fitting procedure has almost a binary behaviour between $\alpha = 1$ and $\alpha = 2.5$. This is illustrated by the small number of radial points having $\alpha \in]1.2, 2.2[$ and the numerous radial points where for the PACS data series α is close to 1, whereas for the MIPS data series it is close to 2.5. This seems not so realistic as dust is expected to be continuously distributed between the ISM and young star environment and possibly show that α is not properly constrained by the SED fitting procedure.

On the lower left image of 2.6 we note that $< U >$ exhibits a pronounced decrease with increasing radius at small radii, although this decrease has a different slope in PACS data series and MIPS data series and may be deemed exponential only on a more restrained radial range than $M_{\star,fit}$, we will comment more on this suject later on. $< U >$ estimates from PACS and MIPS data series are globally discrepant from $R/R25 = 1$ to $R/R25 = 1.4$. This may well be due to the observed difference in measured surface brightness levels between MIPS 160 and PACS 160 as well as between MIPS 160 and the three SPIRE bands, from $R/R25 = 0.75$ on to larger radii.

On the lower right image of 2.6, we remark that M_d the local dust mass is clearly not following the same trend with galacto-centric distance as the local stellar mass $M_{\star,fit}$, or the local ISRF hitting dust $< U >$. This is at odds with what was hinted at by Muñoz-Mateos (2009) as these authors concluded it was possible to describe dust distribution by a scale length only 10 to 20 % larger than stellar content. On the contrary for NGC 7793, our fitted dust masses are fairly constant in $R/R25 \in [0, 0.7]$ and decrease abruptly in MIPS data series on the radial range $R/R25 \in [0.7, 1.4]$. The behaviour of dust masses from PACS data series is less clear-cut on $R/R25 \in [0.7, 1.3]$, but it is more mildly decreasing overall from $R/R25 = 0.7$ to $R/R25 = 1.3$ than those from MIPS data series.

The upper left figure 2.7 shows a fairly constant contribution to dust luminosity from PAH in the range $R/R25 \in [0, 0.9]$ and a rising contribution from PAH at larger radii for both MIPS and PACS data series. Our procedure also shows a smoothly rising fraction of PAH being ionized on $R/R25 \in [0, 0.8]$ whereas the strong rise of the PAH luminosity fraction at larger radii in $R/R25 \in [0.9, 1.4]$ is concomitant with fully ionized PAH grains as well as relatively stronger evidence of $\alpha \approx 2.5$ at larger radii (more diffuse cirrus-like components).

The lower left figure 2.7 shows a $\sigma(U)$ trend with radius fairly well following the $< U >$ trend (see the lower left figure 2.6).

The lower right figure 2.7 shows a χ^2_{red} increasing overall with increasing radius, although this is not a monotonic increase. This is a rather general feature for the whole sample of galaxies. The general increase of χ^2_{red} with galacto-centric radius is very probably due to the increase of

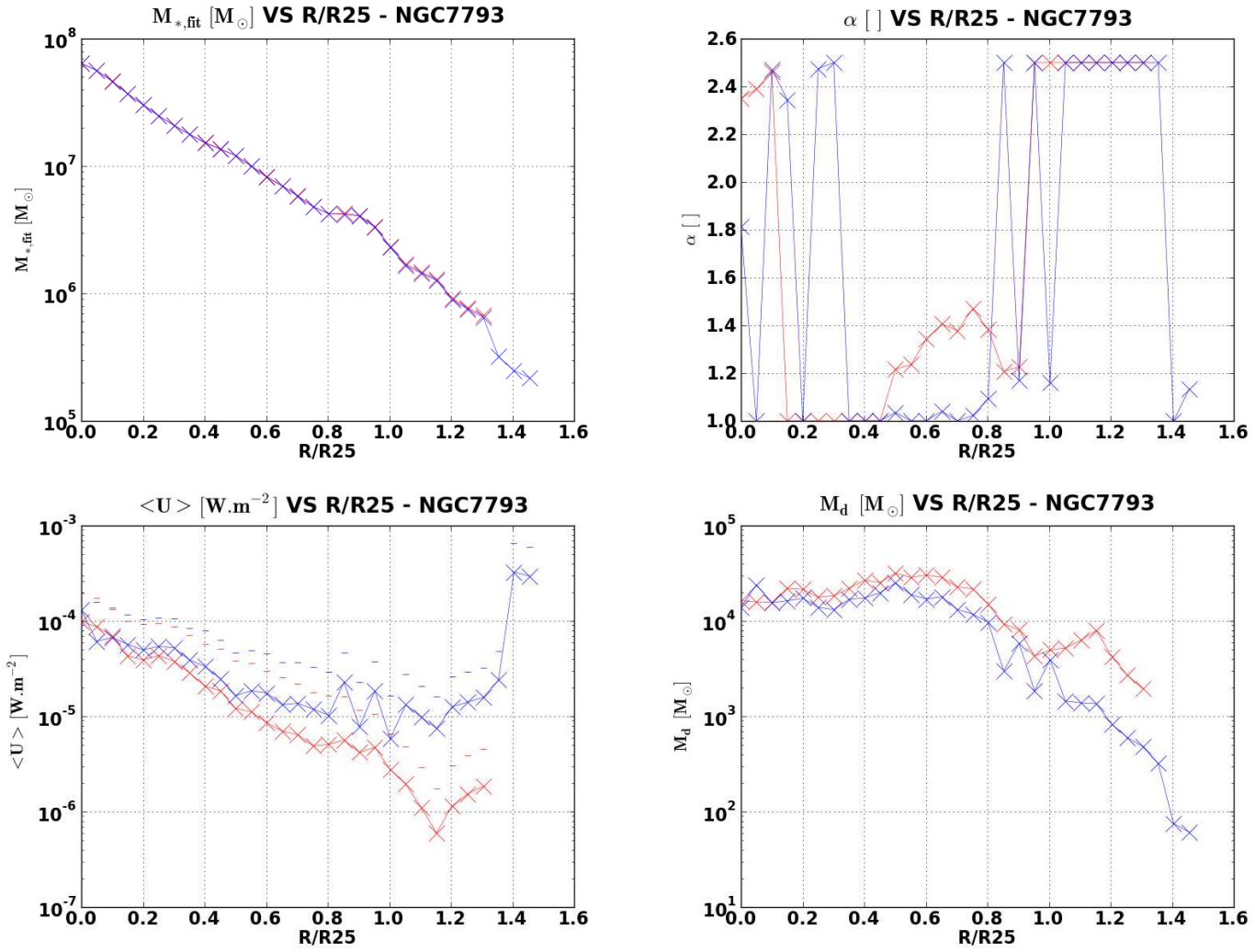

Figure 2.6: We give in these figures fitting results against $R/R25$ radii for NGC 7793. $M_{\star,fit}$ are values of the stellar mass necessary to remove the NIR-MIR stellar continuum, if we suppose that the only stellar source at these wavelengths is a 1 Gyr old stellar population. The errorbars on the figure representing $< U >$ are values of $\sigma(< U >)$, the standard deviation of the distribution of U along the line of sight.

noise impact on lower surface brightness levels.

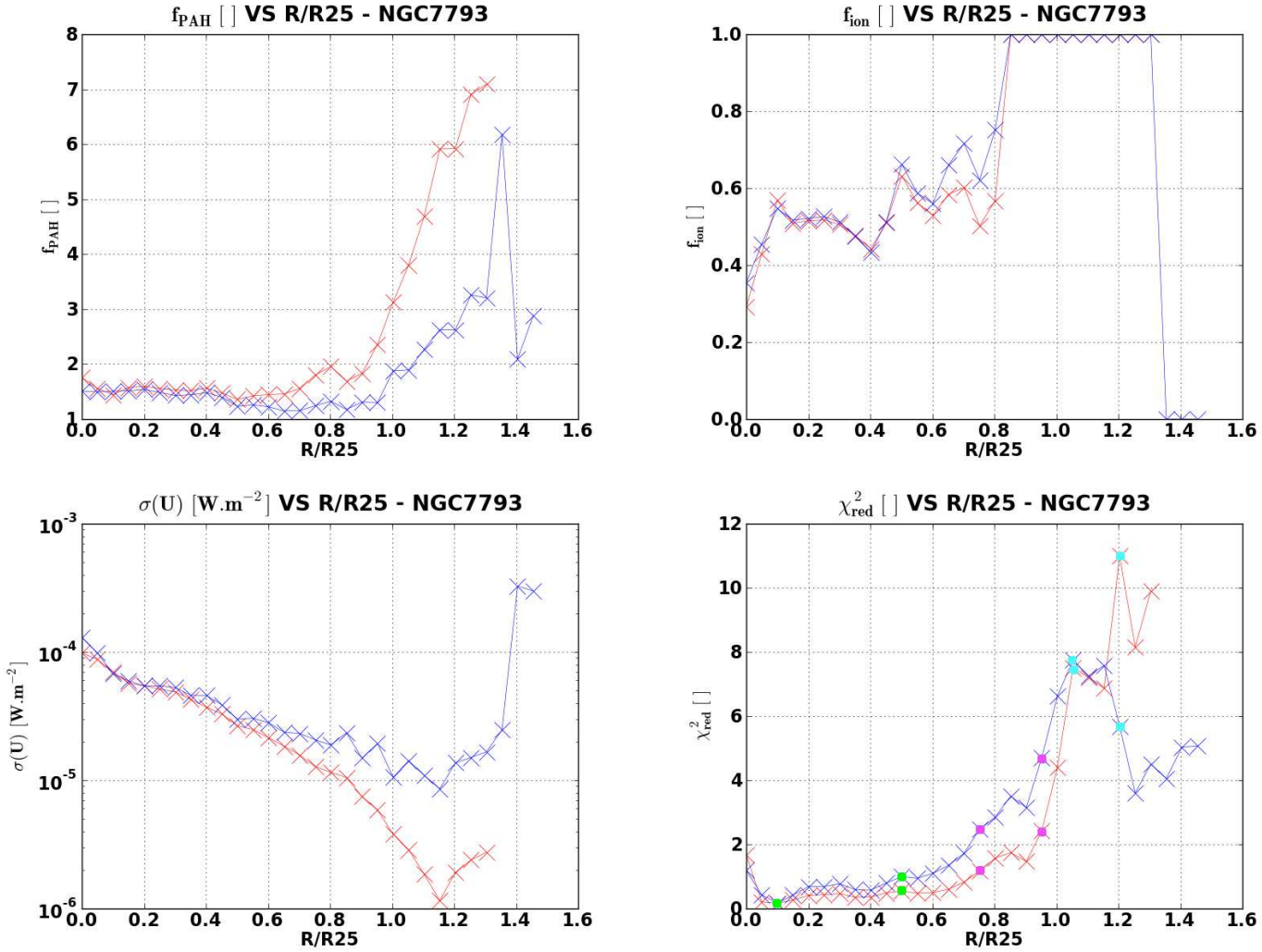

Figure 2.7: We give in these figures fitting results against $R/R25$ radii for NGC 7793.

Trying to understand the luminosity of the bulk of the dust mass we look at the upper left-hand ($M_{\star,fit}$), bottom left hand ($< U >$) and right hand (M_d) figures 2.6. These three quantities are nearly independent results from the fit. According to Galliano et al. (2011) after a SED fitting resulted in $< U >^0$ and M_d^0, a slight variation imposed on $< U >$ to obtain $< U >^1$ ($\neq < U >^0$), followed by a slightly different fitting of this SED, keeping $< U >$ constant at $< U >^1$, is likely to produce a fitted $M_d^1 \neq M_d^0$ to compensate for the change in $< U >$, whereas a similar procedure is likely to have no effect on $M_{\star,fit}$. With these caveats, we see that $M_{\star,fit}$ which is linked to starlight luminosity does not seem to be very strongly correlated to $< U >$ on the full radial range we explore. At first $< U >$ decreases with decreasing $M_{\star,fit}$ on $R/R25 \in [0, 0.8]$, but on $R/R25 \in [0.8, 1.4]$, $< U >$ stays rather constant and even increases when $M_{\star,fit}$ keeps on decreasing in increasingly outer radii. We remark that this change of behaviour is noticeably occuring when the dust mass starts decreasing outward in the radial range $R/R25 \in [0.8, 1.4]$ whereas it is approximately constant at smaller radii. This is the rationale to plot not only M_d and $< U >$ against $M_{\star,fit}$ but also $M_d \times < U >$. Thus we select NGC 7793 and NGC 2841, NGC 7331, two other galaxies amid those in which our method found

strong coherence between dust and stellar disk. In those three galaxies we plot on logarithmic scales $< U >$, $M_d \times < U >$ and M_d against $M_{\star,fit}$ (see figure 2.8 page 109; we give in section 4.6 the graphs for the whole CDO sample for the azimuthal averaging is justified).

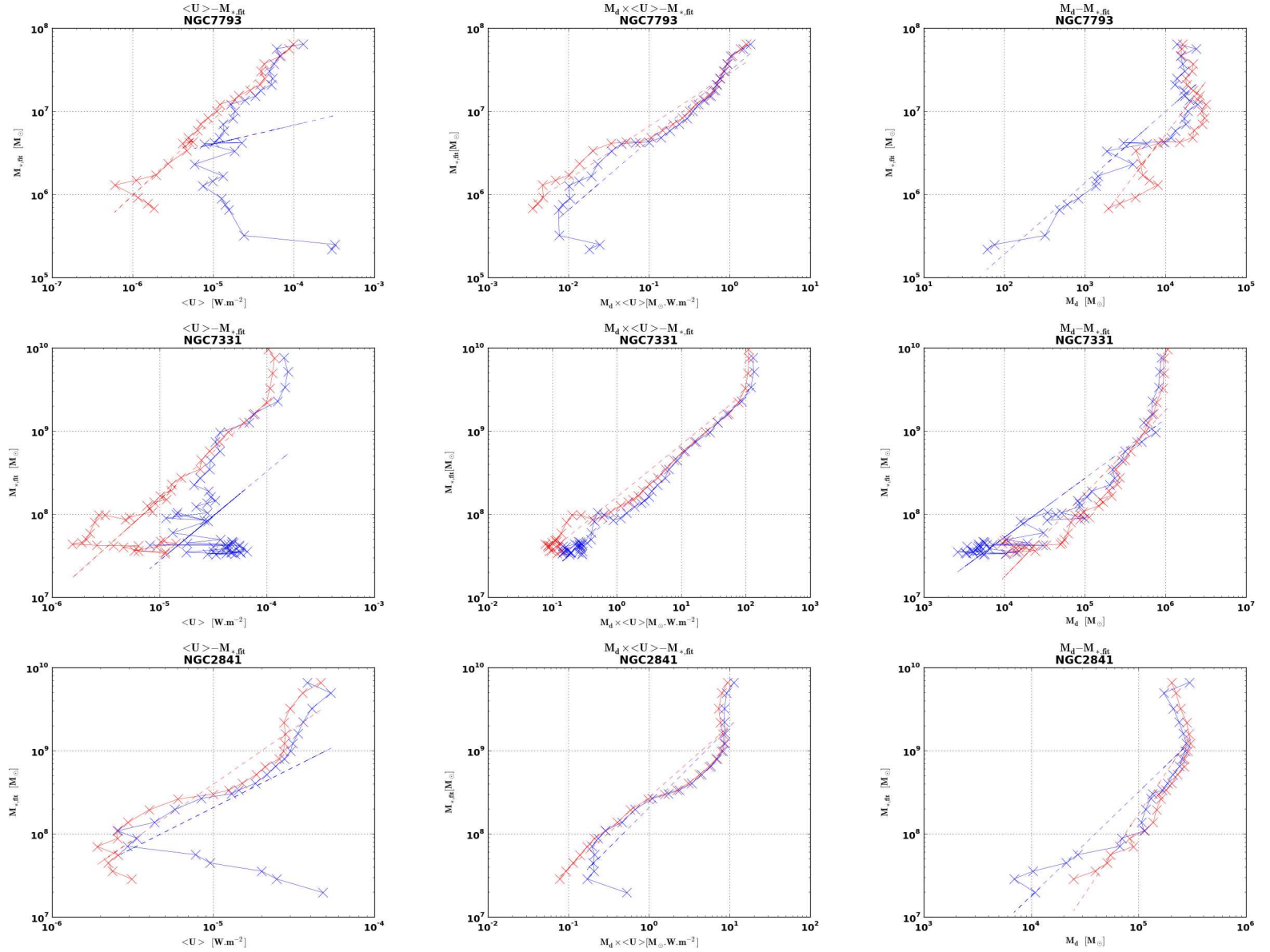

Figure 2.8: We give in these figures from top to bottom linear correlations in NGC 7793, NGC 7331, NGC 2841 between logarithm of $< U >$ against $M_{\star,fit}$ (left panel), $M_d \times < U >$ against $M_{\star,fit}$ (middle panel), and M_d against $M_{\star,fit}$ (right panel). Dust mass or stellar mass are in $M_\odot$ and $< U >$ in $W.m^{-2}$.

For these three galaxies we remark that the best linear correlation is obtained between $M_d \times < U >$ and $M_{\star,fit}$.

2.4 Links between ISRF, stellar mass and dust mass

Thus we plot in figure 2.9 the squared Pearson coefficient for linear correlations between logarithms of x and y, with $x \in \{< U >, M_d \times < U >, M_d\}$ and $y = M_{\star,fit}$ for our whole sample of galaxies. The results of these correlations are of the form $y = b \times x^a$. We will show a and b in subsequent graphs. We first plot squared Pearson coefficients averaged over our total sample (squares), CDO sample (triangles up), non-CDO sample (triangles down).

We remark that $M_{\star,fit}$ is much better correlated with $M_d \times < U >$ than separately with $< U >$ or M_d, in every subsamples (total, CDO , non CDO). This means that the stellar mass content seems more correlated with $M_d \times < U >$, a quantity integrating dust properties and the radiation field, than with just the ISRF bathing grains averaged over the dust mass, $< U >$, or the total dust mass, M_d.

We will interpret further the correlation $M_d \times < U > - M_{\star,fit}$ in this section and try to elucidate its meaning in the following sections of this chapter. We remark that the $M_{\star,fit} - M_d \times < U >$ correlation is more striking in the CDO sample than in the total sample and non-CDO sample.

As correlations in MIPS data series are overall less stringent, notably $< U > - M_{\star,fit}$, than in PACS data series we will talk about them later on. We remark that the correlation between $< U >$ and $M_{\star,fit}$ is associated with squared Pearson coefficient as low as $r^2 \approx 0.80$ in PACS data series. We interpret this as follows. First, when $M_{\star,fit}$ increases toward inner galactic radii, the typical stellar density increases. Therefore correlations between $< U >$ and $M_{\star,fit}$ being not very stringent means that the radial changes in the stellar density are not very tightly linked with how much dust heating changes radially. This seems to show that radiations heating the dust are not produced locally. It is in agreement with ***galactic disk ISM being generally translucent to dust heating radiations***.

We also note that correlations between M_d and $M_{\star,fit}$ not being very stringent either, means that the link between the dust life cycle and the stellar content history is not straightforward. This is expected as dust components are probably formed in stars, but cosmic dust is also probably subjected to shattering by SN-shocks, growth in the ISM, as well as possible transport of the ISM across the galactic disk (see Mattsson and Andersen, 2012).

The correlation of $M_{\star,fit}$ with M_d is more homogeneous between PACS and MIPS data series than the correlation of $M_{\star,fit}$ with $< U >$. This may stem from our results being more coherent between PACS and MIPS data series for M_d than for $< U >$. This in turn is understandable as M_d is probably more affected by SPIRE bands ($\lambda \geq 250 \mu m$) which do not change between PACS and MIPS data series thus yielding coherent results between PACS and MIPS data series, whereas $< U >$ is probably more affected by bands between $70 \mu m$ and $160 \mu m$ in which the main variations between PACS and MIPS data series are concentrated. Furthermore, as we know that MIPS 160 exhibit disagreements with SPIRE data and PACS data, whereas PACS data series are better sampling the wavelength range $\lambda \in [70\,\mu m,\, 160\,\mu m]$ which is likely to prove important to determine $< U >$, we are more keen to trust $M_{\star,fit} - < U >$ for PACS data series than for MIPS data series. We see that in PACS data series the correlation $M_{\star,fit} - < U >$ is slightly better in CDO than in the total and non-CDO samples.

We recall that we fitted simple correlations for which $y = b \times x^a$ with $x \in \{< U >, M_d \times < U >, M_d\}$ and $y = M_{\star,fit}$. The units used are $M_\odot$ for $\{M_d, M_{\star,fit}\}$, and W/m^2 for $< U >$. We remark that amid all these correlations the narrowest distributions of a and b are obtained for correlation $M_d \times < U > - M_{\star,fit}$, supporting previously found evidence that this correlation is more physically meaningful than $M_d - M_{\star,fit}$ or $< U > - M_{\star,fit}$ taken separately.

We here remark that the b values obtained for the correlation $M_{\star,fit} - M_d$ are very much dispersed from one object to another. As this b quantity is close to the average ratio of $M_{\star,fit}/M_d$

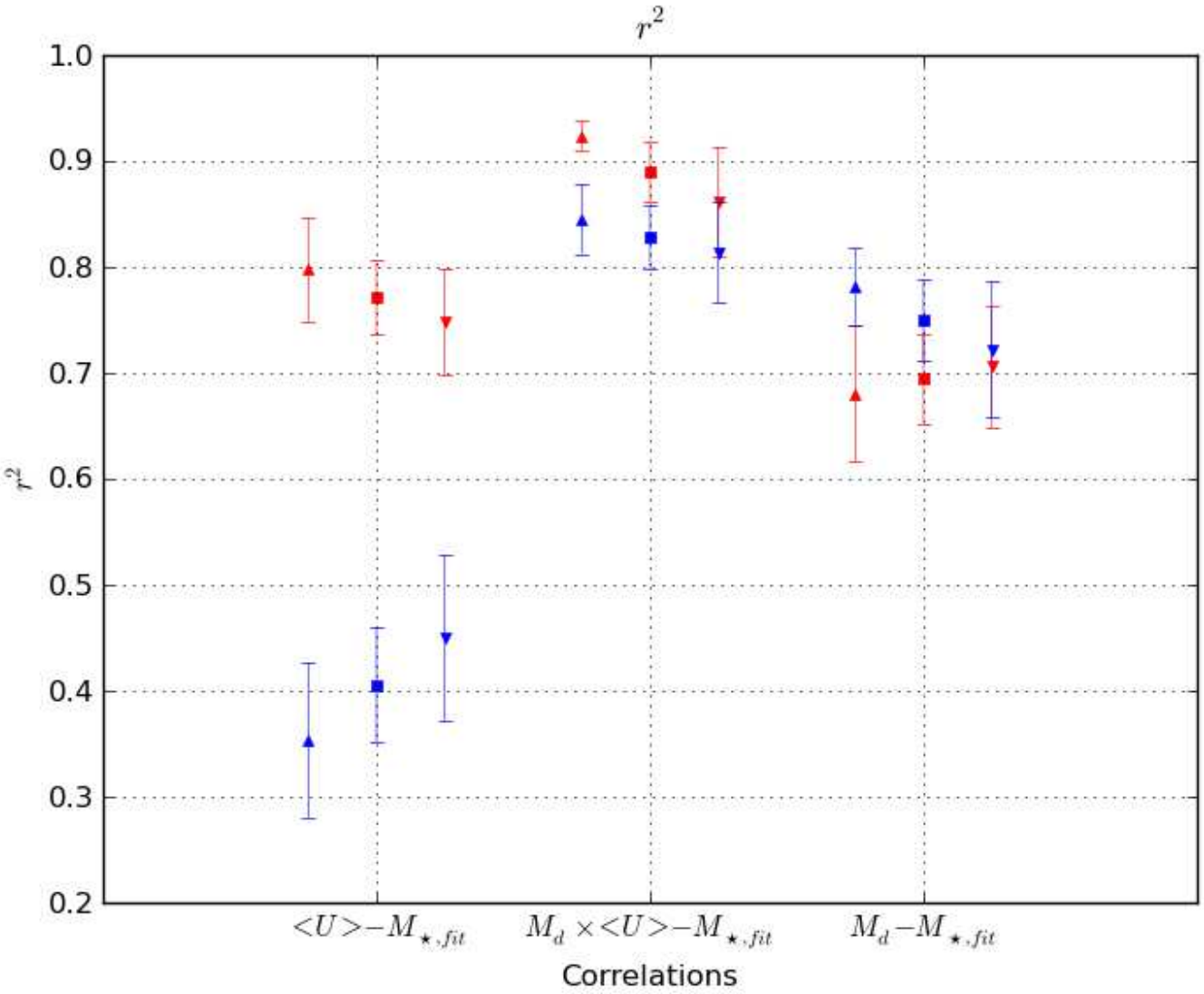

Figure 2.9: We give in this figure squared Pearson coefficients averaged over the CDO sample (upward triangle), our total galaxy sample (squares) and the non CDO sample (downward triangle) respectively for linear correlations between logarithms of: $< U >$ and $M_{\star,fit}$; $M_d \times < U >$ and $M_{\star,fit}$; M_d and $M_{\star,fit}$. Errorbars are error on the mean. PACS data series is in red and MIPS data series in blue.

across the disk (for this correlation $a \in [0.8, 1.4]$), this finding is consistent with previous studies showing that the stellar density is not univocally linked to a value of dust density.

As $< U >$, the ISRF bathing dust is very probably linked to starlight, it seems legitimate to posit that $M_d \times < U >$ is also linked to starlight. Thus we will in the following sections find a plausible interpretation of $M_d \times < U >$, compute IR densities of power, as well as stellar luminosity and assess the relation between stellar luminosity and $M_{\star,fit}$ to refine our understanding of the $M_{\star,fit} - M_d \times < U >$ correlation.

2.4.1 Power intercepted by dust

In this section we build a physical quantity linked to $M_d \times < U >$ without taking into account dust absorption. As dust absorption is wavelength dependent, taking it into account would require using the spectrum of radiations heating dust, e.g. using the ISRF provided by Mathis et al. (1983) and is not mandatory to provide a valid interpretation of $M_d \times < U >$.

We first recall that our model uses the dust grain size distribution derived by Zubko et al. (2004) for the dust model BARE-GR-S, we show this size distribution on figure 2.10.

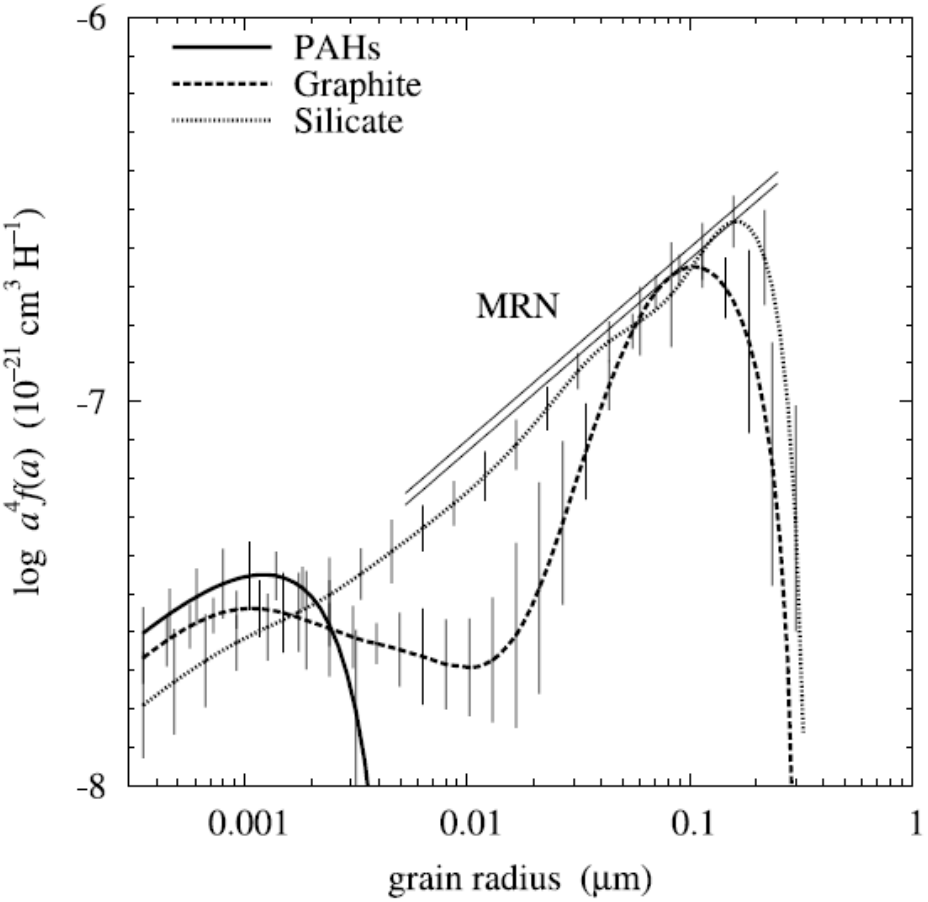

Figure 2.10: We reproduce another part of figure 4 from Zubko et al. (2004) showing the grain size distribution for the BARE-GR-S model. Silicates contribution is the light densely dotted line, the bold dotted line shows the contribution from graphite, and the continuous strong line shows the contribution from PAH. MRN refers to Mathis et al. (1977).

In this figure the number dn_x with $x \in \{\text{silicates, graphite, PAH}\}$ is the number of grains

in the radius interval $[a, a+da]$ with $dn_x = f_x(a)da$.

We approximate this size distribution by supposing that each dust component obeys the Mathis et al. (1977) size distribution $dn_x = K_x\, a^{-3.5} da$ between a_- and a_+. For all dust component x we take $a_{-,x} = 3.10^{-4}\mu m$ and we respectively take for silicates, graphite and PAH, $a_{+,x} = 0.3\mu m$, $0.3\mu m, 3.5 \times 10^{-3}\mu m$.

We also recall that, in BARE-GR-S, 67% of the dust mass is silicates, 29 % graphite, 5% PAH. We will refer to these percentages as P_x. Each of these components have respective densities of $3.5\, g/cm^3$, $2.24\, g/cm^3$ and $2.24\, g/cm^3$. We will refer to these densities as ρ_x.

The total mass of dust is M_d and we note that for each dust component:

$$M_d \times P_x = \int \rho_x \frac{4}{3}\pi a^3 dn_x \tag{2.8}$$

$$= \int \rho_x \frac{4}{3}\pi a^3 K_x a^{-3.5} da \tag{2.9}$$

Integrating this we obtain:

$$\frac{3}{8\pi} \times \frac{M_d\, P_x}{\rho_x \left(\sqrt{a_+} - \sqrt{a_-}\right)} = K_x \tag{2.10}$$

We would also like to estimate the cumulated surface density of power intercepted by all dust grains at each galactic radius, D_d. This is a meaningful quantity as, if we consider that each dust grain re-emit a fraction, f, of the ISRF in which it is bathed, the luminous output of dust mass $f\, D_d\, S$ inside the galactic surface S equivalent to the pixel area.

The surface density of power available to all dust grain is:

$$D_d \approx \frac{1}{S} \times < U > \sum_x \int \pi a^2 dn_x \tag{2.11}$$

expressed in $L_\odot/kpc^2$.

We compute

$$\sum_x \int \pi a^2 dn_x = \frac{3}{4} M_d \sum_x \frac{P_x}{\rho_x} \times \frac{a_{-,x}^{-0.5} - a_{+,x}^{-0.5}}{\sqrt{a_{+,x}} - \sqrt{a_{-,x}}} \tag{2.12}$$

thus by noting

$$1/m_s = \frac{3}{4} M_d \sum_x \frac{P_x}{\rho_x} \times \frac{a_{-,x}^{-0.5} - a_{+,x}^{-0.5}}{\sqrt{a_{+,x}} - \sqrt{a_{-,x}}} \approx 8.3 \times 10^{34} m^2/M_\odot$$

we obtain:

$$D_d = \frac{< U > \times M_d}{S \times m_s} \tag{2.13}$$

In the previous formula the only quantities depending on galacto-centric radius are $< U >$, M_d and D_d. D_d is in $L_\odot/kpc^2$, S is the SPIRE 500 pixel equivalent galactic disk surface which is fixed for each galaxy, and m_s is fixed because we chose a specific dust model namely BARE-GR-S.

Thus $M_d \times < U >$ can be related to the power available to be intercepted by dust. Part of this power is absorbed and entirely reradiated mostly isotropically, the rest is reflected or transmitted. The absorbed fraction of the power intercepted by dust depends on wavelength and varies between 1 and 1/10 for wavelengths typical of starlight i.e. wavelengths smaller than $1\mu m$ (see Galliano, 2004 p.36).

2.4.2 Densities of power in various wavelength domains

In this section we will define surface densities of power corresponding to different IR domains to probe their relations with D_d.

We first examine surface density of power at different galacto-centric radii. These are luminosities divided by the physical galactic surface area equivalent to the pixel, expressed in $L_\odot.\mathrm{kpc}^{-2}$. We found in Giovanelli and Haynes (1994) that a realistic value of the ratio of dust to stellar scale height is 0.5. Thus assuming as we do that dust and stars are distributed inside the same disk with same thickness is only an approximation. Under this approximation, the surface density of luminosity for the dusty and stellar contents, can be compared at different radii.

We now focus on the following quantities:

- $D_\star$, density of power radiated by stars,
- D_x, density of power emitted by the galaxy in a wavelength range noted x (e.g. x =FIR).

We will define x's and all these densities in more details below.

First we define $D_\star = L_\star/S$ with S the physical surface of the pixel. We note that Skibba et al. (2012) used data between $0.15\mu m$ and $50\mu m$ to estimates the stellar luminosity as

$$L_\star = f_S \times L_{3.6\mu m},$$

with $f_S \in [100, 300]$ for Kingfish galaxies (see Skibba et al., 2012). These authors made the caveat that such a method introduces at least a 25% error because of the distribution of $L_\star/L_{3.6\mu m}$ inside each galaxies and between galaxies. We thus use the convenient relation

$$L_\star = 200 \times L_{3.6\mu m},$$

although we keep in mind that it is only an approximation.

We also compute $D_x = L_x/S$ with $L_x = \int_x L_\nu(\nu)\mathrm{d}\nu$ for different wavelength ranges noted x. We note that our numerical integration has a limited accuracy due to the fact that we use trapezoidal approximation for integration.

The different wavelength ranges, x, are listed below (wavelengths are given in μm):

- x=[3.6,8.0]: NIR+MIR ;
- x=[24,100]: warm dust ;
- x=[160,500]: cold dust.
- x=[5.8,500]: dust emission as defined by Skibba et al. (2012).

We also combine these to produce:

- x=[24,500]: FIR ;
- x=[3.6,500]: total infrared (TIR) ;

2.5 Stellar luminosity and stellar mass

Before going on, we wish to assess the link between the stellar luminosity $L_\star$ as quantified by Skibba et al. (2012), and the output parameter $M_{\star,fit}$. $M_{\star,fit}$ is a stellar mass estimate which depends on the global SED shape and supposes a 1 Gyr old stellar population. Even if most of the variations of $M_{\star,fit}$ are due to NIR-MIR surface brightnesses it is a bit influenced by surface brightnesses at longer wavelengths and thus varies from MIPS data series to PACS data series, whereas $L_\star$ does not. That is the reason why the link between $L_\star$ and $M_{\star,fit}$ is different in MIPS data series and PACS data series.

We now attempt a correlation between $M_{\star,fit}$ and $L_\star$, with $M_{\star,fit}$ in $M_\odot$ and $L_\star$ in $L_\odot$. We obtain for each galaxy a squared Pearson linear correlation coefficient, that we note r^2 as well as coefficients a and b such that

$$L_\star = b \times M_{\star,fit}^a \,.$$

We note that amid our 46 galaxies, only 12 galaxies in MIPS data series and 9 in PACS data series have $r^2 < 0.98$. These numbers become respectively 5 and 6 if we replace the condition $r^2 < 0.98$ by $r^2 < 0.90$. We also remark that 31 galaxies have $r^2 > 0.98$ in both MIPS and PACS data series. $L_\star$ seems thus reasonably well correlated with $M_{\star,fit}$, and as $L_\star$ is completely independent from our SED fitting procedure, we will henceforth explore in more details links between $M_d \times < U >$ and $L_\star$ rather than between $M_d \times < U >$ and $M_{\star,fit}$.

2.6 Links between emission at different wavelengths and power intercepted by dust

We investigate in this subsection whether the luminous power felt by dust collectively could be linked to the observed luminous output in different wavelength ranges.

Thus we attempt a linear correlation between logarithms of two surface densities of power seen as functions of the galacto-centric distance r. The first density of power is $D_d(r)$ further simply noted D_d.

The second density of power $D_x(r)$, simply noted D_x, is either of the following densities: D_{TIR} (noted D_T), $D_{NIR+MIR}$ (D_{N-M}), D_{FIR} (D_F), D_{warm} (D_w), D_{cold} (D_c), $D_{dust,skibba}$ ($D_{d,S}$). We refer to any of the previous densities as D_x.

Therefore all these correlations are refered to as $D_d - D_x$ correlations. They all result in relations

$$D_d(r) = b \times D_x(r)^a.$$

We plot on figure 2.11, the squared Pearson linear correlation coefficient obtained for these correlations. For galaxies whose squared Pearson coefficients are larger than 0.98 we show a coefficients on figure 2.12 (page 117) and b coefficients on figure 2.13 (page 118). We provide in figure 2.14 (page 119) the count of these galaxies fullfilling the condition $r^2 \geq 0.98$.

First we see on graph 2.11, that radial correlations $D_d - D_x$ are stronger in PACS data series than in MIPS data series. This may stem from MIPS data SEDs lacking the PACS $100\mu m$ point that is included in PACS data SEDs, as well as the more approximate estimate of $< U >$ extracted from MIPS data series as compared to PACS data series. These arguments point to somewhat more approximate results in MIPS data series as compared to PACS data series. We will come back to this point when examining $D_d - D_{warm}$ correlation.

We also remark that all correlations are close to linear with $a \in [1, 1.55]$ (see fig. 2.12). We remark that the most linear correlations are between D_d and D_{TIR}, $D_{NIR-MIR}$, D_{FIR}, D_{cold} whereas correlations between D_d and D_{warm}, $D_{d,S}$, $D_\star$ are more non-linear.

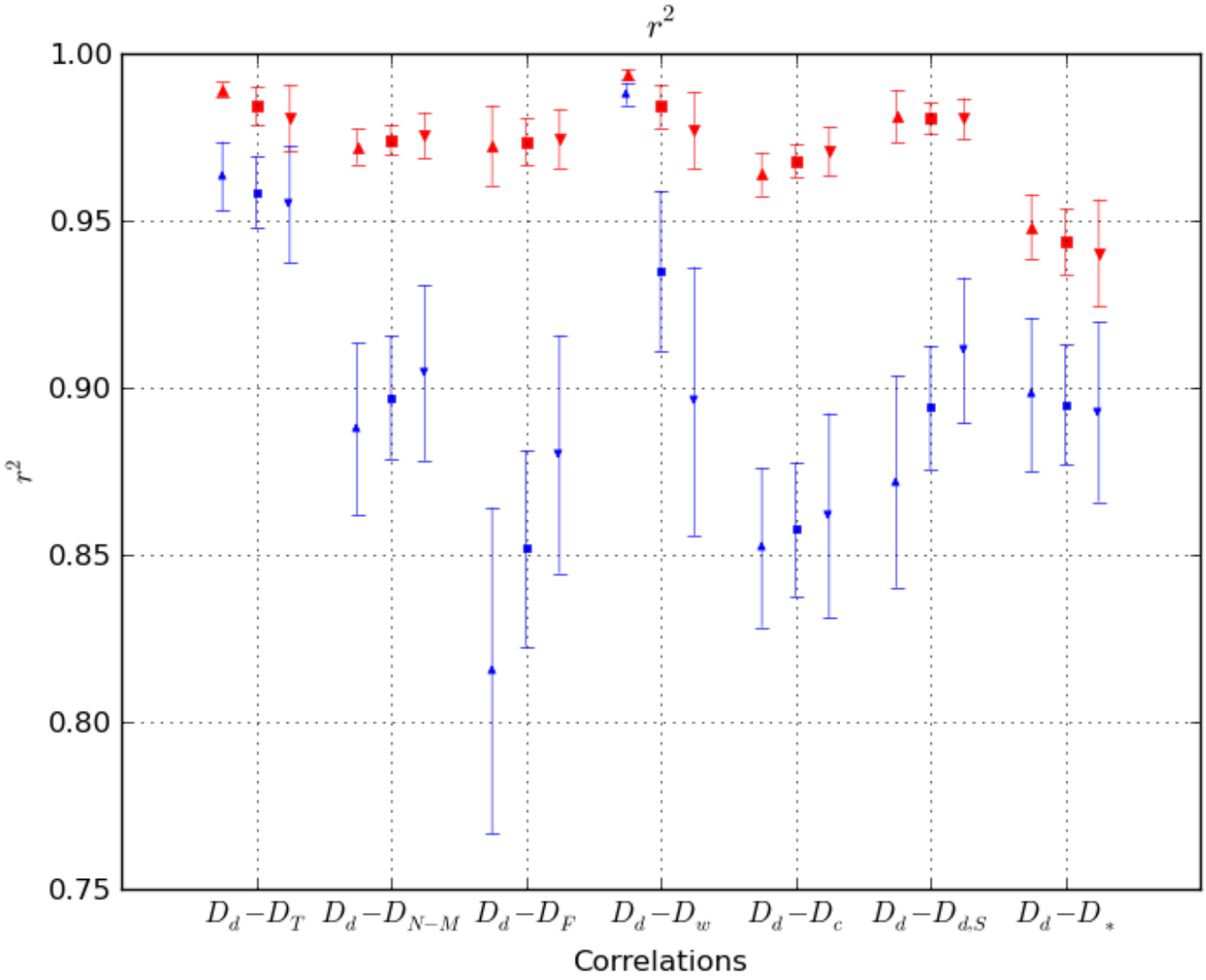

Figure 2.11: We give in this graph averages over all galaxies of squared Pearson correlation coefficients for linear regressions between logarithms of D_d and either: D_{TIR} noted D_T, $D_{NIR+MIR}$ noted D_{N-M}, D_{FIR} noted D_F, D_{warm} noted D_w, D_{cold} noted D_c, $D_{dust,skibba}$ noted $D_{d,S}$. The errorbars are the errors on the means. MIPS data series results are in blue and PACS data series in red. We show results for our complete sample of galaxy (squares), for the CDO sample (upward triangles) and the non CDO sample (downward triangle). We warn the reader that the ordinate scale is different from graph 2.9.

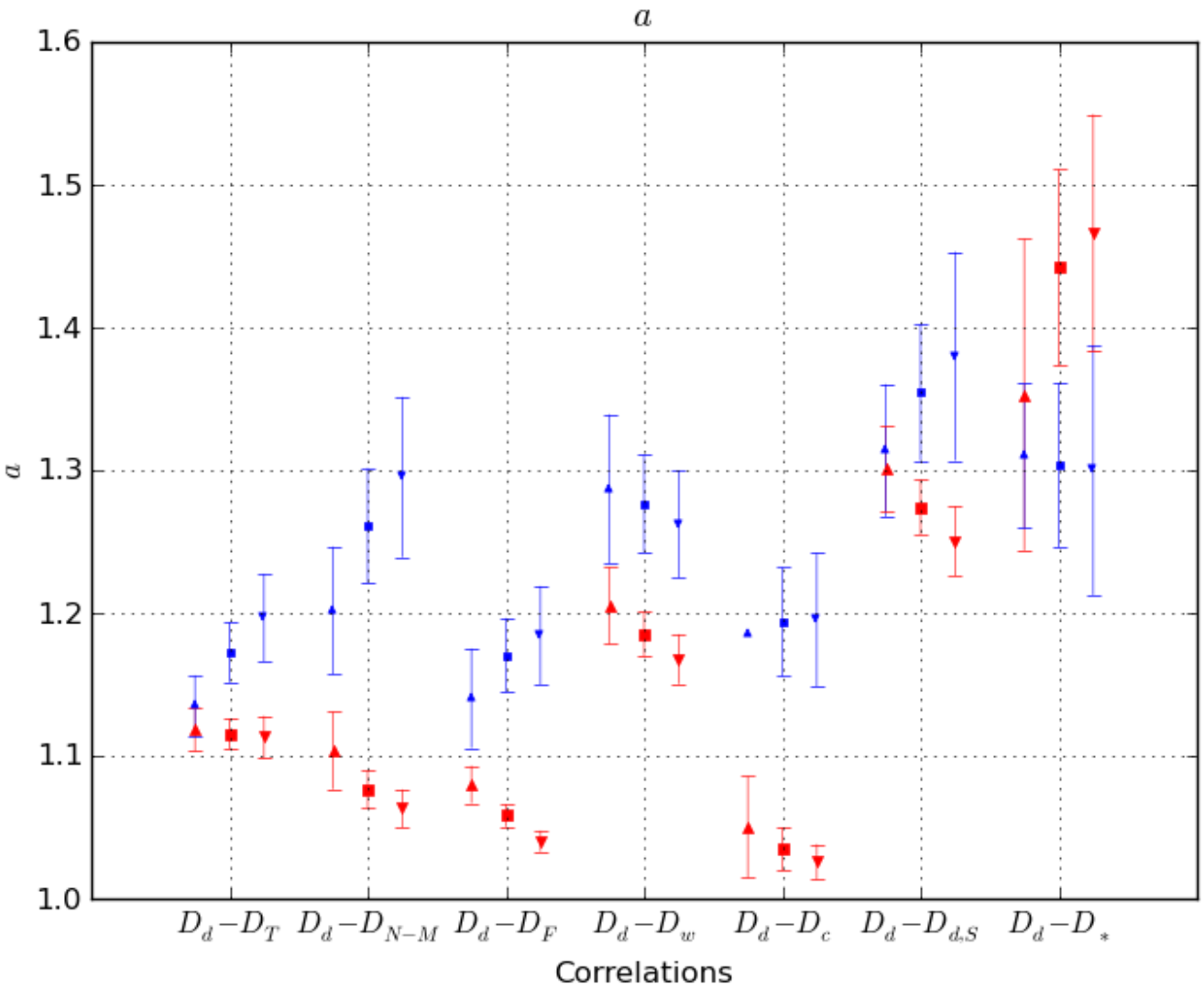

Figure 2.12: We give in this graph averages of a over all galaxies for which squared Pearson coefficient are higher than 0.98. We recall that these squared Pearson coefficient result from the linear regressions between logarithms of D_d and either: D_{TIR} noted D_T, $D_{NIR+MIR}$ noted D_{N-M}, D_{FIR} noted D_F, D_{warm} noted D_w, D_{cold} noted D_c, $D_{dust,skibba}$ noted $D_{d,S}$. We refer to any of the previous densities as D_x so that all these correlations are refered to as $D_d - D_x$ correlations. They all result in relations $D_d = b \times D_x^a$. The errorbars are the errors on the means. MIPS data series results are in blue and PACS data series in red. We show results for our complete sample of galaxy (squares), for the CDO sample (upward triangles) and the non CDO sample (downward triangle).

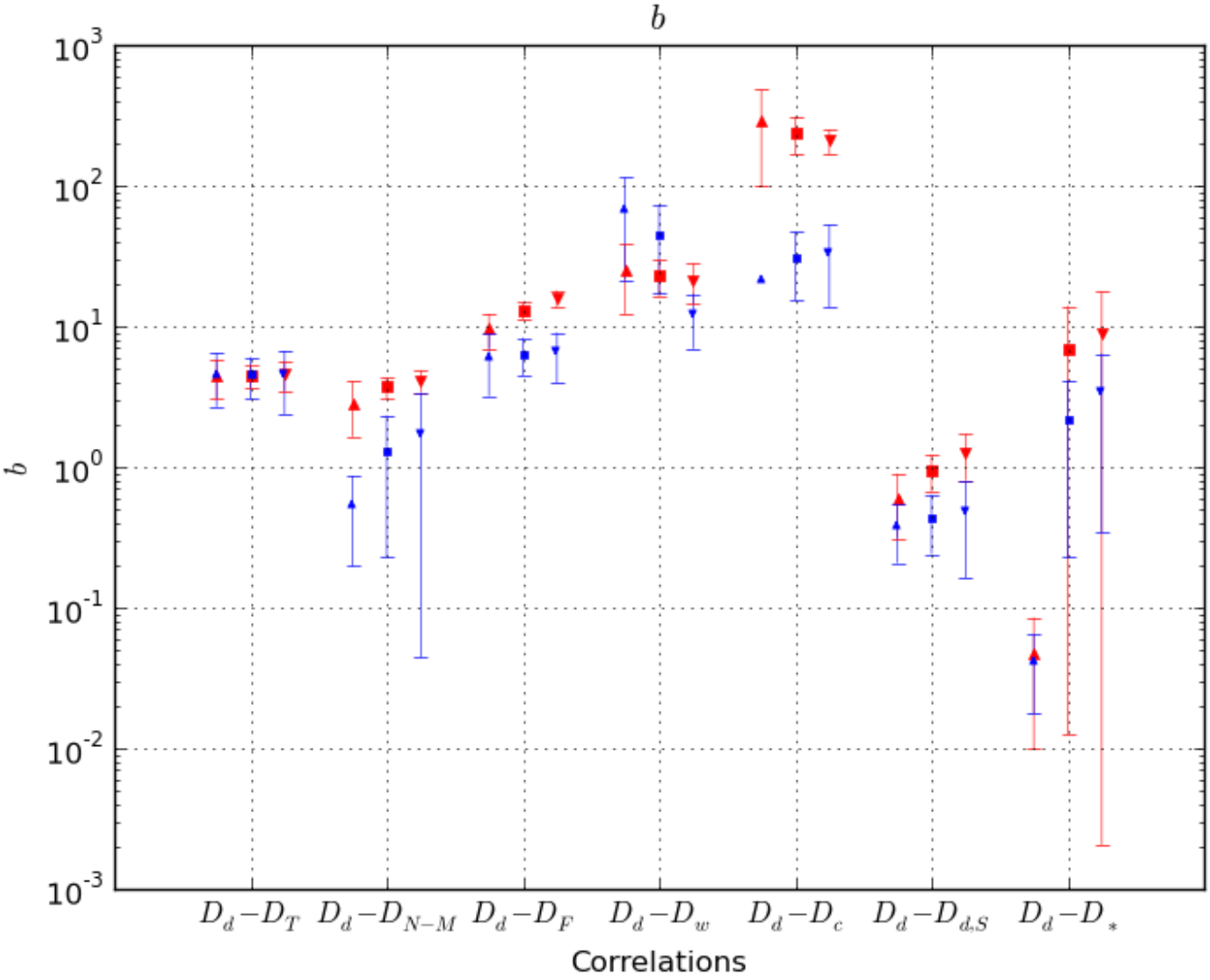

Figure 2.13: We give in this graph averages of b over all galaxies for which squared Pearson coefficient are higher than 0.98. We recall that these squared Pearson coefficient result from the linear regressions between logarithms of D_d and either: D_{TIR} noted D_T, $D_{NIR+MIR}$ noted D_{N-M}, D_{FIR} noted D_F, D_{warm} noted D_w, D_{cold} noted D_c, $D_{dust,skibba}$ noted $D_{d,S}$. We refer to any of the previous densities as D_x so that all these correlations are refered to as $D_d - D_x$ correlations. They all result in relations $D_d = b \times D_x^a$. The errorbars are the errors on the means. MIPS data series results are in blue and PACS data series in red. We show results for our complete sample of galaxy (squares), for the CDO sample (upward triangles) and the non CDO sample (downward triangle).

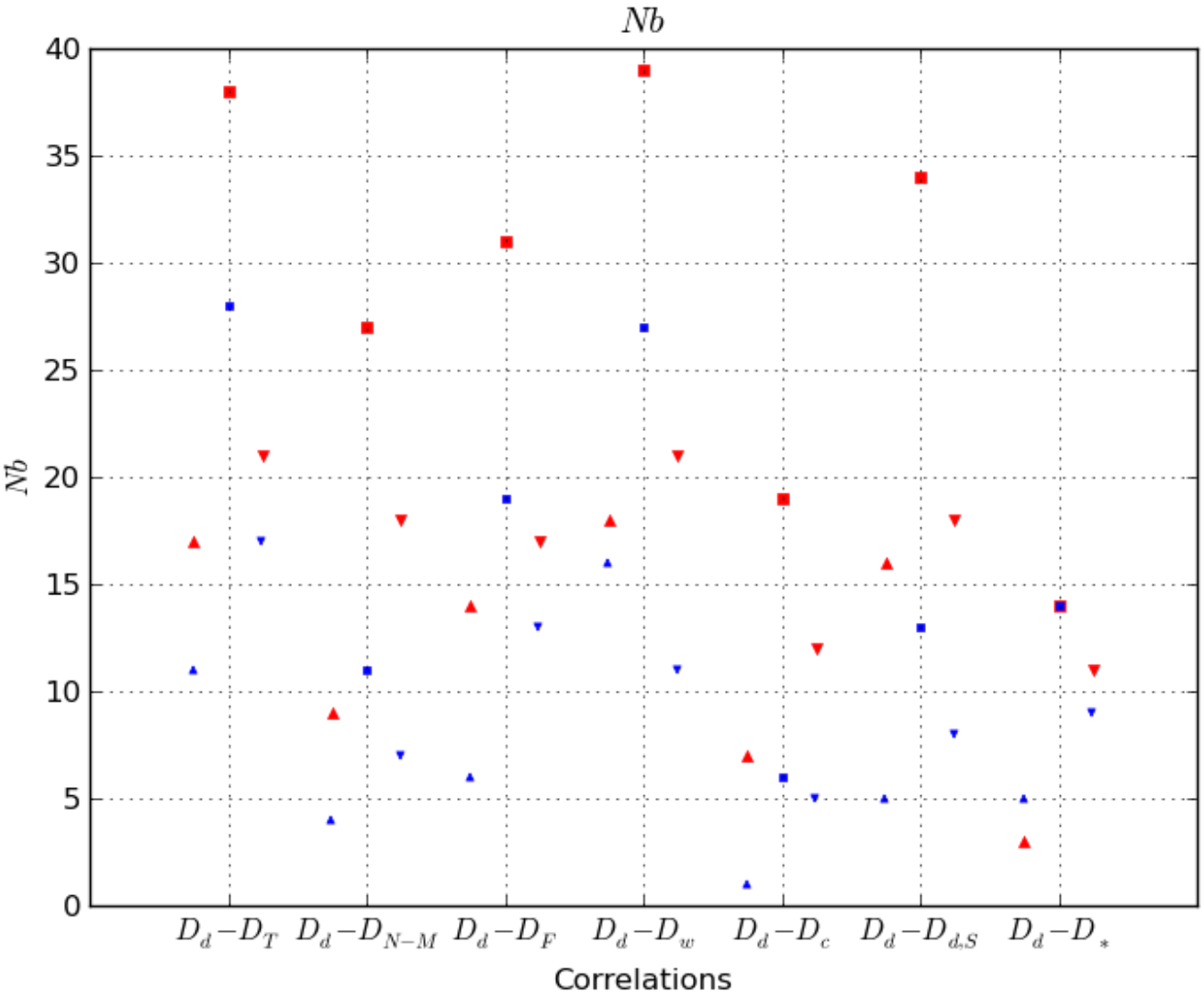

Figure 2.14: We give in this graph the number of galaxies for which squared Pearson coefficient are higher than 0.98. We recall that these squared Pearson coefficient result from the linear regressions between logarithms of D_d and either: D_{TIR} noted D_T, $D_{NIR+MIR}$ noted D_{N-M}, D_{FIR} noted D_F, D_{warm} noted D_w, D_{cold} noted D_c, $D_{dust,skibba}$ noted $D_{d,S}$. We refer to any of the previous densities as D_x so that all these correlations are refered to as $D_d - D_x$ correlations. They all result in relations $D_d = b \times D_x^a$. MIPS data series results are in blue and PACS data series in red. We show results for our complete sample of galaxy (squares), for the CDO sample (upward triangles) and the non CDO sample (downward triangle).

Our results showing b values between unity and a few hundred for all correlations except $D_d - D_\star$ as well as the power intercepted by dust D_d having values similar to the power emitted by dust according to Skibba et al. (2012) confort our interpretation of D_d and the neglect of dust absorption and especially its spectral dependence.

The ratio $D_d/D_\star$ seems much more dispersed than other ratios D_d/D_x (see figure 2.12). For this reason we will examine this ratio and try to understand it better in a subsequent section of this work, although we can already remark that D_d and other surface densities of power in dust dominated wavelength ranges are of a very different nature from $D_\star$.

We find that there is a squared Pearson coefficient (r^2) level above which are located almost all correlations in PACS data series and below which are located almost all correlations in MIPS data series. In more detail, all correlations in PACS data series fullfill the condition $r^2 \geq 0.95$ except $D_d - D_\star$. The only correlation in MIPS data series fullfilling $r^2 \geq 0.95$ is $D_d - D_{TIR}$ (for all galaxy subsamples) as well as $D_d - D_{warm}$ only for the CDO sample. These seem to support our previous conclusion that our results are more consistent in PACS data series than in MIPS data series.

We remark that none of the $D_d - D_\star$ correlations in any of the subsamples (CDO, total, non-CDO) fullfills the condition $r^2 \geq 0.95$. Actually the correlation $D_d - D_\star$ is the least stringent of all those presented in figure 2.11 in PACS data series. We warn that the ordinate scale is different in graphs 2.9 and 2.11 and $D_d - D_\star$ is nonetheless a stronger correlation than any of the three correlations, $M_d \times < U > - M_{\star,fit}$, $M_d - M_{\star,fit}$, $< U > - M_{\star,fit}$ shown in figure 2.9. We conclude that D_d is better correlated with $L_\star$ than with $M_{\star,fit}$ backing up the fact that the power intercepted by dust, D_d seems more related to the stellar luminous output than with the stellar mass.

As we can see on the r^2 graph 2.11, $D_d - D_{TIR}$ is one of the best correlations presented and thus we deduce that D_d is strongly related to D_{TIR}. This is backed up by the a quantities of this correlation found inside $[1.1, 1.2]$ for both data series and all subsamples, thus relatively close to unity resulting in a close to linear relation between D_{TIR} and D_d. This is also further supported by the b quantities for the $D_d - D_{TIR}$ relation (see fig. 2.13) found to be in almost perfect agreement between PACS and MIPS data series and also between all galaxy subsamples (total, CDO, non-CDO). We note that these b values are located in the 2-7 range. This means that if we neglect the difference between $a \approx 1.15$ and unity, the power dust could absorb based on its geometrical cross section is equivalent to 2-7 times as much as the power emitted by galaxies in the total infrared. This is compatible with the fact that dust emission is included in D_{TIR} while we did not include dust absorption in our calculation of D_d. Thus, as galaxies are not opaque and D_d represents the power intercepted, not the power absorbed by dust, D_d may be larger than D_{TIR}.

The r^2 graph 2.11 also shows that D_d is strongly related to D_{warm} in the CDO sample. This idea takes an unexpected turn as, when selecting only $r^2 \geq 0.98$, no important discrepancy is found for a or b values between CDO, total and non-CDO sample, and we find that the total number of galaxies exhibiting $r^2 \geq 0.98$ for this correlation is actually the highest for PACS data series and the second highest after $D_d - D_{TIR}$ for MIPS data series. Thus in galaxies where dust intercepted power is well traced by warm dust emitted power, the link between these two quantities seems rather independent from the presence of a dust disk.

Conclusion

We find that the product between the dust mass and the ISRF to which dust is subjected, $M_d \times < U >$, is proportionnal to the power geometrically intercepted by dust without taking absorption into account. This latter quantity is correlated with the total IR luminous output, the relationship between the two being close to linear.

The power intercepted by dust is very well correlated with the dust emitted power as estimated by Skibba et al. (2012), although the relation between the two is non-linear in the sense that the power intercepted by dust increases more rapidly than the power emitted by dust. This last fact speaks in favor of a slightly lower absorption of power by dust in higher radiation fields.

We note that the trend between D_d and $D_\star$ could have been foreseen from the results of Skibba et al. (2012). These authors found that L_{dust}/M_{dust} is better correlated with T, the temperature of cold dust grains, than L_{dust} alone. This is very consistent with our findings as the power intercepted by dust D_d has values a factor of a few larger than the total energy emitted by the dust phase, i.e. $D_d \propto L_{dust}/S$. In turn this factor could be entirely due to absorption, varying between 1 and 1/10 in ISRF with different stellar population distributions.

We find that D_d is well correlated with L_{dust}/S and thus $< U > \propto D_d/M_{dust} \propto L_{dust}/M_{dust} \propto < T^6 >$ with T the dust grain temperature.

Furthermore D_d combines M_d and $< U >$. M_d is the dust mass which is well represented by the bulk of the dust mass, and $< U >$ is the most probable value of the radiation field heating the bulk of the dust mass (because it is estimated as an integral over the dust mass distribution). Thus the most massive component of dust which is also the cold component, has an important weight in D_d. We remark that the apparent disconnection between cold dust temperature and heating sources was already hinted at by Galametz et al. (2012). We claim that a possible connection between cold dust emission and heating sources can be recovered at least through the power collectively intercepted by dust, D_d, as we find that it is correlated across galactic disks with heating sources, i.e. the total stellar content represented by $D_\star$ extrapolated from the old stellar luminous output.

We acknowledge that a crucial point that still needs to be more precisely understood is the dust mass distribution inside galaxies, especially the dust to gas ratio. The understanding of the origin of this dust mass distribution goes well beyond the scope of this thesis and we thus refer the reader to Mattsson and Andersen (2012) and Mattsson et al. (2012) for further details on this subject. We will however investigate how surface mass densities behaves w.r.t. stellar surface densities inside this chapter in a later section.

2.7 Power intercepted by dust against stellar surface density of power

In this section we come back to the correlation of D_d with $D_\star$. We recall that we obtained a relatively good correlation $D_d = b \times D_\star^a$ with average squared Pearson coefficients larger than 0.88 for MIPS data series, and larger than 0.93 for PACS data series. However a values obtained in these correlations were relatively larger than unity ($a > 1.3$) meaning that this correlation is not universal, and that b values could not be used as estimates of $D_d/D_\star$. As this latter ratio is linking dust intercepted power to the power provided by stars it is meaningful, and thus we analyze it in more detail in this section.

We find that the D_d quantity follows radial trends remarkably similar to those of $D_\star$ inside all galaxies in our sample. We give the characteristic example of NGC0337 on the graph 2.15. It shows that $L_\star$ varies over two order of magnitude in the whole galactic disk whereas the dynamic range of variation of $D_d/D_\star$ is smaller than one order of magnitude.

Even after taking into account radial variations of $D_d/D_\star$ and binning galaxies in groups of 4 to 6 in fig. 2.16, $D_d/D_\star$ is associated with a typical error on the mean of ~ 2 for each bin.

Thus we attempt correlations between this latter ratio and global galactic properties. The table 2.3 gives our results and we show related graphs in figures 2.16, 2.17. We also plot in graph 2.19 the variations of $D_d/D_\star$ with morphological stage and in SA, SB galaxies. In these

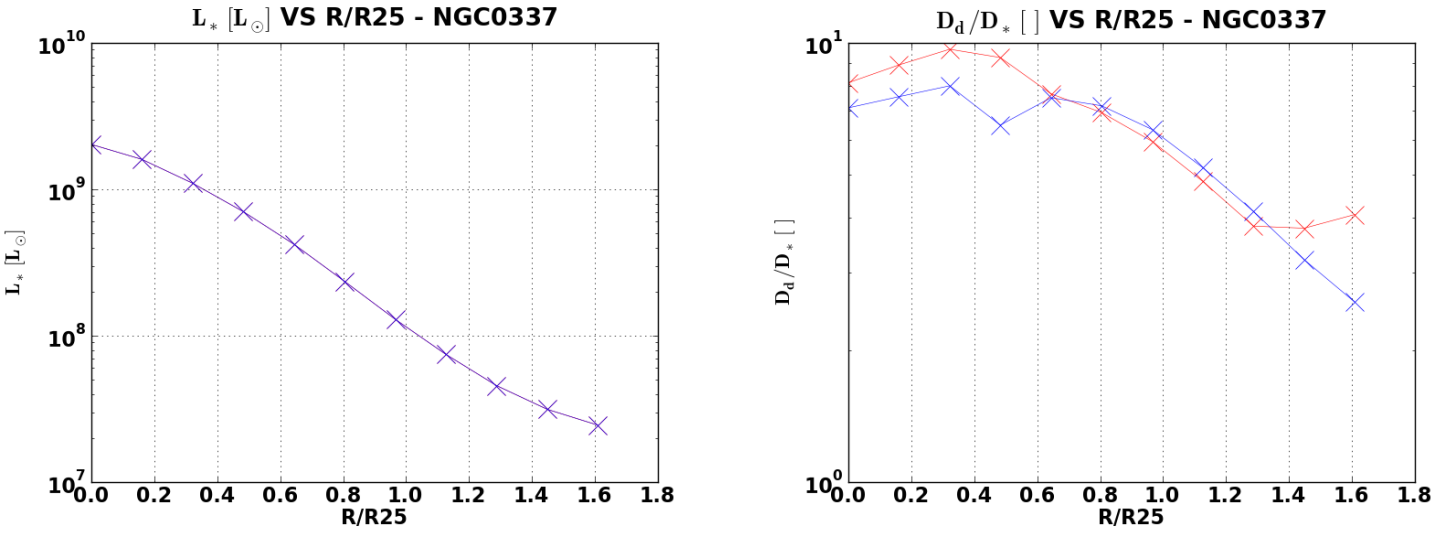

Figure 2.15: We give in these graphs for NGC0337, the stellar luminosity $L_\star$ as a function of radius in units of R25, as estimated by Skibba et al. (2012) as well as the ratio $D_d/D_\star$ of the energy geometrically intercepted by dust (without taking absorption into account) divided by the energy emitted by stars also seen as a function of radius in units of R25.

graphs each plotted $D_d/D_\star$ value is an average for a number N_{gal} of galaxies. Thus errorbars in these graphs are error on the mean, noted $\sigma_m(D_d/D_\star)$, in the sense:

$$\sigma_m\left(D_d/D_\star\right) = \frac{1}{N_{gal}} \times \sqrt{\sum_i^{N_{gal}} VAR_i\left(D_d/D_\star\right)}$$

with $VAR_i\left(D_d/D_\star\right)$ the variance associated with radial variations of $D_d/D_\star$ in the i^{th} galaxy. We make here the caveat that these errors on the mean are not only due to fitting errors and noise associated with the background signal, but probably also include dispersion associated with the mean value due to physical variations.

We also warn that errors on each physical property P in figures 2.16, 2.17 do not take into account measurement errors and are computed as :

$$\sigma_m\left(P\right) = \frac{\sqrt{VAR_{N_{gal}}\left(P\right)}}{\sqrt{N_{gal}}}$$

for each bin containing N_{gal} galaxies with $VAR_{N_{gal}}\left(P\right)$ the variance of P in the bin. These errors on the mean are also due to physical dispersions of the property P.

We first recall that $D_\star$ is an estimator of the stellar luminous output, i.e. the source of heating inside disk galaxies. D_d is the power intercepted by dust, non-linearly correlated with $D_\star$, a little more linearly correlated with the warm dust luminous output in the majority of our total sample, and even more linearly correlated with the TIR luminous output in all our total sample. Thus we also remind that $D_d/D_\star$ values can physically be larger than one because D_d does not take into account the dust absorption or equivalently because of starlight reflection and diffusion.

We find that the strongest correlation presented in this section is $D_d/D_\star - SFR$. We could possibly interpret the $D_d/D_\star - SFR$ correlation as showing that star formation is mainly seen in

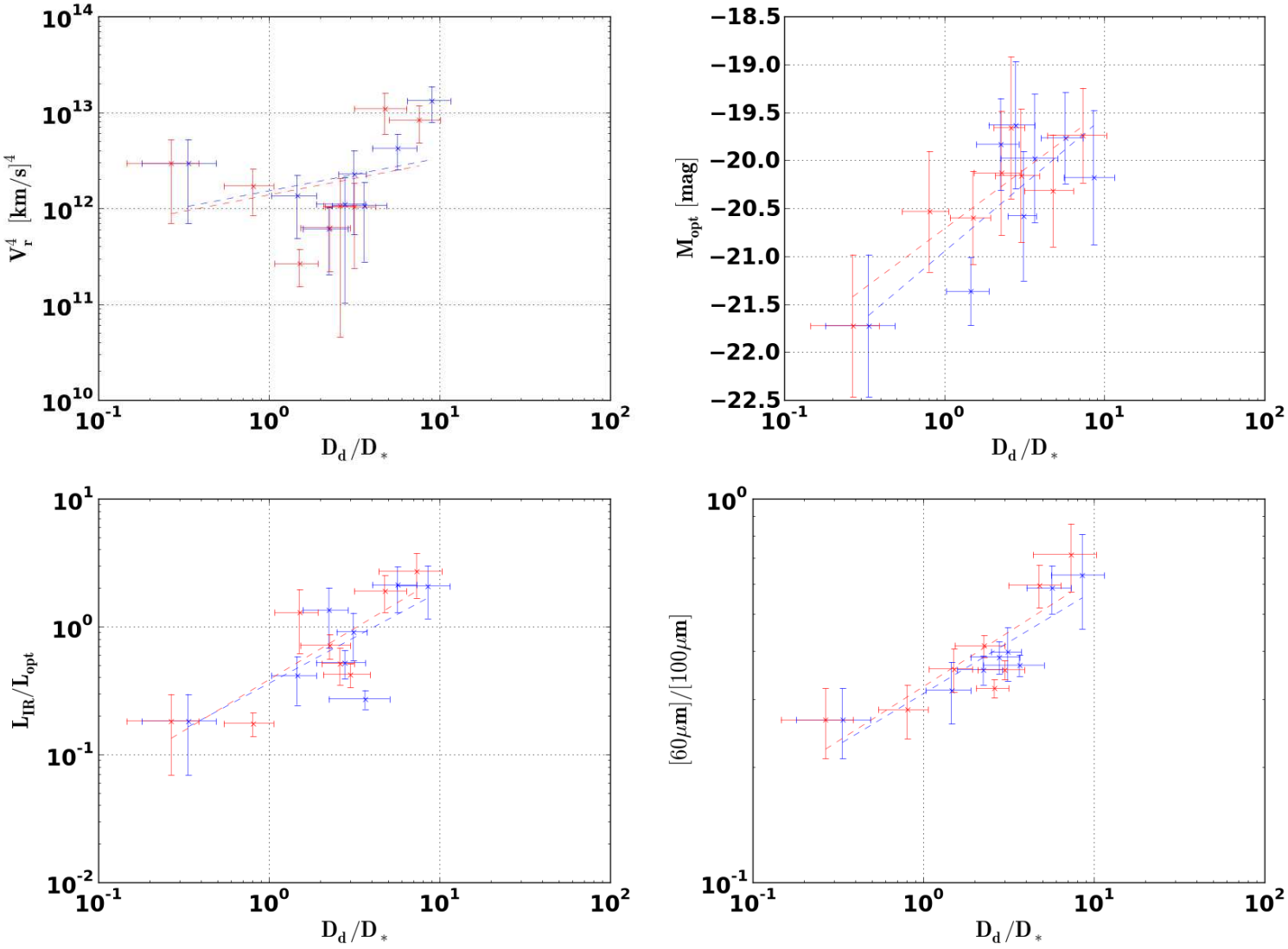

Figure 2.16: We give in these figures plots of correlations between global galactic properties and $D_d/D_\star$. For more statistical relevance we stacked galactic values of $D_d/D_\star$ 6 by 6 in increasing order. The smallest bin of $D_d/D_\star$ only includes 4 galaxies. In reading order ordinates are parameters available on Kingfish official website: maximum rotational velocity of the galaxy $V_r^4\,[km.s^{-1}]^4$, total optical absolute magnitude $M_{opt}\,[mag]$, infrared over optical global luminosity ratio L_{IR}/L_{Opt}, global colour $[60\mu m]/[100\mu m]$.

	MIPS data series			PACS data series		
y	a	b	r^2	a	b	r^2
$V_r^4\,[km/s]^4$	3.412e-01	1.515e+12	0.121	3.432e-01	1.374e+12	0.082
$log(M_{H,tot})\,[M_\odot]$	1.932e-01	9.418e+00	0.442	2.328e-01	9.453e+00	0.682
L_{IR}/L_{Opt}	7.172e-01	3.589e-01	0.58	8.002e-01	3.833e-01	0.677
$M_{opt}\,[mag]$	6.115e-01	-2.095e+01	0.591	5.376e-01	-2.072e+01	0.757
$[60\mu m]/[100\mu m]$	2.681e-01	3.101e-01	0.808	2.843e-01	3.234e-01	0.72
$SFR\,[M_\odot.yr^{-1}]$	6.485e-01	5.990e-01	0.797	6.130e-01	7.300e-01	0.865

Table 2.3: In this table are shown outputs from attempted correlations between galactic properties and $D_d/D_\star$. All these correlations are of the form $y = b \times x^a$ with y given in the table and $x = D_d/D_\star$, except for $y \in \{M_{opt}, log(M_{H,tot})\}$ for which $y = a \times ln(x) + b$.

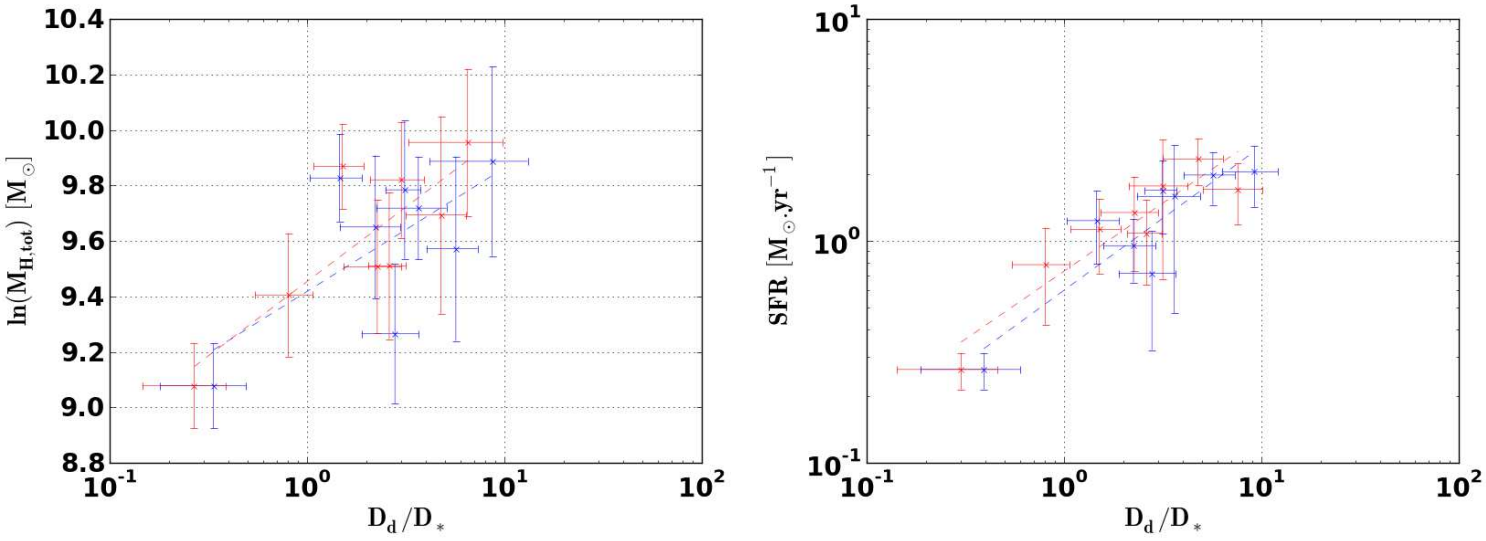

Figure 2.17: We give in these figures plots of our correlations between global galactic properties and $D_d/D_\star$. For more statistical relevance we stacked galactic values of $D_d/D_\star$ 6 by 6 in increasing order. The smallest bin of $D_d/D_\star$ only includes 4 galaxies. In reading order ordinates are the logarithm of the galaxy total atomic gas mass $log(M_{H,tot})\,[M_\odot]$ and global star formation rate $SFR\,[M_\odot.yr^{-1}]$ as available on Kingfish official website.

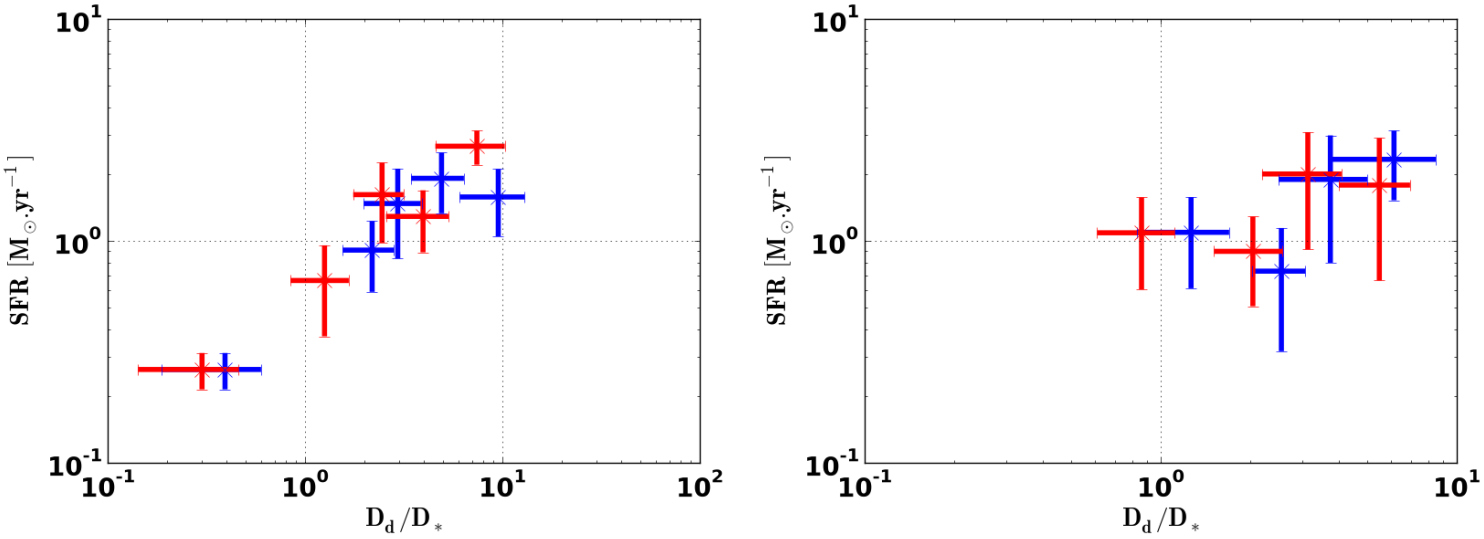

Figure 2.18: We give in these figures plots of global galactic SFR and $D_d/D_\star$ for non CDO galaxies (left) and CDO galaxies (right). For more statistical relevance we stacked galactic values of $D_d/D_\star$ 6 by 6 in increasing order. The smallest bin of $D_d/D_\star$ only includes 4 galaxies.

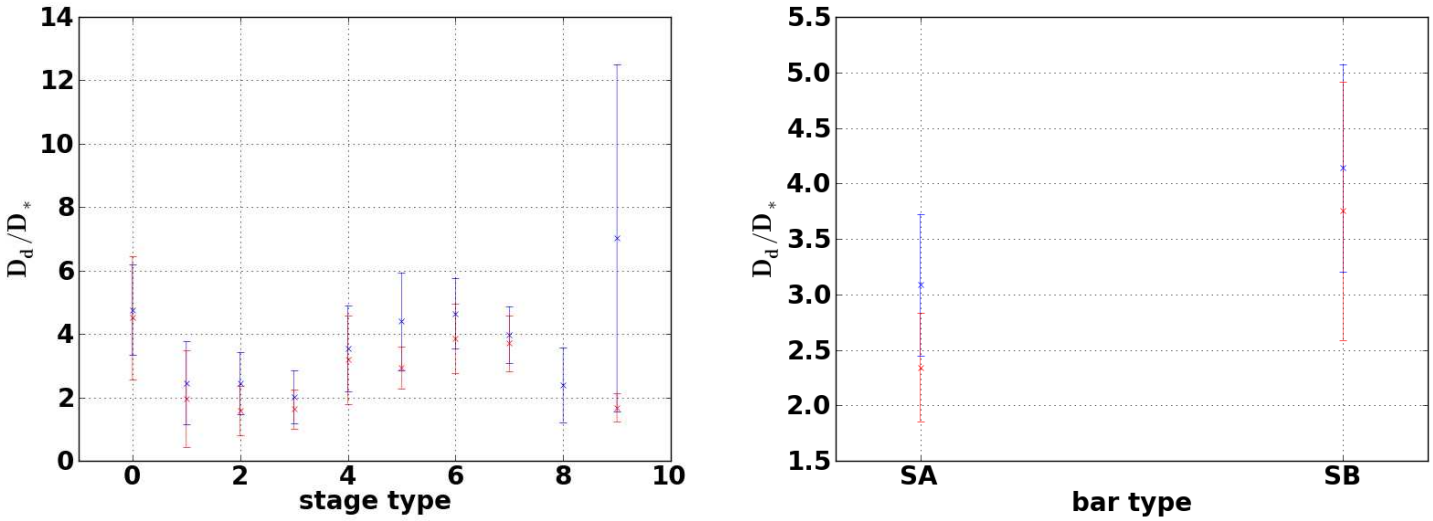

Figure 2.19: We give in this graph averages of $D_d/D_\star$ per bin of stage type as well as for SA and SB galaxies. We do not show results for S0 as the role of bars in S0 galaxies is still unclear with respect to its role in spiral galaxies. We did not show SAB galaxies either to offer a more striking comparison between strongly barred galaxies and non barred galaxies. The errorbars are the errors on the mean.

galaxies where dust intercepts a significant quantity of the stellar luminosity, whereas when dust intercepts less energy as compared to what is emitted by stars, there is much less star formation. It shows that the presence of dust is clearly connected to star formation. We also find that this correlation is sublinear ($a \approx 0.65 - 0.61$ for MIPS and PACS data series) meaning that the quantity of stellar power intercepted by dust increases by much when the global galactic star formation rate increases only a little. There is no contradiction between $D_d/D_\star$ being correlated with the total SFR and not correlated with the total mass of atomic hydrogen (see below). This could be justified by the Schmidt-Kennicutt law involving the total gas surface density (atomic and molecular) on the first hand, and surface density of star formation on the second hand. However it is known that the surface density of atomic hydrogen bears very tenuous relation with the surface density of star formation as shown by Kennicutt (2008).

By distinguishing between CDO and non CDO galaxies, we obtain that the flux intercepted by dust divided by the stellar flux seems more correlated to SFR and thus to young stellar populations flux in non CDO galaxies (see left figure 2.18) whereas this trend is rather less conspicuous in CDO galaxies (see right figure 2.18). This could be interpreted as follows: we know that young stars may be distributed in structures strikingly differing from the general old stellar disk (e.g. spiral arms). As in non CDO galaxies, dust is too seemingly inside structures differing from the disk, dust may well be more heated by young stars in non CDO galaxies as compared to CDO galaxies. In CDO galaxies, we showed that isophotes of dust maps are prominently associated with the old stellar disks thus it seems reasonable to obtain a weaker link between young stellar populations and dust heating in CDO galaxies.

Turning to graphs 2.19 we observe an increase of the quantity of stellar power intercepted by dust from stage type 3 to 6. Stage types 3-4 corresponds to types where Muñoz-Mateos (2009) found the highest dust surface densities. Thus we point that the galaxies where dust intercepts the largest quantity of stellar power are seemingly not the same as those presenting the highest surface densities of dust. This is possibly because later type galaxies have more dust enshrouded stars. We also warn that stage type 8 is only represented by one galaxy (NGC4236) thus our graph has a very poor statistical signifiance in this bin. We also remark that dust intercepts a larger quantity of stellar power in galaxies with a strong bar.

The good $D_d/D_\star - SFR$ correlation may partly explain why the color $[60\mu m]/[100\mu m]$ is well correlated with $D_d/D_\star$. $[60\mu m]/[100\mu m]$ increases when dust is warmer. This color ratio is known to be a qualitative tracer of star formation as in the local universe star formation occurs in places where dust abounds, and star forming regions have enhanced proportions of young massive stars which are fierce dust heating sources. We have seen that D_d is well correlated with the surface density of power emitted by warm dust. We could possibly interpret this relatively strong $D_d/D_\star - [60\mu m]/[100\mu m]$ correlation as the sign that when dust intercepts a larger quantity of the stellar emitted luminosity, dust is warmer.

We find that in more luminous galaxies $D_d/D_\star$ is smaller. This could be understood if there is a process to destroy dust or to at least impede dust interception of the stellar power in more luminous galaxies. This is very consistent with Mattsson and Andersen (2012) finding that dust grows more rapidly in galaxies less luminous in visible light. The a fitted for this correlation ($a \approx 6.1 - 5.4$ for MIPS and PACS data series respectively), also show that $D_d/D_\star$ decreases faster than the galactic luminosity increases, i.e. the process impeding dust interception of stellar power in more luminous galaxies is non-linear.

We see that on average $D_d/D_\star$ increases with increasing L_{IR}/L_{OPT}. This correlation is interesting because it is a globally estimated ratio, whereas $D_d/D_\star$ is locally estimated. This correlation is rather expected because D_d is locally well correlated with TIR emission thus with L_{IR}/S_{gal} with S_{gal} the galactic surface and $D_\star$ is estimating the luminous output of stars which in reality encompasses as well NIR surface brightness, optical surface brightness, which is

L_{OPT}/S_{gal}, and UV surface brightness. Interestingly we find that the $D_d/D_\star - L_{IR}/L_{OPT}$ is not so strong in the sense that $r^2 \approx 0.58 - 0.67$ respectively for MIPS and PACS data series, which are very low values of squared Pearson coefficient. To explain this we reckon that $D_\star$ is a NIR stellar luminosity tracer which could probably have difficulties to trace well the more hotter and younger stellar population emitting in the optical. Thus turning around these arguments, as the average value of D_d across the galactic disk is probably close to L_{IR}/S_{gal}, the not so strong $D_d/D_\star - L_{IR}/L_{OPT}$ correlation probably means that $D_\star$ is rather different from L_{OPT}/S_{gal}. We however finds that this correlation as mild as it may be , is the most linear of all the correlations we present in this section with a a coefficient around 0.7-0.8.

We find a weaker correlation between $D_d/D_\star$ and the total atomic gas mass $M_{H,tot}$ with r^2 values of 0.442 and 0.682 respectively for MIPS and PACS data series. This not so strong correlation shows that the link between gas mass and the power intercepted by dust w.r.t. the power of stellar origin is relatively tenuous. We find that this correlation is associated with a power $a \approx 0.2$ making it sublinear and actually the most non-linear correlation presented in this section. This means that the ratio $D_d/D_\star$ increases with increasing gas mass but also that $D_d/D_\star$ increases much faster than the global atomic gas mass. It could be understandable if one admits the existence of a star formation threshold in terms of gas density, as, in this perspective, increasing a little the gas mass could dramatically increase the stellar mass which produces dust components, enhancing dust formation and therefore dust capability to intercept power of stellar origin. Such thresholds could also explain the presence of relatively abrupt slopes in dust mass radial profiles.

We note that using the Tully-Fisher relation and a relatively constant mass-to-light ratio observed inside nearby disk galaxies we obtain a link between the maximum rotationnal velocity V_r and stellar mass, such that $V_r^4 \propto M_\star$ (see van der Kruit and Freeman, 2011). Thus V_r^4 is a proxy for the total stellar mass. We see that the worst correlation obtained in this section is between V_r^4 and $D_d/D_\star$. Thus as the total stellar content is strongly linked to the galactic star formation history, this star formation history seems relatively independant from the quantity of power intercepted by dust w.r.t. the power of stellar origin.

2.8 Dust and stellar surface density

2.8.1 The Sersic profile

Mass and luminosity surface density radial profiles of galaxies are already modeled as Sersic profiles (see Dutton, 2009). Thus in this section we inspect dust and stellar mass surface densities S_m as quantified by Sersic profiles (see Graham and Colless, 1997):

$$S_m = S_{m,max} \times exp\left[-\left(R/R_e\right)^{1/n}\right] ,$$

with n the Sersic index, R_e the effective Sersic radius. A useful approximate relation that we will use, links the half mass radius $R_{1/2}$ (radius enclosing half of the mass) to R_e by the following formula:

$$R_{1/2} \approx R_e \times (2n - 1/3)^n$$

In the case of the exponential decrease, $n = 1$ and we recover

$$R_{1/2} \approx R_e \times 5/3$$

We compute that the mass enclosed inside this estimate of $R_{1/2}$ is around 0.4963 times the total mass. This total mass is obtained by integrating down to infinite radius an exponential

surface density profile. Thus in the case of an exponential profile we find an error of around 0.7%, giving an order of magnitude of the error we make by using the half mass radius approximate relation showed above.

We also warn that using Sersic profile is an approximation especially for dust surface densities which exhibit central holes in some galaxies.

To fit Sersic profiles on dust and stellar surface densities radial profiles we use the following technique: we first extract the maximum surface density of the entire radial profile, noted $S_{m,max}$ and we attempt linear correlations between S_m and R of the form

$$ln\left(-ln\left(\frac{S_m}{S_{m,max}}\right)\right) = A \times ln\,(R/R25) + B$$

We recover $n = 1/A$ and $R_e = e^{-B/A}$.

2.8.2 Size, shape and central level of surface density for stars and dust

We now discuss the results from Sersic fitting of mass surface density radial profiles, for dust and stars.

Examples of Sersic functions fitted on dust and stellar surface density profiles are given on figures 2.20. We see on these plots the example of the dust density profile of NGC0925 which cannot be well represented by a Sersic function as well as NGC 0628 and NGC 0337 whose dust density profiles can be relatively well represented by Sersic profiles. We also remark on these graphs that stellar and dust surface density profiles even when both can be represented by Sersic functions seem to exhibit different trends with galacto-centric radius.

We plot $1 - r^2$, with r^2 the squared Pearson coefficients for these fitting (see figure 2.21) along with the threshold from which Sersic fitting can be said acceptable, i.e. $r^2 = 0.80$ (below the pink line for stellar density profiles and left to the green line for dust density profiles). We also mark on this graph the global average values for MIPS (blue) and PACS (red) data series of $1 - r^2$ along with the associated error on the means. In the following we note r_d and r_* respectively the Pearson coefficients for Sersic fitting of dust and stellar radial surface density profiles.

We remark that these average values are well below the pink line for both MIPS and PACS data series. This means that on average Sersic fitting of stellar density profiles are acceptable, whereas the average values of $1 - r_d^2$ being close to the green line show that single Sersic profiles are much worse at describing dust density profiles. More precisely only 4-5 galaxies (resp. for PACS and MIPS data series) are really unsatisfactorily fitted by a Sersic profile (above the pink line), whereas around half of the dust density profiles (27 and 26 resp. for MIPS and PACS data series) are acceptably represented by Sersic profiles, the other half ranging from badly represented ($1 - r^2 \gtrsim 0.2$) to erroneous ($1 - r^2 \approx 1$).

We find in the upper panel of fig. 2.22 that the average value of r^2 either for stellar or dust surface densities does not change by selecting stage type later (top left fig. 2.22) or earlier than 5 (top right fig. 2.22). Thus for both of stellar and dust density profiles, we find no simple dependence of the quality of Sersic fitting with stage type.

We also observe in the lower panel of fig. 2.22 that SB galaxies (lower left graph of figure 2.22) have overall slightly higher $1 - r^2$ than SA galaxies (lower right graph of figure 2.22). This is especially conspicuous concerning $1 - r_d^2$ values, as there are more crosses left to the green line on the lower right graph of fig. 2.22 than on the lower left graph of fig. 2.22. It means that on average barred galaxies have smaller r_d^2 values than non barred galaxies and therefore have on average dust density profiles much less acceptably fitted by a single Sersic profile. This may be the sign that bars affect the dust density profiles so that they cannot be well respresented by a

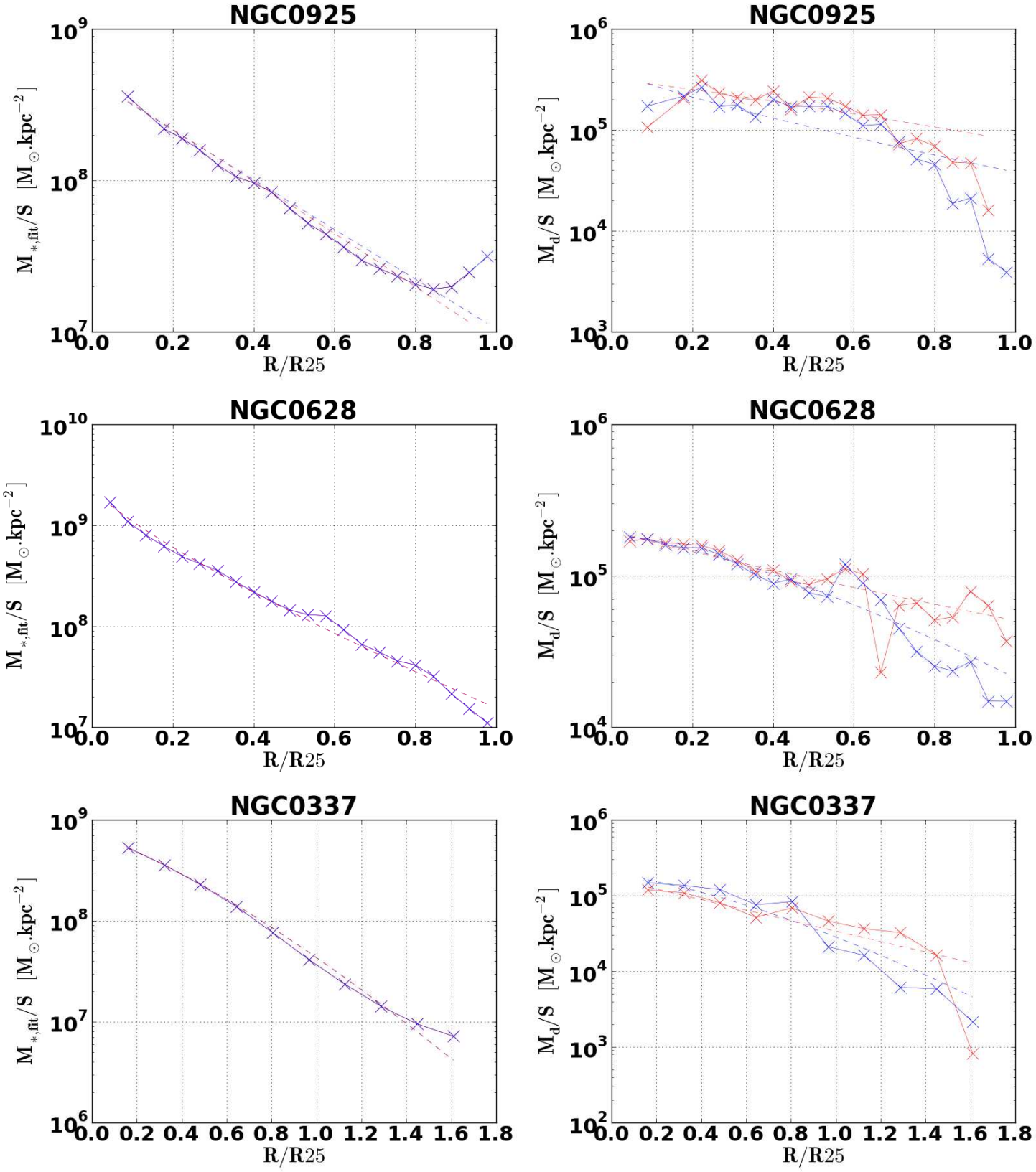

Figure 2.20: These are examples of Sersic fitting of stellar and dust surface density profiles. Values of r^2 are $(0.916, 0.84)_{\text{dust}}$ and $(0.997, 0.997)_{\text{stellar}}$ for dust and stellar surface density profiles in (MIPS,PACS) data series respectively for NGC 0337. For NGC0628 and NGC0925 squared Pearson coefficients are as follows: $(0.951,\ 0.848)_{\text{dust}}$, $(0.991,\ 0.991)_{\text{stellar}}$ and $(0.232,\ 0.589)_{\text{dust}}$, $(0.963,\ 0.977)_{\text{stellar}}$.

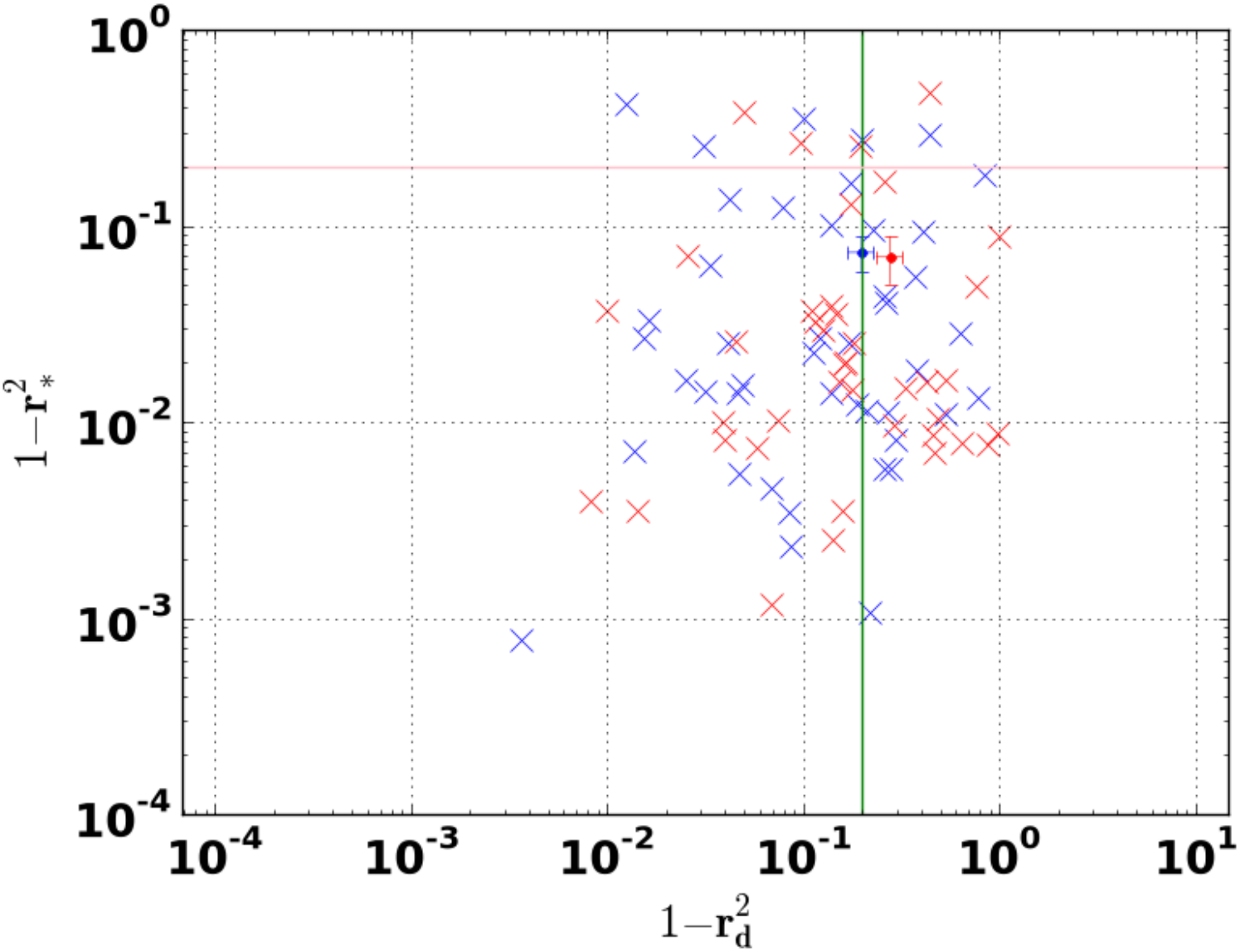

Figure 2.21: We give in this figure $1-r^2$ with r^2 the squared Pearson coefficient for Sersic fitting of stars ($1-r^2_*$, ordinates) and dust ($1-r^2_d$, absissa) surface densities. The dots associated with errorbars are the average values resp. for MIPS and PACS data series with the associated errors on the means. MIPS data series are in blue, PACS data series in red. Pink and green line show the level corresponding to $1-r^2 = 0.2$ resp. for stellar density profiles and dust density profiles.

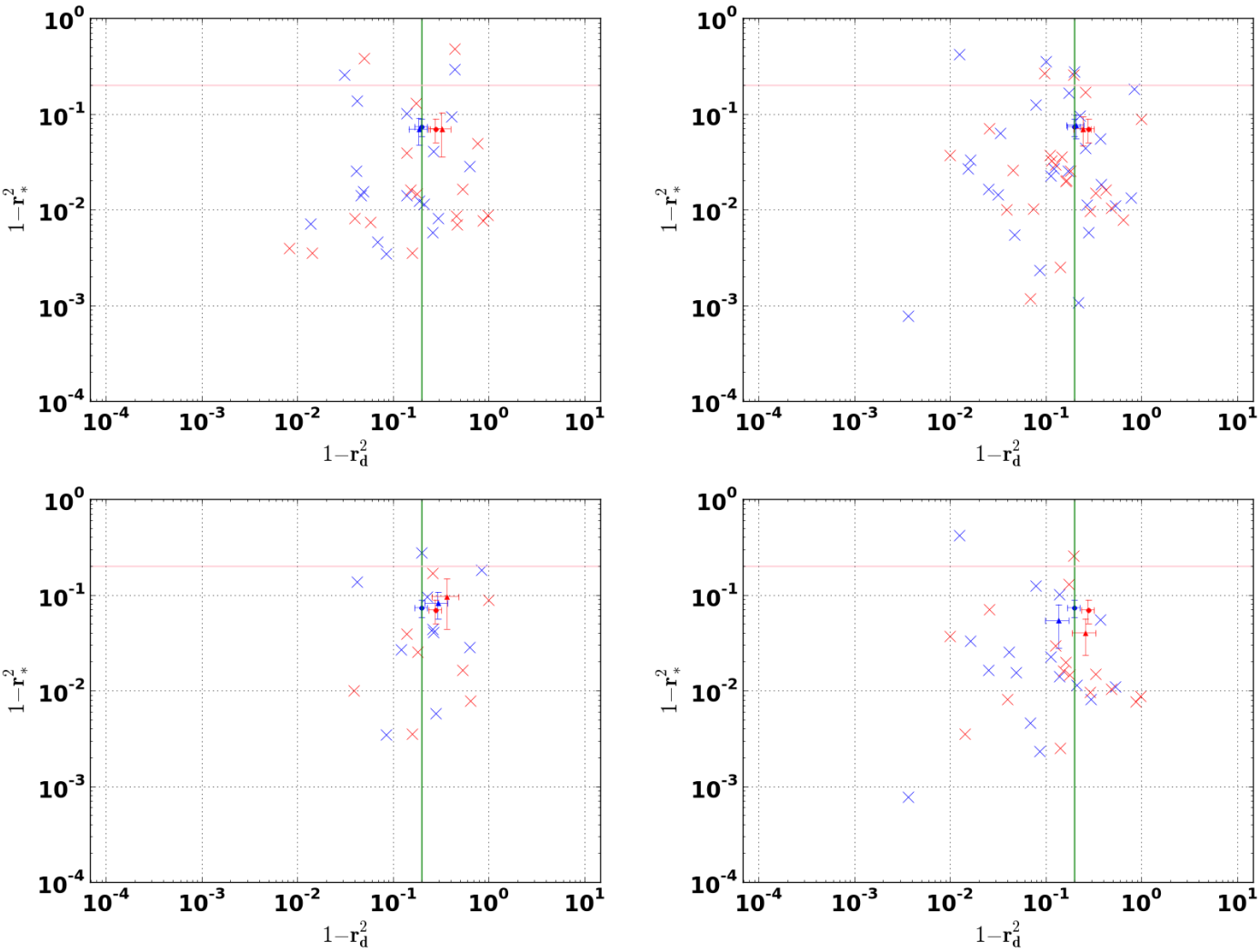

Figure 2.22: In reading order, we give in these figures $1 - r^2$ for galaxies with the following properties: stage types larger than or equal to 5 (top left), stage types smaller than 4 (top right), bar type SB (lower left), bar type SA (lower right). r^2 is the squared Pearson coefficient for Sersic fitting of stars ($1 - r_*^2$, ordinates) and dust ($1 - r_d^2$, absissa) surface densities. The total average and error on the mean is marked with a dot, whereas the average and error on the mean for galaxies with the hereabove mentionned specific properties is marked with a triangle. MIPS data series are in blue, PACS data series in red.

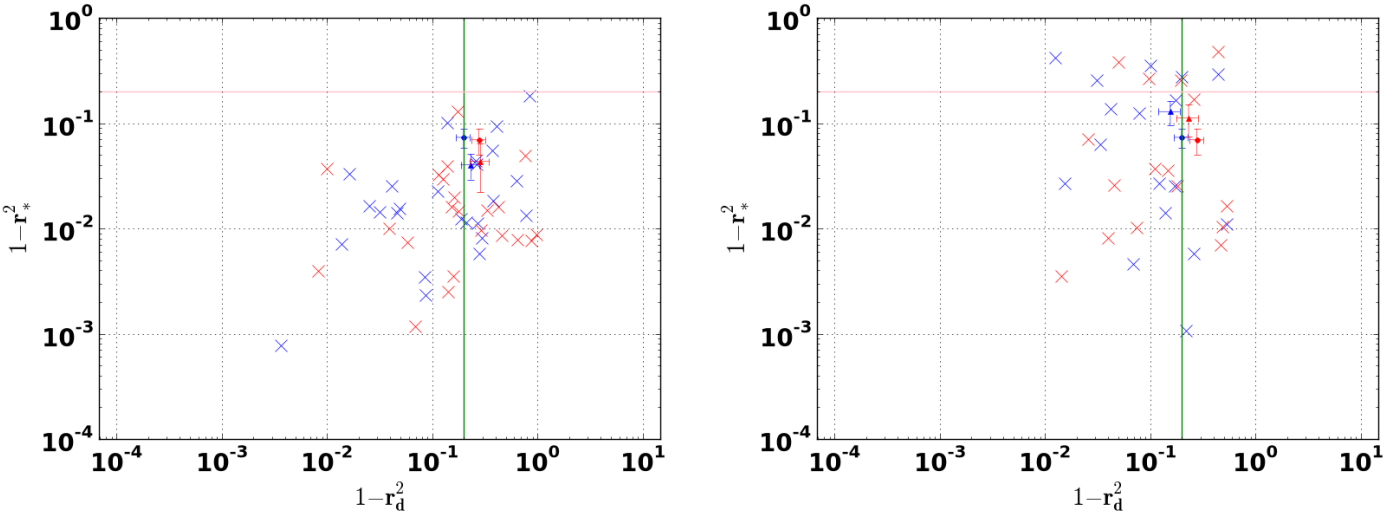

Figure 2.23: In reading order, we give in these figures $1 - r^2$ for galaxies with the following property: lower SFR than average (left) or higher SFR than average (right). r^2 is the squared Pearson coefficient for Sersic fitting of stars ($1-r_*^2$, ordinates) and dust ($1-r_d^2$, absissa) surface densities. The average SFR of our total galaxy sample is $1.36\,M_\odot/yr$. The total average and error on the mean is marked with a dot, whereas the average and error on the mean for galaxies with the hereabove mentionned specific properties is marked with a triangle. MIPS data series are in blue, PACS data series in red.

single Sersic profile, whereas the proportion of galaxies without bars having their dust density profiles acceptably well represented by a single Sersic profile is more important.

Even though this latter trend of r_d^2 with bar type seems only marginally significant with regards to our small galaxy sample, it is important in our study as only two barred galaxies (NGC0337, NGC1097) have both of their dust and stellar density profiles acceptably represented by a single Sersic function in all data series (r^2 values higher than 0.8 for Sersic fittings of both dust and stellar density profiles, in both MIPS and PACS data series ; more graphically in the lower left graph 2.22 only two couples of red and blue crosses are simultaneously on the left of the green line and below the pink line). Thus selecting only galaxies in which the stellar and dust density profiles are acceptably well fitted by a Sersic profile would almost remove all barred galaxies.

We remark that in figure 2.23 crosses seem shifted upward in the graph on the right as compared to the graph on the left. Thus we conclude that, although galaxies with higher SFR (right graph 2.23) seem to have stellar surface densities less well fitted by a single Sersic profile than average, their dust surface density profiles are as well fitted as average by a single Sersic profile. We conclude that the stellar surface density profiles of more star forming galaxies seem slightly more irregular than the ones of more quiescent galaxies, although this is not the case for their dust surface density profiles.

Interestingly this latter trend, for galaxies exhibiting better agreement between their stellar density profile and a Sersic profile, to have lower SFR, does not correspond to a broad morphological trend as stellar surface density profiles in galaxies of stage type later than 5, are not better or worse fitted by Sersic functions than the ones in galaxies of types earlier than 4.

However we know that SFR increases in later stage type galaxies (see Romanishin, 1990). This is acceptable because our galaxy sample is reduced and that the dispersion of SFR also

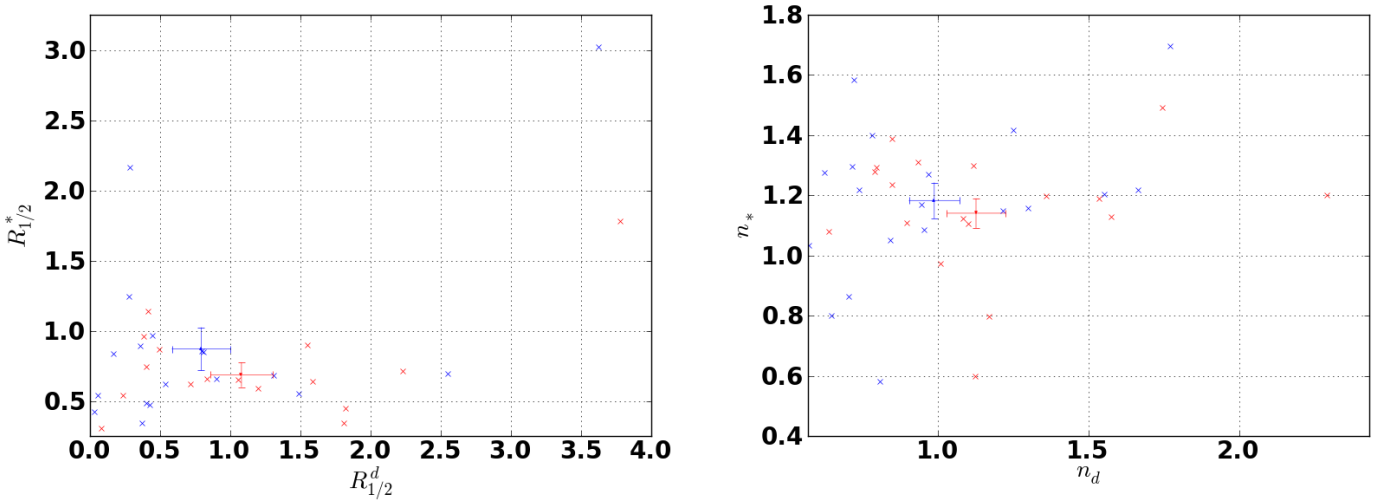

Figure 2.24: In reading order, we give in these figures $R_{1/2}$ in units of R25 (left picture) as well as n (right picture) for Sersic profiles of stellar (ordinates) and dust (absissa) surface densities in cases where the Sersic fitting procedure is acceptably successful , i.e. when $r^2 \geq 0.8$. We do not plot PACS data series results on the $R_{1/2}$ graph for NGC 3184 even though the Sersic fitting procedure is acceptably successful for this galaxy as, for NGC 3184, we find $R_{1/2,dust,PACS} = 21.7 \times R25$ whereas $R_{1/2,dust,MIPS} = 0.79 \times R25$. For this galaxy $R_{1/2,dust,MIPS}$ is more coherent with $R_{1/2,stars}$ which is found to be respectively 0.86 and 0.93 in units of R25 for MIPS and PACS data series. We find that this discrepancy between $R_{1/2,dust}$ in PACS and MIPS data series results from the low surface brightness discrepancy between MIPS and PACS measurements. This is surprisingly a case where MIPS data series seem to yield better results than PACS data series.

increases in later stage types.

2.8.3 Half mass radius and Sersic index

We plot on fig. 2.24 our results concerning half mass radii and Sersic indices in the 19 galaxies for which Sersic fitting of dust and stellar surface densities are acceptable ($r^2 \geq 0.80$ for Sersic fitting of both dust and stellar density profiles, in both MIPS and PACS data series). We note that the spread in both Sersic index and half mass radius distributions increases approximately twofold from stellar profiles to dust profiles.

On average we find that R25 is close to the radius enclosing half of either the dust and stellar mass (see left graph 2.24). But the spread of the distribution of $R_{1/2,d}$ is large, going all the way from $R_{1/2,d}/R25 < 0.1$ to $R_{1/2,d}/R25 > 3$ and beyond, with only NGC 3184 (not shown on the picture because the fitting of PACS data series is faulty) and NGC 4321 having $R_{1/2,d}/R25 > 3$. The spread of the distribution of $R_{1/2,\star}$ is smaller and many of the galaxies exhibit $R_{1/2,\star} \in [0.25, 1.30]$ with only two galaxies $R_{1/2,\star} \in [1.75, 3.10]$ (NGC 4321, NGC 7331). If we exclude the three data points most distant from the average we could consider that the obtained distribution is located close to $R_{1/2,\star} \in [0.25, 1.0]$ whereas $R_{1/2,d} \in [0.0, 1.75]$. With these comparisons we conclude that these two distributions are compatible in terms of average, the dust distribution being only larger. This is expected as R25 is a measurement of the size of galaxies extracted from a part of the spectrum where stars dominate the emission. We find that on average, over all galaxies, half of the dust mass is enclosed in a region of space similar to the one enclosing half of the stellar mass, but our results show a large variability between objects especially for dust profiles.

We see on graphs 2.25 that the radius enclosing half of the stellar mass $R_{1/2,\star}$ decreases in units of R25 from ~ 0.75 in galaxies with stage type earlier than 4 to ~ 0.5 in galaxies with stage type later than 5. A similar decrease from 1.1 to 0.6 is seen from galaxies having SFR higher than average to galaxies having SFR lower than average. This means the half stellar mass radius is comprised in a size similar to a constant surface brightness size such as R25 in early type galaxies (high surface brightness galaxies) or separately in high SFR galaxies (high luminosity galaxies), whereas in later type galaxies or low SFR galaxies half of the stellar mass is comprised in a smaller radius than R25.

Taking into account the errorbars on $R_{1/2,d}$, we see no variation of $R_{1/2,d}$ in units of R25 with stage or SFR. Thus our data are consistent with later type spiral galaxies having a larger fraction of their total stellar mass inside R25 than earlier type spiral galaxies, whereas around half of the total dust mass is inside R25 similarly for early and late type spirals.

Turning to Sersic indices (see right graph 2.24) we note that stellar density profiles exhibit Sersic indices $n_\star \in [0.55, 1.65]$. What is more, these stellar surface density Sersic indices are very often larger than 1, thus stellar density profiles decrease more rapidly on average than exponential density profiles. This is probably because we include in the profile inner galactic regions which are known to be more concentrated than exponential (e.g. the stellar bulge). However on average Sersic indices for dust surface densities are relatively close to exponential although the dispersion in Sersic index is large for dust with $n_d \in [0.5, 1.75]$ (except for NGC3184 which has $n_d \approx 2.5$ in PACS data series whereas for this galaxy $n_d \approx 0.94$ in MIPS data series).

We plot in figure 2.26 the relations between Sersic index for dust and stellar surface densities and note the interesting trend: the stellar Sersic index is lower separately in galaxies with type later than 5 as compared to earlier than 4, and in galaxies with lower SFR than average as compared to galaxies with higher SFR than average. This hints at more quiescent galaxies having global stellar density profiles closer to exponential than more star forming galaxies which are seen to exhibit on average stellar surface density profiles decreasing more rapidly than exponential. Similarly later types seem to have global stellar density profiles closer to

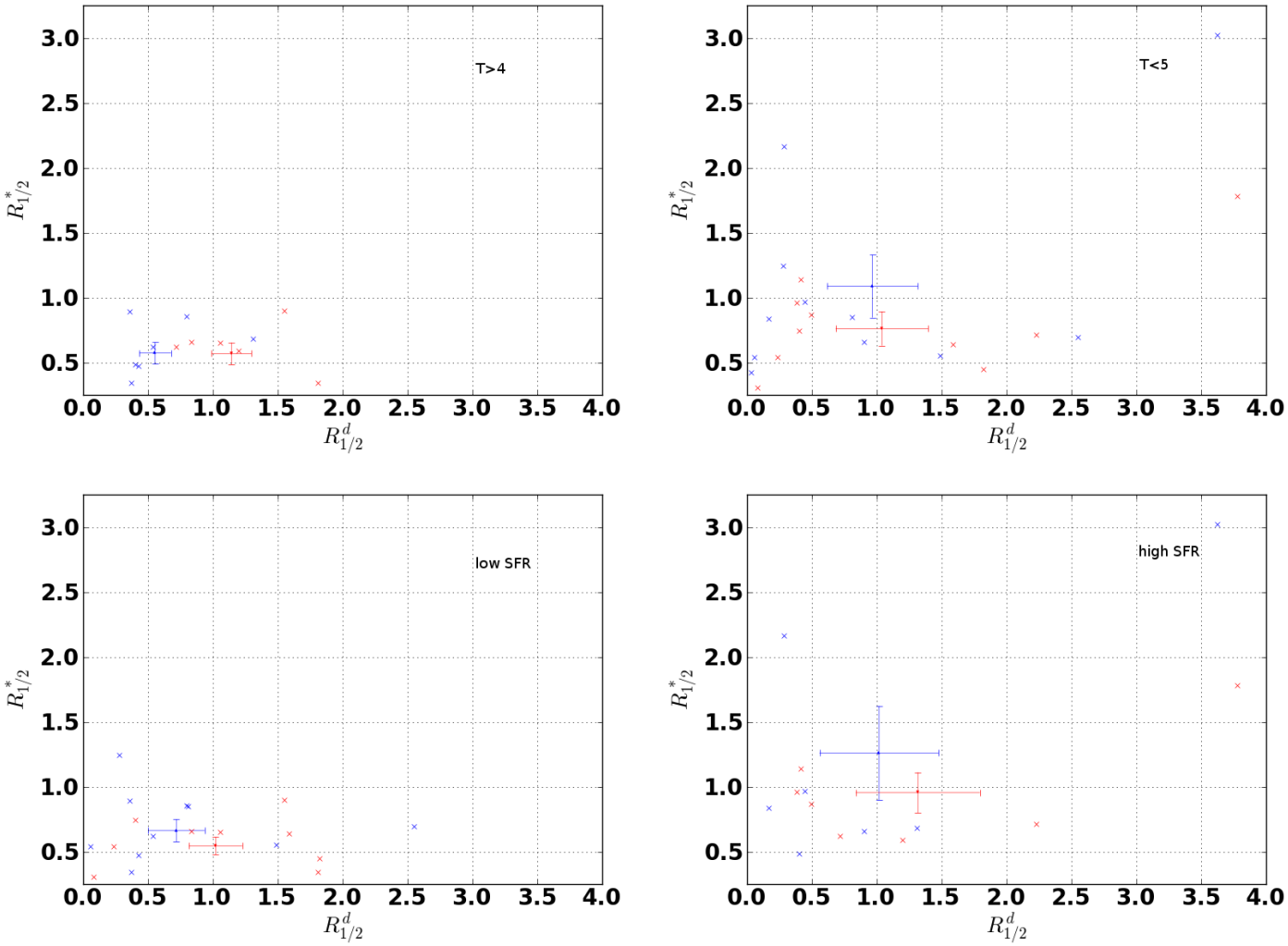

Figure 2.25: We give in these figures Sersic half mass radius $R_{1/2}$ in units of R25, corresponding to surface density profiles of stars (ordinates) and dust (absissa), in cases where the Sersic fitting procedure is acceptably successful, i.e. when $r^2 \geq 0.8$, with r^2 the squared Pearson coefficient for Sersic fitting. In reading order, galaxies plotted are those found with the following properties: stage types larger than or equal to 5 (top left), stage types smaller than 4 (top right), lower SFR than average (bottom left) or higher SFR than average (bottom right). The average SFR of our total galaxy sample is $1.36\,M_{\odot}/yr$. The average and error on the mean is marked with a triangle. MIPS data series are in blue, PACS data series in red.

exponential and earlier types seem to have global stellar density profiles decreasing more rapidly with radius than exponential.

For dust surface density, on the contrary, we see that our data are consistent with stage type or SFR having no strong influence on how dust surface density decreases with radius in a sub group of mainly non barred galaxies (as mentionned before only two barred galaxies have both radial profile of dust and stellar surface densities well fitted by Sersic functions).

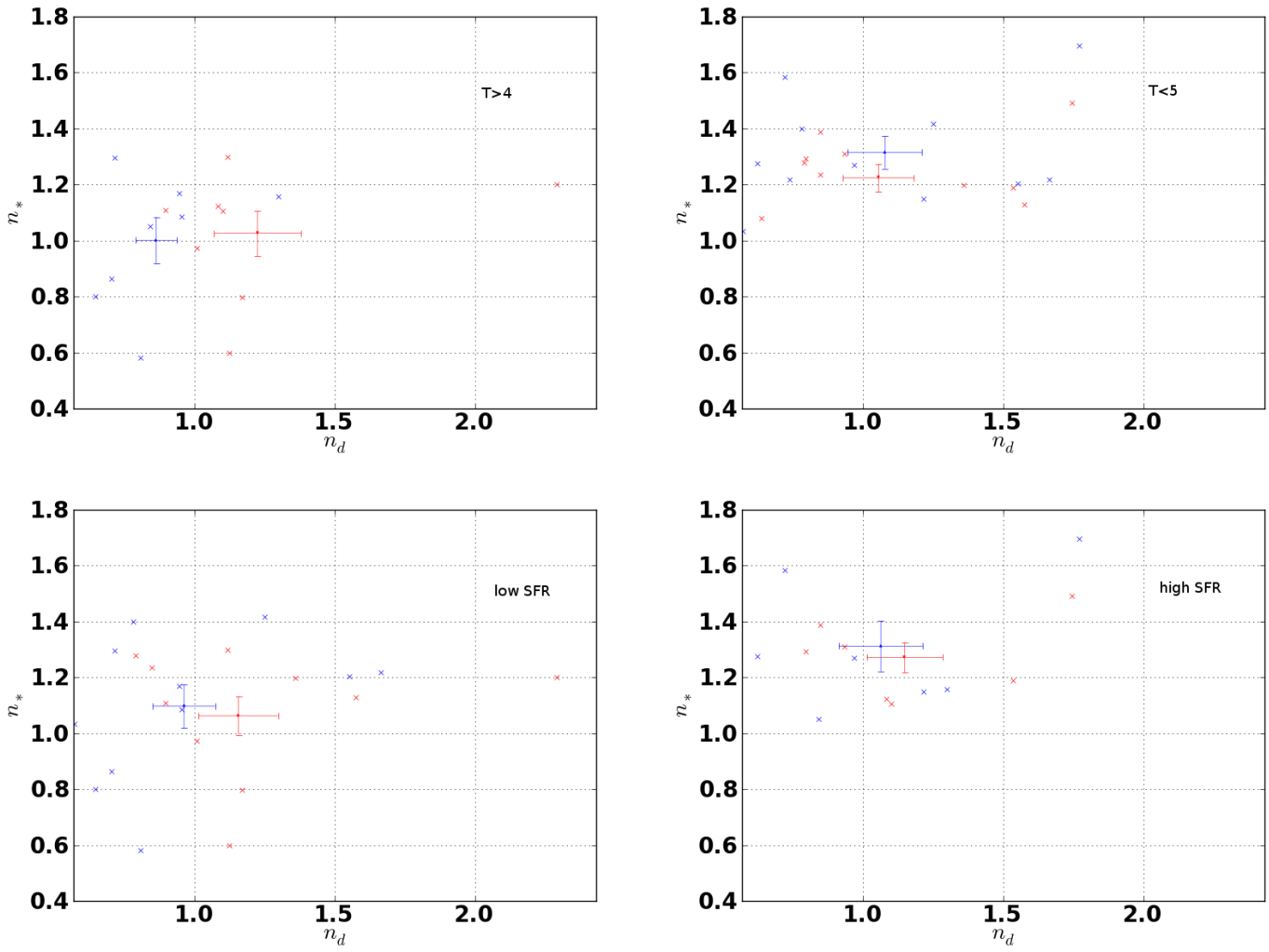

Figure 2.26: We give in these figures Sersic indices n corresponding to surface density profiles of stars (ordinates) and dust (absissa), in cases where the Sersic fitting procedure is acceptably successful, i.e. when $r^2 \geq 0.8$, with r^2 the squared Pearson coefficient for Sersic fitting. In reading order, galaxies plotted are those found with the following properties: stage types larger than or equal to 5 (top left), stage types smaller than 4 (top right), lower SFR than average (bottom left) or higher SFR than average (bottom right). The average SFR of our total galaxy sample is $1.36\,M_\odot/yr$. The average and error on the mean is marked with a triangle. MIPS data series are in blue, PACS data series in red.

2.8.4 Maximum surface densities of stars and dust

We now examine maximum surface densities against stage types and bar types. These maximum surface densities are relatively independant from the Sersic fitting procedure as their extraction does not require linear regression.

We plot on figure 2.27, the maximum stellar surface densities stacked by bin of stage type (right graph 2.27) and bar type (left graph 2.27). We find that the stellar surface density exhibits similar trends with stage type in MIPS and PACS data series. The stellar density decreases from stage type 2 to later stage types. As the radial stellar density profiles decrease strongly with radius in all our galaxies, maximum surface densities represent central surface densities. This is consistent with galaxies of earlier stage type in the range of stage type $t \in [2, 9]$ having larger stellar densities in their central parts. Stage types $t \in [0, 2]$ have rather broad dispersions and are rather in agreement with each other in terms of maximum stellar densities with a small decrease toward earlier stage types from 2 to 0. We warn that in those early types spheroids are more prevalent possibly rendering our method, which relies on azimuthal averaging, more approximate.

We also see that barred galaxies have smaller central stellar densities than non barred galaxies. This could possibly hint at bars preventing stellar content in central galactic region from increasing to similar levels as those found in non barred galaxies, possibly because of the ability of bars to redistribute momentum, and thus prevent large densities from gathering in central regions (see Athanassoula, 2003).

We plot on figure 2.28 the maximum dust surface densities for our whole galaxy sample (except IC2574[2]) stacked by bin of stage type (upper right figure 2.28) and bar type (upper left figure 2.28).

We wish to compare maximum dust surface densities to maximum stellar surface densities. This is doable if we compare dust and stellar maximum surface densities obtained in rather close radial galactic regions. Maximum stellar surface densities are found in all our galaxies at the galactic center, whereas the location where the maximum dust surface density is obtained is not the galactic center in some galaxies. We find that maximum surface densities of dust are close to the dust surface densities found in the radial range $R/R25 \in [0.1, 0.2]$ except for 11 galaxies. These are NGC7793, IC2574, NGC1291, NGC5474, NGC4725, NGC2841, NGC4579, NGC1377, NGC3773, NGC3627, NGC3049. We name this sample of 11 galaxies S-11. In these latter galaxies the maximum surface densities of dust are found at $R/R25 > 0.2$. To be able to compare dust to stellar maximum surface densities, we first compare the graph of maximum dust surface density against stage type and bar type for our total galaxy sample and our total galaxy sample from which we exclude S-11. Thus we make the same plots as the upper figures 2.28 but excluding S-11 and we obtain the lower figures 2.28. We find that upper and lower graphs are strongly similar and thus excluding S-11 from our galaxy sample does not modify the maximum dust surface density distribution. From this point on, in our total galaxy sample from which we exclude S-11, we call maximum dust surface densities, $[0.1 - 0.2]$ dust surface densities.

We remark that, excluding S-11 or not, maximum dust surface densities increase from stage type 0 to 4. At later stage types than 4 the behaviour is less monotonic and especially uncertain in types later than 7 because of our low number of galaxies. Nonetheless in our sample of galaxies, the highest dust surface densities (upper right graph 2.28) and the highest $[0.1 - 0.2]$ dust surface densities (lower right graph 2.28) are consistently found in stage types 4 and 6. This is relatively coherent with Muñoz-Mateos (2009) finding stage type 3-4 (Sb-Sbc) having

[2]Our SED fitting procedure yields erroneous results in the dust mass radial profile of this galaxy, possibly because of its relatively low surface brightness as compared to the background signal.

higher surface densities than spiral galaxies of earlier types.

We see in the lower left graph 2.28 that the bars are also possibly linked to mechanism preventing the central dust surface densities to reach the levels observed in non barred galaxies. Analyzing the dust density profile of barred galaxies in our sample would require a more complex method than direct Sersic fitting as only two barred galaxies in our sample have dust radial profiles acceptably fitted by Sersic functions. Furthermore as we see that dust surface densities are similarly decreasing in presence of a bar for our total sample and in our sample obtained after removing S-11, the lower than average maximum surface density of dust seems a general feature of galaxies with bars, whether the maximum dust surface density is measured close to the galactic center (total galaxy sample minus S-11) or not (S-11 sample). In turn, as maximum dust surface densities are also lower in early type galaxies (at least from stage 0 to 6), this is consistent with bars being stronger overall in earlier type galaxies (see Chapelon et al., 1999) and earlier type galaxies having much less dust than later type galaxies (see Smith and Eales, 2012).

We plot on figure 2.29 the dust to stellar maximum surface density ratio for our total galaxy sample from which we excluded S-11. As we excluded S-11 and we are confident that central stellar densities are relatively close albeit higher than their values at $R/R25 \approx 0.1 - 0.2$ we consider that ratios plotted on figure 2.29 are close to the dust to stellar surface density ratios at $R/R25 \approx 0.1 - 0.2$ (albeit probably systematically underestimated by a rather constant factor due to the decrease of the stellar surface density from $R/R25 = 0$ to $R/R25 \in [0.1, 0.2]$). This enables to compare maximum surface densities of stars and dust at a similar inner radial location for all galaxies.

In this line of reasoning, we compare the left fig. 2.27 page 139 (maximum stellar surface densities against bar type) to the lower left fig. 2.28 page 140 (maximum dust surface densities against bar type for all galaxies in which this maximum is obtained at radius $R/R25 \in [0.1, 0.2]$) and note that the decrease of the dust surface density at $R/R25 \approx 0.1 - 0.2$, possibly due to the presence of a bar, is milder than the decrease of the stellar density. This results on the left figure 2.29 in an increasing ratio of dust to stellar maximum surface density from non barred to barred galaxies in the region $R/R25 \approx 0.1 - 0.2$. We stress that we obtain this result only for the subset of galaxies whose maximum dust surface density is reached close to the center. Therefore in these galaxies, the presence of bar seems to be linked with an increased fraction of dust material with respect to stellar material in the $R/R25 \approx 0.1 - 0.2$ region.

We also see on the right fig. 2.29 that the dust to stellar maximum surface density ratio measured at $R/R25 \approx 0.1 - 0.2$ increases from stage type 2 to 6 with a possible increase from stage type 2 to 0. This is interestingly matching relatively well the trend found between the ratio of the quantity of power intercepted by dust over the stellar power output, $D_d/D_\star$, between stage types 0 to 6 represented on fig. 2.19 (125). This possibly shows that the relative dust and stellar surface densities explain the variations of the power intercepted by dust w.r.t. the available power of provided by old stellar populations in galaxies with stage types $t \in [0, 6]$.

2.9 Conclusion on our study of cosmic dust and stellar galactic content

In the second part of this thesis we explored physical properties of dust w.r.t. the stellar content.

We found that many of our disk galaxies exhibit close to exponentially decreasing stellar mass densities which is consistent with common knowledge on disk galaxies. The ISRF shining on dust is often discrepant between MIPS and PACS data series whereas the dust mass is less discrepant. This is consistent with the average ISRF shining on dust to be mainly extracted from bands close to the range $70\mu m$ to $160\mu m$ which is typically the one where we expect discrepancies

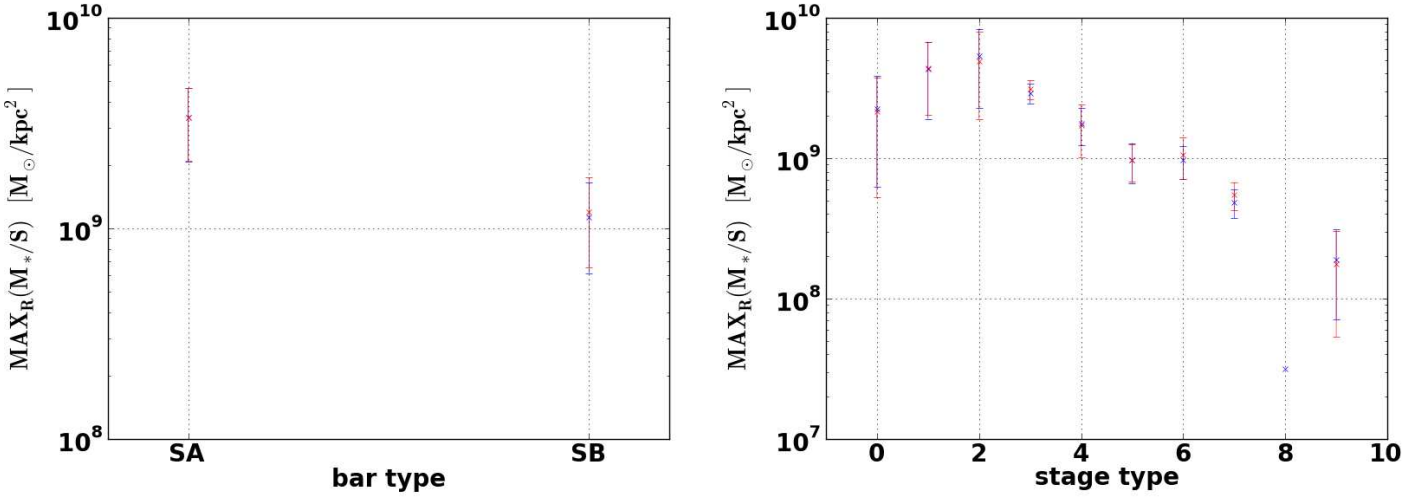

Figure 2.27: We give in these figures the maximum surface density of stars. We average this quantity over SA and SB galaxies (left graph) and over each bin of stage type (right graph). The stage type 8 is only represented by one galaxy. MIPS and PACS data series are respectively in blue and red.

between PACS and MIPS. As dust masses are extracted rather from the wavelength range $250\mu m$ to $500\mu m$ where MIPS and PACS data series do not differ (this is the wavelength range of SPIRE) we can expect dust masses not to differ between PACS and MIPS data series.

We found that dust surface densities do not in all cases decrease as smoothly as stellar densities with galacto-centric radius (see e.g. NGC 7793).

We then investigated the links between M_d/S, $< U >$ and $M_{\star,fit}/S$. We found that across our disk galaxies $M_{\star,fit}/S$ is better correlated with the product of M_d/S and $< U >$ rather than with any of the two separately.

We also remarked that these correlations are stronger for PACS data series than MIPS data series. As MIPS data are found to be less in accordance with PACS data, and also in somewhat mediocre agreement with SPIRE (especially at low surface brightness), whereas PACS data are in good agreement with SPIRE, we are more convinced by PACS data series results rather than MIPS data series results. We also stress that MIPS data series may have less well constrained SEDs because they lack the $100\mu m$ channel present in PACS data series. Thus it is possible that our MIPS/PACS data series separation is slightly biased toward more realistic SEDs in PACS data series.

The relatively weak correlation between $< U >$ and $M_{\star,fit}/S$ probably means that dust is not simply heated more across the disk when the stellar surface density increases. This probably hints at radiations heating dust in regions distant by a substancial fraction of the galactic optical radius from the region where these radiations originate. The weak correlation between M_d/S and $M_{\star,fit}/S$ is probably due to the life cycle of dust being not simply linked to the star formation history as shown for instance by Mattsson et al. (2012).

Interestingly we found (see figure 2.9 on page 111) that the $M_d/S \times < U > -M_{\star,fit}/S$ correlation can be said to be a disk specific correlation as this correlation is more stringent inside galaxies where our disk orientation extraction is more successful (CDO sample).

The latter observation is true for all $M_d/S \times < U > -M_{\star,fit}/S$, $M_d/S - M_{\star,fit}/S$ and $< U > -M_{\star,fit}/S$ correlations in PACS data series. We found that all of them are stronger in

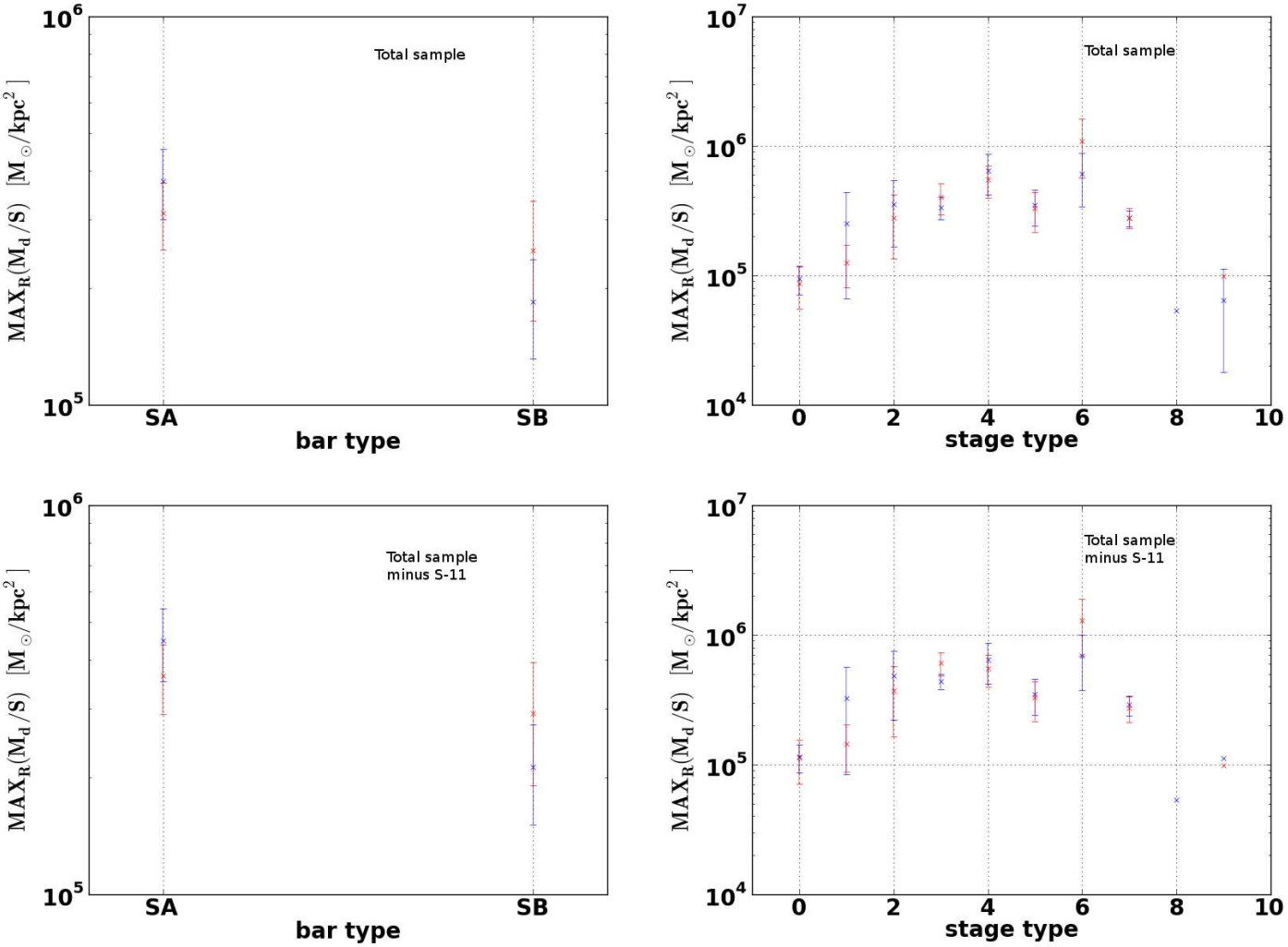

Figure 2.28: We give in the upper figures the maximum surface density of dust. We average this quantity over SA and SB galaxies (upper left graph) and over each bin of stage type (upper right graph). The stage type 8 is only represented by one galaxy. MIPS and PACS data series are respectively in blue and red. We do not include in these graphs the maximum dust density of IC2574 as our SED fitting procedure is erroneous in this case, possibly because of the low surface brightness observed in this galaxy. The lower figures are the same than to upper figures except that we removed galaxies in which the maximum surface densities of dust are significantly different from those found in the radial range $[0.1, 0.2]$ in units of R25. The excluded galaxies are the following: NGC7793, IC2574, NGC1291, NGC5474, NGC4725, NGC2841, NGC4579, NGC1377, NGC3773, NGC3627, NGC3049.

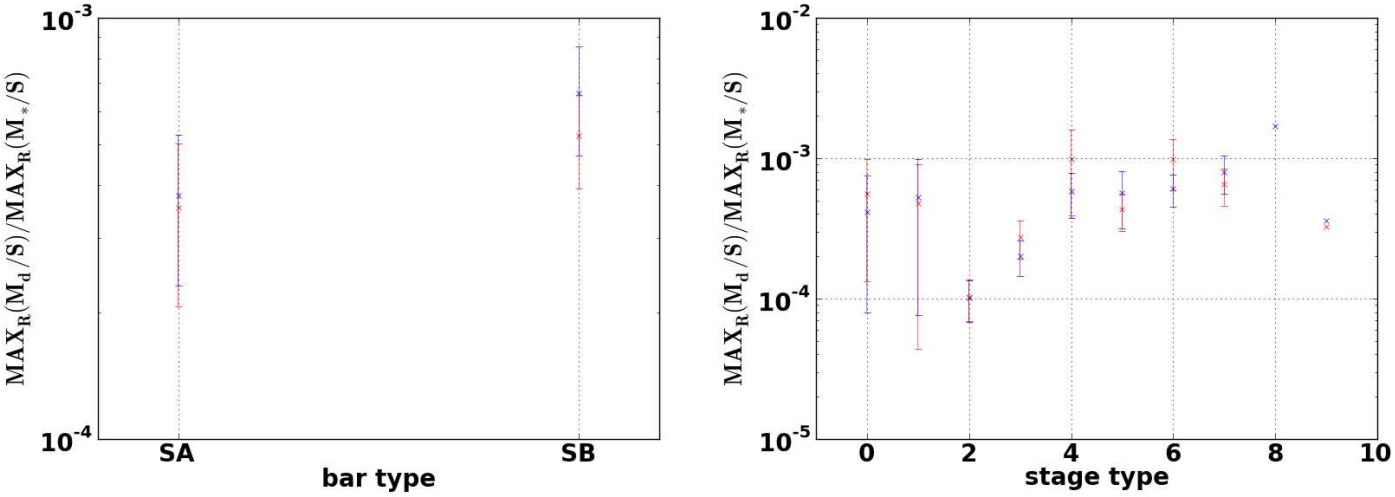

Figure 2.29: We give in these figures the ratio of the maximum surface density of dust over the maximum surface density of stars. We average this quantity over SA and SB galaxies (left graph) and over each bin of stage type (right graph). The stage type 8 is only represented by one galaxy. MIPS and PACS data series are respectively in blue and red. As compared to our total galaxy sample, we removed from this graph galaxies in which the maximum surface densities of dust are found in a radial range significantly different from $[0.1, 0.2]$ in units of R25. These are the following galaxies: NGC7793, IC2574, NGC1291, NGC5474, NGC4725, NGC2841, NGC4579, NGC1377, NGC3773, NGC3627, NGC3049.

the galaxies where our disk orientation extraction is more efficient (CDO). This seems consistent with the fact that dust disks are more easily related with stellar disks in CDO or at least that the azimuthally averaged SED profiles are more physically meaningful in CDO galaxies.

We found $M_d/S - M_{\star,fit}/S$ correlation consistent with a dependence of the dust to stellar ratio on other variables relatively independant of either of these two, e.g. the molecular gas mass and the metallicity (see Mattsson et al., 2012).

We interpreted $M_d/S \times < U >$ as being proportional to the surface density of power geometrically intercepted by dust D_d. This power is different from the power absorbed by dust. To compute the latter, one needs to use the precise spectral dependance of the ISRF shining on dust as well as dust absorption.

The stellar density of luminous power $D_\star$ computed by Skibba et al. (2012) tightly correlated with the stellar surface mass density extracted by our SED fitting.

We found the total dust emitted density of power from Skibba et al. (2012) to be comparable to the density of power geometrically intercepted by dust D_d and the $D_\star$ to have a distribution of values w.r.t. D_d.

We found that the power intercepted by dust is very well, but rather non linearly, correlated with the power emitted by warm dust. This correlation is stronger for galaxies in which the shapes of isophotes across all FIR wavelengths are in better agreement (CDO sample). This possibly means that when warm dust (the bulk of the dust emission) is morphologically more coherent with cold dust (the bulk of the dust mass) when there is a precise link between what is emitted by warm dust w.r.t. the power intercepted by all components of dust. However we find that this link between the power geometrically intercepted by dust D_d and the warm dust luminous output D_{warm} is probably the same in all objects when both quantities are radially

well correlated whether it is CDO or not.

Our correlation results show that the power intercepted by dust is between 10 and 100 times the power emitted by warm dust. This is in agreement with dust absorbing probably at least 10 times more power than warm dust. The surface density of power intercepted by dust is also well, and closer to linearly, correlated with the total infrared surface density of power. We could possibly interpret these facts as hinting at a large fraction of dust geometrically intercepting power emitted by the same sources which heat warm dust.

We found that the power intercepted by dust is close to linearly correlated with the power emitted by cold dust although the latter is much smaller than the former because D_d is the power intercepted by all dust not only the cold one.

The $D_d/D_\star$ ratio is preferably between 1/10 and 1/100 in galaxies for which our methodology found consistent disk orientation between dust and stellar map isophotes. In other galaxies $D_d/D_\star$ is more dispersed between 10 and 1/100. The reason for the stronger correlation seen between the power intercepted by dust and the stellar output in galaxies where stellar and dust isophotes are more homogeneous in shapes, could be that in these latter galaxies both phases are homogeneously distributed inside the same structure i.e. the disk.

We then turn to examining how $D_d/D_\star$ changes between galaxies, and whether it has links with galaxy properties. We first observed that $D_d/D_\star$ has relatively small dispersion in each galaxy showing that the power intercepted by dust is close to a constant fraction of the luminous power emitted by stars in each disk galaxy, although this former ratio varies from one galaxy to another. This fact in itself makes this ratio an interesting local quantity which could be compared between disk galaxies. This is also a clue that these old stellar populations may well be rather convincing dust heating sources.

A tenuous but linear correlation between $D_d/D_\star$ and L_{IR}/L_{OPT} is found, probably showing that L_{OPT} is not very well correlated with local estimate of the old stellar population luminosity as estimated by $D_\star$ in the NIR-MIR. This speaks for the use of more realistic estimates of the density of power emitted by stars and further research to find whether these estimates are related to D_d or not.

Our finding that galaxies with high optical luminosities have rather low $D_d/D_\star$ values is consistent with the existence of a process impeding dust interception of stellar power in more luminous galaxies. We argue this could be caused by dust growth being dampened in more luminous galaxies (see Mattsson and Andersen, 2012).

A relatively strong correlation is found for $D_d/D_\star$ with SFR, meaning that dust intercepts geometrically more stellar light when stellar nurseries are more active. This trend is more conspicuous in galaxies where dust is less homogeneously distributed in the disk (non CDO galaxies). This is consistent with dust being more heated by SFR regions and star forming structures such as spiral arms in galaxies where we do not find strong evidence of dust disks, i.e. where the structures mostly inhabited by old stellar populations do not have dusty counterparts.

However the correlation being sublinear, SFR is only a little increased when $D_d/D_\star$ increases by much. As previously said this calls for more investigation in the link between dust and star formation to better explain how dust is related to SFR, and especially the link between the radiative transfer from power emitted by stars to power emitted by dust and how this is affected by SFR.

We find that the quantity of power intercepted by dust w.r.t. the stellar power is maximum in stage types: $5-6 = Sc-Scd$, differing from the morphological stage types where the maximum surface densities of dust is found: $3-4 = Sb-Sbc$. We also find that galaxies with a strong bar have a power intercepted by dust larger w.r.t. their power of stellar origin. These two trends can be explained relatively well by the dust to stellar ratio of maximum surface densities in a close to central radial range of $R/R25 \approx 0.1-0.2$. We call this ratio R. We found that R

exhibits very similar trends with stage type and bar type to the trend of $D_d/D_\star$ (comparison between figure 2.19 page 125, and figure 2.29 page 141).

Furthermore we find that the dust to stellar ratio of maximum surface densities (R) seems to exhibit a trend with stage type more similar to the spiral structure strength (see fig. 2.30 on page 143). All this hints at the spiral structure strength being connected to the dust to stellar ratio of maximum surface density at least in galaxies with stage types later than 2. In turn this ratio of dust to stellar maximum surface density seems the main driver of the dust intercepted power with respect to the old stellar population luminous output. It means that the quantity of power the dust collects w.r.t. the available stellar power, is to a relatively large extent explained by the relative amounts of dust and stars.

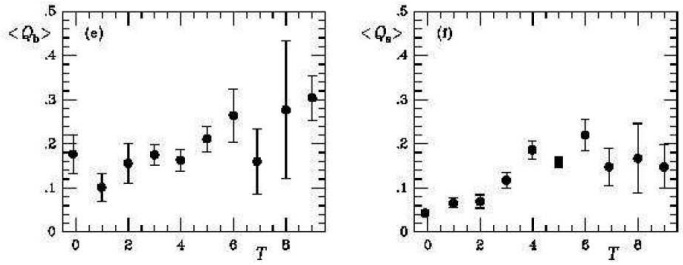

Figure 2.30: This figure is a part of the figure 6 from Buta et al. (2005) giving averages of Q_b and Q_s the bar and spiral structure strength against stage type.

The extraction of maximum dust surface densities and maximum stellar surface densities is a prerequisite to make Sersic fitting of dust and stellar surface density profiles. However we not only used them in the Sersic fitting procedure but we also analyzed how they vary w.r.t. galaxy properties. We found that earlier stage types have larger central surface densities of stars which is consistent with earlier types having an increased prevalence of central spheroidal component (spheroids have larger face-on surface stellar densities than disks see Benson et al., 2007). We find smaller maximum surface densities of stars inside barred galaxies, and alike smaller maximum surface densities of dust inside barred galaxies. This hints at a mechanism, possibly angular momentum redistribution by bars, yielding less concentrated inner regions of disk galaxies in barred galaxies. The maximum dust surface densities are located in stage types 4-6 which is marginally in agreement with Muñoz-Mateos (2009).

We now turn to the fitting of our dust and stellar surface densities with pure Sersic profiles. This is clearly an approximation as standard decomposition of stellar profiles often use an exponential disk plus a Sersic bulge. Our findings are as follows.

The pure Sersic profiles are rather acceptable (squared Pearson coefficient higher than 0.8) for stellar surface densities, whereas they are failing at representing correctly half of our galaxy sample concerning dust density profiles. We checked that success or failure in this Sersic profile fitting is not determined by galaxies having more consistent shapes of isophotes in all our wavelength bands (CDO/non CDO), nor stage type earlier or later than 5. However barred galaxies seem to present more failures in Sersic profile fitting of dust density profiles, than non barred galaxies, while having a bar is rather not affecting Sersic fitting of stellar density profiles. This is consistent with bars having a strong effect on the dust surface mass densities, preventing them to adopt a radial behaviour close to the one adopted by stars (Sersic profile).

This seems also rather consistent with what we already saw, namely that the presence of a galactic bar is perturbing isophotal shapes of cold dust maps (which gather the bulk of the dust mass) especially inside disk associated regions even beyond the bar, whereas galactic bars leave

the dispersion of isophotal shapes unchanged in disk associated regions of stellar maps beyond the bar location.

Galaxies with higher SFR having stellar profiles less well fitted by Sersic functions, we argue that these star forming galaxies exhibit on average more structures likely to perturb the stellar density profile such as spiral arms. However we find no dependence of the Sersic fitting of dust surface density profile with SFR. This hints at the global SFR not having as strong a perturbing effect on the dust surface density profile as it has on the stellar surface density profile, which is odd. Incidentally we find this conclusion well in agreement with the fact that galaxies where our disk orientation method extract coherent disk orientations across the maximum available number of FIR bands (CDO sample), have strictly the same average SFR as compared to galaxies where our method finds more discrepancies between isophotal shapes in different FIR bands (non CDO sample). This could hint at star formation being not very tightly linked with dust surface density alone and probably is the sign that star formation and dust surface density have to be studied at least together with a measure of (molecular and/or atomic) gas surface density.

We will now consider results of our Sersic fitting in galaxies where it is successful. We first note that on average we find an agreement between Sersic index of stellar (1.15 ± 0.08, the error is the error on the mean) and dust (1.07 ± 0.16) surface density profiles. However even for well fitted Sersic profiles the widths of Sersic index and Sersic half mass radius distributions increase twofold from stellar surface density profiles to dust surface density profiles. This could be construed as dust exhibiting surface mass density profiles different from those observed in the stellar phase. It could be linked to the fact that the dust production and growth is not directly linked to the stellar phase.

We note that the vast majority of our normal nearby disk galaxies have a central component differing from a pure exponential disk (Sersic index not equal to 1). More precisely we find Sersic profiles decreasing faster than exponentially in stellar surface density profiles. This could be due to the fact that we do not take into account separately the bulge and the disk, and thus Sersic fitting of stellar density profiles may well be affected by the central stellar bulges.

Similarly considering only galaxies with mass density profiles well fitted by Sersic functions, we find that later type galaxies exhibit more exponential stellar density profiles than earlier types. In earlier types the decrease with radius of the stellar surface mass density profile is faster. This is consistent with the Sersic fitting using the inner regions of the disk to fit a profile, as we know that earlier types have more prevalent classical bulges, which are famous for being more concentrated than exponential.

We are confident that:

- Sersic indices closer to 1 for dust density profiles than for stellar density profiles as well as
- Sersic indices being seemingly not linked to the stage type for dust whereas those two quantities are linked for the stellar phase

are physical results showing that the dust density profiles exhibit no evidence for bulges.

Chapter 3

Summary and Perpectives

Summary

In my PHD work I explored the links between the physical properties of interstellar dust and other components of nearby spiral galaxies especially their stellar content. I worked on 46 disk galaxies from KINGFISH with IRAC/MIPS/PACS/SPIRE maps (3.6 - 500 microns). A bias is usually introduced in estimating disk orientations by using only a single surface brightness isophote. Thus I devised different surface brightness levels separated by constant steps in surface brightness and extracted isophotes at these levels in all FIR maps as well as in all IRAC 4.5 microns maps. To further assess the coherence of the shapes of isophotes across galactic disks, I built a quantitative indicator of the difference in shape between two ellipses with same center and same semi-major axis.

I defined an acceptable level of difference between isophote shapes, by comparing disk orientations found in litterature. Using this level, I found regions inside the galactic disks where the isophotal shapes are similar. From these, I extracted one disk orientation per wavelength band. I found in the vast majority of the disk galaxy maps, be it dominated by stellar or dust emission, that a large fraction of the isophotes I extracted are coherent with the idea of an underlying disk. Comparing, for each galaxy, disk orientations extracted at all wavelengths, I found evidence in 20 galaxies out of 46, that on radial ranges as large as 1/3 of the visible disk (as measured by R25), the shapes of isophotes are morphologically similar. Thus for these 20 galaxies I devised consistent disk orientations both for the stellar and dust content. These 20 galaxies are less luminous, less emitting in the IR w.r.t. the optical, less barred, and characterized by later stage types than average. I also found that the disk orientations devised by my photometric method yield results more similar to H-α kinematic orientations than another photometric study based on a single isophote level.

Using the orientations I found and H-alpha dynamics disk orientations, I averaged azimuthally surface brightnesses to produce radial spectral energy distributions (SED) profiles. Once fitted with a cosmic dust emission model, they resulted in radial profiles of dust and stellar content properties. I found the dust intercepted power to be proportionnal to the product of the total dust mass and the average ISRF shining on dust. This former quantity is better correlated with the bolometric stellar luminosity than any of the dust mass or the dust heating ISRF separately. Thus the old stellar populations may be an important heating source for dust. The power intercepted by dust is also very well correlated with the total infrared power. The dust intercepts a larger quantity of power coming from stars in more actively star forming galaxies.

Dust exhibit radial mass surface density profiles less well described by Sersic functions than stellar ones. When both profiles are well fitted by Sersic functions, stellar density profiles have smaller half mass radii than the isophotal optical radius (R25) separately in later type galaxies,

but also in more quiescent galaxies. Sersic index and half mass radius distributions have larger widths for dust than for stellar surface density profiles.

I also found that the ratio of dust over stellar surface density is an important factor to explain the variations with galactic morphological type of the ratio of dust intercepted power over the power emitted by old stellar populations. This later link could be intertwined with spiral structure strength in stage types later than 2.

Perspectives

As noted by Kennicutt et al. (2011), the study of resolved nearby galaxies form a vital bridge between more local approaches, e.g. studies of individual interstellar clouds and star-forming regions in the Galaxy, and the globally integrated measurements available for distant galaxies. For this reason the work reported in this thesis could be interestingly extended to sets of more numerous and possibly more distant of galaxies.

The methodology presented in this thesis for extracting and comparing shapes of dust and stellar components are automatic and therefore suitable to be used in the study of large data sets. Nonetheless it could possibly be interesting to pursue the work presented in this thesis, by building a more efficient isophote extraction technique than the one I used, as this would probably allow to look at more numerous isophotes and thus get a finner view of the isophotal shape variations inside galaxies. We recommend to attempt isophotal shape comparison with the D distances presented in the appendices rather than the one noted D in the main body of the thesis, and named D_{integ} in the appendices, because D_{integ} is more time consuming to use and present some drawbacks as compared to the D presented in the appendices. We also consider that using isophotes probing exponentially spaced surface brightnesses may enable a more thorough exploration of the full extent of disks inside disk galaxies. Furthermore in this case semi-major axis of isophotes could probably be more linearly spaced which would render interpretations of the trends between EXT region properties and semi-major axis of EXT regions more straightforward and easy to come by.

Lower threshold of D distance than the one we use in this work for EXT regions could possibly enable to estimate the correlation between semi-major and semi-minor axis which is expected in the description of galactic disks as oblate spheroids (see Hubble, 1926) especially in CDO galaxies.

We think that a possible improvement of our method to extract consistent disk orientations, would involve a systematic comparison between isophote shapes and an isophote shape found where the distance in elliptical shape between consecutive isophotes is minimum.

The non linear relation between power intercepted by dust and warm dust emission would require further investigation to be elucidated.

An interesting possibility to continue this research would be to take into account dust absorption to refine the interpretation of $M_d \times < U >$. For instance it could be possible to assume different realistic ISRF spectra scaled by $< U >$ or use the one provided by Mathis et al. (1983) and see how dust intercepted power modulated by absorption matches the luminous output of dust. Although there are already some clues hinting at the bulk of the dust mass being subjected to the general ISRF (Grootes et al., 2013 finds that 85% of dust mass resides in translucent structures), the spectrum of the ISRF bathing dust still is an open field of research complicated by the fact that the ISRF is known to change in different environments within galaxies, for instance in different structures such as between arm and interarm regions, or bulge and disk regions (see Worthey, 2000).

Another conceivable direction to improve this work would be to use hot and young stellar population light in the NUV and/or FUV and to check whether the ISRF shining on dust or

the power collectively intercepted by dust depend on it.

One could also possibly improve the approximate estimate of the galactic surface equivalent to a SPIRE 500 pixel, by taking into account a non zero thickness of the disk. This could be done for instance by taking into account in each band the thickness associated to the dominating emission source of the band (e.g. it is expected that dust and stars distributions have not the same thickness inside disks of disk galaxies).

Another way of improving our method of investigation would be to convolve all band maps strictly to the same PSF before applying the SED fitting.

More generally future research on dust emission could possibly greatly benefit from taking into account more accurate estimates of the stellar density or estimates of stellar density more specific to different stellar populations than the one we used in this work.

Chapter 4

APPENDICES

4.1 Notations

$M_\odot$	$=1.9891$	$\times 10^{30}$	kg	: solar mass;
h	$=6.62606957(29)$	$\times 10^{-34}$	$m^2.kg.s^{-1}$	: Planck constant;
c	$=2.99792458$	$\times 10^{8}$	$m.s^{-1}$	: speed of light in vacuum;
k	$=1.3806488(13)$	$\times 10^{-23}$	$m^2 kgs^{-2}K^{-1}$	: Boltzmann constant;
pc	$=3.08567758$	$\times 10^{16}$	m	: parsec;

λ: wavelength;
ν: frequency;
σ: sky background standard deviation in intensity;
μ: sky background average intensity;
T: temperature.

4.2 Abbreviations

AGB: asymptotic giant branch
e.g.: exampli gratia
FMR: fundamental metallicity relation
FIR: far infrared
FUV: far ultraviolet
IMF: initial mass function
i.e.: id est
IR: infrared
IRAC: Infrared Array Camera
ISM: interstellar medium
ISRF: interstellar radiation field
LIRG: luminous infrared galaxy
LMC: Large Magellanic Cloud
MIR: middle infrared
MIPS: Multiband Imaging Photometer for Spitzer
NaN: Not a Number
NED: NASA/IPAC Extragalactic Database
NIR: near infrared
NUV: near ultraviolet
PACS: Photodetector Array Camera and Spectrometer
PAH: polycyclic aromatic hydrocarbon
PNe: planetary nebula
SED: spectral energy distribution
SFR: star formation rate

SFH:	star formation history	ULIRG:	ultra-luminous infrared galaxy
SMC:	Small Magellanic Cloud	UV:	ultraviolet
SN:	supernova	VSG:	very small grains
SPIRE:	Spectral and Photometric Imaging Receiver	w.r.t.:	with respect to

4.3 Derivation of expressions for the discrepancy D_{integ} between 2 ellipses with same center and same semi-major axis

In the euclidean plane, we choose an ellipse of semi-major axis length equal to unity, and minor over major axis ratio equal to e, with $0 \leq e \leq 1$.

Taking one semi-major axis as [OX) and one semi-minor axis as [OY) so that (O,[OX),[OY)) is a direct frame and $(O, \vec{u_X}, \vec{u_Y})$ the canonically associated direct orthonormal basis which canonically associates one couple of coordinates (X, Y) to each point P of the plane. We get:

$$\frac{X^2}{1} + \frac{Y^2}{e^2} = 1$$

Thus there is the continuous mapping:

$$\left\{ \begin{array}{ccc} \mathbb{R} & \rightarrow & [-1,1] \times [-e,e] \\ \theta & \mapsto & \left\{ \begin{array}{rcl} X & = & \cos\,\theta \\ Y & = & e\,\sin\,\theta \end{array} \right. \end{array} \right. \tag{4.1}$$

And thus for a point P on the ellipse, the square of the radial distance is :

$$OP^2 = R^2 = X^2 + Y^2 = \cos^2\,\theta + e^2\,\sin^2\,\theta \tag{4.2}$$

In this latter mapping θ is different from the α, angular polar coordinate associated with $(O, \vec{u_X}, \vec{u_Y})$. We recall $\alpha = ([OX), [Or))$ with $[O, r)$ a radial direction and α positively counted in the trigonometric sense. We thus get, when $X \neq 0$:

$$\frac{Y}{X} = \tan\,\alpha = e\tan\,\theta \tag{4.3}$$

Thus we get :

$$R^2 = \frac{1 + e^2\tan^2\,\theta}{1 + \tan^2\,\theta} = \frac{1 + \tan^2\,\alpha}{1 + \dfrac{\tan^2\,\alpha}{e^2}} \tag{4.4}$$

Relabelling $\alpha = t - PA$ with t the angular polar coordinate in the case where the initial ellipse is rotated with respect to (w.r.t.) to a new direct frame $(O, [Ox), [Oy))$. In this new frame the position angle, PA, is non zero.

Thus we get from (4.4),

$$R(t) = \sqrt{\frac{1 + \tan^2\,(t - PA)}{1 + \dfrac{\tan^2\,(t - PA)}{e^2}}} \tag{4.5}$$

and inverting it yields four possible t, two of which are,

$$t(R) \equiv PA \pm \arctan\left(\sqrt{\frac{1-R^2}{\left(\frac{R}{e}\right)^2 - 1}}\right) \pmod{2\pi} \tag{4.6}$$

and the two others:

$$t(R) \equiv \pi + PA \pm \arctan\left(\sqrt{\frac{1-R^2}{\left(\frac{R}{e}\right)^2 - 1}}\right) \pmod{2\pi} \tag{4.7}$$

Although 4 solutions are found, the only ones we consider in computing radial integral of circular arcs are those of equation (4.6) as we chose only one side of the semi-minor axis.

4.4 Why I_r does not change when $|\Delta PA| = 90°$, $max(e_1, e_2)$ is fixed and $min(e_1, e_2)$ varies.

We see on picture 1.14 page 56, that for a position angle difference of 90°, when, for example e_1 is fixed, as long as e_2 does not exceed e_1, I_r seems to take similar values.

This is due to the fact that when position angle difference is 90°, equation (1.2) page 54 can be illustrated by picture 4.1, which shows that in this case the area representing the integral of equation (1.2), page 54, is independent of the flatter ellipse and only depends on the thicker ellipse.

4.5 Two other notions of distance for ellipses of same center and same semi-major axis

N.B. : In this section PA is the position angle between x-axis and semi-major axis, and e the axis ratio.

With the two ideas that

- a rotation by π around its center leaves an ellipse unchanged,
- when the difference of position angle is kept fixed, ellipses of axis ratios closer to 1 are more and more similar,

it becomes increasingly clear that the space (e, PA) resemble a sphere or more precisely half a sphere. It is also legitimate to wonder whether a disk could be used here instead of a sphere.

To be more precise the entire (e, PA) space for ellipses is $[0, 1] \times [-\pi/2, +\pi/2]$. The point at $(e, -\pi/2)$ is identified with the one at $(e, +\pi/2)$ for each possible value of e, and points at $(1, PA)$ are all identified together whatever the value of PA.

A remarkable difference between the disk representation of (e, PA) space and the sphere representation is shown by the length of the path representing the continuous transformation of an ellipse into another one. For the sphere representation, between extreme cases $(e, PA) = (0, 0)$ and $(e, PA) = (0, \pi/2)$ the distance is equal to π for the two paths:

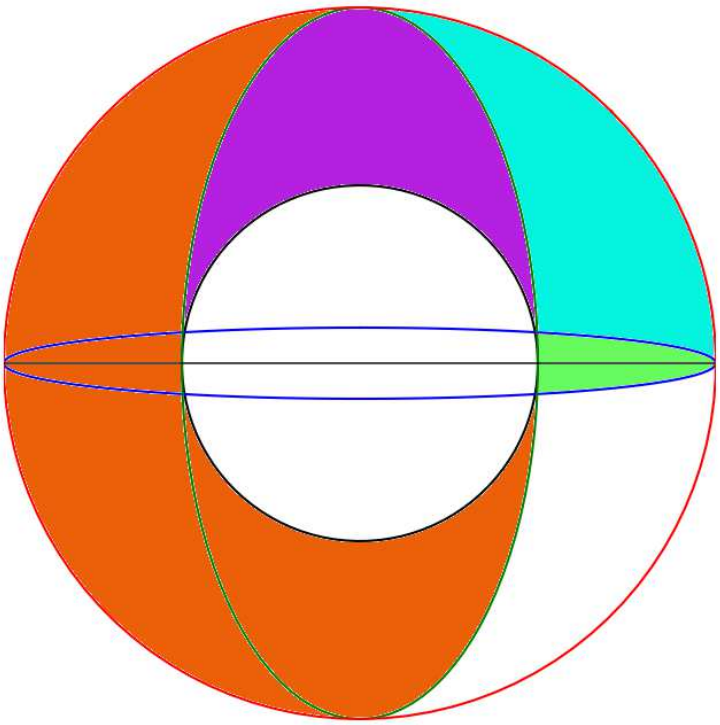

Figure 4.1: Area concerned by equation (1.2) page 54. The integral of difference of θ_{le} is the violet area plus light blue area, and the integral of the difference of θ_{ri} is the blue area plus green area. As both parts are added together we retrieve something equivalent to the orange area. This total area can be written formally as violet area plus blue area plus half of the green area (which does not depend on the blue ellipse axis ratio) plus the blue area plus half of the green area (which does not depend on the blue ellipse axis ratio either). The orange area can be drawn without drawing the blue ellipse, thus it does not depend on it. We could also rephrase this by noting that the borders of the orange area are the black inner circle, which has a radius equal to the axis ratio of the thicker ellipse, the red unit circle, and the green thicker ellipse. None of these borders are a part of the blue ellipse. This explains the invariance of I_r concerning the flatter of the two ellipses when position angle difference is 90°. This invariance is respectively less stringent when position angle difference is 45°, and has totally disappeared when position angle difference is 0° (see respectively pictures 1.13 and 1.12 page 55).

- one in which we depart from the ellipse $(e, PA) = (0, 0)$ by inflating it until $(e, PA) = (1, 0)$ is reached and then identifying $(e, PA) = (1, 0) = (e, PA) = (1, \pi/2)$ we deflate $(e, PA) = (1, \pi/2)$ until $(e, PA) = (0, \pi/2)$ is reached.
- another in which we only rotate the ellipse $(e, PA) = (0, 0)$ until $(e, PA) = (0, \pi/2)$ is reached.

On the disk however the second path is $\pi/2$ times larger, i.e. in the case each ellipse is represented on the unit circle by the point whose polar coordinates are $(r = 1 - e, \theta = 2PA)$ in polar coordinates $((r = 1-e = 0, 2PA)$ being the center and $(r = 1-e = 1, 2PA)$ the boundary). Another way of saying it is that the shorter transformation for the disk representation is not the shorter one for the sphere representation.

Intuitive justification of the expression $(1 - e, 2PA)$**.** In the expression $(1 - e, 2PA)$ a factor 2 is present in front of PA to span the whole disk angular range $[-\pi, +\pi]$ with PA taken in $[-\pi/2, +\pi/2]$. $1 - e$ is taken for polar radius instead of directly e because points with $e = 0$ and different PAs have to be different from one another whereas points with e=1 and different PAs have to be identified to single point (the same ellipse: the unit circle) for any value of PA.

4.5.1 Spherical distances

On a sphere the distance between two points is given by:

$$\begin{aligned} D_{sph} \quad & (\theta_1, \phi_1, \theta_2, \phi_2) = \\ = \quad & 2 \times Arcsin\sqrt{\frac{1 - cos(\theta_1 - \theta_2) + [1 - cos(\phi_1 - \phi_2)]sin(\theta_1)sin(\theta_2)}{2}} \end{aligned}$$

So we can similarly define either of the two

$$\begin{aligned} D_{\theta,lin}(PA_1, PA_2, e_1, e_2) &= \frac{1}{\pi} \times D_{sph}((1 - e_1) \times 90°, 2 \times PA_1, (1 - e_2) \times 90°, 2 \times PA_2) \\ D_{\theta,arccos}(PA_1, PA_2, e_1, e_2) &= \frac{1}{\pi} \times D_{sph}(arccos(e_1), 2 \times PA_1, arccos(e_2), 2 \times PA_2) \end{aligned}$$

The factor $\frac{1}{\pi}$ is put so that the maximum distance is 1.

4.5.2 Flat distances

On a disk the distance between two points defined by their polar coordinates (r, θ) is:

$$\begin{aligned} D_{disk} \quad & (r_1, \theta_1, r_2, \theta_2) = \\ = \quad & \sqrt{r_1^2 + r_2^2 - 2r_1r_2cos(\theta_1 - \theta_2)} \end{aligned}$$

At the beginning of section 4.5 we remarked that a good way to devise a notion of distance between ellipses is computing the euclidean distance between points of the unit disk which, for each ellipse characterized by (e, PA), has polar coordinates $(1 - e, 2PA)$. Thus we obtain:

$$\begin{aligned} D_{flat} \quad & (PA_1, PA_2, e_1, e_2) = \\ = \quad & \frac{1}{2}\sqrt{(1 - e_1)^2 + (1 - e_2)^2 - 2(1 - e_1)(1 - e_2)cos(2PA_1 - 2PA_2)} \end{aligned} \tag{4.8}$$

The factor $1/2$ is posited to obtain a maximal distance of 1.

Furthermore there is a biunivocal way to extract from two ellipses with same semi-major axis (set to 1) and same center (origin of the frame), two points, one for each ellipse, the distance between which may describe the distance between ellipses. To extract such a point from an ellipse, we consider an ellipse, we apply to each of its points a transformation of its radius keeping its angular coordinate fixed, i.e. in polar coordinates:

$$(r, \theta) \to (1 - r, \theta) \tag{4.9}$$

This transformation of coordinates is considered because if we do not consider any transformation of coordinates, the most basic choice of point which depends on axis ratio and position angle is not convenient for comparing ellipses. That is to say if we do not consider any transformation of coordinates, a point on the ellipse, which depends on position angle and axis ratio, is the tip of the semi-minor axis. If we define directly the distance between ellipses as the distance between tips of semi-minor axis, we see that for two ellipses of very small axis ratios the distance between ellipses will be very small for all position angles. This is not corresponding to a very good indicator of how different two ellipses are, because for two very thin ellipses with position angles as different as $\pi/2$, a lot of points of each ellipse is far from the other ellipse. That is why we cannot compare directly points of each ellipse which depends on axis ratio and position angle. So we have to devise a transformation of coordinates like (4.9) which will transform ellipses into something more easily comparable, or at the very least which will transform ellipses into some shapes exhibiting a point which depends on initial axis ratio and position angle, so that a notion of distance between these points may be a good indicator of how much the initial ellipses differ.

Transformation (4.9) is also connecting the shape of real ellipses to the idea exposed at the beginning of section 4.5, which is that a good space for devising distances between ellipses can be the unit disk itself.

The image of an ellipse under transformation (4.9) has a shape similar to the symbol 8. The two tips (upper and lower) of the 8 being located at the (two) points $(1-e; PA+\pi/2[\pi])$. Amid these two points, one has a principal determination of polar angle in $[-\pi/2, +\pi/2]$. We take this point and double its polar angle so that its polar coordinates become $(1 - e; 2PA + \pi[2\pi])$ One can check that the euclidean distance between two such points is the same as (4.8).

4.5.3 Maps of distances

We plotted the resulting D distances separating varying couples of ellipses on table 4.1.

We see that D_{flat} exhibits higher overall values than $D_{\theta,lin}$ and $D_{\theta,arccos}$ on the middle column.

Focusing on each line, we remark that there is a similarity separately for $D_{\theta,lin}$ and $D_{\theta,arccos}$ and a dissimilarity for D_{flat} of levels of distance between ellipses at the following locations:

- $(|\Delta PA| = \pi/4, e_1 = e_2 = 0)$, bottom left hand corner of the middle column image on table 4.1;
- $(|\Delta PA| = 0, e_1 = 0, e_2 = 1)$, top left hand corner of the left column image on table 4.1;

This is due to the fact that $D_{\theta,lin}$, $D_{\theta,arccos}$ stem from distance on a sphere whereas D_{flat} stem from distance on a disk. The explanation is similar to the one presented at the beginning of section 4.5.

Table 4.1: From upper to lower line are shown D_{flat}, $D_{\theta,lin}$, $D_{\theta,arccos}$ and D_{integ}. D_{integ} is the D distance defined in section 1.4.3. We show distances $D(|\Delta PA|, e_1, e_2)$ between two ellipses of same center and same semi-major axis. Axis ratios and position angles are (e_1, PA_1) and (e_2, PA_2). We write $|\Delta PA| = |PA_1 - PA_2|$. x-axis and y-axis are respectively e_1 and e_2. From left to right we show distances obtained for $|\Delta PA|$ fixed at 0, $\pi/4$ and $\pi/2$.

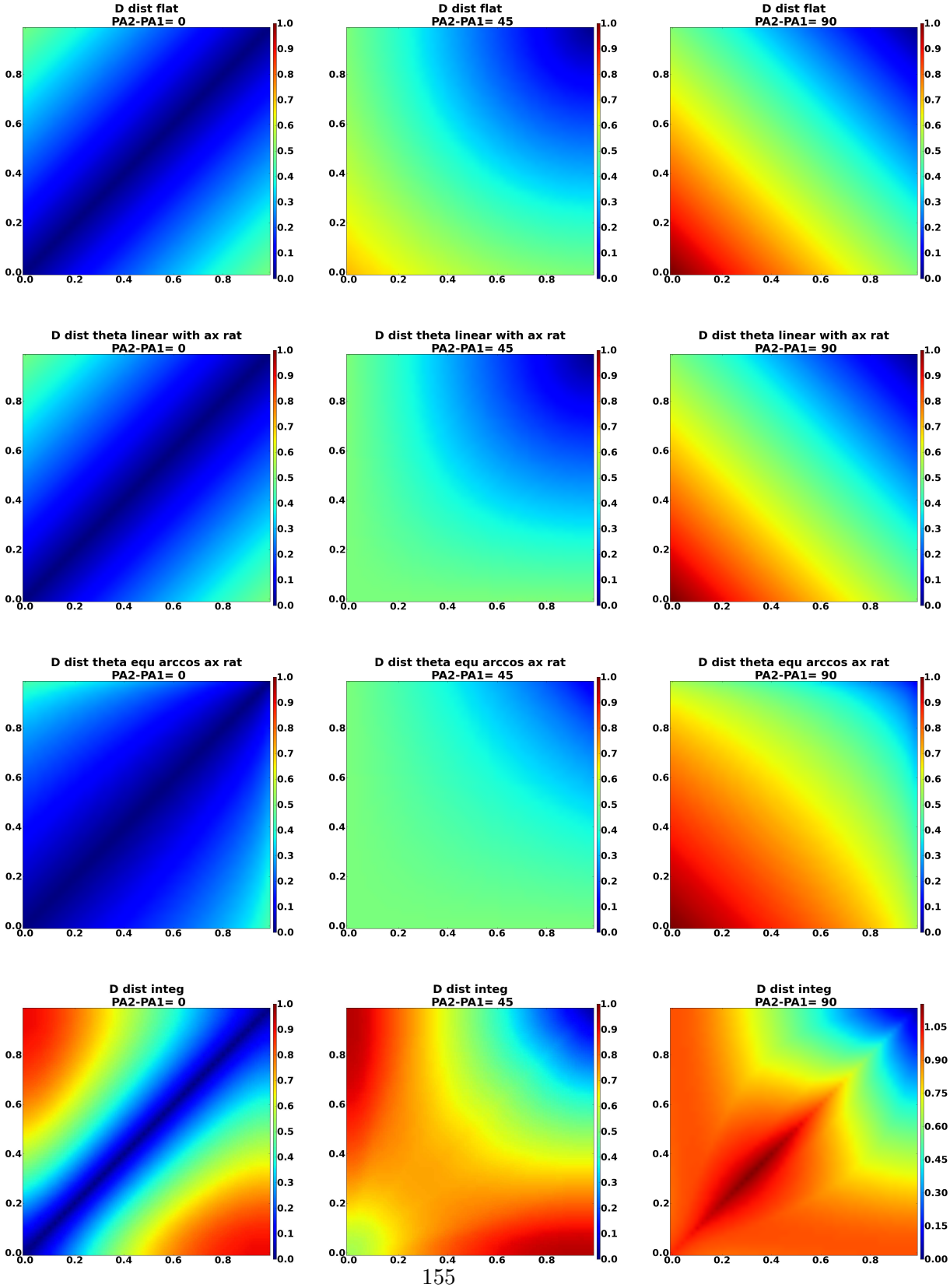

However when comparing D_{integ} to the analytic distances presented in the last few sections it is clear that D_{integ} is separating more clearly different ellipses (higher D values), especially for a difference of position angle of 0. That is the reason why we " strenghened " D_{flat}, $D_{\theta,lin}$, $D_{\theta,arccos}$ by applying to them a simple polynomial transform which consistently pushes the obtained distances toward 1. To do this we apply the transform:

$$D_{analytic,transformed} = 1 - (1 - D_{analytic,untransformed})^n$$

where n is taken such that $D_{analytic,transformed}(|PA_1 - PA_2| = \pi/4, e_1 = 0.5, e_2 = 0.5) = D_{integ}(|PA_1 - PA_2| = \pi/4, e_1 = 0.5, e_2 = 0.5)$. Thus :

$$n = \frac{\log(1 - D_{integ}(|PA_1 - PA_2| = \pi/4, e_1 = 0.5, e_2 = 0.5))}{\log(1 - D_{analytic,untransformed}(|PA_1 - PA_2| = \pi/4, e_1 = 0.5, e_2 = 0.5))}$$

Respectively for D_{flat}, $D_{\theta,lin}$, $D_{\theta,arccos}$ the obtained n indices are 2.649, 2.850, 2.124. We show modified distances together with D_{integ} in table 4.2.

We first notice the strong resemblance of $D_{flat,transformed}$, $D_{\theta,lin,transformed}$. From this we can first conclude that both disk and sphere topologies can as well be used to build indicators of how different two ellipses are.

Secondly we see that there are broadly 3 behaviours to compare:
$\{D_{flat,transformed}, D_{\theta,lin,transformed}\}$, $D_{\theta,arccos,transformed}$ and D_{integ}.

On the left column of table 4.2 we see that $D_{\theta,arccos,transformed}$ and D_{integ} exhibit somewhat opposite trends; e.g. the blue valley (small D values) vertical size is decreasing (resp. increasing) with abscissa representing axis ratios. For $\{D_{flat,transformed}, D_{\theta,lin,transformed}\}$ there is no increase of the size of the blue valley which is much more consistent with common sense as there is no reason to consider something else than

$$D(|\Delta PA| = 0^\circ, e_1 = 0.8, e_2 = 0.6) = D(0, 0.6, 0.4) = D(0, 0.4, 0.2).$$

On the middle column of table 4.2 we see that the D level is increasing at the bottom left hand corner, from bottom to top image. The highest the value of D in this location is, the best, because on middle column images, ellipses are more and more different when the point considered is closer to bottom left hand corner. Thus with this argument, images in the middle column are ordered from bottom to top as the worst to best indicator of how distant two different ellipses are. This can be marginally questionned because the very small blue patch and large green patch in the top right hand corner of $D_{\theta,arccos,transformed}$ w.r.t. other D distances, is probably due to non linear increase in $D_{\theta,arccos,transformed}$ when axis ratios decrease from unity. This latter behaviour tends to show less variations of distances between increasingly different ellipses and thus does not correspond to a good indicator of how distant two elliptical shapes are. Thus choosing the worst D distance in the middle column between the two bottom images is not clear cut but the best D distances are clearly the two top, i.e. $\{D_{flat,transformed}, D_{\theta,lin,transformed}\}$, with a slight preference for $D_{flat,transformed}$ as it has a slightly higher bottom left hand corner maximum value than $D_{\theta,lin,transformed}$.

On the right column of table 4.2, the non linearity of $D_{\theta,arccos,transformed}$ with axis ratios decreasing from unity is clearer. As there is further no good reason to think that

$$D(|\Delta PA| = 90^\circ, e_1 = 0.8, e_2 = 0.8) \neq D(|\Delta PA| = 90^\circ, e_1 = 1.0, e_2 = 0.6)$$

as is the case for the two bottom images and not for the two top images, once again the two top images are preferred over the two bottom images.

We see on table 4.2 that $D_{flat,transformed}$, $D_{\theta,lin,transformed}$, D_{integ} present the highest contrast amid the 4 distances when $|\Delta PA| = \pi/4$. As we try to build an indicator of how different

Table 4.2: We give in this figure same plots as table of figure 4.1 but for transformed distances.

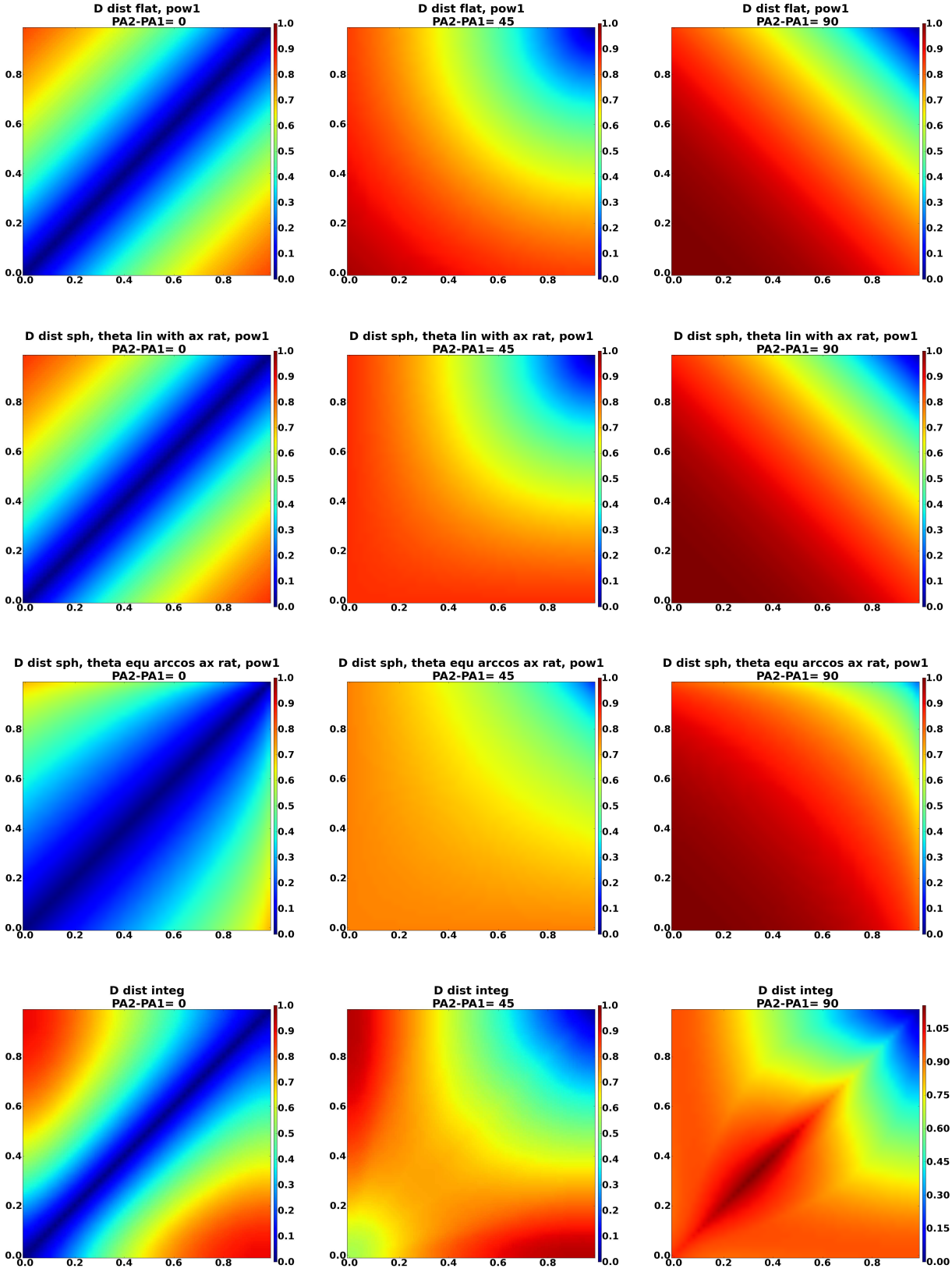

two ellipses are, we search for an indicator exhibiting a high contrast. This argument further excludes $D_{\theta,arccos,transformed}$ from the search of such an indicator.

Besides even if values atteigned by D_{integ} are a little higher than those atteigned by $\{D_{flat,tr},\ D_{\theta,lin,tr}\}$ at $|\Delta PA| = \pi/2$, and D_{integ} presents a higher contrast at $|\Delta PA| = 0$ than $\{D_{flat,tr},\ D_{\theta,lin,tr}\}$; these latter distances exhibit trends qualitatively similar to D_{integ} when ellipse parameters are varied, and D_{integ} has rather strange iso-D contours whereas $\{D_{flat,tr},\ D_{\theta,lin,tr}\}$ generally have iso-D contours much easier to understand. All this makes $\{D_{flat,tr},\ D_{\theta,lin,tr}\}$ the easiest-to-use indicators of how different two ellipses are. It is also worth noting that they are much less time consuming to compute than D_{integ}.

4.6 Stellar mass against: dust heating field, dust intercepted starlight and dust mass.

We show in this section graphs for the CDO sample of stellar mass $M_\star$ in a galactic area S (S is constant for each galaxy and corrected for inclination), for all radii (at which galactic emission dominate) against:

- average dust heating field $< U >$,
- dust mass M_d,
- $M_d \times < U >$ which is proportionnal to the dust intercepted starlight.

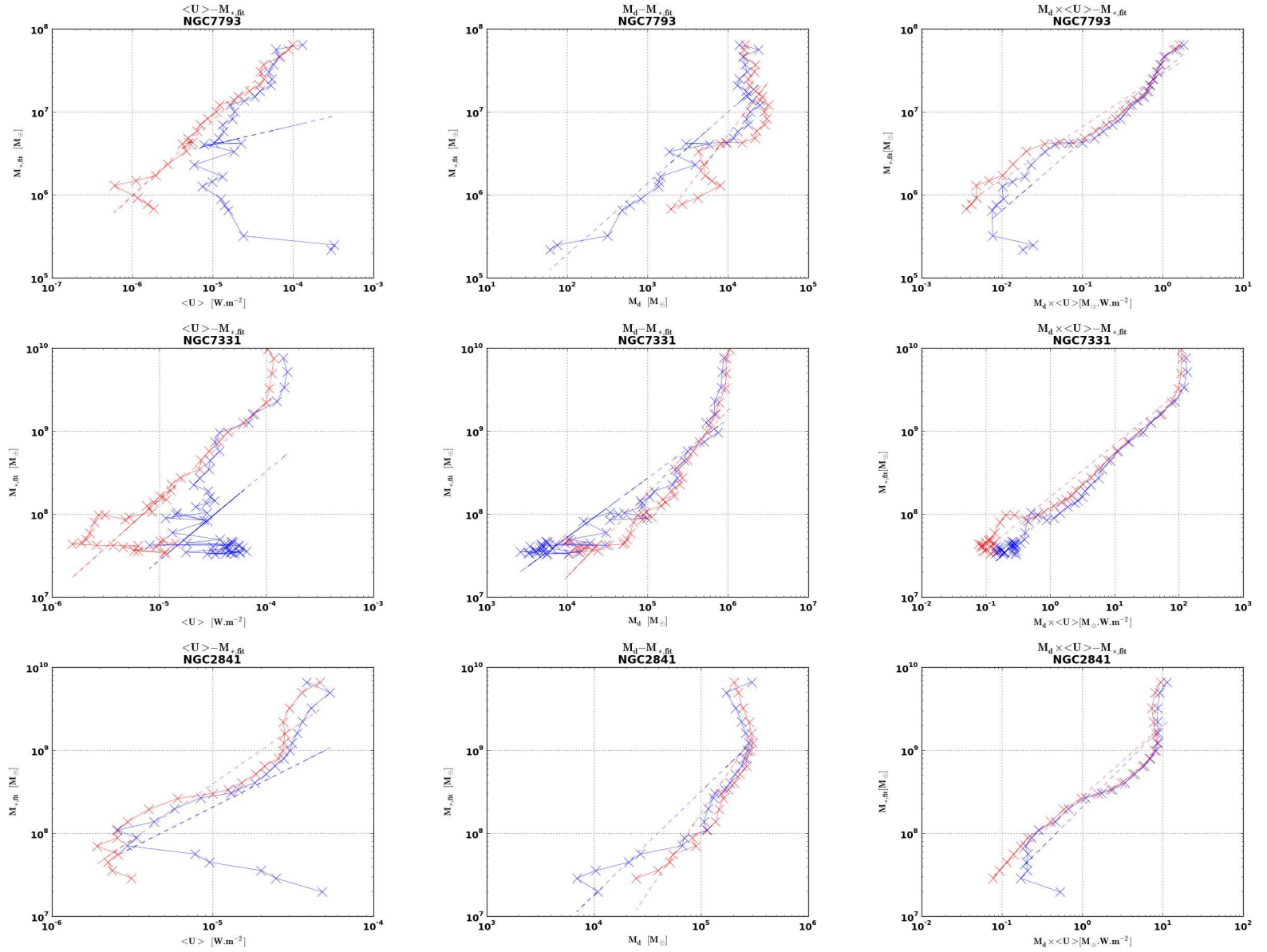

Figure 4.2: We give in these figures from top to bottom linear correlations in NGC 7793 ($S = 0.11\,kpc^2$), NGC 7331 ($S = 2.5\,kpc^2$), NGC 2841 ($S = 2.2\,kpc^2$) between logarithm of $< U >$ against $M_{\star,fit}$ (left panel), M_d against $M_{\star,fit}$ (middle panel), and $M_d \times < U >$ against $M_{\star,fit}$ (right panel). Dust mass or stellar mass are expressed in solar units, $M_\odot$, and $< U >$ in $W.m^{-2}$.

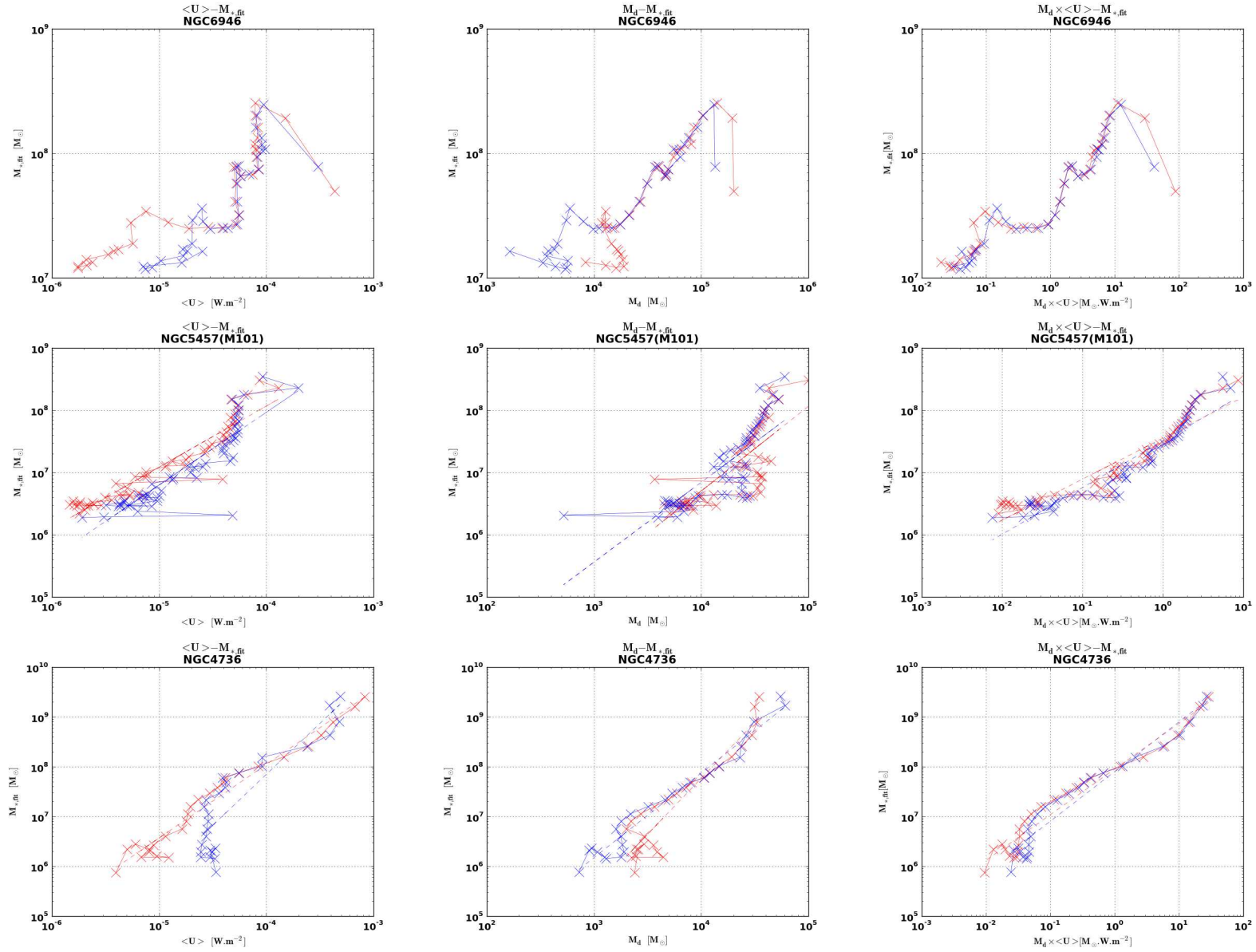

Figure 4.3: We give in these figures from top to bottom linear correlations in NGC 6946 ($S = 0.24\,kpc^2$), NGC 5457 ($S = 0.24\,kpc^2$), NGC 4736 ($S = 0.13\,kpc^2$) between logarithm of $< U >$ against $M_{\star,fit}$ (left panel), M_d against $M_{\star,fit}$ (middle panel), and $M_d \times < U >$ against $M_{\star,fit}$ (right panel). Dust mass or stellar mass are in $M_\odot$ and $< U >$ in $W.m^{-2}$.

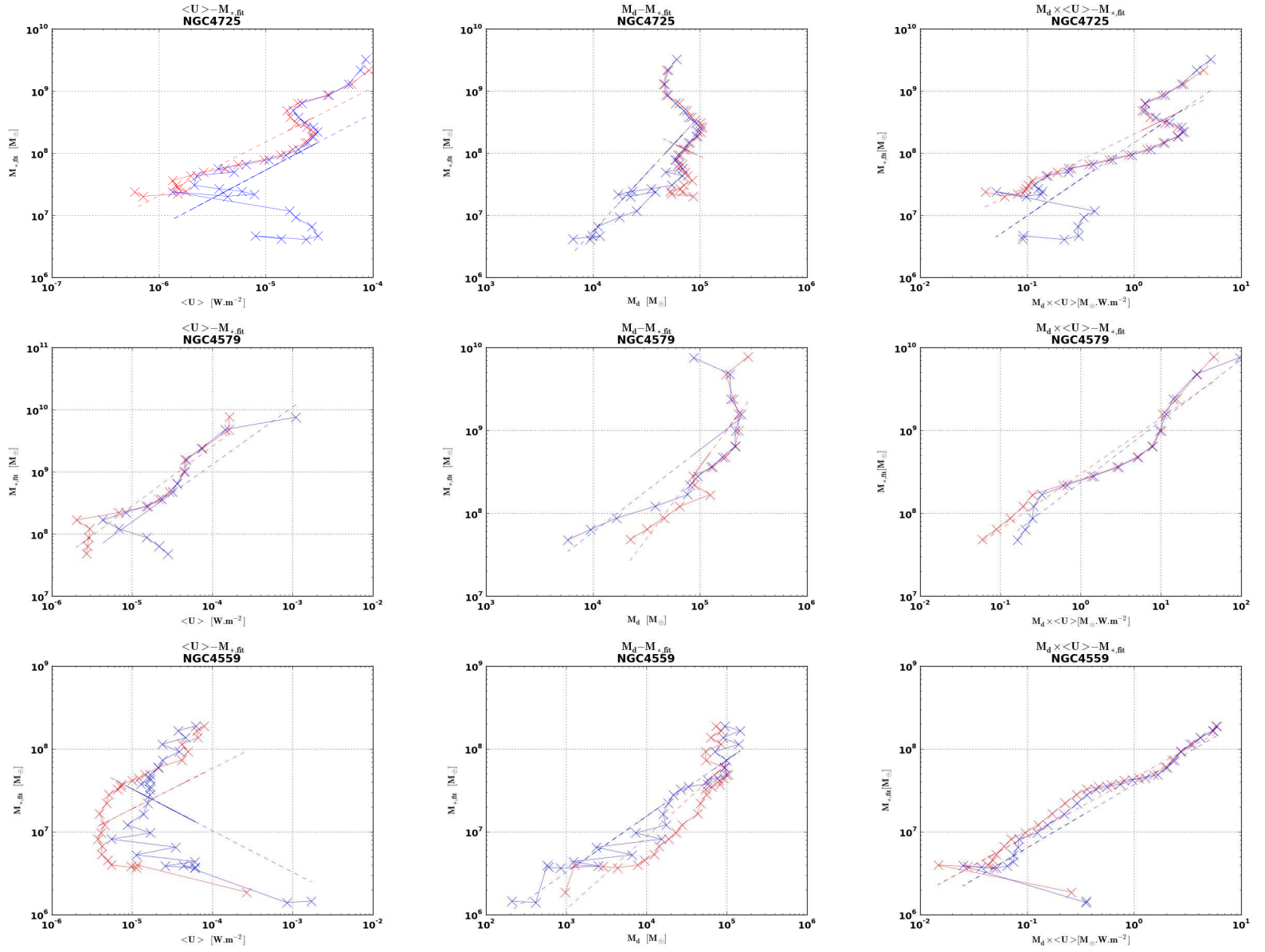

Figure 4.4: We give in these figures from top to bottom linear correlations in NGC 4725 ($S = 1.1\,kpc^2$), NGC 4579 ($S = 1.5\,kpc^2$), NGC 4559 ($S = 0.52\,kpc^2$) between logarithm of $< U >$ against $M_{\star,fit}$ (left panel), M_d against $M_{\star,fit}$ (middle panel), and $M_d \times < U >$ against $M_{\star,fit}$ (right panel). Dust mass or stellar mass are in $M_\odot$ and $< U >$ in $W.m^{-2}$.

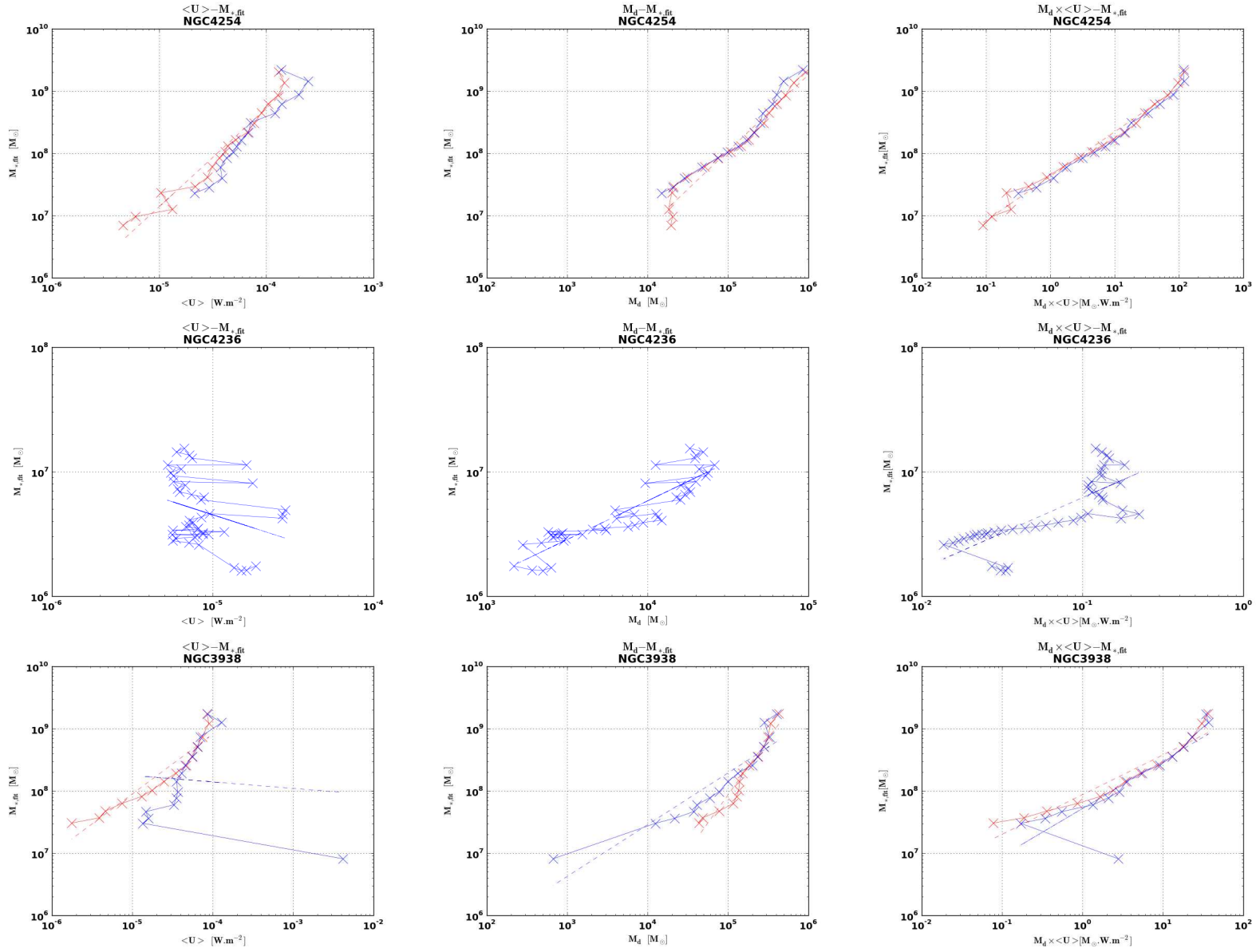

Figure 4.5: We give in these figures from top to bottom linear correlations in NGC 4254 ($S = 1.2\,kpc^2$), NGC 4236 ($S = 0.49\,kpc^2$), NGC 3938 ($S = 1.6\,kpc^2$) between logarithm of $< U >$ against $M_{\star,fit}$ (left panel), M_d against $M_{\star,fit}$ (middle panel), and $M_d \times < U >$ against $M_{\star,fit}$ (right panel). Dust mass or stellar mass are in $M_\odot$ and $< U >$ in $W.m^{-2}$. The SED fittings of PACS data series extracted from NGC 4236 are erroneous.

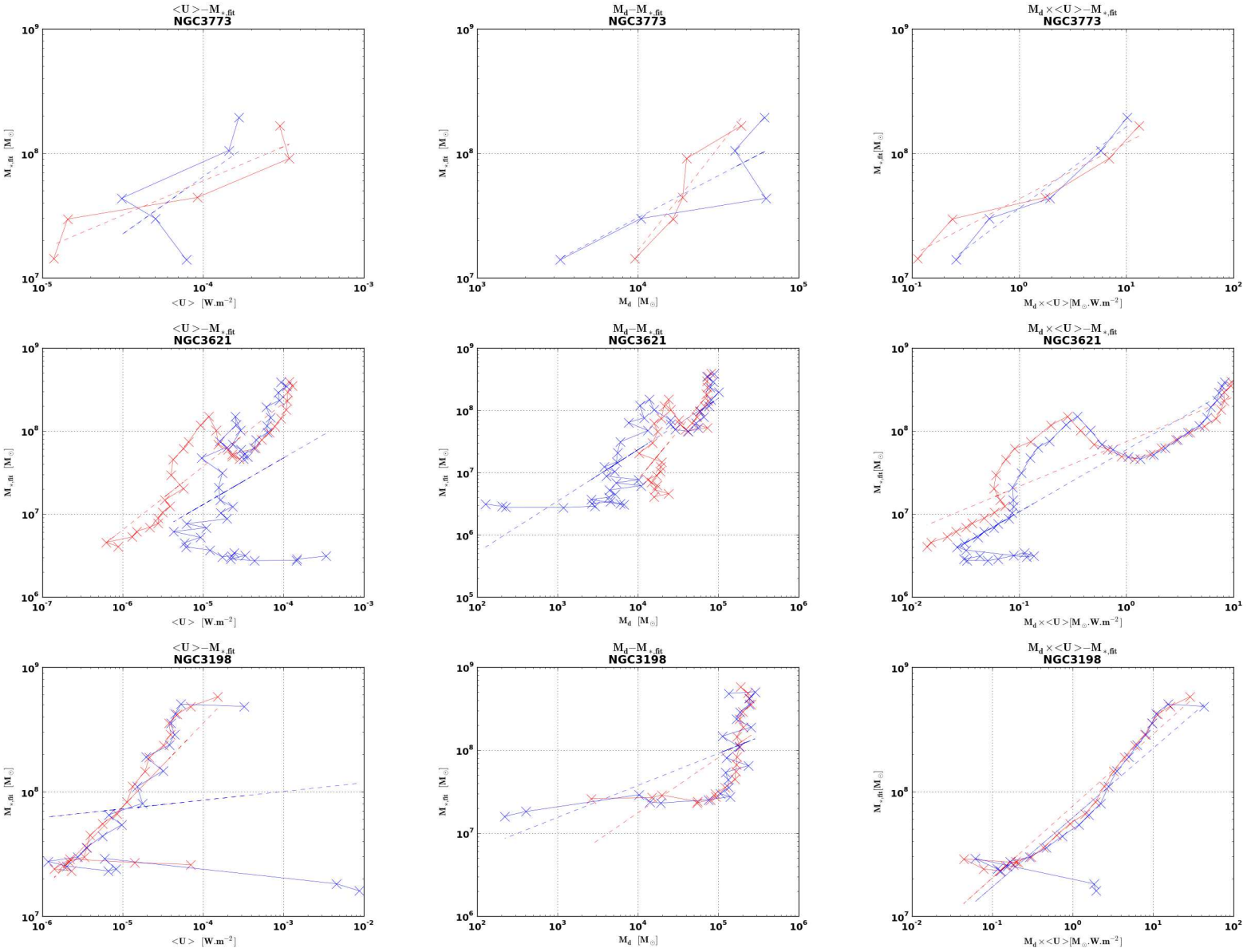

Figure 4.6: We give in these figures from top to bottom linear correlations in NGC 3773 ($S = 0.77\,kpc^2$), NGC 3621 ($S = 0.45\,kpc^2$), NGC 3198 ($S = 2.3\,kpc^2$) between logarithm of $< U >$ against $M_{\star,fit}$ (left panel), M_d against $M_{\star,fit}$ (middle panel), and $M_d \times < U >$ against $M_{\star,fit}$ (right panel). Dust mass or stellar mass are in $M_\odot$ and $< U >$ in $W.m^{-2}$.

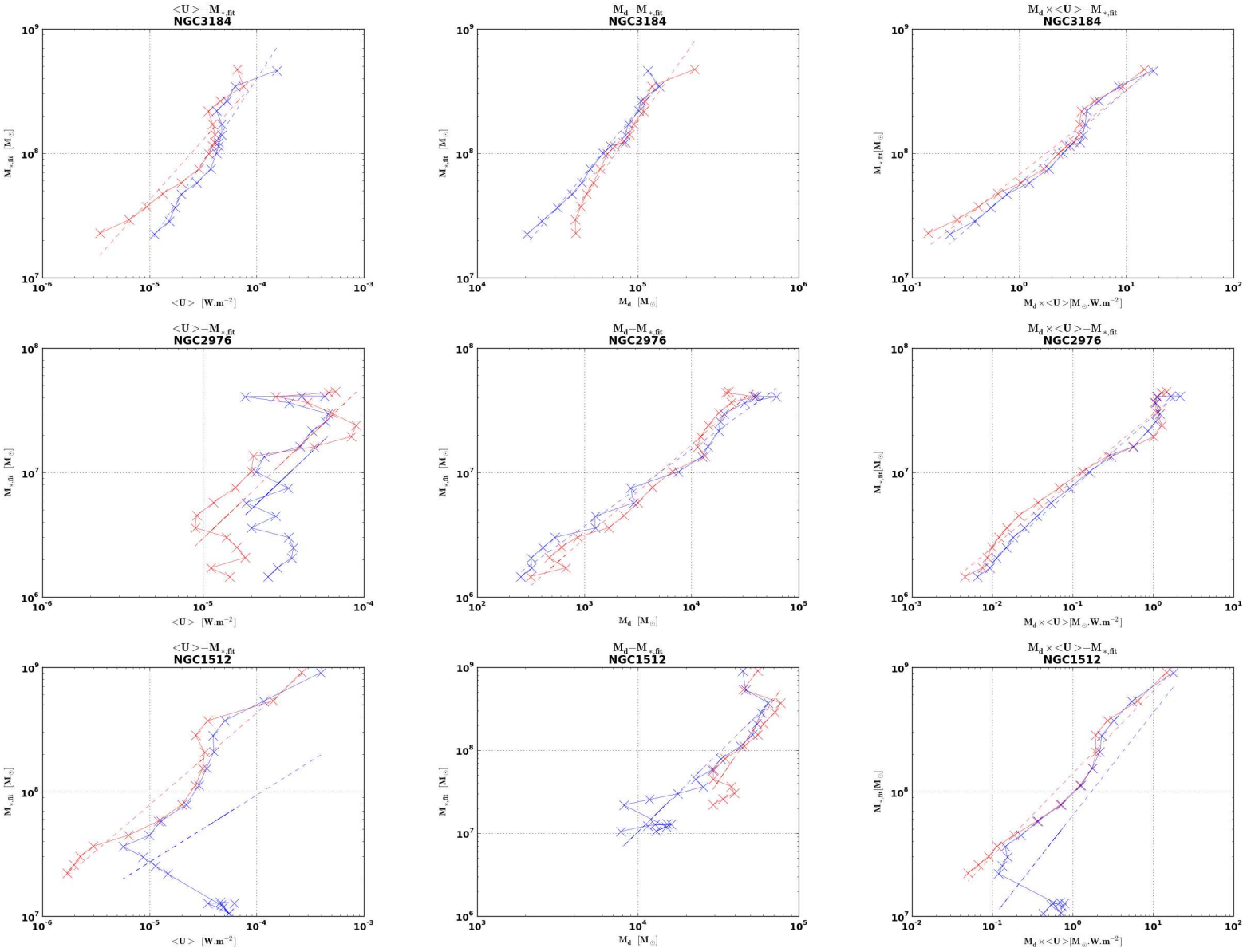

Figure 4.7: We give in these figures from top to bottom linear correlations in NGC 3184 ($S = 0.66\,kpc^2$), NGC 2976 ($S = 0.13\,kpc^2$), NGC 1512 ($S = 0.99\,kpc^2$) between logarithm of $< U >$ against $M_{\star,fit}$ (left panel), M_d against $M_{\star,fit}$ (middle panel), and $M_d \times < U >$ against $M_{\star,fit}$ (right panel). Dust mass or stellar mass are in $M_\odot$ and $< U >$ in $W.m^{-2}$.

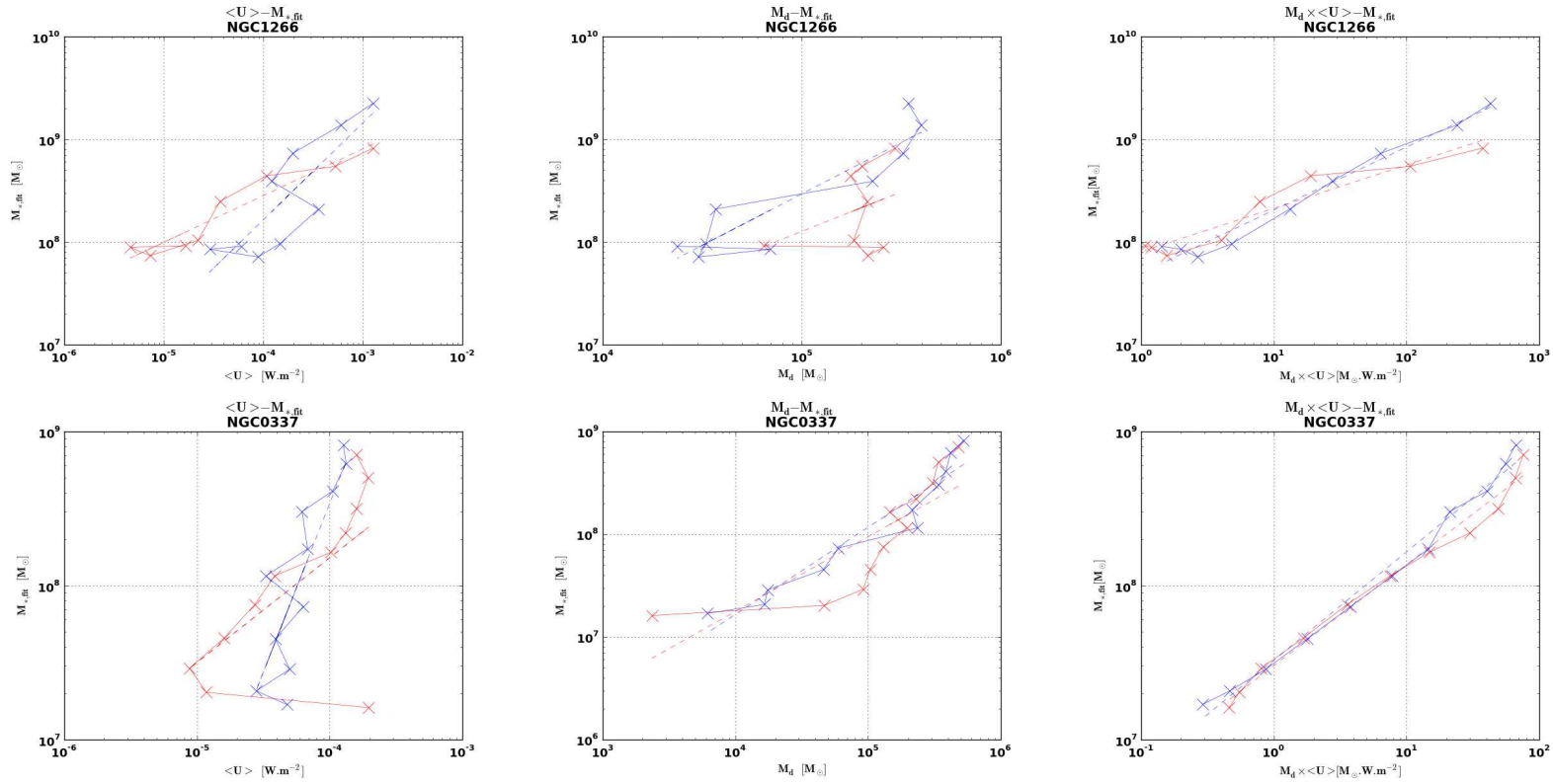

Figure 4.8: We give in these figures from top to bottom linear correlations in NGC 1266 ($S = 5.6\,kpc^2$) and NGC 0337 ($S = 2.8\,kpc^2$) between logarithm of $< U >$ against $M_{\star,fit}$ (left panel), M_d against $M_{\star,fit}$ (middle panel), and $M_d \times < U >$ against $M_{\star,fit}$ (right panel). Dust mass or stellar mass are in $M_\odot$ and $< U >$ in $W.m^{-2}$.

Bibliography

Roberto G. Abraham and Sidney van den Bergh. *The Morphological Evolution of Galaxies.* Science, 2001.

J. A. L. Aguerri, A. M. Varela, M. Prieto, and C. Muñoz-Tuñón. *Optical surface photometry of a sample of disk galaxies I. Observations and data reduction.* The Astronomical Journal, 2000.

Rene Andrae, Tim Schulze-Hartung, and Peter Melchior. *Dos and don'ts of reduced chi-squared.* The Astrophysical Journal, 2010.

G. Aniano, B. T. Draine, and D. Calzetti. *Modeling Dust and Starlight in Galaxies Observed by Spitzer and Herschel: NGC 628 and NGC 6946.* The Astrophysical Journal, 2012.

R. S. Asano et al. *Dust formation history of galaxies: dependence on the sources of dust production.* ASP Conference Series, 2011.

L. Athanassoula. *Angular Momentum Redistribution and the Evolution and Morphology of Bars.* Lecture Notes in Physics, 2003.

M. Baes, J. Fritz, N. Rangwala, et al. *Fir/Submm spectroscopy with Herschel: First results from the VNGS and H-Atlas surveys.* Baltic Astronomy, 2011.

Robert H. Becker et al. *Evidence for Reionization at $z \sim 6$: Detection of a Gunn-Peterson Trough in a z=6.28 Quasar.* The Astronomical Journal, 2001.

G. J. Bendo, A. Boselli, A. Dariush, et al. *Investigations of dust heating in M81, M83 and NGC 2403 with the Herschel Space Observatory.* The Monthly Notices of the Royal Astronomical Society, 2011.

G. J. Bendo et al. *Variations in 24μm morphologies among galaxies in the Spitzer Infrared Nearby Galaxies Survey: New insights into the Hubble sequence.* The Monthly Notices of the Royal Astronomical Society, 2007.

G. J. Bendo et al. *The JCMT Nearby Galaxies Legacy Survey III: Comparisons of cold dust, polycyclic aromatic hydrocarbons, molecular gas, and atomic gas in NGC 2403.* The Monthly Notices of the Royal Astronomical Society, 2009.

G. J. Bendo et al. *The Herschel Space Observatory view of dust in M81.* Astronomy & Astrophysics, 2010.

A. J. Benson, D. Dzanovic, C. S. Frenk, et al. *Luminosity and stellar mass functions of disks and spheroids in the SDSS and the supermassive black hole mass function.* The Monthly Notices of the Royal Astronomical Society, 2007.

F. Biegel and L. Blitz. *A Universal Neutral Gas Profile for Nearby Disk Galaxies.* The Astrophysical Journal, 2012.

Blanton. *NYU-VAGC: a galaxy catalog based on new public surveys.* The Astrophysical Journal, 2005.

Howard E. Bond et al. *HD 140283: A Star in the Solar Neighborhood that Formed Shortly After the Big Bang.* The American Astronomical Society, 2013.

C. Bot et al. *Multi-wavelength analysis of the dust emission in the Small Magellanic Cloud.* Astronomy and Astrophysics, 2004.

Mia S. Bovill and Massimo Ricotti. *Pre-reionization fossils, ultra-faint dwarfs, and the missing galactic satellite problem.* The Astrophysical Journal, 2009.

V.A. Bruce et al. *The Morphologies of Massive Galaxies at 1¡z¡3 in the CANDELS-UDS Field: Compact Bulges, and the Rise and Fall of Massive Disks.* The Monthly Notices of the Royal Astronomical Society, 2012.

R. Buta. *Mean Morphological Types of Bright Galaxies.* The Astronomical Journal, 1994.

R. Buta, S. Vasylyev, et al. *The Distribution of Bar and Spiral Arm Strengths in Disk Galaxies.* The Astronomical Journal, 2005.

R. Buta et al. *Decreased Frequency of Strong Bars in S0 Galaxies: Evidence for Secular Evolution?* The Astrophysical Journal, 2010a.

Ronald J. Buta et al. *Mid-Infrared Galaxy Morphology from the Spitzer Survey of Stellar Structure in Galaxies (S^4G): The Imprint of the de Vaucouleurs Revised Hubble-Sandage Classification System at* $3.6\mu m$. the Astrophysical Journal, 2010b.

Carignan. *Observational study of the spiral galaxy NGC 6946, II: HI kinematics and mass distribution.* Astronomy and astrophysics, 1990.

Moshe Carmeli et al. *The Cosmic Time in Terms of the Redshift.* Foundations of Physics Letters, 2006.

Bernabé Cedrés, Jordi Cepa, Angel Bongiovanni, et al. *Density waves and star formation in grand design spirals.* Astronomy and Astrophysics, 2013.

C. J. Cesarsky and M. Sauvage. *A Mid and Far Infrared View of Galaxies.* Astrophysics and Space Science, 1999.

Yu-Yen Chang et al. *Shape Evolution of Massive Early-Type Galaxies: Confirmation of Increased Disk Prevalence at* $z \geq 1$. The Astrophysical Journal, 2012.

S. Chapelon, T. Contini, and E. Davoust. *Starbursts in barred spiral galaxies. V. Morphological analysis of bars.* Astronomy and Astrophysics, 1999.

Cristina Chiappini et al. *Imprints of fast-rotating massive stars in the Galactic Bulge.* Nature, 2011.

O. Daigle et al. *H-α kinematics of the SINGS Nearby Galaxies Survey. I.* The Monthly Notices of the Royal Astronomical Society, 2005.

Julianne J. Dalcanton, David N. Spergel, and F. J. Summers. *The formation of disk galaxies.* The Astrophysical Journal, 1997.

Dale, George Helou, Alessandra Contursi, Nancy A. Silbermann, and Sonali Kolhatkar. *The infrared spectral energy distribution of normal star-forming galaxies.* The Astrophysical Journal, 2001.

J. I. Davies et al. *200μm ISO observations of NGC 6946: evidence for an extended distribution of cold dust.* The Monthly Notices of the Royal Astronomical Society, 1999.

R. S. de Jong. *Near-infrared and optical broadband surface photometry of 86 face-on disk dominated galaxies. III. The statistics of the disk and bulge parameters.* Astronomy and Astrophysics, 1995a.

Roelof S. de Jong. *Near-infrared and optical broadband surface photometry of 86 face-on disk dominated galaxies III. The statistics of the disk and bulge parameters.* Astronomy and Astrophysics, 1995b.

Gérard de Vaucouleurs. *Classification and morphology of external galaxies.* Encyclopedia of Physics, vol. 53, Ed. S. FlÃŒgge, Springer-Verlag, Berlin, 1959.

Gérard de Vaucouleurs et al. *Second Reference Catalogue of Bright Galaxies.* Texas Press, 1976.

Gérard de Vaucouleurs et al. *Third Reference Catalogue of Bright Galaxies. I: Explanations and references. II: Data for galaxies between 0h and 12h. III: Data for galaxies between 12h and 24h.* Library of Congress, 1991.

Victor P. Debattista et al. *Disk Assembly and the M_{BH}-sigma Relation of Supermassive Black Holes.* The Astrophysical Journal, 2013.

I. Dicaire et al. *H-α kinematics of the SINGS Nearby Galaxies Survey. II.* Monthly Notices of the Royal Astronomical Society, 2008.

H. Dole et al. *The Cosmic Infrared Background Resolved by Spitzer.* Astronomy & Astrophysics, 2008.

Elena D'Onghia et al. *Self-perpetuating spiral arms in disk galaxies.* The Astrophysical Journal, 2013.

S.P. Driver et al. *Two-phase galaxy evolution: the cosmic star-formation histories of spheroids and discs.* The Monthly Notices of the Royal Astronomical Society, 2013.

Yohan Dubois et al. *Feeding compact bulges and supermassive black holes with low angular-momentumcosmic gas at high redshift.* The Monthly Notices of the Royal Astronomical Society, 2012.

P.-A. Duc et al. *Gas segregation in the interacting system Arp 105.* Astronomy & Astrophysics, 1997.

Aaron A. Dutton. *On the origin of exponential galaxy disks.* MNRAS, 2009.

Aaron A. Dutton and Frank C. van den Bosch. *The angular momentum of disc galaxies: implications for gas accretion, outflows, and dynamical friction.* The Monthly Notices of the Royal Astronomical Society, 2012.

David Elbaz and Catherine J. Cezarsky. *A Fossil Record of Galaxy Encounters.* Science, 2003.

Debra Meloy Elmegreen et al. *Galaxy Morphologies in the Hubble Ultra Deep Field: Dominance of Linear Structures at the Detection Limit.* The Astrophysical Journal, 2005.

P. B. Eskridge et al. *The Frequency of Barred Spiral Galaxies in the Near-Infrared.* The Astrophysical Journal, 2000.

Laura Ferrarese and David Merritt. *A Fundamental Relation Between Supermassive Black Holes and Their Host Galaxies.* The Astrophysical Journal, 2000.

Michel Fioc and Brigitte Rocca-Volmerange. *PEGASE: a UV to NIR spectral evolution model of galaxies, Application to the calibration of bright galaxy counts.* Astronomy and Astrophysics, 1997.

Andrew Fitzgibbon, Maurizio Pilu, and Robert B. Fisher. *Direct Least Square Fitting of Ellipses.* IEEE, 1999.

J. Franco, F. Ferrini, and G. Tenorio-Tagle. *Star Formation, Galaxies, and the Interstellar Medium.* Press syndicate of the University of Cambridge, 1993.

K. C. Freeman. *On the disks of spiral and S0 galaxies.* The Astrophysical journal, 1970.

Dimitri A. Gadotti. *Structural properties of pseudo-bulges, classical bulges and elliptical galaxies: an SDSS perspective.* The Monthly Notices of the Royal Astronomical Society, 2008.

M. Galametz et al. *Mapping the cold dust temperatures and masses of nearby Kingfish galaxies with Herschel.* The Monthly Notices of the Royal Astronomical Society, 2012.

F. Galliano, S. Hony, J.-P. Bernard, C. Bot, S. C. Madden, J. Roman-Duval, M. Galametz, A. Li, M. Meixner, C. W. Engelbracht, V. Lebouteiller, K. Misselt, E. Montiel, P. Panuzzo, W. T. Reach, and R. Skibba. *Non-standard grain properties, dark gas reservoir, and extended submillimeter excess, probed by Herschel in the Large Magellanic Cloud.* Astronomy and astrophysics, 2011.

Frèdèric Galliano. *Ètude Multi-Longueurs d'Onde de Galaxies Naines Proches : Propriètès des Milieux Interstellaires.* Paris Sud University, 2004.

Karl Gebhardt et al. *A Relationship Between Nuclear Black Hole Mass and Galaxy Velocity Dispersion.* The Astrophysical Journal, 2000.

Riccardo Giovanelli and Martha P. Haynes. *Extinction in Sc Galaxies.* The Astronomical Journal, 1994.

Riccardo Giovanelli and Martha P. Haynes. *Dependence on luminosity of photometric properties of disk galaxies: surface brightness, size, and internal extinction.* The Astronomical Journal, 1995.

Nickolay Y. Gnedin and Andrey V. Kravtsov. *On the Kennicutt-Schmidt Relation of Low-Metallicity High-Redshift Galaxies.* The Astrophysical Journal, 2010.

K. D. Gordon et al. *Spatially Resolved Ultraviolet, H-alpha, Infrared, and Radio Star Formation in M81.* The Astrophysical Journal, 2004.

Karl D. Gordon, Charles W. Engelbracht, George H. Rieke, et al. *The Behavior of the Aromatic Features in M101 H II Regions: Evidence for Dust Processing.* The Astrophysical Journal, 2008.

F. Governato et al. *Cuspy No More: How Outflows Affect the Central Dark Matter and Baryon Distribution in Λ CDM Galaxies.* The Monthly Notices of the Royal Astronomical Society, 2012.

Alister Graham and Matthew Colless. *Some effects of galaxy structure and dynamics on the Fundamental Plane.* The Monthly Notices of the Royal Astronomical Society, 1997.

Robert J.J. Grand et al. *Dynamics of stars around spiral arms in an N-body/SPH simulated barred-spiral galaxy.* The Monthly Notices of the Royal Astronomical Society, 2012.

M. W. Grootes et al. *Gama/H-Atlas: the Dust Opacity - Stellar Mass Surface density Relation for Spiral Galaxies.* The Astrophysical Journal, 2013.

P. J. Grosbol. *Morphology of Spiral Galaxies. I. General Properties.* Astronomy and Astrophysics, 1985.

Brent Groves et al. *The heating of dust by old stellar populations in the Bulge of M31.* The Monthly Notices of the Royal Astronomical Society, 2012.

G. Hinshaw et al. *Five-year Wilkinson Microwave Anisotropy Probe Observations: Data Processing, Sky Maps, and Basic Results.* The Astrophysical Journal, 2009.

B. W. Holwerda et al. *The Opacity of Spiral Galaxy Disks IX; Dust and Gas Surface Densities.* Astronomische Nachrichten, 2013.

E. Hubble. *Extra-galactic nebulae.* The Astrophysical Journal, 1926.

T. H. Jarrett et al. *The 2MASS large galaxy atlas.* The Astronomical Journal, 2003.

A. E. Jaskot and M. S. Oey. *The origin and optical depth of ionizing radiation in the "Green Pea" galaxies.* The Astrophysical Journal, 2013.

Linhua Jiang et al. *Physical properties of spectrscopically-confirmed galaxies at $z \sim 6$. II. Morphology of the reste frame UV continuum and Lyman α emission.* The Astrophysical Journal, 2013.

Tobias Kaufmann et al. *Angular Momentum Transport and Disk Morphology in SPH Simulations of Galaxy Formation.* The Monthly Notices of the Astronomical Society, 2006.

R. C. Kennicutt, D. Calzetti, G. Aniano, P. Appleton, L. Armus, P. Beirão, A. D. Bolatto, B. Brandl, A. Crocker, K. Croxall, D. A. Dale, J. Dononvan Meyer, B. T. Draine, C. W. Engelbracht, M. Galametz, K. D. Gordon, B. Groves, C.-N. Hao, G. Helou, J. Hinz, L. K. Hunt, B. Johnson, J. Koda, O. Krause, A. K. Leroy, Y. Li, S. Meidt, E. Montiel, E. J. Murphy, N. Rahman, H.-W. Rix, H. Roussel, K. Sandstrom, M. Sauvage, E. Schinnerer, R. Skibba, J. D.T. Smith, S. Srinivasan, L. Vigroux, F. Walter, C. D. Wilson, M. Wolfire, and S. Zibetti. *KINGFISH - Key Insights on Nearby Galaxies: A Far-Infrared Survey with Herschel: Survey Description and Image Atlas.* Publications of the Astronomical Society of the Pacific, 2011.

Robert C. Kennicutt. *The Schmidt Law: Is it Universal and What are its Implications?* The Monthly Notices of the Royal Astronomical Society, 2008.

Robert C. Kennicutt et al. *The Global Schmidt Law in Star-forming Galaxies.* The Astrophysical Journal, 1998.

M. G. Kitzbichler and S. D. M. White. *A calibration of the relation between the abundance of close galaxy pairs and the rate of galaxy merger.* The Monthly Notices of the Royal Astronomical Society, 2008.

J. H. Knapen and P. C. van der Kruit. *Scale-length determinations of exponential discs of spiral galaxies - A comparison.* Astronomy & Astrophysics, 1991.

Jin Koda, Nick Scoville, and Tetsuo Hasegawa. *Physical Conditions in Molecular Clouds in the Arm and Interarm Regions of M51.* The Astrophysical Journal, 2012.

J. Kormendy and Robert C. Kennicutt. *Secular Evolution and the Formation of Pseudobulges in Disk Galaxies.* Astronomy & Astrophysics, 2004.

Labbé et al. *Large disk-like galaxies at high redshift.* The Astronomical Journal Letters, 2003.

David R. Law et al. *An HST/WFC3-IR morphological survey of galaxies at $z = 1.5 - 3.6$. I. Survey description and morphological properties of star-forming galaxies.* The Astrophysical Journal, 2012a.

David R. Law et al. *An HST/WFC3-IR morphological survey of galaxies at $z = 1.5 - 3.6$. II. The relation between morphology and gas-phase kinematics.* The Astrophysical Journal, 2012b.

David R. Law et al. *High Velocity Dispersion in a Rare Grand Design Spiral Galaxy at Redshift z =2.18.* Nature, 2012c.

Adam K. Leroy et al. *The Star Formation Efficiency in Nearby Galaxies: Measuring where Gas Forms Stars Effectively.* The Astrophysical Journal, 2008.

Lauren A. MacArthur et al. *Structure of Disk-dominated Galaxies. II. Color Gradients and Stellar Population Models.* The Astrophysical Journal, 2004.

Alan Macdonald. *Comment on "The Cosmic Time in Terms of the Redshift", by Carmeli et al.* Foundations of Physics Letters, 2013.

S. Madden et al. *The elusive ISM of dwarf galaxies: excess submillimetre emission and CO-dark molecular gas.* Proceedings of the 5th Zermatt Symposium, 2011.

Eliseo Stefano Maini. *Robust Ellipse-Specific Fitting for Real-Time Machine Vision.* Lecture Notes in Computer Science Volume 3704, 2005, pp 318-327, 2005.

F. Mannucci and G. Cresci. *Galaxy metallicity near and far.* Invited talk at the 54th SAIt congress, Naples, 4-7 May 2010, 2010.

Karen L. Masters et al. *Galaxy Zoo: Bars in Disk Galaxies.* The Monthly Notices of the Royal Astronomical Society, 2010a.

Karen L. Masters et al. *Galaxy Zoo: passive red spirals.* The Monthly Notices of the Royal Astronomical Society, 2010b.

J. S. Mathis, P. G. Mezger, and N. Panagia. *Interstellar radiation field and dust temperatures in the diffuse interstellar matter and in giant molecular clouds.* Astronomy and Astrophysics, 1983.

John S. Mathis, William Rumpl, and Kenneth H. Nordsieck. *The size distribution of interstellar grains.* The Astrophysical Journal, 1977.

Lars Mattsson and Anja C. Andersen. *On the dust abundance gradients in late-type galaxies: II. Analytical models as evidence for massive interstellar dust growth in SINGS galaxies.* The Monthly Notices of the royal Astronomical Society, 2012.

Lars Mattsson et al. *On the dust abundance gradients in late-type galaxies - I. Effects of destruction and growth of dust in the interstellar medium.* The Monthly Notices of the royal Astronomical Society, 2012.

Christopher F. McKee and Eve C. Ostriker. *Theory of Star Formation.* The Annual Review of Astronomy and Astrophysics, 2007.

J. Mendez-Abreu et al. *Structural properties of disk galaxies I. The intrinsic ellipticity of bulges.* Astronomy & Astrophysics, 2007.

Erin Mentuch et al. *A Simple Connection Between the Near- and Mid-infrared Emission of Galaxies and Their Star Formation Rates.* The Astrophysical Journal, 2010.

L. Mestel et al. *On the Galactic Law of Rotation.* The Monthly Notices of the Astronomical Society, 1963.

I. Minchev et al. *A New Mechanism for Radial Migration in Galactic Disks: Spiral-Bar Resonance Overlap.* The Astrophysical Journal, 2010.

Miguel F. Morales and J. Stuart B. Wyithe. *Reionization and Cosmology with 21 cm Fluctuations.* The Annual Review of Astronomy and Astrophysics, 2010.

J.C. Muñoz-Mateos. *Radial distribution of stars, gas and dust in SINGS galaxies: II. Derived dust properties.* The Astrophysical Journal, 2009.

Juan Carlos Muñoz-Mateos. *Analysis of the spatial distribution of stars, gas and dust in nearby galaxies.* Proceedings of the X Scientific Meeting of the Spanish Astronomical Society, 2012.

S. Naoz et al. *The first stars in the universe.* The monthly notices of the royal astronomical society, 2008.

T. Okamoto. *The origin of pseudobulges in cosmological simulations of galaxy formation.* The Monthly Notices of the Royal Astronomical Society, 2012.

D. Pierini and C. S. Möller. *Dust emission in the far-IR as a star formation tracer at $z = 0$: systematic trends with luminosity.* The Monthly Notices of the Royal Astronomical Society, 2003.

Planck Collaboration. *Planck 2013 results. XVI. Cosmological parameters.* Astronomy and Astrophysics, 2013a.

Planck Collaboration. *Planck 2013 results. I. Overview of products and scientific results.* Astronomy & Astrophysics, 2013b.

M. Pohlen and I. Trujillo. *The structure of galactic disks.* Astronomy and astrophysics, 2006.

M. Pohlen et al. *The case of M99 (NGC 4254) and M100 (NGC 4321).* Astronomy and Astrophysics, 2009.

C. C. Popescu et al. *A comparative study of the spatial distribution of ultraviolet and fra infrared fluxes from M101.* European Space Agency proceeding, 2005.

M. Prieto et al. *Optical Surface Photometry of a Sample of Disk Galaxies. II Structural Components.* Astronomy and astrophysics, 2000.

Radburn-Smith. *Outer-disk populations in NGC7793: evidence for stellar radial migration.* The Astrophysical Journal, 2012.

Brant E. Robertson et al. *Early star-forming galaxies and the reionization of the Universe.* Nature, 2010.

W. Romanishin. *Star Formation in Spiral Galaxies I. Halpha Observations.* The Astronomical Journal, 1990.

Rok Roskar et al. *Clues to Radial Migration from the Properties of Outer Disks.* The Galaxy Disk in Cosmological Context, Proceedings International Astronomical Union Symposium No. 254, 2008.

H. Roussel et al. *The impact of bars on the mid-infrared dust emission of spiral galaxies: global and circumnuclear properties.* Astronomy & Astrophysics, 2001a.

H. Roussel et al. *The relationship between star formation rates and mid-infrared emission in galactic disks.* Astronomy & Astrophysics, 2001b.

Hélène Roussel. *Scanamorphos: a map-making software for Herschel and similar scanning bolometer arrays.* Publications of the Astronomical Society of the Pacific, 2013.

Kanak Saha, Roelof de Jong, and Benne Holwerda. *The onset of warps in Spitzer observations of edge-on spiral galaxies.* The Monthly Review of the Royal Astronomical Society, 2009.

Laura V. Sales et al. *The Origin of Disks and Spheroids in Simulated Galaxies.* The Monthly Notices of the Royal Astronomical Society, 2012.

Rubèn Sánchez-Janssen and Dimitri A. Gadotti. *Evidence for Secular Evolution of Disc Structural Parameters in Massive Barred Galaxies.* The Monthly Notices of the Royal Astronomical Society, 2012.

Marc Sauvage, Richard J. Tuffs, and Cristina C. Popescu. *Normal Nearby Galaxies.* Space Science Reviews, 2005.

Marc Sauvage et al. *The central region of spiral galaxies as seen by Herschel M81, M99 & M100.* Astronomy & Astrophysics, 2010.

M. Schmidt et al. *The Rate of Star Formation.* The Astrophysical Journal, 1959.

L. Searle and R. Zinn. *Compositions of halo clusters and the formation of the galactic halo.* The Astrophysical Journal, 1978.

Shiyin Shen et al. *THE MORPHOLOGICAL-DEPENDENT TULLY-FISHER RELATION OF SPIRAL GALAXIES.* The Astrophysical Journal, 2009.

F. Simien and G. de Vaucouleurs. *Systematics of bulge-to-disk ratios.* The Astrophysical Journal, 1986.

R. A. Skibba, C. W. Engelbracht, D. Dale, et al. *The Spatial Distribution of Dust and Stellar Emission of the Magellanic Clouds.* The Astrophysical Journal, 2012.

M. W. L. Smith and H. L. Gomez S. A. Eales. *The Hershel Reference Survey: Dust in Early-Type Galaxies and across the Hubble Sequence.* The Astrophysical Journal, 2012.

Gary Steigman. *Primordial Nucleosynthesis in the Precision Cosmology Era.* The Annual Review of Nuclear and Particle Science, 2007.

Kyle R. Stewart et al. *Angular Momentum Acquisition in Galaxy Halos.* The Astrophysical Journal, 2013.

L. A. M. Tasca and S. D. M. White. *Quantitative morphology of galaxies from the SDSS. I. Luminosity in bulges and discs.* Astronomy & Astrophysics, 2011.

Alar Toomre. *On the gravitational stability of disk of stars.* The Astrophysical Journal, 1964.

R. B. Tully. *Nearby Galaxies Catalog.* Cambridge University Press, 1988.

P.C. van der Kruit and K.C. Freeman. *Galaxy Disks.* Annual Review of Astronomy and Astrophysics, 2011.

A. Vogler et al. *Dissecting the spiral galaxy M83: mid-infrared emission and comparison with other tracers of star formation.* Astronomy & Astrophysics, 2005.

Jing Wang, Guinevere Kauffmann, and Roderik Overzier. *The GALEX Arecibo SDSS survey - III. Evidence for the inside-out formation of Galactic discs.* The Monthly Notices of the Royal Astronomical Society, 2011.

Peng Wang and Tom Abel. *Dynamical treatment of virialization heating in galaxy formation.* The Astrophysical Journal, 2008.

Guy Worthey. *Synthetic Stellar Populations.* Encyclopedia of Astronomy and Astrophysics, 2000.

Chun Xu et al. *Redshifts of emission-line objects in the Hubble Ultra-Deep Field.* The Astronomical Journal, 2007.

R. Yates et al. *The relation between metallicity, stellar mass and star formation in galaxies: an analysis of observational and model data.* The Monthly Notices of the Royal Astronomical Society, 2012.

H. J. Zahid et al. *The observed relation between stellar mass, dust extinction and star formation rate in local galaxies.* The Astrophysical Journal, 2012.

H. Jabran Zahid et al. *The Chemical Evolution of Star-Forming Galaxies Over the Last 11 Billion Years.* The Astrophysical Journal, 2013.

D. Zaritsky et al. *HII Regions and the abundance properties of spiral galaxies.* The Astrophysical Journal, 1994.

Zubko, Dwek, and Arendt. *Interstellar dust models consistent with extinction, emission, and abundance constraints.* The Astrophysical Journal, 2004.

Acknowledgements

My thesis advisor Marc Sauvage helped me, and helped me out so many times I can hardly count them. Without his will, patience and very sensible character, this work would altogether not exist. His strong support in tough periods of my thesis was salutary for this work to reach its completion. For all these I am very grateful to him.

This thesis benefited from the hard work of others. Notably from the SED fitting method provided by Frederic Galliano, who also gave me all the keys to use it and explain it in a fruitful way.

I am grateful to Guillaume Pineau des Forets for his strong words encouraging me to work harder, thus making me more aware of my responsibilities. He explained to me the situation of work expected from a Ph.D. student in a direct straightforward and simple way. Hearing people clearly formulating thoughts can be very beneficial at times, if not all the time.

Sophie Félix found the unhoped-for availability to point many of my mistakes in this text.

Sacha Hony first recognised it would be great to extend my exploration of galactic maps to IRAC 4.5 microns maps. This resulted in the early extension of my work to all four IRAC bands. Sacha also introduced me to DS9 which enabled me to more easily draw ellipses on galactic maps. It proved actually crucial as almost half of my thesis is figuring out how to consistently quantify the variations of elliptical shapes of isophotes extracted from galaxy maps and what one can do with that.

Pierre Chanial and Nicolas Barbet got me started with PYTHON programming language. Without their help I would probably still be drawing ellipses by hand.

Aurelie Romy showed me sympathy right from the beginning of my first month of Ph.D. She explained to me where I could find some useful piece of information when I needed it, at the early stages of the thesis writing.

I want to thank Suzanne Madden for her very positive words with regards to my work.

Bertrand Morin let me gladly share his office during these three years. Discussing tea and all sorts of subjects (including work) in a friendly and cool-headed atmosphere was very recreative.

I remember a useful discussion I had with Hervé Aussel going back to CEA after swimming. It gave me some ideas about what questions I should ask myself regarding my thesis work.

Once a week for three years, I presented in front of the general public of the Palais de la Découverte, popularization talks about stellar objects and galaxies. This enabled me to realize that I was able to speak in front of and interactively with a relatively large audience. I am especially thankful to Denis Savoie, Stéphane Fay, Johan Kieken and all the people from the Département d'Astronomie who make what they can to keep up the quality together with the simplicity of the scientific material presented to the public in the Palais.

I had enjoyable and pleasant discussions at CEA around a meal, a tea or a coffee machine with Marin Cortial, Piotr Tourkine, Sophie Félix, Noémie Hamon, Michel Maugan, Soumen Basak, Mainetti Gabriele, Rihab Mechri, Lebouteiller Vianney, Wu Ronin and many other who will probably recognise themselves if they read those lines. I cheerfully thank all of them for that.

All the family I have especially my parents and my sister supported me unconditionnally during this three year time. I probably could not have been able to work as hard without their moral support.

I remember old days when my grandmother Simonne Drouhet used to help me to work one hour a day everyday during summer holidays. My grandfather Jean Drouhet was the first to

show me the stars, the moon and explain to me the nightsky. They sure both have their share in this work.

It is dubious that I would have been able to complete this work without the loving presence of Camille Béatrix and the strong support I received from as well as the kind and comforting discussions I had with members of her family.

Actually many people contributed more than I could say to my thesis by treating me good during holidays, so that I could work a lot during these calm periods of time which proved very beneficial. I had the strong memory of such working holidays first with my parents reading litterature on my thesis subject near Saint Flour, then in Saint-Raphael with Claude Camut, in Gex with Jeannine Camut, in Marvejols with Dror and Isabelle Alexinitzer, where I created the D distance between ellipses, and then during the thesis writing in Arcachon and Villefranche sur Saone with Pascal Béatrix , Francine Camut and Vincent Béatrix.

I would not have been able to work as a Ph.D. student without the trust that Achille Stocchi granted me at the end of my NPAC year, as bad as were my academic results in comparison with other students of the master that year.

Many of my professors and internship advisors had a positive teaching attitude which gave me the courage to head toward starting a thesis. I quote some of their names here, gratefully: Mr Rivera, Mr Browaeys, Mr Barbet-Massin, Mr Foulon, Mr Amiot.

Many other people that I do not personally thank here played an important role in the fact that I wrote a thesis in Astrophysics, I thank them also globally.